Electrochemical Cellular and Nucleic Acid Based Biomarker Detection of Neuroblastoma.

Colm Montgomery. B.Sc.

Thesis Submitted to Dublin City University for the Degree of Doctor of Philosophy.

School of Chemical Sciences

Dublin City University

Research Supervisor:
Prof. Robert J. Forster

January 2018

Declaration

I hereby certify that this material, which I now submit for assessment on the programme of study leading to the award of Ph.D. is entirely my own work, and that I have exercised reasonable care to ensure that the work is original, and does not to the best of my knowledge breach any law of copyright, and has not been taken from the work of others save and to the extent that such work has been cited and acknowledged within the text of my work.

Signed: _____

ID No.:_____

Date: _____

Table of contents.

Acknowledgements.

First and foremost I would like to thank Prof. Robert Forster for his continued guidance and tuition. Throughout the course of this PhD his boundless knowledge, patience and enthusiasm for research has been a guiding light, and for the past four years, it truly has been an honour to work in your research group.

I would like to extend my most sincere gratitude to the members of our research group, both past and present. I'd like to thank Elaine, Kellie, Hazel and Bincy for their invaluable help in teaching a biochemistry graduate electrochemistry. I won't say that each of you taught me everything I know because I'd say you all have reputations and careers that you'd like to keep intact, but you were each very much involved in making sure I'm at least less clueless on the way out than I was on the way in and for that I'll be forever grateful. I would also like to thank Dave, Ausra, Andrea, Mohammad, Eoin and Kerileng for their friendship, advice and help over the course of my work in DCU, and for making the lab a great place to work. Special thanks have to be made to the wonderful Samantha Douman for introducing me to the wonderful, albeit tricky, world of electrochemiluminescence, without your help I'd probably still to this day be sitting in that tiny room with no windows, in the dark, trying to make something light up!

I also need to thank the most important people in DCU, the Bruddars, Hons and Sahns. My deepest gratitude goes out to the synthesis squad in x246, where I could regularly be found mooching reagents. The genius that is Chris Burke, the instigator of the Nubar Thirsty Thursdays, over the years has done so much for me that if I was to list it here I wouldn't be able to lift this book, but suffice to say that his friendship was the most important part, I'm looking forward to the day you're running the School of Chem! Then I'd like to thank Darragh "Doc" O'Connor for keeping me in fits of laughter as only a true FCS specialist would know how, Ash better get you that bulldog soon. Aurélien Gimenez, you were one of the first people I met in our office back in the day and I still had to check that I was putting the accent over the right 'e' in your name, ohh well, as they say in France, "Banjarno". I have to thank the great Dr. Liamy Dealz Frayne, for our regularly informal seminars on "why I think electrochemistry is a load of rubbish", and for keeping me company on the weekends in the freezer that is DCU on a Saturday, you kept me going on a strict diet of nicotine, coffee and chocolate all the way up to the thesis submission. I also don't know where I'd be without Aisling Byrne. From showing me how to split cells in week one, to helping me get Raman results and confocal right up to the end, the work in this thesis bears more of your handiwork than I could ever give you credit for, but I think the most important thing you ever did in DCU was start the infamous Cawffee whatsapp, and then after that I never did a tap of work before 11am again. Then I need to give special mention Eadaoin "Hon" Carthy, you really do lift up the grim NCSR and BDI labs with just your personality, I don't think I've ever seen you

without a smile on your face doing the rounds between the buildings and I can never thank you enough for everything you've done for me from drawing and cutting chips to just showing me the trick with the vending machine. Then, the up and coming star of the MPRG, Laura o'Reilly, you've kept me laughing over coffee over the years and thank you for that, I hope I can do the same over the next few months leading up to the transfer and viva. Be grand, if I can do it, you'll sail through! Thanks as well to Suzanne McMahon for keeping me going through this, I think you spent nearly a full summer convincing me to keep at it and not leave with a masters, I never thought I'd get to this point, you're sorely missed around DCU. I have to sincerely thank Steve "pidgey" Lyons for some of the most mental sessions I've ever been on, the drinking game in DCU really got stepped up the day you started your PhD here, and for that reason alone I don't think there's anyone in the college that can call you Softboi. And last of the sahns, but certainly not least is Guilherme Berselli, thanks for all the tunes and I hope you keep it rockin' in the lazer room!

Then I need to thank some of the most important people in my life, the lads and girlos from home! In no particular order, Luke, Eoin, Darragh, Billy, Rooney, Rachel, Girvo, Liga, Vinny, Carina, Bren, Conkey, Dean, Louise, Derek, Nello, Liz, Jeremy, Laura, Rob, Simo, Lauren, Mark, Orlaith, Potter, Big Phillo, Mark and Sean. Over the last four years we've gone from the bricker to Pillester and I sincerely hope we never stop. The numerous sessions, partys, birthdays, weddings, and christenings over the last four years have been some of the best in my life, I love you all and you'll probably never realise how instrumental you all were in getting Dr. Monto through, but trust me when I say I couldn't have done it without you all. I also have to give a special mention to Rockleyboys™, Player1, Padge Maughan, and Jer909, may that old Xbox never die.

I want to thank my family for their love and support through my time in DCU. To my sis and bro, Ciana and Cillian, love you guys. Thanks to Cian who'd never be shy of dropping in for a cuppa tae, or a cheeky beer, and a good two hour chin wag. But most of all I want to thank the fabulous woman that is my mother Mairead. You have loved and supported me in every decision I've made from day one, and I'm lucky to have a person I can rely on as much as you. I promise, if I ever head back to college again, I'll learn something useful like car repair or plumbing!

And finally I'd like to thank Louise. Words can't describe here how much you mean to me and no matter how many long tough days I had in the lab, knowing I had you to go home to at the end of it all was what kept me going. Without your love and support none of this would have been possible.

…so for one last time, CELLS. ARE. DEAD.

Glossary of Acronyms

3MPA	-	3-Mercaptopropionic Acid
AFM	-	Atomic Force Microscopy
Ag/AgCl	-	Silver/ Silver Chloride Reference Electrode
AgNP	-	Sliver Nanoparticles
AuNP	-	Gold Nanoparticles
Bio-FET	-	Field Effect Transistor based Biosensors
cDNA	-	Complementary DNA
CTC	-	Circulating Tumour Cells
CV	-	Cyclic Voltammetry
CBTF	-	sodium 4-((4-(cyanoethynyl)benzoyl)oxy)-2,3,5,6-tetrafluorobenzenesulphonate
DCC	-	Dicyclohexylcarbodiimide
DMF	-	Dimethylformamide
DMSO	-	Dimethyl Sulfoxide
DNA	-	Deoxyribonucleic acid
DPBS	-	Dulbecco's Phosphate Buffered Saline
DPV	-	Differential Pulse Voltammetry
ECL	-	Electrochemiluminescence
EDC	-	1-ethyl-3-(3-dimethylaminopropyl)carbodiimide hydrochloride
EIS	-	Electrochemical Impedance Spectroscopy
EMEM	-	Eagle's Minimal Essential Media

EtOH	-	Ethanol
FcMeOH	-	Ferrocene Methanol
FeSEM	-	Field emission Scanning Electron Microscopy
H_2O_2	-	Hydrogen Peroxide
H_2SO_4	-	Sulphuric Acid
HPLC	-	High Pressure Liquid Chromatography
HRP	-	Horseradish Peroxidase
ITO	-	Indium Tin Oxide
LNA	-	Locked Nucleic Acid
MDHA	-	16-mercaptohexadecanoic acid
miRNA	-	Micro RNA
mRNA	-	Messenger RNA
MLCT	-	Metal to Ligand Charge Transfer
NSL	-	Nanosphere Lithography
NHS	-	N-Hydroxysulphosuccinamide
PB	-	Phosphate Buffer
PBS	-	Phosphate Buffered Saline
PCR	-	Polymerase Chain Reaction
PDB	-	Polydimethoxybenzidine
PEG	-	Polyethylene Glycol
PNA	-	Peptide Nucleic Acid
proPTNP	-	Probe Labelled PTNP
PtNP	-	Platinum Nanoparticles

PtNP-Ab	-	Antibody Labelled PtNP
R	-	Resistance
R_{ct}	-	Charge Transfer Resistance
RGD	-	Arginine-Glycine-Aspartate Peptide
Rluc	-	*Renilla* Luciferase
RNA	-	Ribonucleic Acid
RT – qPCR	-	Reverse Transcriptase - quantitative PCR
$Rubpy_3$	-	Ruthenium II tris-bypyridine
$RuPICNH_2$	-	ruthenium (II) (bis-2,2-bipyridyl)-2(4aminophenyl) imidazo[4,5-f][1,10]phenanthroline
SAM	-	Self-Assembled Monolayer
SEM	-	Scanning Electron Microscopy
SERS	-	Surface Enhanced Raman Spectroscopy
SEECL	-	Surface Enhanced Electrochemiluminescence
THF	-	Tetrahydrofuran
T_m	-	Melting Temperature
TPA	-	Tripropylamine
UTR	-	Untranslated Region

List of Figures

nucleic acid binding protein with a high affinity for the binding of RNA duplexes. Upon hybridisation of the target miRNA with a probe the duplex becomes bound to the CIRV 19 and this event confers a change in the surface chemistry of the semiconducting channel, effectively acting as a gate and changing the capacitance of the silicon nanowires. This change in capacitance can be used to measure the concentration of miRNA bound to the BioFET. Reproduced from Ramnani, P., et al., *Electronic Detection of MicroRNA at Attomolar Level with High Specificity.* Analytical Chemistry, 2013. **85**(17): p. 8061-8064[55].

Page 25: Figure 1.7. Amperometrically based system developed by Gao in 2012 for the detection of miRNA. The miRNA target is complementary to the distal region of the hairpin loop and upon hybridisation the loop changes conformation to a linear strand with a single stranded proximal region. This allows a glucose oxidase conjugate nucleic acid strand to hybridise and under an applied potential the oxidation of glucose can be detected by an increase in current. This increase in current is proportional to the number of miRNA target strand hybridised to the array. Reproduced from Gao, Z.Q., *A highly sensitive electrochemical assay for microRNA expression profiling.* Analyst, 2012. **137**(7): p. 1674-1679 [34].

Page 27: Figure 1.8. Schematic representation of an amperometric miRNA detection strategy based on a gap hybridisation assay developed by Pöhlmann and Sprinzl. A four component RNA hybridisation complex, including a fully hybridised miRNA target, is stabilised by the base stacking energy created by adjacent nucleotides and brings the Esterase 2 enzyme within close proximity to the electrode surface. Esterase 2 can then catalyse the hydrolysis of p-aminophenyl butyrate to the electroactive probe p-aminophenol. The high turnover rate of Esterase 2 and the redox recycling of quinonimine to p-aminophenyl gives a two-fold amplification to signal generated and this electrochemical signal is proportional to the amount of miRNA hybridised to the electrode. Reproduced from Pöhlmann, C. and M. Sprinzl, *Electrochemical Detection of MicroRNAs via Gap Hybridization Assay.* Analytical Chemistry, 2010. **82**(11): p. 4434-4440 [51].

Page 29: Figure 1.9. Schematic representation of an amperometrically based miRNA detection strategy developed by Gao and Yang. Hybridisation of the target miRNA to the capture probes on the surface of the electrode is followed by the covalent linking of the 3' end of the target to an OsO_2 nanoparticle. The OsO_2 nanoparticle then catalyses the reduction of hydrazine under a constant applied potential which is detected as an increase in current. Reproduced from Gao, Z.Q. and Z.C. Yang, *Detection of microRNAs using electrocatalytic nanoparticle tags.* Analytical Chemistry, 2006. **78**(5): p. 1470-1477[39].

Page 37: Figure 1.10. An example of the use of an enzyme probe to mediate an amplified electrochemical signal for the detection of miRNA developed by Zhou et al. Following a the hybridisation of the miRNA target to the stem loop probe, the probe undergoes a conformational change and biotin moiety of the probe becomes exposed at the surface of the electrode. The HRP-Streptavidin conjugate is bound to the duplex through the interaction of streptavidin and biotin and the HRP can then catalyse the formation of benzoquinone from hydroquinone and H_2O_2. The enzyme

is placed in an ethanolic solution of 3MPA until a monolayer is formed on the surface(C). The array is then placed in THF to remove the polystyrene template revealing the bare surface of the inner cavity(D). The array is placed in a 1µM solution of thiolated capture RNA until a monolayer is formed (E). The array is carboxy-termini of the 3MPA are then activated through EDC-NHS coupling and anti-GD2 antibodies are conjugated to the upper surface.

Page 109: Figure 3.2. Scanning Electron Microscopy images obtained with a probe current of 35 µA and accelerating voltage of 20 kV showing the progression of microcavity electrodeposition. Atomic force microscopy data showing the formation of a three dimensional microcavity array comprised of microcavities with a depth of 1.5µm

Page 110: Figure 3.3. Cyclic voltammetry of a planar gold-silicon wafer carried out in 10mM H_2SO_4 vs Ag/AgCl at a scan rate of 100 mV/s before (blue) and after (red) the electrodeposition of a 5µM gold microcavity array to the surface. The increase in the oxide peak at approximately 800mV from planar gold to the microcavity array is indicative of an increase in the microscopic electrode surface area. Note: tick marks on the y-axis are given in 100 µA increments.

Page 115: Figure 3.4. Cyclic voltammograms of a microcavity array at varying stages of modification in 10mM H_2SO_4 between 1500 and -200 mV at a scan rate of 100 mV s^{-1} vs. Ag/AgCl. Changes in the microscopic area of the microcavity array can be seen as changes in the charge related to the reduction of gold oxide. From the newly formed microcavity array (blue) to the formation of a MDHA monolayer (red) a decrease in the surface area can be observed. The removal of the polystyrene template (green) then leads to an increase in total surface area as the clean inner surface of the microcavities is exposed. Finally a decrease in the total surface area is observed as the capture RNA monolayer is formed (orange). Note: tick marks on the y-axis are given in 100 µA increments.

Page 120: Figure. 3.5. SE SEM images of cells captured to microcavity arrays modified with anti-GD2 IgG (left) compared with microcavity arrays lacking a cell capture agent (right). A clear difference is seen in the capture efficiencies of microcavity arrays that have been modified with anti-GD2 IgG compared with those of unmodified microcavity arrays.

Page 124: Figure 3.6. Spectrophotometric data from Alamar Blue™ assay of Sk-N-AS cells captured to microcavity arrays for eight hours and trypsinized from the surface, and control cells for comparison, showing the fluorescent intensity of resorufin as resazurin is reduced.

Page 125: Figure 3.7. SEM images of antibody captured Sk-N-AS neuroblastoma cells on 5µm cavities following 1, 2 and 4 hours of incubation. Cells as time progresses cells are shown to be reverting from a spherical to a dendritic morphology typical of cultured neuroblasts giving preliminary indications that captured cells remain viable.

Page 129: Figure 3.8. Confocal images of cells at x400 magnification treated with DiOC6 (green) and DRAQ-7 (red) dyes illuminated with a 488 nm Argon laser to show the progression of lysis by osmotic imbalance as an onset of DRAQ-7 localisation within nuclei.

$RuPICNH_2$. All ECL was carried out in 100mM phosphate buffer with 50mM TPA as co-reactant vs. Ag/AgCl at a scan rate of 100 mV/s.

Page 202: Figure. 4.23. ECL intensities of Planar and AuNP ITO electrodes plotted as a function of [miR-132] incubated with the electrode surface. All ECL measurements were carried out in 100mM phosphate buffer vs. Ag/AgCl with 50mM TPA as co-reactant.

Colm Montgomery

Electrochemical Cellular and Nucleic Acid Based Biomarker Detection of Neuroblastoma

Abstract.

The rapid, specific, and sensitive detection of biomarkers for disease state and progression has become an expansive field in research due to advances in both the understanding of biomarkers and diagnostic detection strategies. The detection of both cellular and molecular biomarkers through electrochemical means provides a rapid and sensitive strategy for the detection of specific markers of disease, in this case neuroblastoma. Chapter 1 of this thesis reviews the current literature reports on both cellular and molecular biomarkers for neuroblastoma disease progression as well as detection methods, both electrochemical and otherwise, that may be applied to the detection of neuroblastoma.

In Chapter 2 the detection of cellular biomarkers of neuroblastoma via electrochemical analysis is discussed, chiefly focusing on the immobilisation of neuroblastoma cells to an electrode surface and the subsequent detection of immobilised cells through electrochemical impedance spectroscopy and amperometric detection of electrocatalytic platinum nanoparticles. Following on from this, Chapter 3 focuses on the detection of a molecular biomarker of neuroblastoma disease progression, miR-132. This detection strategy relies on the partial hybridisation of the miRNA target, miR-132, to a self-assembled monolayer of nucleic acid strands on the surface of an electrode. Electrocatalytic platinum nanoparticles uniformly decorated with probe oligonucleotides are then hybridised to the free end of the miRNA target and detected amperometrically through the electrocatalytic reduction of H_2O_2 at the nanoparticle surface.

The focus of this work then shifts in Chapter 4 to the formation of a detection strategy based on electrochemiluminescence, whereby a luminophore, Ruthenium II (bis-2,2-bipyridyl)-2(4-aminophenyl) imidazo[4,5-f][1,10] phenanthroline is immobilised to the surface of a nanoparticle decorated electrode surface and is

detected by ECL. This body of work explores possible avenues for the enhancement of the electrochemiluminescent signal generated by immobilised luminophore by plasmonic enhancement of luminescent signal through nanotexturing of electrode surfaces. Chapter 4 then details work carried out to translate this work to a working assay for the detection of miRNA using multiple combinations of nanoparticle (Au/Ag/Pt) and luminophore. By carefully selecting the electrode surface and luminophore an overall enhancement of signal is observed for immobilised probes and a calibration plot for the concentration of miR-132 applied to the electrode surface can be obtained.

Chapter 1.

Literature Review.

1. Literature Review.

1.1. miRNA and Neuroblastoma.

1.1.1. Neuroblastoma Overview.

Neuroblastoma is the most common form of extracranial solid tumour found in children and arises from embryonal malignancies within the sympathetic nervous system. Neuroblastoma in children over the age of eighteen months often requires aggressive multimodal treatment and is associated with a mortality rate of 50 – 60%[1]. However, in cases where patients are children below the age of eighteen months most cases can be cured with moderately intensive treatment and in some cases spontaneous regression can occur whereby no treatment is required[2]. This gives rise to a degree of clinical uncertainty as to whether a malignancy should be approached aggressively in order to affect the highest certainty of disease eradication or use milder treatments to spare the patient the potentially life changing effects of more aggressive treatment. Therefore, it would be favourable to have a fast, highly specific and highly sensitive method of detecting and profiling tumour cells that is minimally invasive. Reliance on age profiling for the identification of aggressive malignancies is not specific and the challenge currently is to develop an analytical approach to define malignancies so that therapeutic approaches may be tailored to patients on an individual basis. Between the 1980s and mid 2000s the standard model for screening of preclinical Neuroblastoma was the detection of catecholamine metabolites in urine[3]. However, this approach offers little information about the intrinsic properties of the metastasis and studies showed that this led to the unnecessary treatment in many cases of patients that would have had a similar outcome if their condition had not have been detected[3, 4]. This led to the cessation of a public health initiative in Japan in 2004 that had been screening infants for neuroblastoma since 1984[5].

Extensive research[6-11] has been carried out to date to identify biomarkers for different disease states of neuroblastoma, including genomic and proteomic approaches. Several studies carried out show that epigenetic regulation of cellular

processes plays an important role in neuroblastoma pathophysiology[6, 9, 11, 12] and for this reason it is an attractive approach for the identification and profiling of tumour cells. Qualitative identification of malignancies through specific epigenetic biomarker detection allows for the profiling of disease pathophysiology. This may provide insights into the disease state and the cellular processes within the malignancy, allowing clinical samples from patients to be profiled on the basis of the diseases exact state of progression. Thus, the patient's treatment can be tailored to their exact disease state, avoiding the possibility of excessive or inadequate treatment.

Patients in the later stages of disease progression and, therefore at a greater risk, have been shown to develop circulating tumour cells (CTC), the incidence of which has been linked to poorer prognoses in patients[13, 14]. Immobilisation and detection of CTC provides a minimally invasive route for the detection of disease as it circumvents the requirement for biopsy tissue sampling. Profiling of CTC can then be carried out to determine the exact pathophysiology of the malignancy and also poses an approach for the study of single cells.

1.1.2. Epigenetic Regulation and miRNA.

The field of epigenetics refers to the variety of physiological traits of a cell that are not due to a change in the sequence of its DNA, but rather the post transcriptional regulation of cellular processes, for example the regulation of messenger RNA translation by smaller genetic elements known as micro RNA (miRNA). miRNA are short non coding strands of RNA, usually around 22 nucleotides (nt) in length. They were discovered in the early nineties by Lee et al in *C. elegans*, when they found that the gene *lin-4* that was previously implicated in the timing of larval egg development did not encode for a protein but instead produced two short strands of RNA 61nt and 22nt in length, of which the former was thought to be a precursor to the latter[15]. These short RNA strands were found to be complementary to sites in the 3' untranslated region (UTR) of the *lin-14* gene that had previously been implicated in the down regulation of *lin-14* expression by Wightman et al. in 1991[16]. Further studies by Wightman et al. in 1993 showed that the transcriptional products of the *lin-4* gene led to reduced levels of the LIN-14 protein without a significant reduction in messenger RNA (mRNA). This led to the proposal of a regulatory pathway in which the silencing of the *lin-14* gene occurs by the base pairing of short *lin-4* RNAs to the 3'UTR of the *lin-14* gene transcript that interrupts protein production at the translation step[17].

Since then the biogenesis and mechanism of repression by miRNA has been elucidated and well documented in the literature. The vast majority of miRNA encoding genes are structurally similar to those of normal protein encoding genes and primary miRNA transcripts (pri-miRNA) are produced by RNA polymerase II, though some may be transcribed by RNA polymerase III. These transcripts in many cases require splicing along with capping and polyadenylation. Within the nucleus, the microprocessor complex, containing the class 2 ribonuclease III enzyme Drosha along with the RNA binding protein DGCR8, carry out the cleavage of Pri-miRNA into stem loop structures of precursor-miRNA. From the nucleus the pre-miRNA are transported to the cytoplasm by RAN-GTP dependent exportin 5 where they are fully processed to miRNA. This final processing step is carried out by the Ribonuclease III enzyme Dicer, which cleaves the stem loop from the pre-miRNA to leave a double stranded miRNA fragment. The strand that is to be used in miRNA

signalling, commonly referred to as the guide strand is then capable of associating with the protein argonaute while the remaining strand is discarded. The protein argonaute is associated with a much larger polypeptide known as the RNA Induced Silencing Complex (RISC) which carries out the silencing of mRNA to post-transcriptionally regulate gene expression within the cell. The complete RISC is directed to the mRNA via the miRNA associated with it and the miRNA hybridises to the mRNA with imperfect complementarity. Importantly, this ability of miRNA to hybridise with their targets in an imperfect manner means that a single miRNA can be implicated in the regulation of many mRNA. Once hybridised the mRNA cannot be translated and is often cleaved or localised to cytoplasmic P-bodies[18].

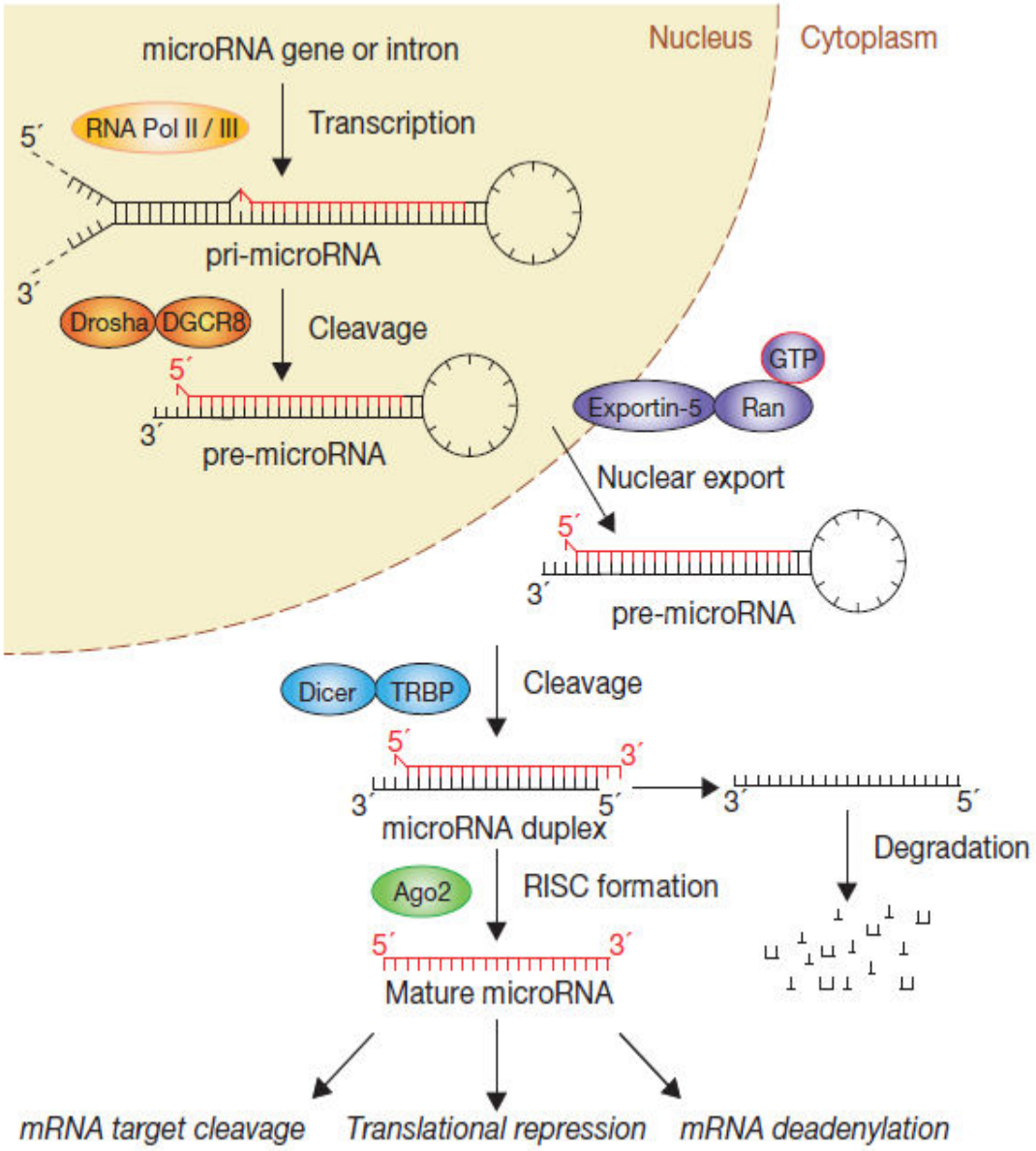

Figure 1.1. Depicted here is the archetypical pathway for miRNA. While many deviations from this linear pathway of expression exist this is by far the most common route for the expression of miRNA and its subsequent cellular regulation action. Reproduced from Winter, J., et al., *Many roads to maturity: microRNA biogenesis pathways and their regulation.* Nature Cell Biology, 2009. **11**(3): p. 228-234.[18]

1.1.3. miRNA and Oncogenesis.

Despite the discoveries made by Wightman & Lee in 1993 the field of miRNA epigenetics did not begin to gain widespread popularity until 2001 when the full extent of the involvement of miRNA in cellular regulation and disease pathophysiology began to develop[19-21]. Since then a great deal of interest has been taken in the regulatory roles of miRNA within the cell. Currently, there is a vast amount of literature detailing the involvement of miRNA in apoptosis and proliferation, and to this end there is a great deal of interest in the relationship between miRNA and cancer. Many studies have shown that the miRNA expression profile of a cancer cell can differ not only from that of a healthy cell, but can also give details about the disease state of certain tumours, including Neuroblastoma[6, 22]. The c-MYC oncogene, for example, which has been shown to be a distinctive feature of malignant Neuroblastoma along with n-myc another oncogene[23], plays a part in a whole host of reprogramming effects of the cell when aberrantly expressed, has also been shown to have a profound effect on the expression profiles of miRNA that have been implicated in the downstream regulation of genes involved in the cell cycle, apoptosis, angiogenesis and metastasis.

The c-MYC oncogenes ability to promote tumorigenesis by miRNA regulation is two-fold. Not only does it decrease the expression of miRNA involved in tumour suppression and apoptosis, but it also increases the expression of miRNA involved in cell proliferation and avoiding apoptosis. For example, c-MYC expression directly promotes the expression of the miR-17-92 miRNA gene cluster that has many roles in the development of cancer. In this cluster, miR-17 and miR-20a help to control the expression of the E2F1-3 genes that control the procession of the cell cycle from G1 to S phase. Overexpression of E2F1-3 can induce G1 cell cycle arrest and therefore expression of the E2Fs requires strict control. The inhibitory effects of these two miRNA, coupled with the promoting effects of MYC on the E2F1-3 locus has been hypothesised to fine tune the timing of activating EF2s and promote the procession of the cell cycle from G1 to S phase to avoid cell cycle arrest[24]. miR-17 along with related miRNA in its cluster also can inhibit the expression of the cyclin dependant kinase p21 which is essential for the cell cycle arrest checkpoints between G1-S and G2-M phases. Therefore, increased concentrations of these miRNA can ensure the

bypassing of DNA damage checkpoints in the cell cycle and therefore promote proliferation[25]. In contrast, many miRNA are also down regulated during aberrant expression of c-MYC that would otherwise inhibit proliferation, for example the miR-34a that controls the production of cyclin dependant kinases (CDK4, CDK6) essential for the formation of the protein kinase complex that facilitates the progression of the cell cycle[26, 27]. Therefore, the combined effects of both up and down regulation of miRNA expression has a powerful combined effect on the proliferation of the cell.

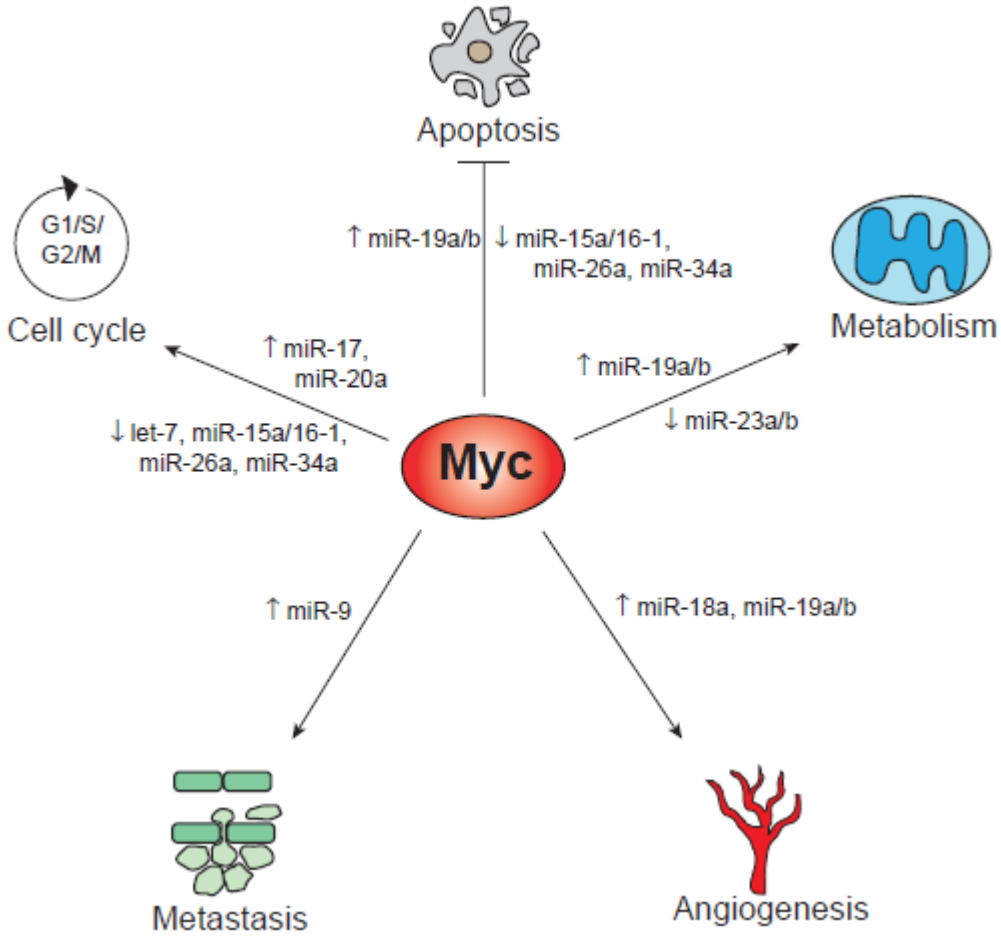

Figure 1.2. Myc mediated oncogenesis. c-Myc along with n-Myc are often found to be involved in the development of neuroblastoma. Here it can be seen that Myc mediated miRNA expression is a precipitating factor in the dysregulation of many processes that promote oncogenesis such as cell cycle upregulation and inhibition of apoptosis. Reproduced from Bui, T.V. and J.T. Mendell, *Myc: Maestro of MicroRNAs.* Genes Cancer, 2010. **1**(6): p. 568-75 [28]

c-MYC expression can also have a profound effect on avoiding apoptotic cell death by inhibiting miRNA directly involved in apoptosis. MYC directly represses the expression of the miR-15a/16-1 cluster that is involved in the silencing of the genes responsible for the formation of the BCL-2 protein that is important for inhibiting apoptosis[29]. Without these miRNA to repress BCL-2 formation the cell cannot transduce apoptosis signals. MYC also represses miR-34a, a direct target of p53 and contributor to p53 dependant apoptosis[27]. Ectopic expression of the miR-17-92 gene cluster has been shown to inhibit apoptosis without having a profound effect on proliferation in mouse models engineered with enhanced c-MYC expression. Furthermore, within this cluster it has been demonstrated that the miR-19 family can increase the signalling of phosphoinositide – 3 kinase (PI3K) by the repression of the PI3K antagonist PTEN[30]. PTEN dephosphorylates phosphatidylinositol-3,4,5-Kinase (PIP3), the target of PI3K. PIP3 regulates the activation of AKT downstream which in turn activates pathways important in cell growth and survival[31].

This underscores the extensive manner in which changes in miRNA expression by only a single oncogene can have a profound effect on a cell and it's differentiation to a tumour precursor. Therefore, if we can understand the targets of miRNA regulation and the processes their targets mediate, then we can use a cell's expression profile of, for example miR-17-92 or miR-34a, to make inferences about the cells disease state or likelihood to contribute to metastasis. This is a prime example of why the direct detection of intracellular miRNA concentrations is gaining interest. Increasing research is being directed into the identification and exploitation of miRNA as biomarkers in diseases such as Neuroblastoma.

1.2. Methods for miRNA detection: Current and Emerging.

1.2.1. Hairpins and Molecular Beacons

Since the discovery of miRNA, many different methods have been developed for their detection [32-39]. These methods may be characterised by the phase in which they are carried out, i.e. solid or solution. In general, solid phase detection methods rely on a hybridisation event between a complimentary strand of RNA covalently bound to a solid support and the target miRNA, this hybridisation event can then be detected and by changing the identity of the label used for each target and several different capture strands may be attached to a single surface giving rise to highly multiplexed assays. However, the drawback is that it is not suitable for the study of miRNA *in vivo*. Conversely, solution phase experiments rely on the hybridisation of a probe strand on RNA in solution with a target, which allows for the detection of miRNA *in vivo*, and in cases where a fluorescent probe is used to produce a signal upon hybridisation of the target and probe. Solution based methods can be used to observe intracellular localisation of miRNA.

As illustrated in *Figure 1.3*, an example of a solution based method similar to this is the employment of a RNA hairpin loop molecular beacon that has a fluorescent dye and a quencher on either ends. In the loop form, the dye and quencher are in close proximity and emission is quenched. Hybridisation with a target miRNA strand causes the dye and quencher to separate turning on emission. Typically, hairpin loops of this nature are single strands of RNA or DNA that have a region of antisense complementarity to a target miRNA flanked by short regions or self-complementarity 4-7nt in length at the 3' and 5' ends, resulting in the formation of a loop structure in the absence of the miRNA target. The 3' and 5' termini are covalently modified with a dye and a suitable quencher so that in the absence of the miRNA target the dye and quencher are in close proximity to one another and no fluorescence is observed. However, upon hybridisation with the target miRNA, the hairpin loop undergoes a conformational change, separating the 3' and 5' termini, with their bound dye and quencher molecules allowing fluorescence to be observed. This offers a highly specific, transfectable method for detecting miRNA targets

within live cells and can be exploited to determine the *relative* concentration of miRNA between intracellular locations, which may be employed to make inferences about their function. However, as a quantification tool, this method performs poorly compared to other methods available due to discrepancies in the amount of beacon successfully transfected within the cell. This method can be used to carry out in vitro quantification[33], but by far the more standard approach for *in vitro* quantification of ribonucleic acids is to use reverse transcriptase PCR (RT - PCR).

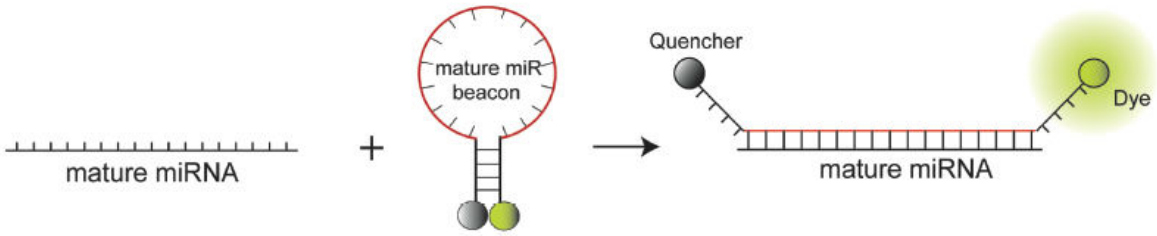

Figure 1.3. Stem loop detection method employed by Baker et al. Hybridisation of a mature miRNA to the stem loop structure of the probe separates the dye and quencher molecules in space as the termini of the probe are separated. This results in the loss of FRET between the two and the fluorescent dye may then be imaged. Therefore, the concentration of miRNA target may be measured as a function of fluorescent intensity Reproduced from Baker, M.B., G. Bao, and C.D. Searles, *In vitro quantification of specific microRNA using molecular beacons.* Nucleic Acids Research, 2012. **40**(2): p. 12 [33].

1.2.2. Amplification by PCR.

Initially used for the detection of mRNA, RT - PCR dramatically increased the sensitivity at which mRNA could be studied compared to existing techniques[40]. RT - PCR is used in the detection of RNA targets by first converting the RNA sequence to complementary DNA (cDNA) using the enzyme reverse transcriptase and then amplifying the cDNA by PCR. As the concentration of PCR products is doubled for each subsequent cycle (assuming 100% PCR efficiency) the number of cycles required to amplify the cDNA to the detection threshold is inversely proportional to the initial concentration of cDNA and therefore the initial concentration of miRNA. Quantitative analysis can be carried out by using a Taqman probe that produces a fluorescent signal with each subsequent amplification step. Taqman probes are short single stranded DNA sequences modified at either end with a fluorescent probe and complementary quencher molecule that suppresses fluorescence. During quantitative PCR the probe hybridises to the DNA to be amplified and is the hydrolysed by the 3'-5' exonuclease of Taq polymerase as it synthesises the nascent strand. As the Taqman probe is hydrolysed the quencher and fluorophore are separated and the concentration of free fluorophore can be measured. Since their initial development, these methods of mRNA detection have allowed cases of minimal disease, either early on or residual following treatment, including Neuroblastoma, to be detected[41-43].

One of the most clinically defining characteristics of neuroblastoma is the increased levels of catecholamine output and as such, nucleic acid based detection methods for the identification of Neuroblastoma are aimed at identifying increased levels of mRNA coding for Tyrosine hydroxylase , the enzyme responsible for catalysing the initial step of catecholamine synthesis. This method has been shown to be a robust and effective diagnostic tool in the detection of minimal residual disease associated with relapse and poor prognosis[22]. This method of quantifying mRNA has also been applied to miRNA. However, the small size of miRNA can pose problems. PCR usually requires a sequence to be at least double the length of the forward and reverse primers, which are usually ~20nt in length to convey good specificity. miRNA themselves are ~22nt in length and therefore are too short to amplify by traditional means. This problem can be overcome by using a stem loop structure to

produce a strand long enough to be amplified that contains the miRNA sequence. Hybridising a stem loop RT primer to the 3' end of the miRNA and initiating reverse transcription produces a strand of cDNA complementary to the miRNA on the 3' end of the stem loop structure. The stem loop itself features a universal primer sequence for the reverse primer to hybridise to and the forward primer is a DNA analogue of the miRNA. Quantification of the PCR products can be carried out in a similar fashion to the method described above. This provides a simple and relatively economical method for the detection and quantification of miRNA. This method has been shown to have improved specificity over linear primers due to base stacking and the spatial minimisation of the stem loop structure.[41] RT-qPCR is considered to be low to medium throughput, meaning that determining the expression profile of many miRNA in a cell for example could prove to be quite labour intensive, however recent work has been carried out to increase the number of miRNA that can be analysed in a single process[37]. Despite this being a useful tool for the analysis of several miRNA concentrations within a reasonably short time frame, it is limited to *in vitro* use despite being a solution phase detection method.

1.2.3. Micro-Arrays.

Despite the progress on PCR, for truly high throughput analysis of miRNA expression a microarray may be required. Micro arrays rely on the hybridisation of a solution phase target nucleic acid to a solid phase capture strand covalently bound to a substrate. Once hybridised the target can usually be visualised using a fluorescent probe. Each spot or feature on a microarray consists of picomoles of identical capture strands of DNA that will specifically hybridise to a target of interest and due to advances in microfabrication tens of thousands of DNA strands may be featured on a single chip allowing for the detection of thousands of different miRNA from a single sample. In the case of miRNA detection, the total RNA content of a sample is reverse transcribed and labelled with a fluorescent reporter molecule or a label/antigen to bind a fluorescent reporter following hybridisation and washing. Further enrichment of short RNA fragments may be carried out by fractionation prior to hybridisation to remove cDNA fragments too large to be miRNA and the resulting enriched sample is applied to the microarray. Following hybridisation, the array is washed and a fluorescent reporter molecule is applied. The microarray is then placed in a scanner which measures the relative fluorescent intensity of each feature on the array, allowing for both qualitative and quantitative analysis of miRNA expression. In a protocol published by Liu et al, the cDNA is labelled with two biotin molecules during reverse transcription and following hybridisation Alexa 647 conjugated Streptavidin is allowed to bind to the biotin. Each Streptavidin conjugate has four Alexa 647 moieties and each biotin on the cDNA can bind one Streptavidin leading to an 8 fold signal amplification of hybridisation signal[38]. Due to the capability of microarrays to carry out the analysis of thousands of miRNA concentrations from a single sample at once, they have become popular features of miRNA profiling studies, as a broad spectrum of a cells epigenetic regulatory processes can be studied in a single instance with relative ease, although for studies that do not require such levels of multiplexed analysis microarrays can be impractical owing to high manufacturing costs.

1.2.4. Quantitation Methods: Quenching.

While these methods previously mentioned require the hybridisation of a miRNA target to produce a detectable signal, methods also exist where hybridisation blocks the transmission of a signal and the observed signal is inversely proportional to the concentration of miRNA. As illustrated in *Figure 1.4.*, Cissell et al have developed both solid phase and solution phase assays based on the competitive inhibition of signalling probe by the target miRNA. In the solid phase assay, a biotinylated DNA complementary to both the target miRNA and a probe modified DNA is immobilised onto a neutravidin coated well plate. The probe DNA strand is labelled with a *Renilla* luciferase(Rluc) probe and both it and the miRNA are added to the well. Both compete to hybridise to the complementary immobilised capture surface of DNA within the well. Following hybridisation, coelenterazine is added to the well which binds to the Rluc probes and undergoes oxidative decarboxylation, resulting in emission of light. A decrease in the amount of light measured from the well results from hybridisation of unlabelled miRNA targets hybridising, thus producing a signal that is *inversely* proportional to the concentration of target miRNA initially introduced into the well, and allows the *in vitro* detection of concentrations of miRNA as low as 5pM[44]. In a similar solution based technique, a target miRNA once again is in competition with a DNA strand for hybridisation to a complementary probe. Here, the competing DNA strand is again modified with Rluc, but now the system is based on the bioluminescence resonance energy transfer (BRET) between the Rluc and a quantum dot (QD) bound to a complementary solution based probe. In the absence of miRNA the Rluc-DNA strand and the QD probe strand hybridise in solution and upon the introduction of coelenterazine as a substrate for the Rluc, a BRET signal is observed. However, in the presence of the target miRNA, hybridisation between the Rluc strand and the QD probe is competitively inhibited by the target miRNA and a decrease in signal is observed. This method has been shown to be sensitive at concentrations as low as 10nM in time frames as short as 30 minutes, resulting in a highly sensitive, rapid and specific assay that has potential applications for in vivo detection of miRNA[45].

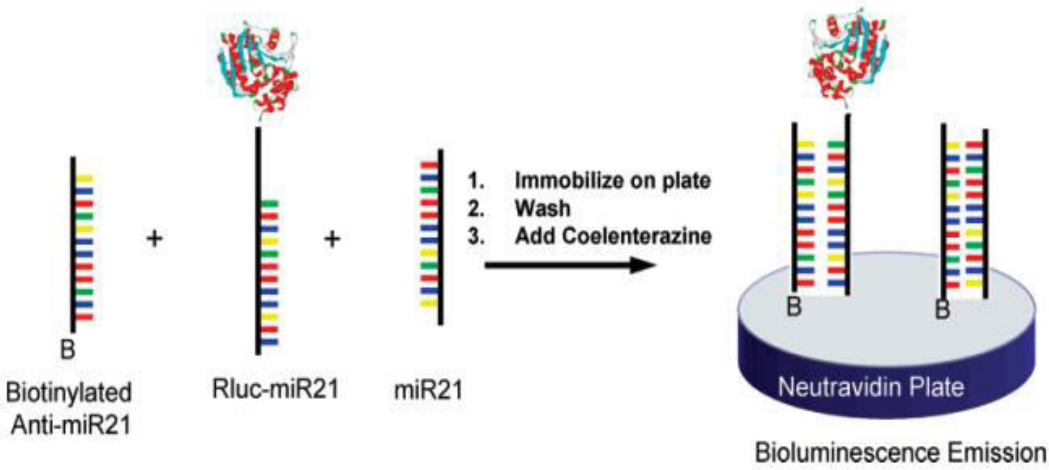

Figure 1.4. Schematic representation of the bioluminescence based miRNA assay developed by Cissell et al. Capture probes on the surface of the neutravidin plate are hybridised with either a luciferase conjugated synthetic miR-21 or an unmodified miR-21 analyte. Both miR-21 strands are complementary to the capture probe on the surface and both compete for hybridisation. Against a control, a decrease in luminescence can be observed that is proportional to the concentration of miR-21 analyte. Reproduced from Cissell, K.A., et al., *Bioluminescence-based detection of MicroRNA, miR21 in breast cancer cells.* Analytical Chemistry, 2008. **80**(7): p. 2319-2325. [44].

While the vast majority of miRNA detection techniques rely on the hybridisation of the target to a complementary strand on DNA/RNA, there are techniques that require no hybridisation step and still achieve single base difference discrimination. In a technique developed by Driskell et al, miRNA targets are allowed to adsorb non-specifically onto silver nanorods on a glass slide. Once adsorbed, surface enhanced Raman scattering is used to detect the adsorbed miRNA. This method has been shown to be capable of discriminating between single nucleotide change in the miRNA sequence and poses as a potentially powerful miRNA identification tool. This process is carried out without the need for hybridisation steps and the miRNA are detected without the need for labelling, however there are drawbacks to this method. This method is suited for use with pure samples of miRNA and reproducible spectra cannot be obtained from complex samples containing several different miRNA sequences, making it useful only as an additional step after a miRNA separation technique. Spectra must also be taken before and after each individual assay to identify their representative raman shift which will lead to labour intensive analysis[46].

1.3. Electrochemically based assays for the detection of miRNA.

1.3.1. Electrochemical detection of miRNA: Overview.

Electrochemical detection of miRNA is gaining increasing popularity due to the inherent benefits associated with electrochemical analysis[47]. The vast majority of electrochemically based assays for the detection of miRNA provide rapid, highly selective and ultra-sensitive solutions for the detection of genetic biomarkers. Extensive research has been carried out on a number of different electrochemical techniques that have the potential to be employed in point of care diagnostic systems due to their ease of manufacture, cost effective analysis and the potential for miniaturisation. The majority of these devices also provide a platform for the direct analysis of miRNA samples, circumventing the need for prior amplification treatment. Such devices may rely on a number of different electrochemical analytical techniques for the transduction and measurement of a signal for the detection of a particular genetic biomarker including potentiometry[48], amperometry[34, 39, 49-51], and impedance spectroscopy[32, 36, 52]. Electrochemical detection of miRNA in solution by potentiometry represents a quick simple and cost effective method of detecting miRNA at sub-nanomolar concentrations. Potentiometric methods involve measuring the potential of a solution between two electrodes in order to determine the concentration of an analyte within the solution and has been used for the detection of miRNA following amplification by RT-PCR by Goda et al in 2012. By using a mixed self-assembly monolayer of sulphobetaine-3-undecanethiol and thiol terminated DNA capture probe strands, target miRNA strands were hybridised to an electrode and this hybridisation conferred a change in the surface potential of the electrode due to the intrinsic negative charge of the oligonucleotide backbone. This change in surface potential through the hybridisation of miRNA targets could be monitored in real time and the limit of detection achieved was 20pM for exosomal miRNA. [48]. However, the LOD of this assay is at the upper end of the typical concentration ranges of circulating miRNA of 200aM – 20pM[53]. Therefore, this approach relies on the amplification of miRNA extracts through PCR, adding to the cost and labour of analysis.

1.3.2. Electrochemical Impedance Spectroscopy Based Detection of miRNA.

For more effective detection of miRNA in solution, a method in which the miRNA is confined to an interface may provide greater sensitivity. Electrochemical impedance spectroscopy has been used in many studies of the interaction of biomolecules throughout the literature and offers a fast, highly sensitive method for the detection of interfacial reactions, such as the hybridisation of a target miRNA to an immobilised probe at the surface of an electrode[47]. Impedance is a measure of the opposition to the flow of an electrical current within a circuit and, similarly to resistance, it is measured in Ohms. However, resistance is a concept that may only be applied to one component of a circuit, the ideal resistor, which must meet certain criteria that make resistance impractical for application in real world settings. For example, for resistance to be applicable to an AC circuit, the current must be in phase with the AC voltage, the resistance must be frequency independent and the resistance must follow Ohm's law at all currents and potentials. Often this is not the case and circuits will demonstrate far more complex behaviour that is only explained by impedance. Electrochemical Impedance Spectroscopy allows for the study of the impact a material bound to the surface of an electrode can have on polar, ionic and dielectric relaxation processes within both the electrolyte and at the electrode surface. For these reasons it has been used in the study of many biological and bioanalytical systems and has been shown, among other uses, as a powerful tool in the field of miRNA detection[32, 36, 52]. For example, in work reported by Peng et al Electrochemical Impedance Spectroscopy (EIS) was utilised as a technique for detection of miRNA[36]. An electrode modified with a mixed monolayer of nucleic acid capture oligonucleotides and 4-mercaptoaniline was used to capture miRNA strands covalently modified with 3nm RuO_2 nanoparticles. Following the hybridisation of the miRNA-RuO_2 conjugates to the electrode, the electrode was immersed in a solution of 3'3-dimethoxybenzidine and H_2O_2 for 60 minutes. The RuO_2 nanoparticles bound to the array via the hybridised miRNA catalysed the formation of a polydimethoxybenzidine (PDB) layer on the surface of the electrode in the immediate vicinity of the nanoparticle catalyst. As PDB is capable of forming an insulating layer on the surface of an electrode, as well having a low porosity leading to a blocked surface of the electrode, transfer of charge from the electrode to

redox species in solution is inhibited, therefore a change in the charge transfer resistance (R_{ct}) can be measured accurately. This, coupled with the cumulative effect of polymerisation and the first order Michaelis-Menten kinetics of PDB formation (relative to the DNAzyme concentration) made PDB the ideal material for impedance based detection. Thus, in this scheme the quantity of nanoparticles (and thus the number of miRNA hybridised) to the array is linearly proportional to the amount of PDB deposited on the surface of the electrode. The development of this polymer formation on the surface of the electrode confers a change in the electrochemical admittance of the electrodes interface and therefore a linear change in the AC impedance of a circuit containing the electrode can be observed in response to PDB deposition. This approach greatly increases the sensitivity of an impedance based detection assay over that of label free detection as the deposition of PDB on the surface of the electrode amplifies the impedimetric effect of miRNA hybridisation due to the non-conductive properties of PDB. This allowed the development of an electrochemical assay with a demonstrated lower limit of detection of 3fM miRNA[36]. In a similar study, Gao et al used an Indium Tin Oxide (ITO) electrode modified with a self-assembled monolayer of charge neutral morpholino capture probes for the label free detection of miRNA by impedance spectroscopy. The charge neutral nature of the morphilino oligonucleotides not only increases the affinity of the array for miRNA targets but also retards the non-specific deposition of dimethoxybenzidine molecules. Following hybridisation of the miRNA target the electrode is immersed in a mix of dimethoxybenzidine, H_2O_2 and Horseradish Peroxidase. PDB is then synthesised at the electrode interface where the negatively charged miRNA is hybridised and the deposition of PDB is measured as a change in the systems impedance. The advantages of this method over the previously mentioned case are the label free nature of this technique as well as a slightly increased limit of detection of 2fM [32]. This technique of hybridisation mediated PDB deposition has also been adapted by Shen et al for the ultrasensitive detection of miRNA targets using impedance spectroscopy. In their work, Shen et al used a gold electrode hybridised modified with a self-assembly monolayer of capture oligonucleotide strands. Following the hybridisation of the target miRNA to the capture oligonucleotides, the array is treated with endonuclease I removing the unhybridised capture strands. A DNA enzyme conjugate, G quadruplex hemin, was then applied to the electrode and hybridised to the lower free portion of the capture-

target hybrid complex, subsequently bringing the enzyme to the surface of the electrode. The electrode was then incubated in dimethoxybenzidine and H_2O_2 and the formation of PDB was once again detected by impedance spectroscopy, with a limit of detection of 2fM [52].

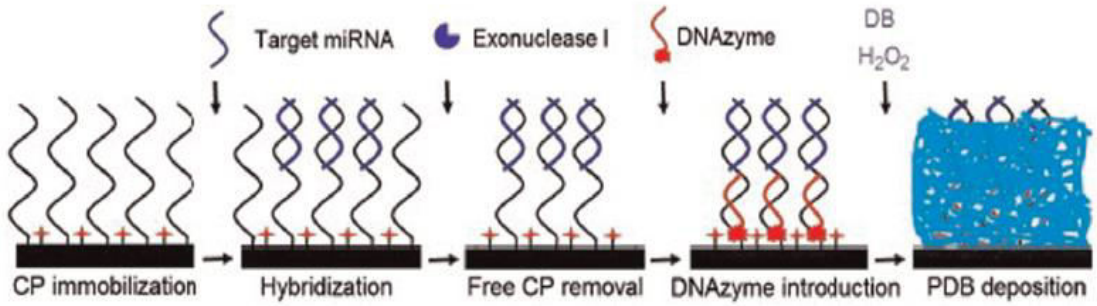

Figure 1.5. Schematic representation of an impedimetric miRNA biosensor developed by Shen et al. Unhybridised strands of capture probe on the surface of the electrode are removed by exonuclease I and hybridised strands remain, allowing the DNA conjugated enzyme to hybridise to the base of the probe and catalyse the formation of PDB, changing the impedance characteristics of the electrode surface. This change in impedance can be related to the concentration of miRNA target applied to the electrode. Reproduced from Shen, W., et al., *A label-free microRNA biosensor based on DNAzyme-catalysed and microRNA-guided formation of a thin insulating polymer film.* Biosensors & Bioelectronics, 2013. **44**: p. 171-176 [52].

1.3.3. Field Effect Transistor Based Detection of miRNA.

Field effect transistor based biosensors (Bio-FET) have significant promise due to their high sensitivity as well as their ability to deliver real time results without the need for direct chemical modification of the miRNA target[54-56]. Bio-FETs can be thought of as a three electrode system consisting of a source, drain and gate, that undergo a change in their source to drain channel conductance due to a change in the electrical environment of the semiconductor material of the channel[54]. In the case of a Bio-FET used to detect miRNA, the semiconductor is modified with a capture strand of nucleic acid that will recognise and hybridise the target miRNA to the surface of the semiconductor. The use of Bio-FETs to detect miRNA is at an advantage over that of other biomolecular detection schemes involving biomarkers derived from peptides due to the highly charged nature of RNA. Upon hybridisation of the negatively charged miRNA strand, the charge density of the semiconductor material is altered which in turn modulates the conductance of the source to drain channel which can be observed as a change in source to drain potential. Therefore, the electrical input of the charged nucleic acid species may be thought of as a gate. Due to the ability of transistors to be manufactured on the nanoscale, the semiconductor gate channel can become sensitive to minute changes in its environment, for example hybridisation of a target miRNA to a capture nucleic acid on the surface of the gate channel. The small size of the transistor (and therefore the gate channel) amplifies the charge of single nuclei acids hybridising to the surface, which can be used to create devices that have extremely low detection limits, thus making these detection schemes incredibly sensitive. Zhang et al reported the use of a silicon nanowire FET (SiNW-FET) based system for the detection of miRNA that comprised of one dimensional SiNW modified with charge neutral peptide nucleic acid (PNA). The PNA has the advantage of having a higher affinity for the target due to a lack of electrostatic repulsion between ribophophate RNA backbones. The charge neutral PNA also confers a minimal change to the charge density of the semiconductor of the Bio-FET. Following the hybridisation of the target to the capture probe a significant change in the conductance of the source to drain channel could be seen and this allowed for the development of a miRNA detection system with a limit of detection of 1fM[54]. Improving upon this design, Ramnani et al in

2013 utilised the CIRV p19 protein as a capture probe for the quantification of miRNA with a detection limit of 1aM, however the CIRV p19 has a poorer ability to differentiate between miRNA targets compared to that of a complementary strand of nucleic acid and should be used purely for quantification of miRNA concentration(*Figure 1.6.*)[55]. Work carried out by Lu et al in 2014 described the use of a complementary metal oxide semiconductor compatible SiNW-FET that allowed for the development of an assay that was capable of detection as low as 600 copies of a single miRNA, ~1zM. In conjunction with an anisotropic wet etching, this allowed for the cost effective manufacture of the nanoscale semiconductor channels that allow for the ultrasensitive, highly selective detection of miRNA[56]. However, the initial costs of fabrication of patterned, pre-etched materials, as well as the intricacies of the initial design process may prove to be only cost effective if carried out on the scale of mass production and research centres may benefit far greater from the use of simpler substrates that allow for the atto to femto molar detection of miRNA targets without the need for advanced fabrication techniques that require specialised equipment.

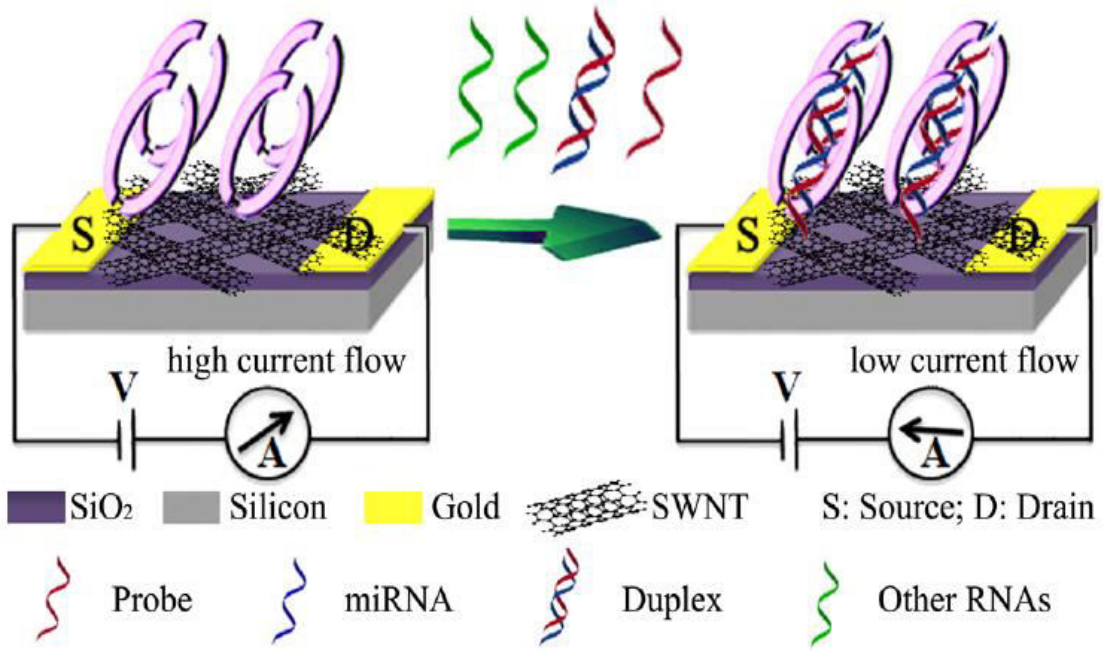

Figure 1.6. Schematic representation of the BioFET system developed by Ramnani et al for the detection of miRNA. Silicon nanowires are used as a semiconductor between the source and drain channels of this field effect transistor. The silicon nanowires are covalently modified with CIRV 19, a nucleic acid binding protein with a high affinity for the binding of RNA duplexes. Upon hybridisation of the target miRNA with a probe the duplex becomes bound to the CIRV 19 and this event confers a change in the surface chemistry of the semiconducting channel, effectively acting as a gate and changing the capacitance of the silicon nanowires. This change in capacitance can be used to measure the concentration of miRNA bound to the BioFET. Reproduced from Ramnani, P., et al., *Electronic Detection of MicroRNA at Attomolar Level with High Specificity.* Analytical Chemistry, 2013. **85**(17): p. 8061-8064[55].

1.3.4. Amperometrically Based Detection of miRNA.

Amperometrically based systems for the electrochemical detection of miRNA are among the most regularly reported in the literature and are highlighted in this review due to their relevance to the work detailed in the later chapters of this report. Amperometry is the detection of an analyte by measuring the current of a system at a constant applied voltage. As a general scheme, an amperometric device will require the immobilisation of the target nucleic acid to the surface of an electrode, often through hybridisation of the target miRNA to a self-assembled monolayer of complementary nucleic acids. This hybridisation event can then be detected through a number of means, for example the electrocatalytic activity of a covalently attached moiety on the target stand. This allows for the direct correlation of the arrays electrocatalytic activity to the number of hybridised miRNA targets. Work published by Gao and Yu in 2007 details the use of an electrocatalytic Ruthenium moiety, [Ru(1,10-phenanthroline-5,6-dione)$_2$Cl$_2$], that has the ability to bond with adenine and guanine under mild conditions for the amperometric detection of miRNA by the electrocatalytic oxidation of hydrazine. Following hybridisation of the target miRNA-Ruthenium complex a potential of 100mV was applied to the electrode and the electrooxidation current was measured in the presence of 5mM hydrazine. The miRNA detection assay had a detection limit of 200fM[49]. Gao and Yu also developed a similar amperometrically based assay for the detection of miRNA by using the osmium complex [Os(4,4'-dimethyl-2,2'-bipyridine)$_2$(Isoniazid)Cl]$^+$ covalently linked to the 3' end of a miRNA strand for the detection of immobilised target miRNA strands by the electrocatalysis of acetic acid by the osmium moiety. The electro-oxidation of the hybridised electrode was measured in the presence of 10mM acetic acid under an applied potential of 150mV vs Ag/AgCl, allowing for the detection of miRNA target concentrations as low as 800fM[50]. These methodologies, while effective at sub-picomolar concentrations, require direct modification of the target miRNA and are therefore less favourable for use in the detection of clinical miRNA samples than assays that only require the hybridisation of the target to a capture nucleic acid and avoid the requirement for the covalent modification of the target. To eliminate the requirement for direct modification or the target, assays may be developed where the electrocatalytic reporter probe in the

assay is bound to a free portion of either the immobilised capture strand on the electrode surface or a free portion of the target miRNA strand following its hybridisation to the capture strand. An example of this was work carried out by Gao in 2012, where an electrode was modified with an oligonucleotide stem loop, where the distal portion is complementary to the target miRNA. This allowed the miRNA target to open the stem loop into a linear strand conformation upon hybridisation, leaving the distal portion of the hybridisation complex free as a single strand. The single stranded region was now available for hybridisation with a second nucleic acid strand, the probe, which was covalently modified with glucose oxidase, bringing the glucose oxidase to the surface. Hybridised probes were then detected by the electrooxidation current of 60mM glucose under an applied potential of 300mV[34].

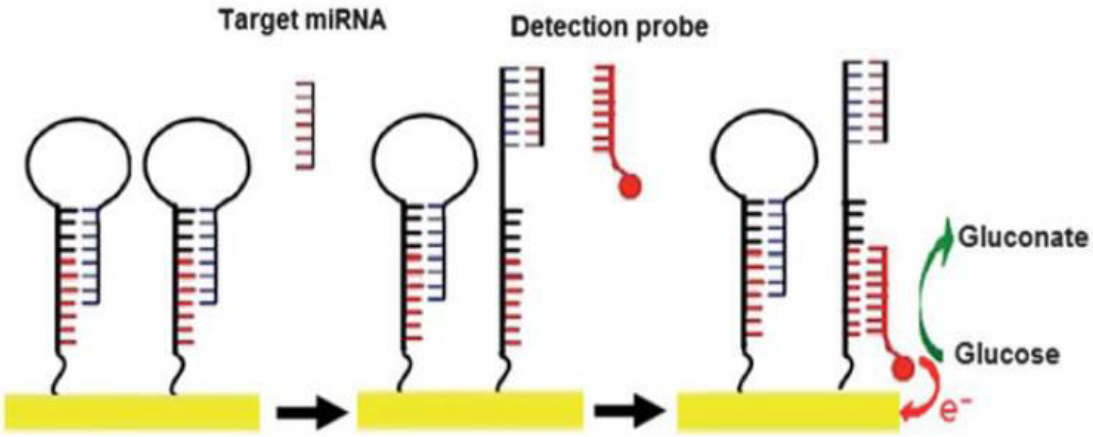

Figure 1.7. Amperometrically based system developed by Gao in 2012 for the detection of miRNA. The miRNA target is complementary to the distal region of the hairpin loop and upon hybridisation the loop changes conformation to a linear strand with a single stranded proximal region. This allows a glucose oxidase conjugate nucleic acid strand to hybridise and under an applied potential the oxidation of glucose can be detected by an increase in current. This increase in current is proportional to the number of miRNA target strand hybridised to the array. Reproduced from Gao, Z.Q., *A highly sensitive electrochemical assay for microRNA expression profiling.* Analyst, 2012. **137**(7): p. 1674-1679 [34].

In another scheme by Pöhlmann and Sprinzl, (*Figure 1.8.*) an electrode was modified with a mixed SAM of thiolated anchoring oligonucleotide and octanethiol. An oligonucleotide was hybridised to the anchoring oligonucleotide on the electrode, featuring two adjacent sites for target strand hybridisation and probe strand hybridisation. A probe oligonucleotide covalently modified with a reporter enzyme, Esterase 2, was then subsequently hybridised to the oligonucleotide. Between the anchoring site and probe site, a target miRNA oligonucleotide was then hybridised, creating a continuous base stacking effect and bringing the reporter enzyme into close proximity with the electrode surface. This allows an electrochemical current to be generated in two steps, firstly by the enzymatic hydrolysis of the substrate p-aminophenyl butyrate to p-aminophenol and secondly, by the redox recycling of quinoneimine to p-aminophenol. This scheme led to an assay that could carry out the detection of miRNA targets to a lower detection limit of 2aM[51]. As the latter approaches mentioned above lack the requirement for the direct modification of the miRNA target, they facilitate the direct analysis of clinical miRNA samples and therefore pose a far more feasible approach for the detection miRNA in a clinical diagnostic setting.

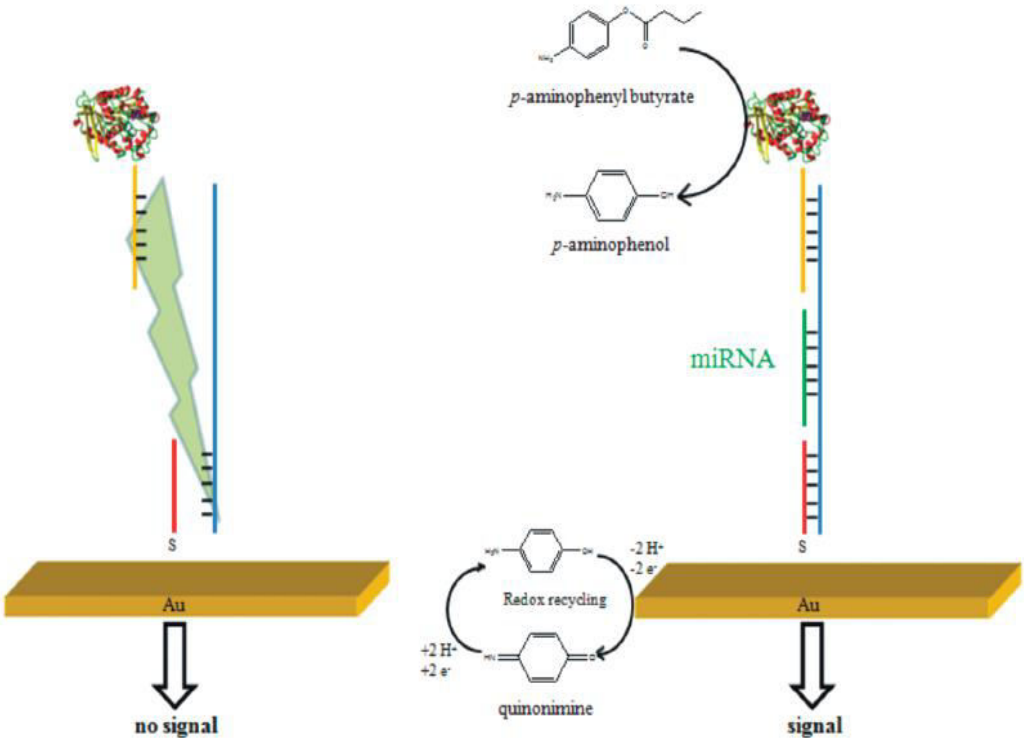

Figure 1.8. Schematic representation of an amperometric miRNA detection strategy based on a gap hybridisation assay developed by Pöhlmann and Sprinzl. A four component RNA hybridisation complex, including a fully hybridised miRNA target, is stabilised by the base stacking energy created by adjacent nucleotides and brings the Esterase 2 enzyme within close proximity to the electrode surface. Esterase 2 can then catalyse the hydrolysis of p-aminophenyl butyrate to the electroactive probe p-aminophenol. The high turnover rate of Esterase 2 and the redox recycling of quinonimine to p-aminophenyl gives a two-fold amplification to signal generated and this electrochemical signal is proportional to the amount of miRNA hybridised to the electrode. Reproduced from Pöhlmann, C. and M. Sprinzl, *Electrochemical Detection of MicroRNAs via Gap Hybridization Assay.* Analytical Chemistry, 2010. **82**(11): p. 4434-4440 [51].

Similar approaches to these studies have been carried out using conjugated catalytically active nanoparticles instead of enzyme conjugates[57-59]. The methods described above circumvent the requirement to directly modify the miRNA target and therefore allow the direct amperometric detection of miRNA from cells or serum and therefore exhibit great potential to be used as user friendly point of care systems. The use of metal nanoparticles for the electrocatalytic detection of nucleic acid biomarkers has gathered a great deal of interest due to their general ease of

modification, their intrinsic electrocatalytic activity and above all their excellent surface area to volume ratio. Several examples can be found throughout the literature on the use of metal nanoparticles in the amperometric detection of DNA[57-59] that give excellent selectivity and display ultrasensitive limits of detection. This work has helped drive the amperometric detection of miRNA using metal nanoparticles as nanocatalysts to generate measurable electrochemical currents as a direct result of miRNA hybridisation. In work reported by Gao et al. in 2006, miRNA targets were hybridised to a capture oligonucleotide on the surface of an electrode and covalently modified with an OsO_2 nanoparticle on the 3' end of the target miRNA, bringing the nanoparticle in contact with the electrode surface. Bound OsO_2 nanoparticles were then capable of generating an amperometric signal by the electrocatalytic oxidation of 30mM hydrazine under an applied potential of 100mV. This provided a means of detecting miRNA in a concentration as low as 80fM[39]. A similar detection strategy, currently unreported in the literature, has been developed by Spain et al involving the modification of electrocatalytic platinum nanoparticles that are capable of generating a measurable current in the presence of H_2O_2. In this work, a self-assembled monolayer of capture oligonucleotides was generated on the surface of an electrode that were complementary to a 10nt portion of a target miRNA. The electrode was incubated with the miRNA and following hybridisation, the electrode was placed in a solution of platinum nanoparticles decorated with a probe oligo nucleotide that was complementary to the remainder of the target miRNA. This led to the immobilisation of platinum nanoparticles on the electrode through target-probe hybridisation that were capable of producing a large current through the electrocatalytic reduction of H_2O_2 to give a sub-picomolar limit of detection of miRNA.

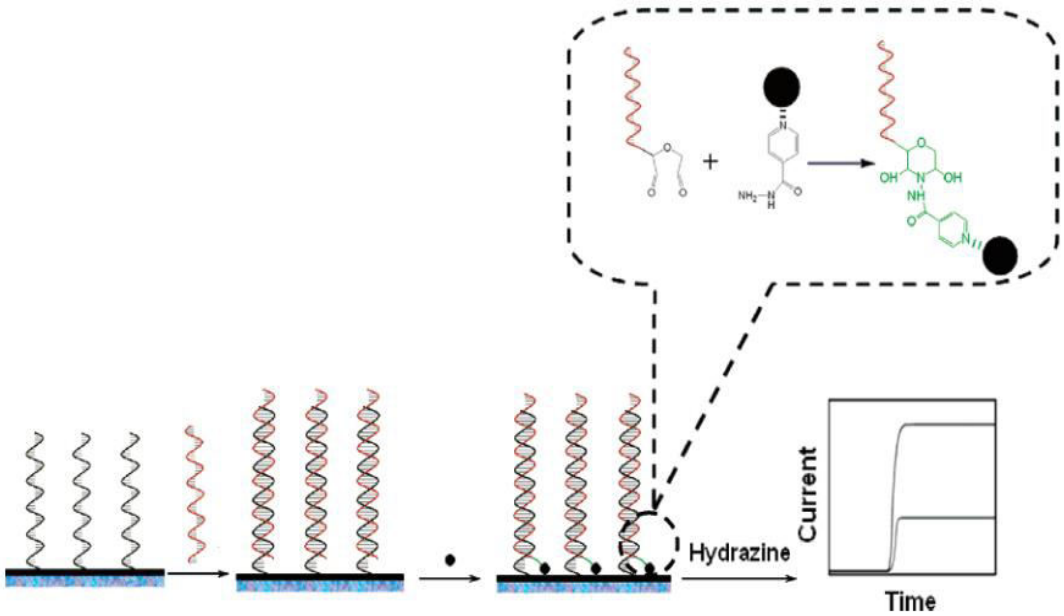

Figure 1.9. Schematic representation of an amperometrically based miRNA detection strategy developed by Gao and Yang. Hybridisation of the target miRNA to the capture probes on the surface of the electrode is followed by the covalent linking of the 3' end of the target to an OsO_2 nanoparticle. The OsO_2 nanoparticle then catalyses the reduction of hydrazine under a constant applied potential which is detected as an increase in current. Reproduced from Gao, Z.Q. and Z.C. Yang, *Detection of microRNAs using electrocatalytic nanoparticle tags.* Analytical Chemistry, 2006. **78**(5): p. 1470-1477[39].

1.4. Amperometric Nucleic Acid Biosensors: Underlying Mechanics.

1.4.1. Oligonucleotide Self-Assembled Monolayers.

The vast majority of electrochemical biosensors mentioned in this review require the formation of a uniform or mixed surface of capture oligonucleotides for the immobilisation of miRNA targets prior to their detection. Self-assembled monolayers (SAM) have been of great interest in the fields of inorganic chemistry and biosensor fabrication due to their ability to control the chemical and physical structure of a surface. Typically, SAM are formed by the adsorption of alkanethiols on a surface and exhibit highly ordered closely packed layers over relatively long ranged distances. One of the most fundamentally functional uses of SAM is the ability to tailor the surface chemistry of a sample for a specific application. For example, a carboxy terminated alkane thiol may be used to produce a surface that is capable of being activated through N-ethyl-N'-(3-dimethylaminopropyl) carbodiimide (EDC)/N-hydroxysuccinimide (NHS) coupling that can be modified with a large number of biomolecules, including antibodies to facilitate the immobilisation of materials from the biomolecular to the cellular scale and form the basis of many bioanalytical techniques and devices. However, in the case of nucleic acid biosensors, the formation of a substrate capable of hybridising a target nucleic acid is typically carried out through the use of a complementary thiolated oligonucleotide strand and exploiting their ability to self-assemble on coinage metals, in particular gold, in monolayers that are highly organised[60]. These provide ideal sensing platforms that retain electrical conductivity to a far greater degree than that of more closely packed alkanethiol monolayers. There are also examples of the use of mixed monolayers of alkanethiol and thiolated oligonucleotide in the formation of biosensors[48, 51]. This use of a heterogeneously produced surface facilitates the improved hybridisation of target to the immobilised capture nucleic acids on the surface of the electrode by reducing the effects of steric hindrance that are associated with a closely packed homogenous monolayer. Another study by Peterson et al proposed that higher density oligonucleotide SAMs may

impede the hybridisation of the target , and the hybridisation efficiency, the percentage of total capture strands that are hybridised, is approximately 95% for a low surface coverage (2 x 10^{12}/cm^2) and approximately 15% for closely packed oligonucleotide monolayers (1.2 x 10^{13}/cm^2)[61].

1.4.2. Oligonucleotide Hybridisation.

The ability to control the hybridisation of nucleic acids is perhaps the most important aspect in the development of nucleic acid biosensors as the vast majority of detection schemes rely on the hybridisation of a target miRNA to an oligonucleotide capture probe. The features of oligonucleotides that control the thermodynamic properties of capture-target oligonucleotide hybridisation include oligonucleotide sequence, double helix conformation and nucleotide backbone composition. While there is no compositional flexibility in the sequence of the oligonucleotides used due to the specific base pairing required for successful hybridisation, the composition of the oligonucleotide backbone can be altered to control the thermodynamic properties of hybridised oligonucleotides, for example PNA and LNA. Therefore, it is of paramount importance that the oligonucleotide used of the hybridisation of miRNA target to a sensing platform is selected on the basis of its thermodynamic properties to give optimal miRNA target hybridisation.

Perhaps the most important consideration when designing a hybridisation based oligonucleotide detection system is the sequence of individual oligonucleotides and the stability of their hybridised duplexes. Hybridisation between strands occurs via the Watson-Crick base pairing of nucleotides, where the purine bases guanine (G) and adenine (A) bond with the pyrimidine bases cytosine (C) and thymine (T) (or uracil (U) in the case of RNA) via hydrogen bonding, the geometry of which ensure the correct pairing of bases. The base pair content of hybridised oligonucleotides, along with strand length, is the most important factor in the determining the T_m (The temperature at which 50% of dsDNA will be dissociated to ssDNA conformation). Given a specific sequence of an oligonucleotide target and the complementary strand(s) to be hybridised to it, if the energy of this interaction is low, then the T_m will be low thus affecting the temperature at which the hybridisation can be carried out. The content of GC pairs have an additive effect on the stability of a double helix confirmation, thus oligonucleotides with high GC content will remain more stable at higher temperatures. Conversely AT or AU pairing has a destabilising effect on double helical confirmation of paired oligonucleotides and this can be observed in regions of high AT content that act as promoters for gene replication in a genome. It

was long believed that this was due to the hydrogen bonding characteristic of GC pairings, and that base stacking was a minor contributor to the stabilisation of double helical oligonucleotides. However, a publication by Yakovchuk in 2006 showed for the first time, the effect both hydrogen bonding and base stacking had on the stability of a double helix separately. The contributions of individual stabilising effects were observed experimentally using complementary polynucleotide sequences and creating very well defined nicks in these sequences that interrupt the base stacking of the effect of adjacent bases in the sequence. The result of this work indicated that the hydrogen bonding of GC pairs does not contribute to stability and that base stacking effects are in fact the primary stabilising factor, while AT/AU pairings are always destabilising[62]. For these reasons when designing oligonucleotide pairing the sequence of neighbouring base pairs must be considered in order to determine the stability of hybridised strand. The T_m of two complementary oligonucleotides is given by:

$$T_m = \frac{\Delta H^\circ}{\Delta S^\circ - R\ln([C1] - ({}^{C2}/_{2})}$$

where C1 and C2 are concentrations of oligonucleotide and C1>C2.

It is important to be aware of the fact that this model holds true for the T_m of synthetic polynucleotides that have regular repeating sequences as they melt in a simple approximate two state transition, however. naturally occurring polynucleotides with heterogeneous sequences will melt in a more complex manner with many stable intermediates, so statistical mechanics must be applied to perform accurate predictions of T_m[63]. ΔH° and ΔS° in this scheme are also calculated on the nearest neighbour model to take into account the contribution of the oligonucleotide sequence. By applying these kinetic and statistical models, it is possible to predict with a good deal of accuracy the T_m of two complementary oligonucleotides and in cases it may be found that the energies of these interactions are too low to facilitate hybridisation of miRNA and complementary strand in a manner that is efficient enough for the development of a ultrasensitive miRNA detection device. Therefore, it may be deemed prudent to choose a different miRNA target to affect maximum sensitivity.

However, systems with low affinities due to their sequence may be improved through the use of oligonucleotide analogues that form more stable duplexes. Interactions between RNA-RNA and RNA-DNA complexes form more stable duplexes than purely DNA based systems (for example where the miRNA target is reverse transcribed to DNA and hybridised to a capture DNA oligonucleotide), partially due to the "A helix" confirmation taken on in RNA hybridisation that is caused due to steric effects of the 2'-OH group in RNA. The electrostatic repulsion of the negatively charged phosphate backbones of target and capture oligonucleotides is also a contributing factor in hybridisation. This effect may be reduced to improve hybridisation between target and capture strands by using synthetic derivatives of nucleic acids that are charge neutral such as peptide nucleic acid (PNA). PNA differs from normal polynucleotides as it is composed of a sequence of nucleotides bound to a backbone of repeating N-(2-aminoethyl)-glycine. The lack of a negatively charged moiety within the backbone of PNA avoids the electrostatic repulsion effects experienced by naturally occurring nucleic acids. The elimination of this repulsive force increases the stability and therefore the T_m of any duplex containing a PNA strand. This leads to an improvement in the thermodynamically controlled hybridisation in nucleic acid detection systems based upon PNA probes, when compared to their DNA/RNA counterparts. Another alternative to purely DNA and RNA based systems is to employ locked nucleic acid (LNA) to improve the stability of duplexes. LNA is a synthetic derivative of RNA where the ribose member of the RNA backbone has been modified, connecting the 2'oxygen with the 4' carbon through a single carbon atom. This bridge forces the ribose to remain in the 3'endo conformation. The effect of this is to increase base stacking interactions in a duplex, making LNA containing duplexes more enthalpically favourable, compared to duplexes of unmodified nucleic acids. Suggestions have also been made that the rigid structure of the ribose unit in LNA may force a single strand into a pre-organised helix conformation, leading to a reduced loss of entropy when forming a duplex[64, 65].

However, in the case of a solid phase sensing platform, where the target miRNA must be hybridised to a capture strand confined to a solid substrate, other considerations must also to made when assessing the thermodynamic properties of the interaction. An important factor to consider is the entropic penalties incurred due

to confining one oligonucleotide strand to the surface. The kinetics of hybridisation will be affected by the inhomogeneity of the sample and the requirement of the transport of target to the solid-liquid interface. However, there also the effects of limiting the probability of the oligonucleotides aligning in the correct manner for hybridisation due to the capture strand being anchored with limited rotational freedom.

1.4.3. Detection Probe Strategies.

Detection of miRNA often relies on hybridisation of miRNA to a probe and the detection of this event. Initial detection strategies relied on the use of a fluorescent beacons and detection was carried out through imaging, for example in microarrays. However, a single fluorescent probe may not produce enough signal through multiple excitation and emission cycles to be detected with a high degree of certainty, as well as the fact that many fluorophores will undergo photobleaching following a number of excitation and emission cycles[66]. However, catalytic probes, for example enzymes, can undergo a practically unlimited number of catalytic cycles without compromising their activity allowing for continuous detection and high signal to noise ratios even for small numbers of hybridisation reactions. For this reason, probes are often chosen that may produce an amplified signal due to their catalytic activity. Horseradish peroxidase (HRP) is often used as a catalytic probe in nucleic acid detection due to its cost effectiveness, the ease with which it maybe conjugated to a nucleic acid probe, the stability of the enzyme, and its relatively high catalytic efficiency of ~850$s^{-1}mM^{-1}$ at 25°C [67]. A generalised scheme for the use of HRP as a reporter molecule relies on the specific immobilisation of HRP to the surface of an electrode, through hybridisation of a conjugated nucleic acid sequence or through a change in the surface chemistry of the electrode as a result of miRNA hybridisation. The HRP is then used to generate a high local concentration of electrocatalytic substrate at the electrodes interface, for example ferrocyanide, phenols, ascorbic acid, etc. The oxidised reaction product may then be used as an electrochemical substrate, becoming reduced at the surface of the electrode through the application of a potential and the resulting reduction current may be detected. For example, Zhou used HRP as a detection probe for identifying the hybridisation of a miRNA to an electrode surface by carrying out the production of benzoquinone from hydroquinone and H_2O_2. In this strategy, a capture probe hairpin loop was immobilised to the surface of an electrode via a thiol group at its 5' end. The hairpin loop was modified with biotin at its 3' end and contained a region of complementarity to the miRNA target. Following hybridisation of the target to this region, the hairpin is forced to undergo a conformational change to become a linear strand exposing the biotin moiety. This allows a streptavidin-HRP conjugate to

become immobilised to the array through the interaction of streptavidin and biotin. As the dissociation constant of this interaction is of the order of 10^{-14} this implies that this binding is in a practical sense irreversible. The electrode was then capable of producing a current response directly proportional to the number of miRNA strands that were hybridised to the array through the catalytic activity of HRP and the electrocatalytic reduction of the resulting product[35]. While this offers an attractive solution for the detection of miRNA through an amplified signal, there are inherent restrictions in the use of enzyme probes, [68].

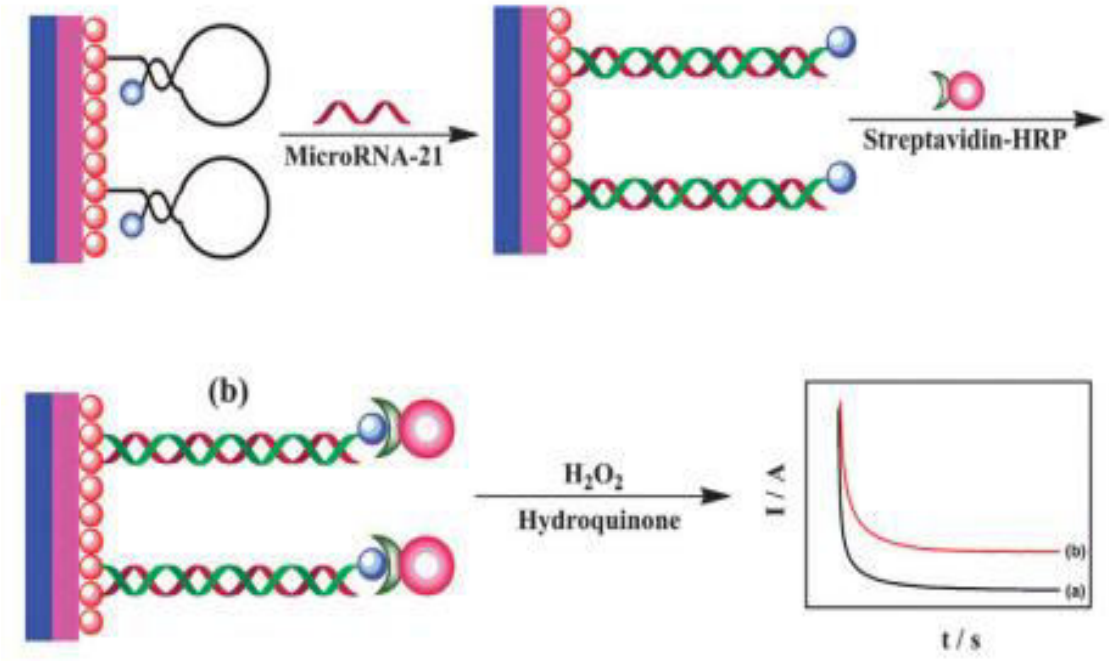

Figure 1.10. An example of the use of an enzyme probe to mediate an amplified electrochemical signal for the detection of miRNA developed by Zhou et al. Following a the hybridisation of the miRNA target to the stem loop probe, the probe undergoes a conformational change and biotin moiety of the probe becomes exposed at the surface of the electrode. The HRP-Streptavidin conjugate is bound to the duplex through the interaction of streptavidin and biotin and the HRP can then catalyse the formation of benzoquinone from hydroquinone and H_2O_2. The enzyme catalysed formation of benzoquinone can then be detected through amperometry Reproduced from Zhou, Y.L., et al., *MicroRNA-21 detection based on molecular switching by amperometry.* New Journal of Chemistry, 2012. **36**(10): p. 1985-1991[35].

While enzymes are useful in the detection of miRNA, a more robust catalytic probe may be required. Extensive research has been carried out in the development of nucleic acid detection strategies that rely on the employment of metal nanoparticles as a detection probe. Enzymatic probes generally contain only a single active site, meaning that only one reaction can be catalysed per probe at any time. Conversely, a metal nanoparticle is capable of carrying out electrocatalysis over its entire surface giving them a much greater activity to volume ratio[69]. In this sense, the nanoparticles may be considered to be acting as ultramicroelectrodes that carry out the electrocatalysis of a substrate to produce an electrochemical signal provided they are close enough to the electrode surface to allow efficient electron transfer. Therefore, only nanoparticles immobilised to the surface are capable of carrying out electrocatalysis. However, such an ultramicroelectrode array of immobilised nanoparticles would theoretically have an upper limit of detection due to the array becoming saturated by nanoparticles at high analyte concentrations. If an electrode exhibited very high levels of nanoparticle immobilisation due to a high concentration of analyte, for example miRNA, there may actually be a decrease in the observed catalytic activity of the nanoparticles. This would be due to a loss in the ability of each single nanoparticle to act as an independent ultramicroelectrode with adjacent diffusion fields overlapping and the overall current being controlled by linear rather than radial diffusion. Therefore, on a planar electrode, a cell immobilised on an electrode may be lysed and will release its miRNA fraction within a localised area. If hybridisation of miRNA targets to an electrode occurs in a localised region of the electrode, and subsequent nanoparticle immobilisation occurs densely in only a single region, the resulting electrochemical signal generated may not be a true indicator of the intracellular miRNA target concentration due to the overlap of diffusion fields of adjacent nanoparticles, leading to irreproducible results and a lower signal to noise ratio than might otherwise be realised.

1.5 Applications of Electrochemiluminescence in Biosensing.

1.5.1. General Principals of Electrochemiluminescence.

Electrochemiluminescence, also referred to as electrogenerated chemiluminescence (ECL), is the generation of radiative energy from the electrochemical formation of reactive species at the surface of an electrode from stable precursors[70]. In general, under an applied potential reactive intermediates are formed that undergo highly energetic electron transfer reactions that result in the formation of an excited state luminophore that subsequently undergoes radiative decay, resulting in luminescence. Following the first detailed report of ECL in the 1960s, the field of ECL has expanded rapidly with thousands of publications ranging from the fundamental and theoretical framework of the technique, to its application in numerous fields including microscopy, light emitting devices and biosensing[71].

As a technique of radiative signal generation, ECL holds many similarities with traditional chemiluminescence, in that both require high energy electron transfer reactions in order to generate excited luminophores. However, in chemiluminescence the generation of luminescence is maintained by manipulation of flow and mixing of solutions, whereas in ECL the generation of luminescence is controlled by the changing the potential of an electrode surface. Thus, one of the single greatest advantages ECL offers over other systems that rely on chemiluminescence is the simplified set up and ease of use. Systems that rely on chemiluminescence (HPLC, CE, FIA, etc.) will typically require multiple streams to accommodate the addition of reagents and precise control over flow rates within the system, leading to complex and expensive apparatus. In contrast, ECL requires only the addition of electrodes to the system to allow the generation of reactants, thus the set up for many ECL systems is remarkably simple by comparison, only requiring the addition of a potentiostat and the incorporation of an electrochemical cell into the system.

The simplicity of an ECL set up is however, not its only advantage over chemiluminescence, or indeed other analytical techniques involving photodetection

of luminescence. In ECL the reactive intermediates required for luminophore excitation are generated *in situ* at the surface of the electrode by changing the potential applied to the surface of the electrode. Therefore, there is good control over both the temporal and spatial aspects of signal generation, meaning that the signal may be generated on command giving the opportunity to synchronise signal generation with the reaction being studied. Also, by incorporation of an array of electrodes into a system, ECL analysis may be multiplexed, for example in a biosensing application, where each individual electrode in an array could be modified for the detection of a different biomolecule and detections could be done rapidly and individually on a single sample.

As ECL is a means for the conversion of electrical energy into photoluminescence, it requires no incident light source for excitation, therefore it avoids problems such as scattering and autofluorescence that other techniques suffer from. However, ECL has drawbacks as well, principally that it relies on the generation of a reactive intermediate at an electrode surface and therefore relies on a high rate of electron transfer to facilitate the chemiluminescent reaction, which must be considered when designing an electrochemical cell. This also implies that there may be an issue with mass transport diffusion in the sense that the generation of intermediates and the excitation of luminophores must occur within close proximity of the electrode surface. In schemes where luminescent probes are in solution, the diffusion of ECL probes to and away from the electrode surface during signal generation will dictate the signal output generated, thus the volume of the electrochemical cell and concentration of luminophore will need to be considered. In the case of surface confined probes, for example a typical sandwich type immunoassay where the electrode surface is modified with antibodies, the available electrode surface area is effectively decreased and therefore there is less working area for the generation of reactive intermediates for luminophore excitation. Another consideration of this is in the case of a co-reactant based system, where the reactive intermediate is generated from the breakdown of a molecule in solution, once the co-reactant radical is formed and subsequently consumed, the addition of more co-reactant for subsequent luminophore excitations is limited by the diffusive transport of spent co-reactant from- and new co-reactant to- the electrode surface. In a bid to limit these effects, 3-dimensional nanostructured electrode surfaces may be designed with the aim of

improving mass transport diffusion, such as nanoparticles deposited to the surface of a working electrode in an ECL cell. In the case of spherical nanoparticles acting as the surface of an electrode, the structure of an electrode decreases in size to the point that the surface becomes smaller than the length of its diffusion distance and at this point the electrode enters a radial diffusion scheme.[72] At this point, the competing effects of linearly diffusing outward spent co-reactant and linearly diffusing inward new co-reactant are dramatically reduced.

1.5.2. Mechanisms for ECL Signal Generation.

Electrochemiluminescence may be generated in a variety of ways, but traditionally the phenomena was observed and studied via the annihilation mechanism. This route of ECL involves the generation of reduced and oxidised radicals of a single luminescent species at the surface of an electrode. When both oxidised and reduced species come in contact electron transfer occurs and the previously reduced species, now exists in an excited state that subsequently decays through radiative emission, as seen in the general scheme below.

$$A - e^- \Rightarrow A^{\bullet +} \quad (1)$$

$$A + e^- \Rightarrow A^{\bullet -} \quad (2)$$

$$A^{\bullet -} + A^{\bullet +} \Rightarrow A^{\bullet} + A \quad (3)$$

$$A^{\bullet} \Rightarrow A + h\nu \quad (4)$$

This is the mechanism for a typical annihilation pathway for ECL. Here a potential is applied to an electrode for a fixed time, t_1, and a reduced species is formed (1). The potential is then stepped in a positive potential direction to form the oxidised species (2). At this point both oxidised and reduced species exist at the electrochemical double layer and undergo annihilation (3), resulting in luminescence (4).

This method for ECL was first studied using Rubrene in the early 1960's[73], as it was known to undergo reversible oxidation and reduction and form reasonably stable anions and cations at accessible potentials. However, for the vast majority of annihilation set ups the reaction conditions involve the use of deaerated organic solvents to access the oxidation and reduction potentials required for the generation of reactive species, and thus, the application of annihilation ECL has been limited.

In contrast to the annihilation ECL pathway, the vast majority of ECL experiments, especially where aqueous media is required, is achieved via the co-reactant pathway, whereby a suitable co-reactant is added to the electrochemical cell that may be oxidised and form a reactive intermediate. This intermediate is then capable of

carrying out electron transfer with the ECL luminophore to produce an excited state that decays subsequently via radiative emission. This mechanism was first studied with the oxidation of oxalate in an aqueous solution, see below.

$$C_2O_4^{2-} - e^- \Rightarrow [C_2O_4^{\bullet-}] \Rightarrow CO_2^{\bullet-} + CO_2 \quad (5)$$

$$A - e^- \Rightarrow A^{\bullet+} \quad (6)$$

$$CO_2^{\bullet-} + A^{\bullet+} \Rightarrow A^{\bullet} + CO_2 \quad (7)$$

$$A^{\bullet} \Rightarrow A + h\nu \quad (8)$$

In this reaction scheme, the same oxidising potential produces both the strong reducing agent $CO_2^{\bullet-}$ from the oxidation of oxalate (5) and the reduced luminophore $A^{\bullet+}$ (6) which can annihilate to give CO_2 and an excited state luminophore $A^{\bullet}$ (7) which will then undergo radiative decay (8). The principal advantage of this is that both the co-reactant and the luminophore are oxidised under the same potential in a single step, avoiding the requirement for a broad potential window required for annihilation ECL, and thus this method of ECL generation is compatible with use in aqueous media. However, oxalate and its oxidation product CO_2 are not compatible with physiological conditions and as such have limited application in the field of biosensing.

For this reason the vast majority of co-reactant based ECL systems employ tripropylamine (TPA) as a co-reactant. The utilisation of TPA allows for the generation of an ECL signal through the co-reactant pathway under biomimetic conditions. In fact, there is a strong pH dependence on the efficiency of the TPA co-reactant based system, with the highest ECL efficiencies being observed at a pH of ~7.5 and therefore it has been invaluable in the field of ECL based biosensor development. Often paired with a transition metal polypyridyl complex, the expected pathway for excitation of a luminophore by TPA is the simultaneous oxidation of both the luminophore and the TPA at the electrode surface and a high energy electron transfer reaction between co-reactant and luminophore resulting in an excited state luminophore that returns to ground state via radiative decay. The forerunning proposed mechanism of action is shown in *Figure 1.11* below. As shown, it is believed that upon oxidation of TPA, the cationic radical loses an α proton and subsequently becomes the strong reducing intermediate, $TPA^{\bullet}$. This may

then reduce the oxidised luminophore, shown here are the transition metal polypyridyl complex $Ru(bpy)_3^{3+}$, to an excited state that may decay via radiative emission. However, this mechanism is disputed and experimental evidence suggests that the other pathways may be involved in the photoemission process, such as the reduction of the luminophore by $TPA^{\bullet}$ to the 1^+ state and a subsequent annihilation reaction with a luminophore in the 3^+ state.

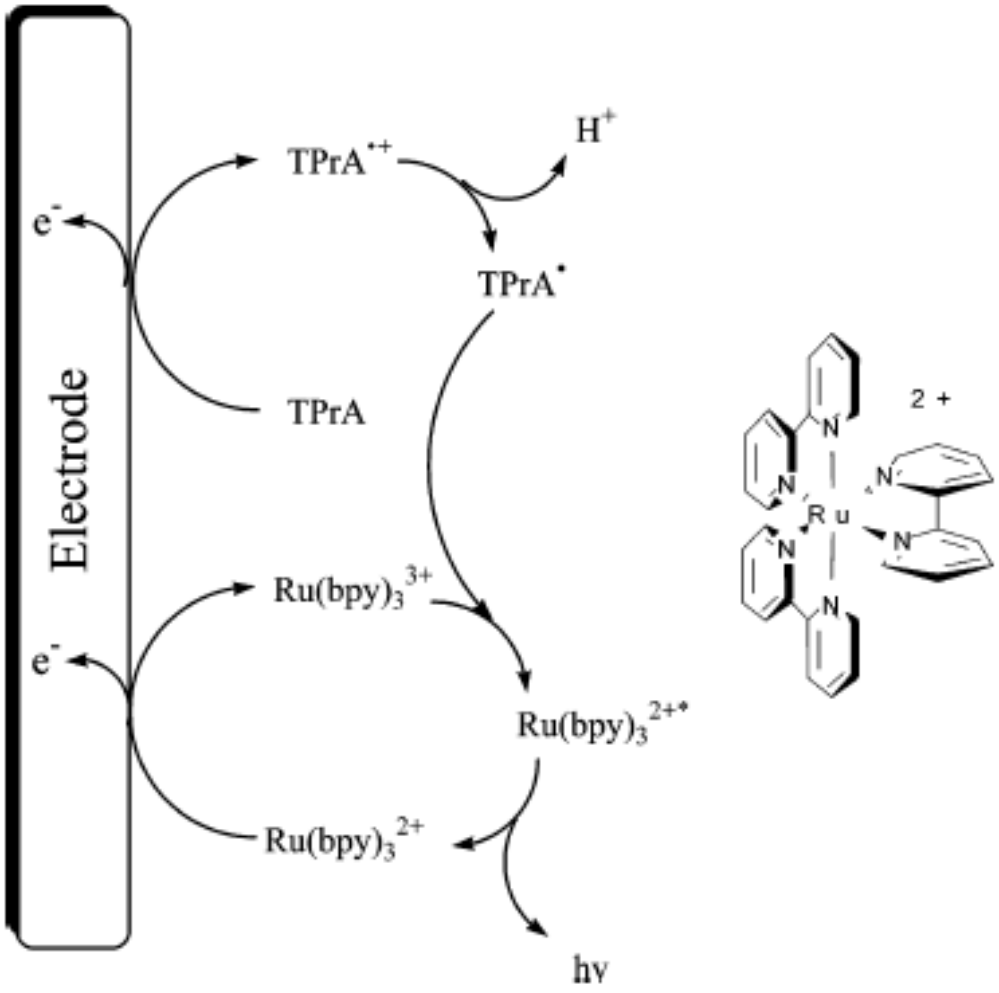

Figure. 1.11. Proposed mechanism for TPA co-reactant mediated ECL generation with $Ru(bpy)_3$. Reproduced from Richter, M.M., *Electrochemiluminescence*. Optical Biosensors: Today and Tomorrow, 2nd Edition, ed. F.S. Ligler and C.R. Taitt. 2008, Amsterdam: Elsevier Science Bv. 317-384.

Regardless of the complexity of the underlying mechanism, co-reactant based ECL has been invaluable in the development in the vast majority of literature reports of ECL based biosensing applications due to its inherent suitability to aqueous media. For example, for an annihilation reaction to be performed on the common ECL luminophore $Ru(bpy)_3^{2+}$, the potential applied to the electrode would be required to be switched from ~1.2 V to ~-1.4V in order to complete the reduction of $Ru(bpy)_3^{2+}$ to $Ru(bpy)_3^{1+}$, which would not be attainable in aqueous media without the violent reduction of water and the evolution of hydrogen gas. However, there are several drawbacks to the use of TPA in ECL systems, notably the toxicity of the compound itself, as well as its poor solubility in water and the requirement for a relatively high concentration (50-100mM for most applications). Although, reports have shown these solubility issues may be addressed with the addition of surfactant to the system and have been shown to give exceptional increases in the ECL efficiency of the system, such as Triton x-100.

In recent years there have also been reports of other methods of generating ECL signal besides the two typical methods discussed above. Hot electron-induced ECL for example, may be utilised to produce an ECL signal that allows for the detection of $Ru(bpy)_3^{2+}$ at sub-nanomolar concentrations. This is carried out by the introduction of hot electrons (defined as electrons with Fermi energies far higher than that of a phase) to the electrolyte solution via an metal/oxide electrode. The oxide layer formed at the surface of the electrode acts as an insulator, preventing the transfer of electrons to the solution until a sufficient electric field has built up across the surface of the oxide layer and the Fermi level of the underlying electrode far exceeds the conduction band of the oxide layer, hot electrons may then tunnel through to the solution[74] where their strong oxidative properties may reduce components of the solution to product strong reductants for the generation of ECL. This example of charge driven ECL induction, was utilised by Ala-Kleme et al. to measure sub-nanomolar concentrations of $Ru(bpy)_3$ [75]. However, the described ECL signal generation method would have poor suitability towards a biosensing application as there may be poor control over the exact nature of solution oxidation and the generation of radicals may be broad and non-homogenous, and result in side reactions damaging both luminophores and biomolecules present, as well as the

potentials applied to the electrode/insulator surface would be in vast excess of the potentials required for co-reactant based ECL systems.

1.5.3. Luminescent ECL probes.

The variety of potential ECL compatible luminescent probes reported in the literature is as wide and varied as the applications that they may be applied to, but for the vast majority of clinical, industrial, and research based ECL applications the preferred probe of choice is often $[Ru(bpy)_3]^{2+}$. This preference is due to the physical and emissive characteristics of the dye, such as its extreme stability, solubility in both aqueous and organic media, high ECL efficiency, and broad stokes shift.

The photophysical characteristics of $Ru(bpy)_3^{2+}$ such as lifetime, quantum yield and emission wavelength are all ideal when designing an ECL system. The photoemission properties of Ru^{2+} polypyridyl complexes are reliant on the promotion of an electron of the metal centre to a π^*-orbital through a metal to ligand charge transfer (MLCT) event and a fast intersystem crossing mechanism to enter a triplet excited state. From this state radiative decay may occur to result in what is formally phosphorescent emission, however, this is not the only route for excited state decay. While in the triplet excited state, deactivation may occur by occupation of a triplet metal centred state, which may lead to instability of the metal-ligand complex. For this reason it is desirable for the phosphorescent lifetime of the luminophore to be short and the lifetime of $[Ru(bpy)_3]^{2+}$ is comparably fast compared to that of other transition metal polypyridyl complexes. Alongside this, the quantum yield in water and ECL efficiency of $Ru(bpy)_3^{2+}$ are 0.065 and 0.05 respectively, which allow for sensitive detection of luminophores. Perhaps one of the most pivotal photophysical characteristics of ruthenium polypyridyl complexes are their inherently large Stokes shifts (>100nm). This large gap between excitation and emission results in remarkably low levels of self-quenching. This allows assays to be developed whereby a high number of luminophores may be confined to a small area, for example the surface of a nanoparticle but only limited self-quenching will occur.

The versatility of the ligand substitutions on Ru^{2+} polypyridyl complexes also opens the door to a whole host of possibilities when designing ECL luminophores for biosensing applications. Relatively simple synthetic pathways have been reported in the literature for the addition of novel ligands to Ru-bis-bipyridine Cl_2 precursors to change the properties of the luminophore to broaden use to various applications. For

example in the case where the covalent conjugation of a luminophore to a biomolecule is desired in order to create an ECL probe in a biosensing application, the addition of a ligand like 2-(4-caboxyphenyl)imidazo[4,5-f][1,10-phenanthroline], or PIC-COOH has been reported in the literature to facilitate a wide number of bioconjugations while maintaining photoluminescent properties comparable to that of $Ru(bpy)_3$.

1.5.4. Applications of Electrochemiluminescence in Biosensing.

Since the initial report of enzymatic biosensor in the early 1960s[76], the field of ECL mediated biosensing has exponentially expanded its application to a wide number of fields and applications including trace analysis, pharmaceutical studies and clinical diagnostics[77]. For the latter of these the impact ECL has had in the fields of both immunosensing and nucleotide probe assays has been exceptional and this trend towards the use of ECL in minimal disease detection is largely due to the inherent advantages of ECL such as broad dynamic range and ultralow sensitivity.

From the initial commercialisation of ECL immunosensing in the 1990s[78], the field of ECL immunosensing has grown considerably in both the number of clinical targets it has been applied to and the methods for signal transduction and enhancement. In fact, the remarkable limits of detection achieved by ECL in recent times may well be seen a driving force and forerunner for further research in the field of minimal disease detection. For example, in the case of Triiothiothyronine, a hormone with a potential to be a biomarker for thyroid function, a potential clinical application for its detection has been reported by Chou et al.[79] utilising a working electrode consisting of graphene oxide nanosheets modified with silver nanoparticles. This scheme involves the immobilisation of the analyte, triiodothyronine, via streptavidin binding to the surface of the electrode from serum samples, utilising graphene oxide as both a highly conductive surface and good surface for high probe loading. This method boasted a detection limit of 50 fg/ml and a linear range of 100 fg/ml – 1ng/ml with high specificity.

The clinical applications of ECL in biosensing are however, not limited to use on biomolecules and there have been reports of ECL being utilised in the detection of inorganic serum contaminants for disease detection, such as heavy metal serum analysis. In the case of lead, a poisonous metal linked with a number of potentially life threatening neurological disorders, current methods for the detection and determination of lead concentration can be both costly, time consuming, complex in both sample preparation and detection, and poorly suited to a point of care setting. However, Gao et al.[80] reported a simple aptasensing platform for the ultrasensitive detection of lead from serum samples. The design, *Figure 1.12*, utilises a self-

assembled monolayer of catalytic DNA-zyme, GR-5, which has a high specificity for lead binding and may catalytically cleave phosphodiester bonds of hybridised nucleic acid strands following lead ion binding. In this scheme the DNA-zyme is hybridised to a RNA strand and then the electrode is incubated with Ruthenium tris-(1,10-phenanthroline)$^{2+}$,[(Ru(phen)$_3$]$^{2+}$, which readily intercalates double stranded oligonucleotides. The electrode is then washed and placed in a serum sample spiked with lead and upon lead binding, the DNA-zyme cleaves the thioester bond of the hybridised RNA strand and this cleavage destabilises the hybridisation complex, releasing Ru(phen)$_3$. The ECL intensity of Ru(phen)$_3$ is then measured using TPA as a co-reactant and this is used to infer the serum concentration of lead. This method has led to the detection of lead down to a limit of 900 fM.

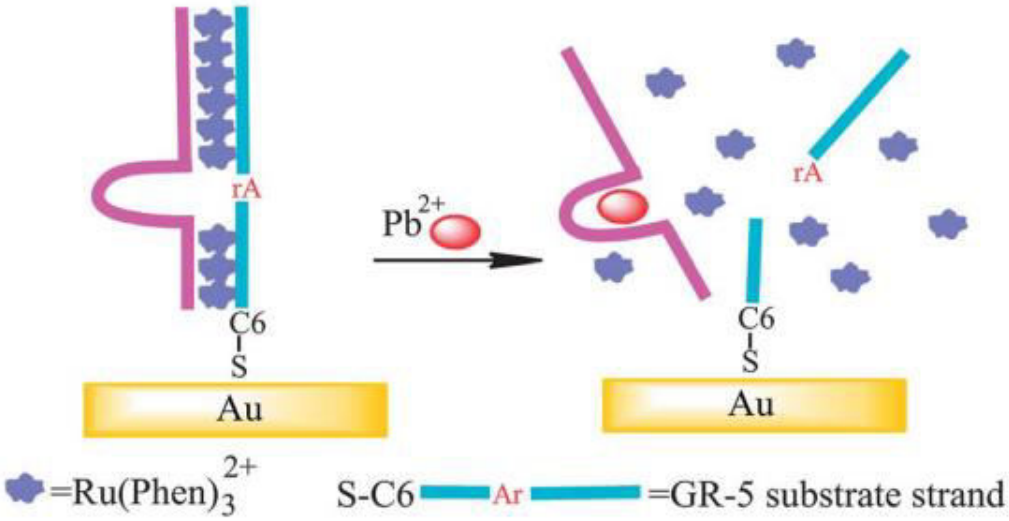

Figure. 1.12. Schematic representation of lead detection scheme. Self-assembled monolayer of thiolated miRNA is hybridised to the surface of an electrode GR-5 (purple) is hybridisation to this strand. Hybridisation complex is then loaded with Ru(phen)$_3$ intercalating ECL probe and upon binding of lead to the DNA-zyme, RNA is cleaved and the hybridisation complex is destabilised, releasing Ru(phen)$_3$. Ru(phen)$_3$ is then detected through ECL and intensity is used to infer lead concentration in serum. Reproduced from Gao, A., Tang, C.X., He, X.W., and Yin, X.B., *Electrochemiluminescent lead biosensor based on GR-5 lead-dependent DNAzyme for Ru(phen)(3)(2+) intercalation and lead recognition.* Analyst, 2013. **138**(1): p. 263-268.

DNA has not only been used as a method for high sensitivity detection, but also as an analyte itself. In a scheme proposed by Dong et al.[81], a hairpin loop of DNA loaded with $Ru(bpy)_3$ is immobilised to the surface of CdSe quantum dots on the surface of electrode with a hybridisation site complementary to that of a DNA target analyte. Upon hybridisation of DNA target to its complimentary site, the hairpin undergoes a conformational change releasing the bound luminophore. The catalytic CdSe nanoparticles on the surface of the electrode can then act as a co-reactant for the generation of ECL signal to result in an ultralow limit of detection limit of 190 aM in human serum.

This example of the use of nanotextured electrode surfaces to facilitate the ultrasensitive detection of minimal disease detection is also observed in a scheme proposed by Hao et el.[82] where the nanotextured surface in this case acts to amplify the ECL signal generation through resonance energy transfer between luminol decorated gold nanoparticles and CdS semiconductor nanocrystals. In *Figure 1.13*. a schematic representation of this detection strategy is observed. The surface of CdS nanocrystals are modified with an oligonucleotide strand containing three distinct binding sites. The site shown in red is complementary to a miRNA target, miR-21 – one of the most upregulated miRNAs in solid tumours. Upon hybridisation this heteroduplex is then excised by a duplex specific nuclease. The electrode is then incubated with two nanoparticle bound oligonucleotide strands, one to bind to the green and red regions (Au probe 1) shown and one to bind the green and blue regions shown (Luminol Au probe). When the red region of the oligonucleotide has been excised following miR-21 hybridisation, the Au probe 1 strand cannot bind and the Luminol Au probe hybridises. This strand functions to quench the ECL intensity of the underlying CdS nanocrystals and instead intensify the signal from luminol. Whereas the Au probe 1 strand serves to enhance the ECL intensity of CdS nanocrystals when no excision of the red region, and thus no hybridisation of miR-21, has taken place. This dual amplification in opposite directions has resulted in an assay with a remarkable limit of detection of 240 aM.

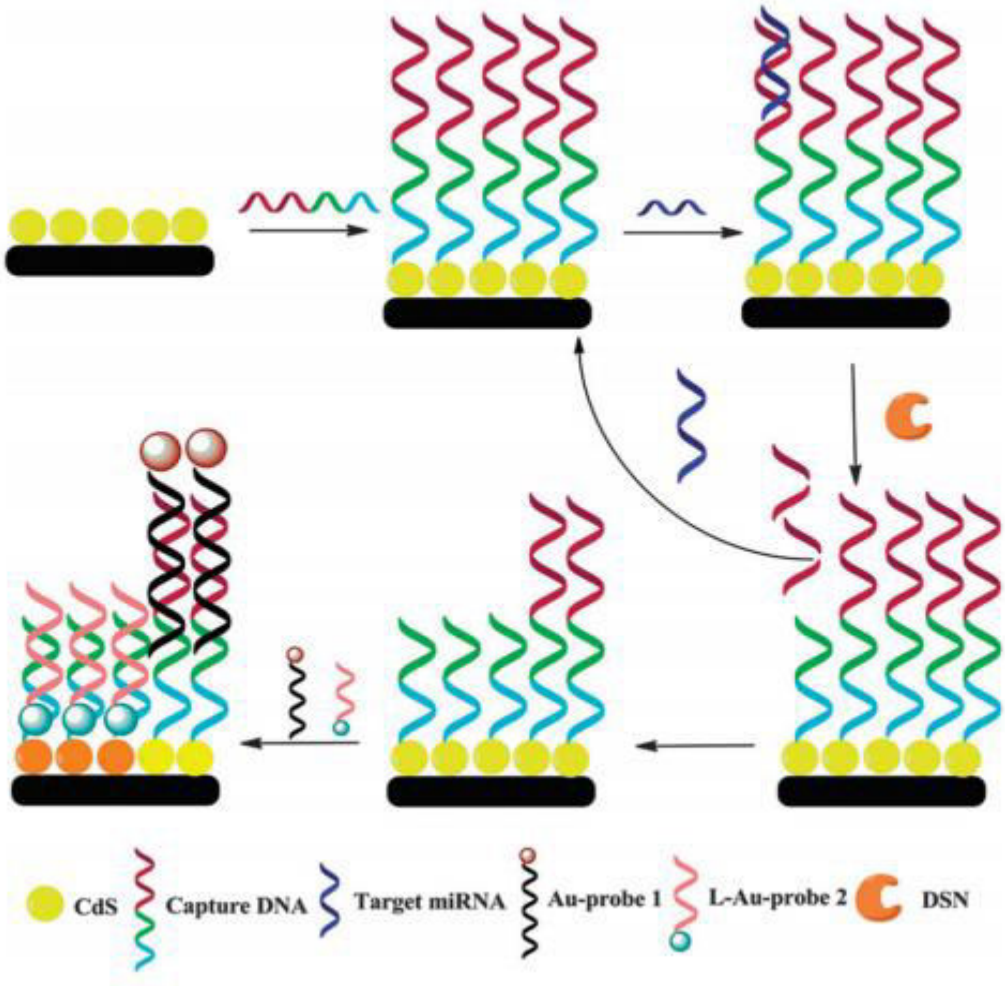

Figure. 1.13. Scheme for ultrasensitive miR-21 detection, relying on the excision of heteroduplexed miRNA and oligonucleotide. The rate of excision controls the ratio of amplified ECL from CdS from Au probe 1 and quenched CdS and enhanced luminol ECL intensity from L Au probe 2. Reproduced from Hao, N., Li, X.L., Zhang, H.R., Xu, J.J., and Chen, H.Y., *A highly sensitive ratiometric electrochemiluminescent biosensor for microRNA detection based on cyclic enzyme amplification and resonance energy transfer.* Chem Commun (Camb), 2014. **50**(94): p. 14828-30.

1.7. Mammalian Cell Capture and *in-situ* Lysis

1.7.1. Mammalian Cell Capture.

In the scheme of detection of circulating tumour cells for the detection of cancer, the is often a need to perform the capture of whole cells from plasma to a surface prior to the detection step necessary for a positive diagnosis. The capture of cells to a solid support may be performed in two ways, non- specific capture and specific capture. In the non specific capture scheme, a surface, for example the surface of an electrode, is often modified with a biomaterial capable of forming a strong interaction with a peptide expressed on the surface of the cells to be captured. The most widely studied peptide for the non specific capture of mammalian cells is the arginine-glycine-aspartate, or RGD, peptide[83]. Throughout the literature there are a great deal of reports of a wide variety of cell types captured onto numerous supports, and the popularity of this peptide use is largely due to both the stability of the short peptide sequence in both solution and in a surface confined regime, the ease with which the peptide may be functionalised to a surface, for example by forming a self assembled monolayer onto a noble metal surface like gold through a thiol group, and the wide variety of targets that the RGD peptide may successfully bind.

The primary target for RGD binding are integrin proteins that are ubiquitously expressed in the extracellular matrix of all mammalian cell types[83]. The formation of self assembled monolayers of non specific capture peptides provides researchers with a scaffold to which cells may be immobilised in biomimetic conditions, and can be used to carry out real time detection of cell capture. In a recent study by Etayash et al[84]. microcantilevers were functionalised with self assembled monolayers of RGD peptide to carry out the capture and detection of human adenocarcinoma cells in real time by measuring the deflection of light focused on the cantilever before and after the arrival of cells onto the cantilever surface. This method provided a simple method for the real time detection of cells whereby the capture of cells could be measured in real time and the formation of the capture surface could be carried out in a simple incubation step, giving rise to cheap and high throughput detection surface formation.

However, this method of performing cell capture in a non specific manner suffers from the drawback that prior to cell capture, samples of cells must be purified, due to the broad specificity of the capture peptide. Therefore in the vast majority of cases, this method for detection would not be compatible with a clinical assay. Therefore the most common approach is to perform highly specific cell capture through the formation of a layer of target specific antibodies on the detection surface. Here, the drawback is often that the functionalisation of a surface with a target specific antibody requires multiple steps, and the complexity of monoclonal antibody manufacture, as well as the cost of monoclonal antibodies, dwarf the labour involved in the synthesis of short non specific peptides such as RGD. However, the benefits of highly specific cell capture often outweigh these perceived difficulties. By tailoring the antibody modified surface to the desired cellular target, cells of a specific type may be captured onto a surface from a complex sample. The formation of the capture surface is often carried out by the initial modification of the capture surface with a material to which the specific antibody may be adhered. In a study by Sherman et al. this way carried out by the formation of a streptavidin covered surface to which biotinylated anti-CD20 antibodies could be immobilised, this then resulted in the formation of a surface whereby cells could be captured specifically from complex samples[85].

In context of the detection of neuroblastoma cells, the identification of cell specific antigens is the most important factor in specific cell capture. As neuroblastoma cells arise from neuroectodermal tumours, they have a unique extracellular matrix, unlike that of typical circulating cells and as such may be specifically captured on this basis. The disialoganglioside, GD2, is a extracellular glycosphyingo lipid of neural cells[86, 87]. In recent times it has been the target of anti-neuroblastoma antibody therapies[87, 88] due to its high degree of tumour- selective expression on cell surfaces. This presents an ideal target for the specific capture and subsequent detection of circulating tumour cells. In a recent study[89], the specific capture of neuroblastoma cells from bone marrow samples was facilitated by the use of such anti-GD2 antibody modified surfaces resulting in the specific capture of 144 cells from ten samples, with a sensitivity of a single tumour cell per 10^6 white blood cells, providing an incredibly powerful tool for the detection and downstream genetic analysis of neuroblastoma cells.

1.7.2. Methods for in situ lysis

Often, following the successful capture of cells and subsequent detection, there may be a need for downstream analysis of the intracellular contents of the captured cell. Therefore following cell capture, a method for the in situ lysis of captured cells is often adopted in order to further characterise and profile pathogens such as circulating malignancies on an individual basis. The most common approach is to apply a lysis buffer containing a reagent that will disrupt the membrane of the cell and result in the cell of the cell and release of its intracellular contents for analysis[90]. This reagent based lysis method, while simple to implement, may result in contamination of the sample and complicate the detection of the analyte. Therefore, it may be advantageous to develop a system for the disruption of cell membranes through a reagent free means. A means of doing this compatible with an electrochemical detection system is to generate a basic environment at the surface where the cell has been captured by the application of a negative potential to this surface[91]. This utilises the localised formation of OH^- ions as a lytic reagent from the saline solution that the cells are immersed in and results in the rupture of the cell membrane and release of the cells intracellular components. This method was used by Lee et al in the development of a platform for the extraction and detection of DNA from cells captured at an electrode surface. This method however is not suited to the detection of RNA due to its sensitivity to basic environments.

A simpler approach is to carry out the physical disruption of the cell membrane by force, by spinning cells in a microfluidic compact disc until disruption of the membrane occurs. This approach was adopted by Kim et al. as a method for the reagent free disruption of cell membranes[92] and is an attractive method for the disruption of cell membranes as the microfluidic platform may then be designed with chambers for further downstream analysis. However, in the case of this system where a high shearing force is generated to disrupt the cell membrane, the intracellular components of lysed cells will forced away from the cell at high speed and mixed with the components of adjacent lysed cells, resulting in a homogenised mix of all cells in the sample, and would not be suitable where it is desirable to study the intracellular components of lysed cells on a singular basis, such as in the scheme of profiling individual cells on their miRNA expression for example.

A far more simple, elegant, reagent free solution is to form osmotic shock of captured cells on a surface by the introduction of a hypotonic solution[93]. This results in the influx of water to the captured cells and eventually the rupture of the cell membrane from the pressure evolved from within the cell. As this method involves merely changing the osmotic potential of the saline solution that the captured cells are surrounded by, it has no potential for sample contamination from buffers. It also avoids the high sheering forces and wide changes in pH discussed in the previous examples that would not be compatible with in situ miRNA profiling of individual cells. Lastly, by controlling the change in osmotic balance the rate of cell lysis may be tightly controlled to rupture the cell membrane in a mild manner, which may prove to be a useful tool in the localisation of the intracellular miRNA fraction of a single cell to an nearby area, thus allowing the intracellular content of a single cell to be probed.

1.7. Conclusion.

In conclusion, Chapter one presents a review of the relevant literature related to electrochemical methods that may be implemented for the ultrasensitive detection of cellular and genetically based biomarkers. This chapter uses neuroblastoma as an example of the clinical challenges that are faced in medical diagnostics and theranostics. Following on from this, miRNA is introduced and the involvement of miRNA in regulation of cellular processes and is explored. Through this it is demonstrated how miRNA are excellent biomarkers for disease and the varying degrees of disease states that may be probed as a result of the changing expression levels of miRNA.

This chapter then continues on to explore the various methods exploited for the detection of miRNA, initially exploring the existing techniques used in biochemical analysis, for example RT-qPCR, microarray analysis, etc.. These methods are then contrasted with electrochemical methods that have recently been reported for miRNA detection, such as impedance based and amperometrically based detection methods. In the majority of electrochemically based methods discussed here, the sensitivity of detection far surpasses that of standard biochemical analysis. Following this, the underlying mechanics of hybridisation based and amperometrically based detection methods are discussed due to their relevance to the following body of work.

This literature review then deals with electrochemiluminescence and its use in the detection of minimal disease markers. The fundamentals of electrochemiluminescence are introduced initially and then a detailed review on the various methods of electrochemiluminescent signal generation is presented. The applications of ECL in the detection of minimal disease are then reviewed, showing recent examples of ECL based methods for the detection of both organic and inorganic biomarkers, finally concluding with examples of ECL being used in the ultrasensitive detection of genetically based biomarkers, and the various methods through which this may be achieved.

The final section of this literature review then looks at the methods available for the non-specific and specific capture of cells, with examples of how neuroblastoma cells may be specifically captured and then subsequently lysed for the analysis of their intracellular contents. Possible lysis procedures are explored with critical analysis of how each may be suited to the detection of miRNA from single cells and how the expression of miRNA may be achieved on a cell by cell basis.

1.7. Bibliography

1. Brodeur, G.M., *Getting Into the AKT.* Journal of the National Cancer Institute, 2010. **102**(11): p. 747-749.
2. Diede, S.J., *Spontaneous regression of metastatic cancer: learning from neuroblastoma.* Nature Reviews Cancer, 2014. **14**(2): p. 71-72.
3. Schilling, F.H., Spix, C., Berthold, F., Erttmann, R., Fehse, N., Hero, B., Klein, G., Sander, J., Schwarz, K., Treuner, J., Zorn, U., and Michaelis, J., *Neuroblastoma screening at one year of age.* New England Journal of Medicine, 2002. **346**(14): p. 1047-1053.
4. Woods, W.G., Tuchman, M., Robison, L.L., Bernstein, M., Leclerc, J.M., Brisson, L.C., Brossard, J., Hill, G., Shuster, J., Luepker, R., Byrne, T., Weitzman, S., Bunin, G., and Lemieux, B., *A population-based study of the usefulness of screening for neuroblastoma.* Lancet, 1996. **348**(9043): p. 1682-1687.
5. Tsubono, Y. and Hisamichi, S., *A halt to neuroblastoma screening in Japan.* New England Journal of Medicine, 2004. **350**(19): p. 2010-2011.
6. Bienertova-Vasku, J., Mazanek, P., Hezova, R., Curdova, A., Nekvindova, J., Kren, L., Sterba, J., and Slaby, O., *Extension of microRNA expression pattern associated with high-risk neuroblastoma.* Tumor Biology, 2013. **34**(4): p. 2315-2319.
7. Chamdin, A., Jarzembowski, J.A., Subramanian, C., Kuick, R., Lee, J.S.J., Kwok, R.P.S., Castle, V.P., and Opipari, A.W., *Bcl6 Is Expressed in Neuroblastoma: Tumor Cell Type-Specific Expression Predicts Outcome.* Translational Oncology, 2009. **2**(3): p. 128-137.
8. Hsu, W.M., Lee, H., Juan, H.F., Shih, Y.Y., Wang, B.J., Pan, C.Y., Jeng, Y.M., Chang, H.H., Lu, M.Y., Lin, K.H., Lai, H.S., Chen, W.J., Tsay, Y.G., Liao, Y.F., and Hsieh, F.J., *Identification of GRP75 as an Independent Favorable Prognostic Marker of Neuroblastoma by a Proteomics Analysis.* Clinical Cancer Research, 2008. **14**(19): p. 6237-6245.
9. Murray, M.J., Raby, K.L., Saini, H.K., Bailey, S., Wool, S.V., Tunnacliffe, J.M., Enright, A.J., Nicholson, J.C., and Coleman, N., *Solid Tumors of Childhood Display Specific Serum microRNA Profiles.* Cancer Epidemiology Biomarkers & Prevention, 2015. **24**(2): p. 350-360.
10. Osman, J., Galli, S., Hanafy, M., Tang, X., and Ahmed, A., *Identification of novel biomarkers in neuroblastoma associated with the risk for bone marrow metastasis: a pilot study.* Clinical & Translational Oncology, 2013. **15**(11): p. 953-958.
11. Viprey, V.F., Gregory, W.M., Corrias, M.V., Tchirkov, A., Swerts, K., Vicha, A., Dallorso, S., Brock, P., Luksch, R., Valteau-Couanet, D., Papadakis, V., Laureys, G., Pearson, A.D., Ladenstein, R., and Burchill, S.A., *Neuroblastoma mRNAs Predict Outcome in Children With Stage 4 Neuroblastoma: AEuropean HR-NBL1/SIOPEN Study.* Journal of Clinical Oncology, 2014. **32**(10): p. 1074-+.
12. Lin, R.J., Lin, Y.C., Chen, J., Kuo, H.H., Chen, Y.Y., Diccianni, M.B., London, W.B., Chang, C.H., and Yu, A.L., *microRNA Signature and Expression of Dicer and Drosha Can Predict Prognosis and Delineate Risk Groups in Neuroblastoma.* Cancer Research, 2010. **70**(20): p. 7841-7850.
13. Kuroda, T., Morikawa, N., Matsuoka, K., Fujino, A., Honna, T., Nakagawa, A., Kumagai, M., Masaki, H., and Saeki, M., *Prognostic significance of circulating tumor cells and bone marrow micrometastasis in advanced neuroblastoma.* Journal of Pediatric Surgery, 2008. **43**(12): p. 2182-2185.

14. Moss, T.J. and Sanders, D.G., *DETECTION OF NEUROBLASTOMA-CELLS IN BLOOD.* Journal of Clinical Oncology, 1990. **8**(4): p. 736-740.
15. Lee, R.C., Feinbaum, R.L., and Ambros, V., *THE C-ELEGANS HETEROCHRONIC GENE LIN-4 ENCODES SMALL RNAS WITH ANTISENSE COMPLEMENTARITY TO LIN-14.* Cell, 1993. **75**(5): p. 843-854.
16. Wightman, B., Burglin, T.R., Gatto, J., Arasu, P., and Ruvkun, G., *NEGATIVE REGULATORY SEQUENCES IN THE LIN-14 3'-UNTRANSLATED REGION ARE NECESSARY TO GENERATE A TEMPORAL SWITCH DURING CAENORHABDITIS-ELEGANS DEVELOPMENT.* Genes & Development, 1991. **5**(10): p. 1813-1824.
17. Wightman, B., Ha, I., and Ruvkun, G., *POSTTRANSCRIPTIONAL REGULATION OF THE HETEROCHRONIC GENE LIN-14 BY LIN-4 MEDIATES TEMPORAL PATTERN-FORMATION IN C-ELEGANS.* Cell, 1993. **75**(5): p. 855-862.
18. Winter, J., Jung, S., Keller, S., Gregory, R.I., and Diederichs, S., *Many roads to maturity: microRNA biogenesis pathways and their regulation.* Nature Cell Biology, 2009. **11**(3): p. 228-234.
19. Lau, N.C., Lim, L.P., Weinstein, E.G., and Bartel, D.P., *An abundant class of tiny RNAs with probable regulatory roles in Caenorhabditis elegans.* Science, 2001. **294**(5543): p. 858-862.
20. Lee, R.C. and Ambros, V., *An extensive class of small RNAs in Caenorhabditis elegans.* Science, 2001. **294**(5543): p. 862-864.
21. Lagos-Quintana, M., Rauhut, R., Lendeckel, W., and Tuschl, T., *Identification of novel genes coding for small expressed RNAs.* Science, 2001. **294**(5543): p. 853-858.
22. Viprey, V.F., Corrias, M.V., Kagedal, B., Oltra, S., Swerts, K., Vicha, A., Ladenstein, R., and Burchill, S.A., *Standardisation of operating procedures for the detection of minimal disease by QRT-PCR in children with neuroblastoma: Quality assurance on behalf of SIOPEN-R-NET.* European Journal of Cancer, 2007. **43**(2): p. 341-350.
23. Westermann, F., Muth, D., Benner, A., Bauer, T., Henrich, K.O., Oberthur, A., Brors, B., Beissbarth, T., Vandesompele, J., Pattyn, F., Hero, B., Konig, R., Fischer, M., and Schwab, M., *Distinct transcriptional MYCN/c-MYC activities are associated with spontaneous regression or malignant progression in neuroblastomas.* Genome Biology, 2008. **9**(10): p. 39.
24. Pickering, M.T., Stadler, B.M., and Kowalik, T.F., *miR-17 and miR-20a temper an E2F1-induced G1 checkpoint to regulate cell cycle progression.* Oncogene, 2009. **28**(1): p. 140-145.
25. Ivanovska, I., Ball, A.S., Diaz, R.L., Magnus, J.F., Kibukawa, M., Schelter, J.M., Kobayashi, S.V., Lim, L., Burchard, J., Jackson, A.L., Linsley, P.S., and Cleary, M.A., *MicroRNAs in the miR-106b family regulate p21/CDKN1A and promote cell cycle progression.* Molecular and Cellular Biology, 2008. **28**(7): p. 2167-2174.
26. Bommer, G.T., Gerin, I., Feng, Y., Kaczorowski, A.J., Kuick, R., Love, R.E., Zhai, Y., Giordano, T.J., Qin, Z.S., Moore, B.B., MacDougald, O.A., Cho, K.R., and Fearon, E.R., *p53-mediated activation of miRNA34 candidate tumor-suppressor genes.* Current Biology, 2007. **17**(15): p. 1298-1307.
27. Chivukula, R.R. and Mendell, J.T., *Circular reasoning: microRNAs and cell-cycle control.* Trends in Biochemical Sciences, 2008. **33**(10): p. 474-481.
28. Bui, T.V. and Mendell, J.T., *Myc: Maestro of MicroRNAs.* Genes Cancer, 2010. **1**(6): p. 568-75.
29. Chang, T.C., Yu, D.N., Lee, Y.S., Wentzel, E.A., Arking, D.E., West, K.M., Dang, C.V., Thomas-Tikhonenko, A., and Mendell, J.T., *Widespread microRNA repression by Myc contributes to tumorigenesis.* Nature Genetics, 2008. **40**(1): p. 43-50.
30. Xiao, C.C., Srinivasan, L., Calado, D.P., Patterson, H.C., Zhang, B.C., Wang, J., Henderson, J.M., Kutok, J.L., and Rajewsky, K., *Lymphoproliferative disease and*

autoimmunity in mice with increased miR-17-92 expression in lymphocytes. Nature Immunology, 2008. **9**(4): p. 405-414.
31. Franke, T.F., Kaplan, D.R., Cantley, L.C., and Toker, A., *Direct regulation of the Akt proto-oncogene product by phosphatidylinositol-3,4-bisphosphate.* Science, 1997. **275**(5300): p. 665-668.
32. Gao, Z.Q., Deng, H.M., Shen, W., and Ren, Y.Q., *A Label-Free Biosensor for Electrochemical Detection of Femtomolar MicroRNAs.* Analytical Chemistry, 2013. **85**(3): p. 1624-1630.
33. Baker, M.B., Bao, G., and Searles, C.D., *In vitro quantification of specific microRNA using molecular beacons.* Nucleic Acids Research, 2012. **40**(2): p. 12.
34. Gao, Z.Q., *A highly sensitive electrochemical assay for microRNA expression profiling.* Analyst, 2012. **137**(7): p. 1674-1679.
35. Zhou, Y.L., Zhang, Z.Y., Xu, Z.N., Yin, H.S., and Ai, S.Y., *MicroRNA-21 detection based on molecular switching by amperometry.* New Journal of Chemistry, 2012. **36**(10): p. 1985-1991.
36. Peng, Y.F. and Gao, Z.Q., *Amplified Detection of MicroRNA Based on Ruthenium Oxide Nanoparticle-Initiated Deposition of an Insulating Film.* Analytical Chemistry, 2011. **83**(3): p. 820-827.
37. Wang, Z.G. and Yang, B.F., *Multiplexing RT-PCR for High-Throughput miRNA Profiling*. Microrna Expression Detection Methods. 2010, Berlin: Springer-Verlag Berlin. 153-157.
38. Liu, C.G., Calin, G.A., Volinia, S., and Croce, C.M., *MicroRNA expression profiling using microarrays.* Nature Protocols, 2008. **3**(4): p. 563-578.
39. Gao, Z.Q. and Yang, Z.C., *Detection of microRNAs using electrocatalytic nanoparticle tags.* Analytical Chemistry, 2006. **78**(5): p. 1470-1477.
40. Bustin, S.A., *Absolute quantification of mRNA using real-time reverse transcription polymerase chain reaction assays.* Journal of Molecular Endocrinology, 2000. **25**(2): p. 169-193.
41. Chen, C.F., Ridzon, D.A., Broomer, A.J., Zhou, Z.H., Lee, D.H., Nguyen, J.T., Barbisin, M., Xu, N.L., Mahuvakar, V.R., Andersen, M.R., Lao, K.Q., Livak, K.J., and Guegler, K.J., *Real-time quantification of microRNAs by stem-loop RT-PCR.* Nucleic Acids Research, 2005. **33**(20): p. 9.
42. Chen, Y.X. and Stallings, R.L., *Differential patterns of microRNA expression in neuroblastoma are correlated with prognosis, differentiation, and apoptosis.* Cancer Research, 2007. **67**(3): p. 976-983.
43. Samaraweera, L., Grandinetti, K.B., Huang, R.J., Spengler, B.A., and Ross, R.A., *MicroRNAs define distinct human neuroblastoma cell phenotypes and regulate their differentiation and tumorigenicity.* Bmc Cancer, 2014. **14**: p. 11.
44. Cissell, K.A., Rahimi, Y., Shrestha, S., Hunt, E.A., and Deo, S.K., *Bioluminescence-based detection of MicroRNA, miR21 in breast cancer cells.* Analytical Chemistry, 2008. **80**(7): p. 2319-2325.
45. Cissell, K.A., Campbell, S., and Deo, S.K., *Rapid, single-step nucleic acid detection.* Analytical and Bioanalytical Chemistry, 2008. **391**(7): p. 2577-2581.
46. Driskell, J.D., Seto, A.G., Jones, L.P., Jokela, S., Dluhy, R.A., Zhao, Y.P., and Tripp, R.A., *Rapid microRNA (miRNA) detection and classification via surface-enhanced Raman spectroscopy (SERS).* Biosensors & Bioelectronics, 2008. **24**(4): p. 917-922.
47. Campuzano, S., Pedrero, M., and Pingarron, J.M., *Electrochemical genosensors for the detection of cancer-related miRNAs.* Analytical and Bioanalytical Chemistry, 2014. **406**(1): p. 27-33.

48. Goda, T., Masuno, K., Nishida, J., Kosaka, N., Ochiya, T., Matsumoto, A., and Miyahara, Y., *A label-free electrical detection of exosomal microRNAs using microelectrode array.* Chemical Communications, 2012. **48**(98): p. 11942-11944.
49. Gao, Z.Q. and Yu, Y.H., *Direct labeling microRNA with an electrocatalytic moiety and its application in ultrasensitive microRNA assays.* Biosensors & Bioelectronics, 2007. **22**(6): p. 933-940.
50. Gao, Z.Q. and Yu, Y.H., *A microRNA biosensor based on direct chemical ligation and electrochemically amplified detection.* Sensors and Actuators B-Chemical, 2007. **121**(2): p. 552-559.
51. Poehlmann, C. and Sprinzl, M., *Electrochemical Detection of MicroRNAs via Gap Hybridization Assay.* Analytical Chemistry, 2010. **82**(11): p. 4434-4440.
52. Shen, W., Deng, H.M., Ren, Y.Q., and Gao, Z.Q., *A label-free microRNA biosensor based on DNAzyme-catalyzed and microRNA-guided formation of a thin insulating polymer film.* Biosensors & Bioelectronics, 2013. **44**: p. 171-176.
53. Tsujiura, M., Ichikawa, D., Komatsu, S., Shiozaki, A., Takeshita, H., Kosuga, T., Konishi, H., Morimura, R., Deguchi, K., Fujiwara, H., Okamoto, K., and Otsuji, E., *Circulating microRNAs in plasma of patients with gastric cancers.* British Journal of Cancer, 2010. **102**(7): p. 1174-1179.
54. Zhang, G.J., *Silicon Nanowire Biosensor for Ultrasensitive and Label-Free Direct Detection of miRNAs*, in *Microrna and Cancer: Methods and Protocols*, W. Wu, Editor. 2011, Humana Press Inc: Totowa. p. 111-121.
55. Ramnani, P., Gao, Y.N., Ozsoz, M., and Mulchandani, A., *Electronic Detection of MicroRNA at Attomolar Level with High Specificity.* Analytical Chemistry, 2013. **85**(17): p. 8061-8064.
56. Lu, N., Gao, A.R., Dai, P.F., Song, S.P., Fan, C.H., Wang, Y.L., and Li, T., *CMOS-Compatible Silicon Nanowire Field-Effect Transistors for Ultrasensitive and Label-Free MicroRNAs Sensing.* Small, 2014. **10**(10): p. 2022-2028.
57. Polsky, R., Gill, R., Kaganovsky, L., and Willner, I., *Nucleic acid-functionalized Pt nanoparticles: Catalytic labels for the amplified electrochemical detection of biomolecules.* Analytical Chemistry, 2006. **78**(7): p. 2268-2271.
58. Kwon, S.J. and Bard, A.J., *DNA Analysis by Application of Pt Nanoparticle Electrochemical Amplification with Single Label Response.* Journal of the American Chemical Society, 2012. **134**(26): p. 10777-10779.
59. Dong, X.Y., Mi, X.N., Zhang, L., Liang, T.M., Xu, J.J., and Chen, H.Y., *DNAzyme-functionalized Pt nanoparticles/carbon nanotubes for amplified sandwich electrochemical DNA analysis.* Biosensors & Bioelectronics, 2012. **38**(1): p. 337-341.
60. Love, J.C., Estroff, L.A., Kriebel, J.K., Nuzzo, R.G., and Whitesides, G.M., *Self-assembled monolayers of thiolates on metals as a form of nanotechnology.* Chemical Reviews, 2005. **105**(4): p. 1103-1169.
61. Peterson, A.W., Heaton, R.J., and Georgiadis, R.M., *The effect of surface probe density on DNA hybridization.* Nucleic Acids Research, 2001. **29**(24): p. 5163-5168.
62. Yakovchuk, P., Protozanova, E., and Frank-Kamenetskii, M.D., *Base-stacking and base-pairing contributions into thermal stability of the DNA double helix.* Nucleic Acids Research, 2006. **34**(2): p. 564-574.
63. SantaLucia, J., *A unified view of polymer, dumbbell, and oligonucleotide DNA nearest-neighbor thermodynamics.* Proceedings of the National Academy of Sciences of the United States of America, 1998. **95**(4): p. 1460-1465.
64. Carlucci, M., Kierzek, E., Olejnik, A., Turner, D.H., and Kierzek, R., *Chemical Synthesis of LNA-2-thiouridine and Its Influence on Stability and Selectivity of Oligonucleotide Binding to RNA.* Biochemistry, 2009. **48**(46): p. 10882-10893.

65. Kierzek, E., Pasternak, A., Pasternak, K., Gdaniec, Z., Yildirim, I., Turner, D.H., and Kierzek, R., *Contributions of Stacking, Preorganization, and Hydrogen Bonding to the Thermodynamic Stability of Duplexes between RNA and 2 '-O-Methyl RNA with Locked Nucleic Acids.* Biochemistry, 2009. **48**(20): p. 4377-4387.
66. Dempsey, G.T., Vaughan, J.C., Chen, K.H., and Zhuang, X.W., *Evaluation of Fluorophores for Optimal Performance in Localization-Based Super-Resolution Imaging.* Biophysical Journal, 2012. **102**(3): p. 725A-725A.
67. Mogharrab, N., Ghourchian, H., and Amininasab, M., *Structural stabilization and functional improvement of horseradish peroxidase upon modification of accessible lysines: Experiments and simulation.* Biophysical Journal, 2007. **92**(4): p. 1192-1203.
68. Hernandez-Ruiz, J., Arnao, M.B., Hiner, A.N.P., Garcia-Canovas, F., and Acosta, M., *Catalase-like activity of horseradish peroxidase: relationship to enzyme inactivation by H2O2.* Biochemical Journal, 2001. **354**: p. 107-114.
69. Katz, E. and Willner, I., *Integrated nanoparticle-biomolecule hybrid systems: Synthesis, properties, and applications.* Angewandte Chemie-International Edition, 2004. **43**(45): p. 6042-6108.
70. Richter, M.M., *ELECTROCHEMILUMINESCENCE*. Optical Biosensors: Today and Tomorrow, 2nd Edition, ed. F.S. Ligler and C.R. Taitt. 2008, Amsterdam: Elsevier Science Bv. 317-384.
71. Richter, M.M., *Electrochemiluminescence (ECL).* Chemical Reviews, 2004. **104**(6): p. 3003-3036.
72. Ying, Y.L., Ding, Z.F., Zhan, D.P., and Long, Y.T., *Advanced electroanalytical chemistry at nanoelectrodes.* Chemical Science, 2017. **8**(5): p. 3338-3348.
73. Hercules, D.M., *Chemiluminescence Resulting from Electrochemically Generated Species.* Science, 1964. **145**(3634): p. 808-9.
74. Gaillard, F., Sung, Y.E., and Bard, A.J., *Hot electron generation in aqueous solution at oxide-covered tantalum electrodes. Reduction of methylpyridinium and electrogenerated chemiluminescence of Ru(bpy)(3)(2+).* Journal of Physical Chemistry B, 1999. **103**(4): p. 667-674.
75. Ala-Kleme, T., Kulmala, S., Väre, L., Juhala, P., and Helin, M., *Hot Electron-Induced Electrogenerated Chemiluminescence of Ru(bpy)32+ Chelate at Oxide-Covered Aluminum Electrodes.* Analytical Chemistry, 1999. **71**(24): p. 5538-5543.
76. Clark, L.C. and Lyons, C., *ELECTRODE SYSTEMS FOR CONTINUOUS MONITORING IN CARDIOVASCULAR SURGERY.* Annals of the New York Academy of Sciences, 1963. **102**(1): p. 29-&.
77. Hu, L.Z. and Xu, G.B., *Applications and trends in electrochemiluminescence.* Chemical Society Reviews, 2010. **39**(8): p. 3275-3304.
78. Blackburn, G.F., Shah, H.P., Kenten, J.H., Leland, J., Kamin, R.A., Link, J., Peterman, J., Powell, M.J., Shah, A., Talley, D.B., and et al., *Electrochemiluminescence detection for development of immunoassays and DNA probe assays for clinical diagnostics.* Clin Chem, 1991. **37**(9): p. 1534-9.
79. Chou, H.T., Fu, C.Y., Lee, C.Y., Tai, N.H., and Chang, H.Y., *An ultrasensitive sandwich type electrochemiluminescence immunosensor for triiodothyronine detection using silver nanoparticle-decorated graphene oxide as a nanocarrier.* Biosensors & Bioelectronics, 2015. **71**: p. 476-482.
80. Gao, A., Tang, C.X., He, X.W., and Yin, X.B., *Electrochemiluminescent lead biosensor based on GR-5 lead-dependent DNAzyme for Ru(phen)(3)(2+) intercalation and lead recognition.* Analyst, 2013. **138**(1): p. 263-268.
81. Dong, Y.P., Gao, T.T., Zhou, Y., Jiang, L.P., and Zhu, J.J., *Anodic Electrogenerated Chemiluminescence of Ru(bpy)3(2+) with CdSe Quantum Dots as Coreactant and Its Application in Quantitative Detection of DNA.* Sci Rep, 2015. **5**: p. 15392.

82. Hao, N., Li, X.L., Zhang, H.R., Xu, J.J., and Chen, H.Y., *A highly sensitive ratiometric electrochemiluminescent biosensor for microRNA detection based on cyclic enzyme amplification and resonance energy transfer.* Chem Commun (Camb), 2014. **50**(94): p. 14828-30.
83. Bellis, S.L., *Advantages of RGD peptides for directing cell association with biomaterials.* Biomaterials, 2011. **32**(18): p. 4205-10.
84. Etayash, H., Jiang, K., Azmi, S., Thundat, T., and Kaur, K., *Real-time Detection of Breast Cancer Cells Using Peptide-functionalized Microcantilever Arrays.* Scientific Reports, 2015. **5**: p. 13967.
85. Sherman, D.J., Kenanova, V.E., Lepin, E.J., McCabe, K.E., Kamei, K., Ohashi, M., Wang, S., Tseng, H.R., Wu, A.M., and Behrenbruch, C.P., *A Differential Cell Capture Assay for Evaluating Antibody Interactions with Cell Surface Targets.* Anal Biochem, 2010. **401**(2): p. 173-81.
86. Soman, G., Yang, X., Jiang, H., Giardina, S., and Mitra, G., *Comparison of GD2 Binding Capture ELISA Assays for Anti-GD2-Antibodies Using GD2-Coated Plates and a GD2-Expressing Cell-Based ELISA.* J Immunol Methods, 2011. **373**(1-2): p. 181-91.
87. Zhang, S., Cordon-Cardo, C., Zhang, H.S., Reuter, V.E., Adluri, S., Hamilton, W.B., Lloyd, K.O., and Livingston, P.O., *Selection of tumor antigens as targets for immune attack using immunohistochemistry: I. Focus on gangliosides.* Int J Cancer, 1997. **73**(1): p. 42-9.
88. Yang, R.K. and Sondel, P.M., *Anti-GD2 Strategy in the Treatment of Neuroblastoma.* Drugs Future, 2010. **35**(8): p. 665-.
89. Carpenter, E.L., Rader, J.A., Ruden, J., Rappaport, E.F., Hunter, K.N., Hallberg, P.L., Krytska, K., O'Dwyer, P.J., and Mosse, Y.P., *Dielectrophoretic Capture and Genetic Analysis of Single Neuroblastoma Tumor Cells.* Front Oncol, 2014. **4**.
90. Lin, Z. and Cai, Z., *Cell lysis methods for high-throughput screening or miniaturized assays.* Biotechnol J, 2009. **4**(2): p. 210-5.
91. Lee, H.J., Kim, J.H., Lim, H.K., Cho, E.C., Huh, N., Ko, C., Park, J.C., Choi, J.W., and Lee, S.S., *Electrochemical cell lysis device for DNA extraction.* Lab on a Chip, 2010. **10**(5): p. 626-633.
92. Kim, J., Hee Jang, S., Jia, G., Zoval, J.V., Da Silva, N.A., and Madou, M.J., *Cell lysis on a microfluidic CD (compact disc).* Lab Chip, 2004. **4**(5): p. 516-22.
93. Graham, J.M., *Homogenization of mammalian cultured cells.* ScientificWorldJournal, 2002. **2**: p. 1630-3.

Chapter 2.

Label-Free Impedance Detection and PtNP Mediated Detection of Captured Sk-N-As Cells

2. Label-Free Impedance Detection and PtNP Mediated Detection of Captured Sk-N-As Cells

2.1. Introduction

In recent times a considerable amount of research interest has been devoted to the electrochemical detection of pathogenic cells from within a host.[1-5] Electrochemical approaches have advantages including the speed of analysis, accuracy of results, potential for miniaturisation and relatively power use and cost, when compared to traditional optical detection. The field of electrochemical cellular pathogen detection has also gathered attention for label free detection following initial cell capture, reducing production and material costs and lead time when developing detection systems[5, 6].

Electrochemical Impedance Spectroscopy (EIS) in particular has recently been identified as a useful label free electrochemical detection method of captured cells due to the fact that a physical change in the surface of the electrode, i.e., resistance and capacitance are measured[1, 5]. This approach to detection of cells therefore could eliminate the need for labelling strategies. This would lead to the development of a scheme that only requires incubation of cells at the electrode surface and electrochemical detection. This capability would significantly improve the analytical turnaround time for clinical point of care settings as well as reducing the user expertise required compared to the labelled strategies of fluorescent microscopy.

Therefore is is the overall aim of the work detailed in this chapter to create a platform where the capture of cells from solution may be facilitated. This involves the formation of a uniform surface that may facilitate efficient specific cell capture, while remaining capable of carrying out the accurate detection of captured cells by an electrochemical means, for example EIS. The approach detailed in this chapter relies on the capture of neuroblastoma cancer cells from suspension and detection of this event in phosphate buffered saline due to a proportional change in the impedance characteristics of the working electrode. The resistance (R) of the circuit in this case

is a useful parameter in the determination of the circuits change in impedance as it is the resistance associated with the transfer of charge from one phase to another (in this case from liquid electrolyte to the solid electrode surface). The changes in the characteristics of the electrode surface for example, capture of cells to the surface, will then give changes in the value for R proportional to the change in the number of cells captured. Therefore, the number of cells captured on the surface of an electrode will have a direct effect on the resistance associated with transfer of charge between the solution and electrode, provided that the distance over which the resistance is being probed is adequate to ensure the biological cells are contributing to the measured resistance. It is well understood [2, 5, 7] that the concentration of supporting electrolyte within the electrochemical cell plays an important role in the distance probed by EIS in the dielectric medium. In particular, with decreasing electrolyte concentration the sensitivity of impedance detection of cells at the surface of the electrode is enhanced due to the relatively long distance probed, as the thickness of the electrochemical double layer increases with decreasing electrolyte concentration[8]. Therefore, it is important to optimise the concentration of supporting electrolyte.

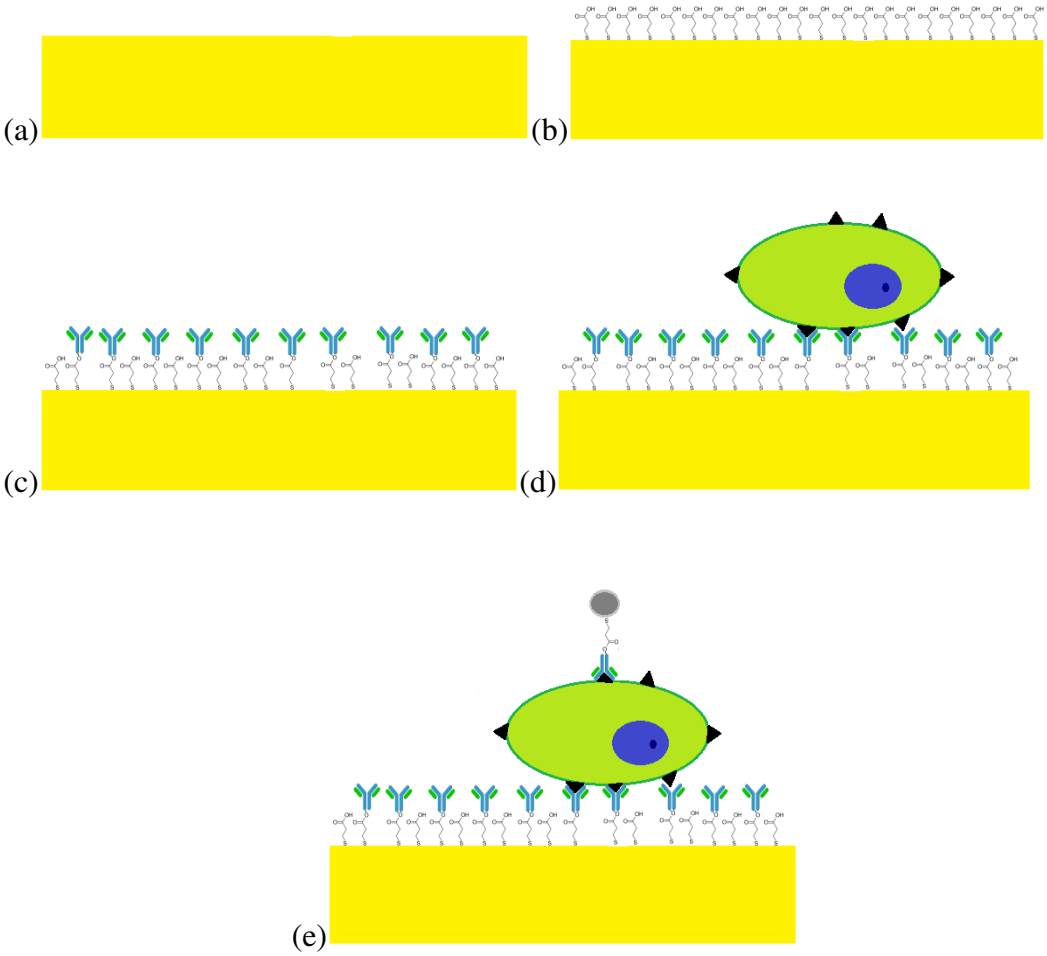

Figure 2.1. Illustration of electrode fabrication scheme and subsequent cell capture and detection. In (a) a planar gold electrode is modified with a monolayer of 3MPA. (b) shows the activation of the carboxyl termini with EDC-NHS so that in (c) antibodies may be covalently bound to the surface of the electrode. In (d) cells are incubated and subsequently captured on the to surface to be detected by electrochemical impedance spectroscopy, while in (e) antibody conjugated nanoparticles are applied to the cell surface for amperometric detection of cells.

As shown in *Figure 2.1*, in this work, a bare planar gold electrode is modified with a self-assembled monolayer of 3-mercaptopropionic acid (3MPA) in order to give an electrode surface that can be modified with antibodies for cellcapture. The carboxy termini of the monolayer surface are then activated via the EDC-NHS coupling in order to couple amino groups within a capture antibody to the surface, resulting in an

electrode surface covalently modified with a cure antibody specifically targeted to the antigen of interest, in this case the GD2 ganglioside expressed on the surface of the neuroblastoma cells[9, 10]. The electrode is then incubated in a known concentration of cells for 30 minutes to facilitate specific antibody/antigen mediated cell capture of neuroblasts to the surface of the electrode and following this the electrode is washed with Dulbecco's Phosphate Buffered Saline (DPBS) in order to remove non-specifically bound cells. The electrode is then placed in an electrochemical cell and the captured cells detected by measuring the change in electrochemical impedance of the circuit before and after cell capture. However, as this strategy relies on the specific capture of cells from suspension over a short period in a static environment, it is important to note that capture efficiency would not be expected to approach 100% without the implementation of a specialised system for improving the efficiency of cell capture, for example, a microfluidic flow device that forces cells in suspension to come in contact with the electrode surface for improved cell capture. Therefore, it is important to correlate the impedimetric response with the actual number of cells captured on the surface. Here, the total number of cells on the surface of each electrode was confirmed by visualisation of the cells through staining and fluorescent microscopy. This allowed the correlation between the number of cells captured and the impedance change to be determined. This is important since the surface coverage of cells may not depend linearly on the suspension concentration.

The inherent properties of a label free detection system limit its sensitivity and limit of detection. For this reason, the results from the label free cell capture detection assay were compared to that of a study carried out using a label, in this case an antibody conjugated platinum nanoparticle (PtNP-Ab). The aim of this detection strategy was to bind electrocatalytic platinum nanoparticles to the surface of cells captured on the electrode and determine the number of cells on the surface by measuring the current associated with electrocatalysis. The performance of this assay could be then compared to a label free system in order to determine the efficacy of label free detection to carry out precise and accurate measurements of the number of cells captured on the electrode surface.

2.2 Experimental

2.2.1. Materials:

2 mm diameter conventional gold disc electrodes were purchased from IJ Cambria, Wales, UK. Anti-human GD2 monoclonal mouse IgG antibodies were purchased from Santa Cruz Biotechnology. Platinum nanoparticles 70 nm diameter (CAS no. 7440-06-4) were purchased from Sigma Aldrich. Sk-N-AS Neuroblastoma cell line was provided by the research group of Prof. R. Stallings in the RSCI Dublin. All other reagents, unless specified otherwise, were purchased from Sigma Aldrich. All aqueous solutions were prepared with milli-Q water.

2.2.2.Instrumentation:

A three electrode electrochemical cell was used throughout this work consisting of a platinum wire as a counter, a Ag/AgCl reference electrode and a 2 mm diameter gold disc working electrode. Cyclic voltammograms were recorded in a 5mM solution of ferrocene methanol (FcMeOH) as a solution phase redox probe, with 1 mM DPBS acting as a supporting electrolyte. All AC impedance and impedance measurements were carried out at open potential in 1mM DPBS in a frequency range of 1 MHz to 0.1 Hz with an amplitude of 25mV vs Ag/AgCl. All electrochemical measurements were carried out using a CHI 760E potentiostat within a faraday cage. Fluorescent microscopy images were carried out using an Olympus IX81 inverted fluorescent microscope. EDX of platinum nanoparticles was carried out using an INCA Operator EDX system coupled to a Hitachi S5500 Field Emission Scanning Electron Microscope. All mammalian cell culture was carried out in a biosafety level II laminar flow cabinet and cell counts were obtained using a standard haemocytometer and an inverted light microscope.

2.3.Procedures.

2.3.1. Fabrication of Capture Surface.

Initially, each gold disc electrode was polished with descending sizes of aluminium oxide particles (5μm, 1μm, 0.3μm and 0.05μm) on a polishing pad for 5 minutes at each stage and sonicated in ddH_2O between polishing stages. The microscopic surface area of each electrode was then measured using cyclic voltammetry in 10 mM H_2SO_4 vs. Ag/AgCl and the surface roughness was determined. The AC impedance and impedance vs. time of each bare electrode was then measured. Electrodes were then placed in a 5mM ethanolic solution of 3MPA for a minimum of 16 hours and then washed with copious amounts of ddH_2O. Again AC impedance and Impedance vs time measurements were carried out. A 5mM solution N-Hydroxysulphosuccinamide sodium (NHS) + 1-ethyl-3-(3-dimethylaminopropyl)carbodiimide hydrochloride (EDC) was made up and electrodes were placed into this immediately and allowed to react for 30 minutes. Electrodes were then washed with ddH_2O and treated with 20μl of 200mg/μl solution of Anti-GD2 IgG for 2 hours. Following this the AC impedance and impedance vs. time measurements were carried out.

2.3.2. Mammalian Cell Culture and Capture.

Sk-N-AS cells were cultured using Eagle's Minimal Essential Media (EMEM). When being resuspended from an adherent state, cells were treated with 1X Accutase™ to preserve extracellular adherent bodies. The cells were then counted using a haemocytometer and drop cast onto electrodes in EMEM for a minimum of 30 minutes. Electrodes were then washed x4 with supplemented Dulbecco's Phosphate Buffered Saline (DPBS) to remove unbound cells and extracellular material. Cells were fixed in 3.7% w/v paraformaldehyde in order to avoid osmotic lysis in the hypotonic electrolyte solution of the electrochemical cell and following fixation, AC Impedance and Impedance vs. time were measured again.

2.3.3. Imaging of Captured Cells.

Fixed cells were treated with a 5μM solution of DiOC6 dye (3,3'-dihexyloxacarbocyanine iodide (λ_{max}=484nm)) in DPBS for 30 minutes and then imaged using fluorescent microscopy. Cell counting was carried out using the cell counting function of ImageJ imaging software.

2.3.4. PtNP Cell Detection Assay.

Antibody conjugated platinum nanoparticles (PtNP) were fabricated by suspending platinum nanoparticles (50-70nm in size) in a 5mM ethanolic solution of 3MPA for a minimum of 16 hours. PtNP were then washed with DPBS by centrifugation (rcf = 5000G, t = 2 minutes) and removal of supernatant for four subsequent wash cycles and finally resuspended in a 5mM EDC-NHS solution in DPBS for 30 minutes. Following this, PtNP were once again centrifuged, the supernatant was discarded and the nanoparticles were resuspended in a 10mg/ml Anti-GD2 DPBS solution and incubated at 37°C for 2 hours. Antibody conjugated PtNP were then stored at 4°C for no longer than one week before use.

Following the captureof Sk-N-As cells to the surface of an electrode and washing of the cells with DPBS, the antibody conjugated PtNPs were applied to the cells and incubated at 37°C for a minimum of 1 hour prior to washing with DPBS to remove unbound PtNP. Subsequently cells were fixed with 3.7% w/v paraformaldehyde. The electrodes were then once again washed with copious amounts of ddH_2O and then placed in an electrochemical cell, with 0.01M H_2SO_4 as a supporting electrolyte. The amperometric i/t curve technique on the CHI 760E system was used to monitor the current produced at an applied potential of -250mV vs Ag/AgCl. For 600 seconds a baseline current was allowed to stabilise and at 600 seconds the program was paused and H_2O_2 was injected into the cell to give a final concentration of 200μM with moderate agitation to ensure a homogeneous solution, the program was resumed and a current increase was observed. At 2400 seconds the program was ceased and the final current was measured.

2.4. Results and Discussion

2.4.1 Capture platform fabrication

In order to fabricate an antibody modified electrode surface for the capture of cells, polished planar electrodes were placed in an ethanolic solution of 3MPA for a minimum of 16 hours to form a monolayer surface of carboxyl termini that may be coupled to antibodies. As the 3MPA molecule is relatively short compared to other traditional monolayer forming molecules such as dodecanethiol and 16-mercapto-hexadecanoic acid, a change in the surface electrochemistry of the gold electrode was difficult to observe in a cyclic voltammogram, as 3MPA is simply too short to significantly change the rate of electron transfer to/from a redox species in solution. As a result, the voltammograms below show little or no passivation of the gold surface in *Figure 2.2*. that would result in lower peak currents and larger peak-to-peak, ΔE_p, values for the ferrocene methanol probe (FcMeOH)

However, by measuring the electrochemical impedance of the electrode before and after the formation of the thiolated monolayer, a large change can be observed. In *Figure 2.3.* it is clearly shown that the resistance (R) associated with the electrode decreases greatly following a 16 hour incubation in 3MPA from a value of 1956Ω to 506Ω. This trend of the electrodes resistance decreasing following the formation of an alkanethiol monolayer appears to be counterintuitive and does not corroborate previous reports in the literature.

This negative change in electrode resistance, while unexpected, was observed reliably for each electrode in this study, and thus is not considered to be anomalous. The change in impedance observed may be explained by detritus on the electrode prior to incubation in the ethanolic 3MPA monolayer solution. Alkanethiol monolayer depostitions have been shown in the literature to be able to clean loosely bound materials from the surfaces of coinage metals, such as gold, and therefore the data suggests that incubation in the monolayer deposition removed materials from the surface of the electrode that had contributed to the anomalously high impedance of the bare gold electrode.

It may also be the case that this change in impedance may be explained in terms of the effect of a change in capacitance of the electrode rather than resistance. For an electrochemical cell where,

$$R_{total} = R_{monolayer} + R_{solution}$$

in the case where a supporting electrolyte of a very low ionic strength is used, the R_{total} value would be expected to be almost equal to that of the $R_{solution}$ value as it is the major contributing factor to resistance. However, if the changes in capacitance are considered, for a cell where,

$$C_{total} = \frac{1}{Cmono} + \frac{1}{CSoln}$$

Here the C_{total} value will be heavily influenced by the smaller value capacitance in the circuit, which would be expected to be the highly ordered, minimally defective monolayer of 3MPA. Thus the impedance measured in this case may be predominantly influenced by the capacitance of the monolayer and thus a negative change in impedance is observed.

Another possible explaination for this change in impedance may be the change in the surface chemistry of the gold electrode following modification with an alcohol terminated monolayer. In a publication on the binding of PNA and DNA self-assembled monolayers on the surface of gold electrodes by Prabhakar et al. [11], a similar trend was observed where following modification of a bare gold surface, the measured resistance of an electrode decreased. The authors in this case gave the explanation that the charged nature of the modified electrode may attract ions from solution to surface and thus reduce the overall cell resistance.

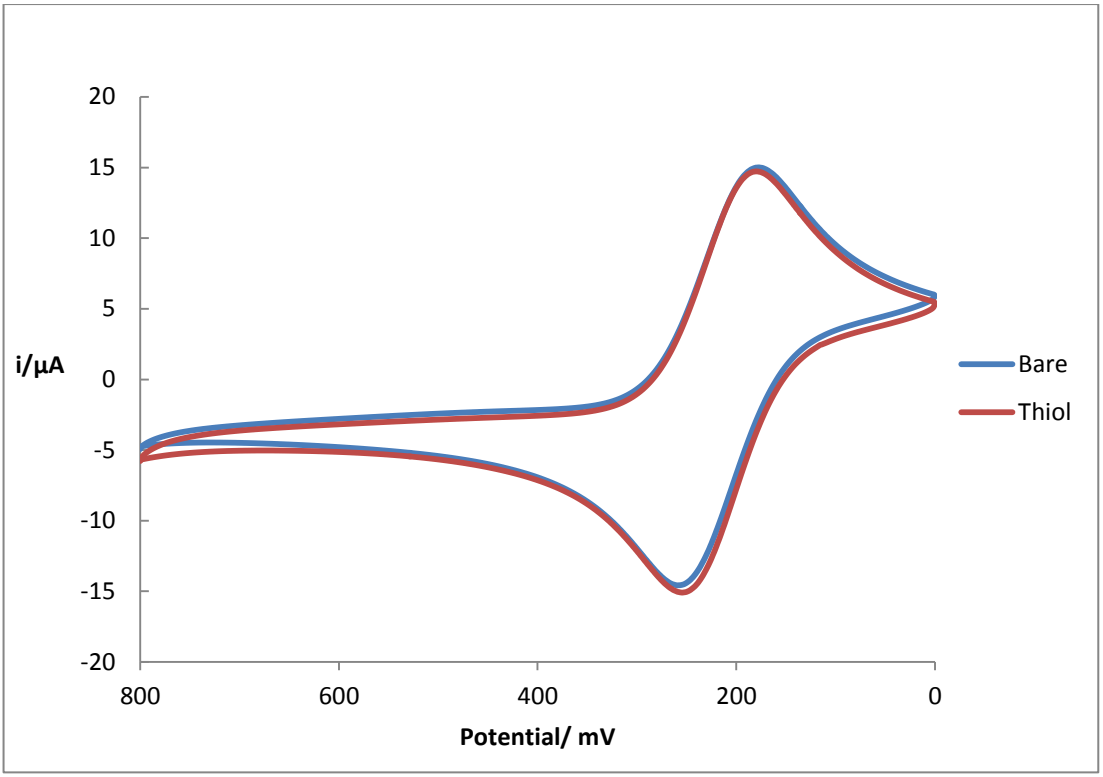

Figure 2.2. Cyclic voltammogram of an electrode before (Blue) and following 3MPA monolayer formation (Red) carried out in a 5mM FcMeOH solution in 10 mM DPBS vs. Ag/AgCl at a scan rate of 100 mV/s,

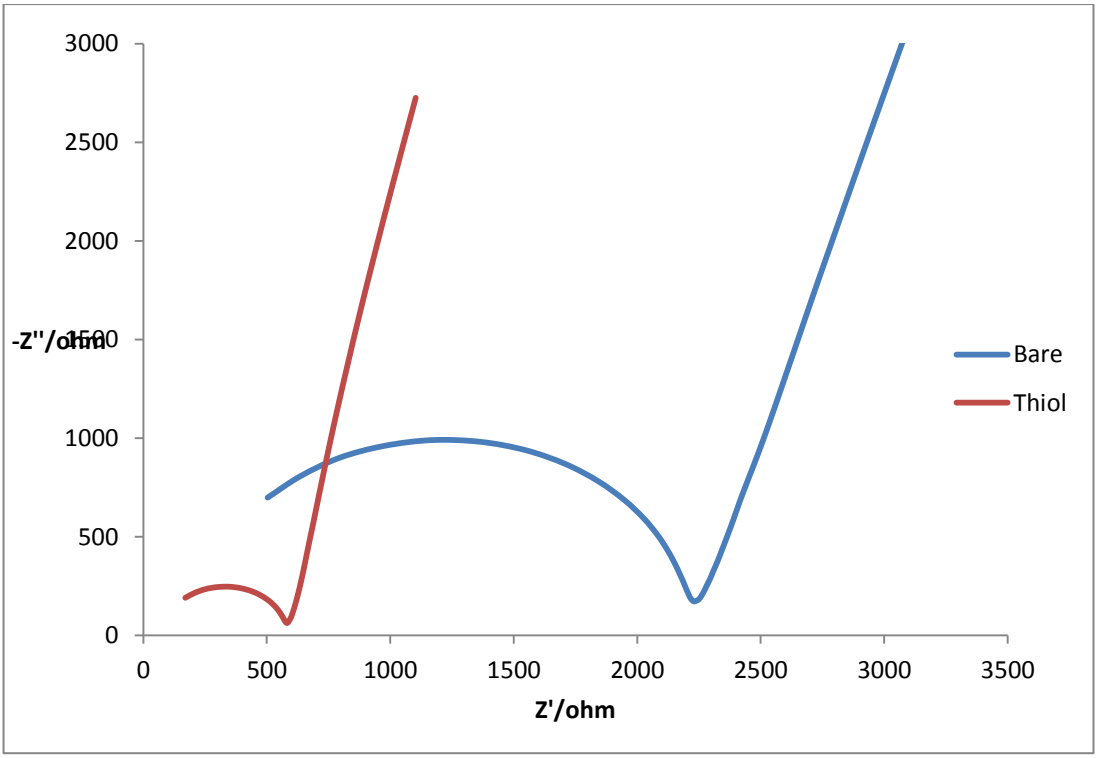

Figure. 2.3. Nyquist plot of impedance of an electrode before (Blue) and after 3MPA monolayer formation (Red) carried out at open potential with an amplitude of 25mV vs Ag/AgCl in 1mM DPBS over a frequency range from 1 MHz to 0.1 Hz.

Following the formation of the monolayer surface, the carboxyl termini of the 3MPA monolayer subunits were activated with EDC-NHS, and following this anti-human GD2 monoclonal mouse IgG antibodies were covalently bound to the surface. As before, visualisation of this process was incompatible with cyclic voltammetry. As shown in *Figure 2.4*., in this case the surface coverage and irregular shape and thus inefficient packing of the antibodies does not facilitate the passivation of the electrode surface to the extent that is appreciable in a cyclic voltammogram. The antibodies themselves, also are not observable directly by voltammetry and are only possibly observed as a small shift in peaks due to a change in the overall charge of the electrode surface. However, once again the change in surface chemistry of the electrode may be observed through electrochemical impedance spectroscopy.

In *Figure 2.5.* a reduction in R from 506 Ω to 382 Ω can be observed following the covalent modification of the electrode surface with antibody. This 123 Ω difference in R is associated with the formation of a monolayer of antibodies on the surface of the electrode. This was carried out in parallel with a control where the electrode was subject to similar modification step, but no antibody was applied and the electrode was instead incubated in clean buffer, also in *Figure 2.5*, giving rise to little or no change in the impedance measured at the electrode surface. However, when the full data set of electrodes used in the assay is considered, the deviation of -123.7Ω, while unexpected, must be considered statistically relevant. For 5 electrodes tested throughout the manufacture of this capture platform, the shift in impedance from a thiol monolayer to an antibody conjugated surface was always negative. The mean shift in impedance for this modification step was -148.4 Ω with a standard deviation of 23.4 Ω.

It is expected that the lack of electrode passivation seen in the cyclic voltammograms before and after antibody modification is proof that the inefficient packing of the antibody facilitates movement of electrolyte solution to and from the electrode surface and thus does not increase the resistance of the circuit. The lack of an increase in impedance following antibody modification, which may have been seemed counter intuitive and anomalous is possibly a result of the inefficient packing of macromolecules like IgG. Considering their relatively large size of 145kDa, they are not expected to exhibit a similar degree of uniform monolayer formation observed for self-assembled monolayers. The bulky nature of macromolecules also

results in a leaky, non-uniform interface at the electrode surface that would be expected to result in only small shifts in impedance.

Regardless, the conjugation of anti GD2 IgG to the surface of an electrode is reliably observed in this study as a net drop in measured impedance, and this decrease in measured impedance may be used as a positive indicator of covalent modification of the electrode with antibody.

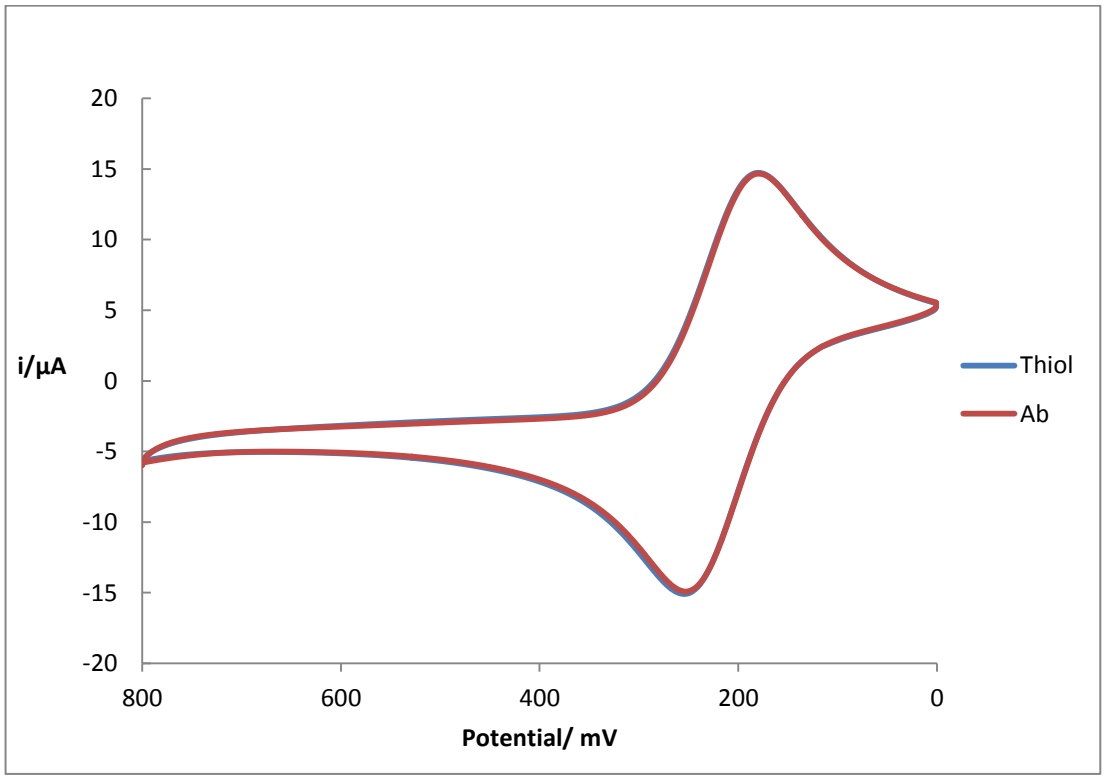

Figure 2.4. Cyclic voltammogram of an electrode before and after antibody conjugation carried out in a 5mM FcMeOH solution of DPBS vs. Ag/AgCl at a scan rate of 100mV/s showing no appreciable decrease in FcMeOH peak from before (Blue) to after (Red) antibody conjugation.

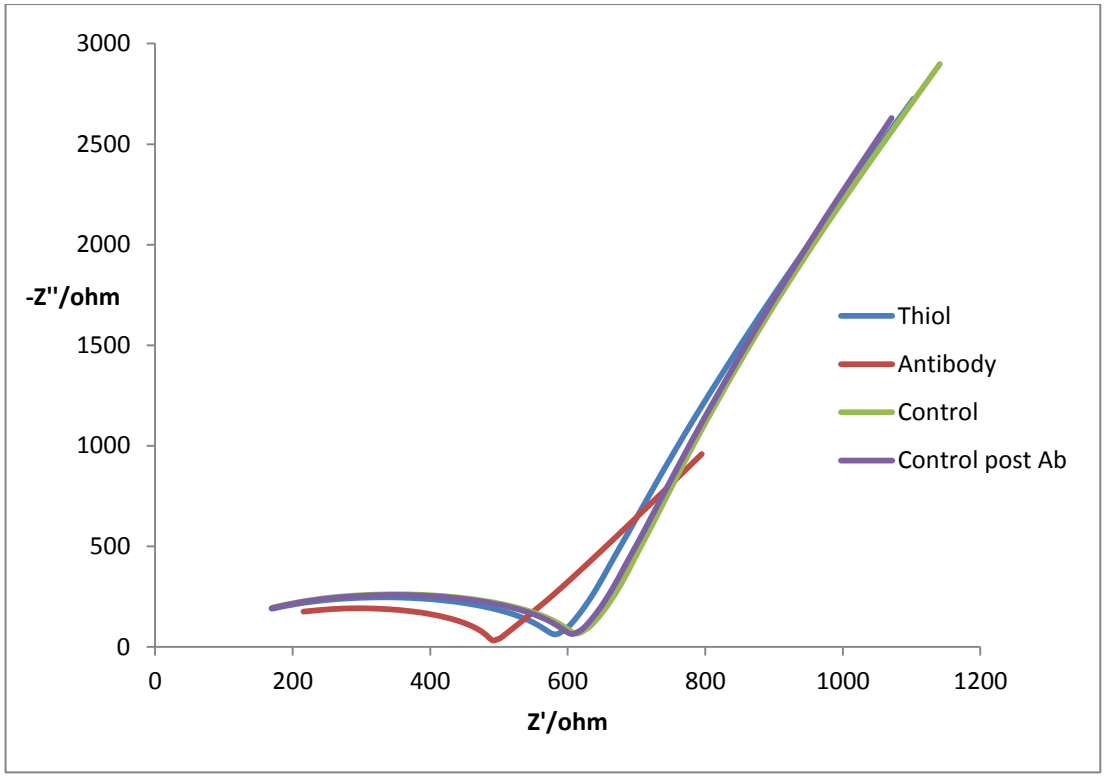

Figure 2.5. Nyquist plot of impedance of an electrode before (Blue) and after (Red)antibody conjugation, and controls before (green) and following (purple)incubation in conjugation buffer carried out at open potential with an amplitude of 25mV vs Ag/AgCl in 1mM DPBS over a frequency range of 1 MHz to 0.1 Hz.

2.4.2. Capture of Sk-N-As Human Neuroblastoma Cells and Label Free Electrochemical Impedance Detection.

Following fabrication electrodes were stored in DPBS at 4°C for no more than 48 hours before use. Before use, the electrodes were heated to 37°C and washed with DPBS. Sk-N-As were cultured as stated above and counted using a standard haemocytometer and serial diluted in into 1ml aliquots of 10^5, 10^4, 10^3, 10^2 and 10^1 cell per 50µl concentrations. Following this, electrodes were incubated with 50µl of cell suspension ranging from 10^5 to 10^1 cells for 30 minutes and then washed with DPBS. *Figure 2.7.* and *Figure 2.8.* show impedance and cyclic voltammograms for each electrode. Following exposure to the cells in suspension, a large change is observed in both the cyclic voltammetry and impedance responses of the electrode indicating that cell capture had been successful.

Figure 2.6. shows that from the voltammograms of antibody modified electrodes to those of electrodes following cell capture there is an appreciable depression in the magnitudes of the reversible redox reaction of FcMeOH for higher cell concentrations. This is an indication of cell capture that can be understood in terms of passivation of the electrode surface area by captured cells. However, the voltammetry is not sensitive enough at lower cell concentrations to provide conclusive proof of cell capture and only poorly characterises the extent to which capture was successful, meaning that a total cell count from this data would be liable to produce errors in electrode passivation recorded versus cells captured at the electrode surface. It is also interesting to note the observed broadening of distance between oxidative and reductive processes following the capture of cells to the surface of the electrode. For *Figure 2.6 (A)*, following the incubation of the electrode with 10^5 cells, the separation between E_{pc} and E_{pa} broadens to 110 mV (Red) from a separation of 73 mV prior to cell capture (Blue), which may be indicative of a decreased rate of electron transfer following cell capture. This change in E_{pc} and E_{pa} separation may also be observed in *Figure 2.6 (B)*, albeit to a lesser extent of 81 mV from 74 mV.

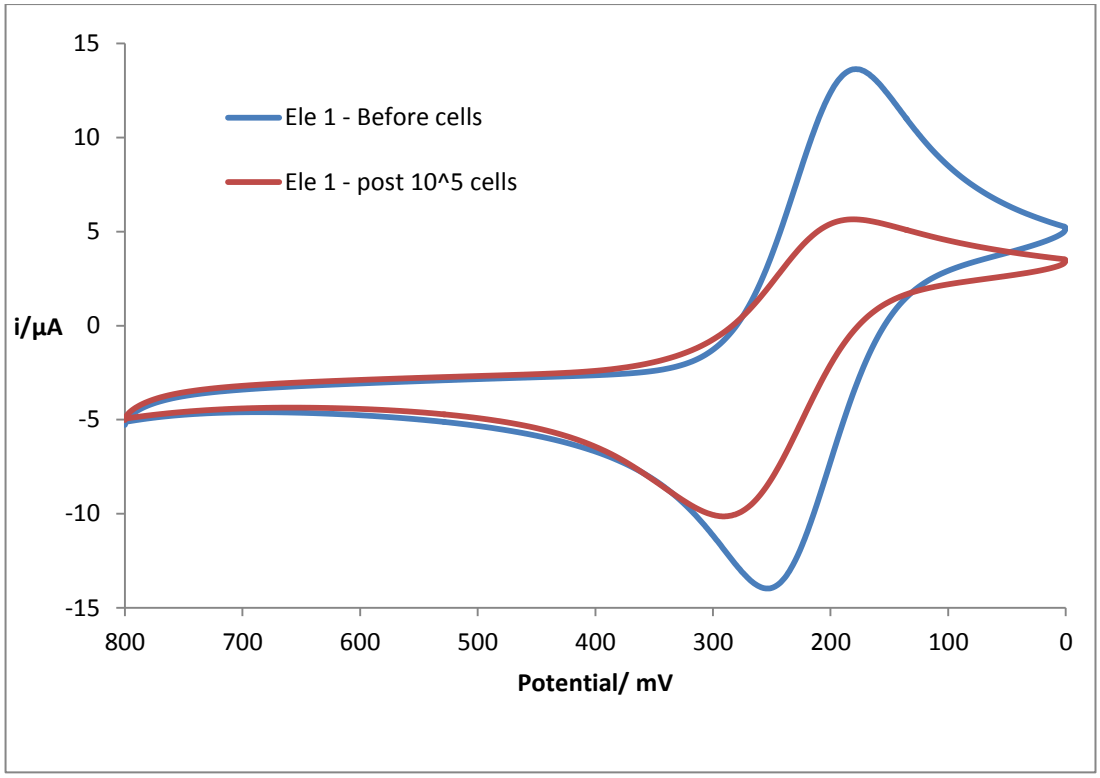

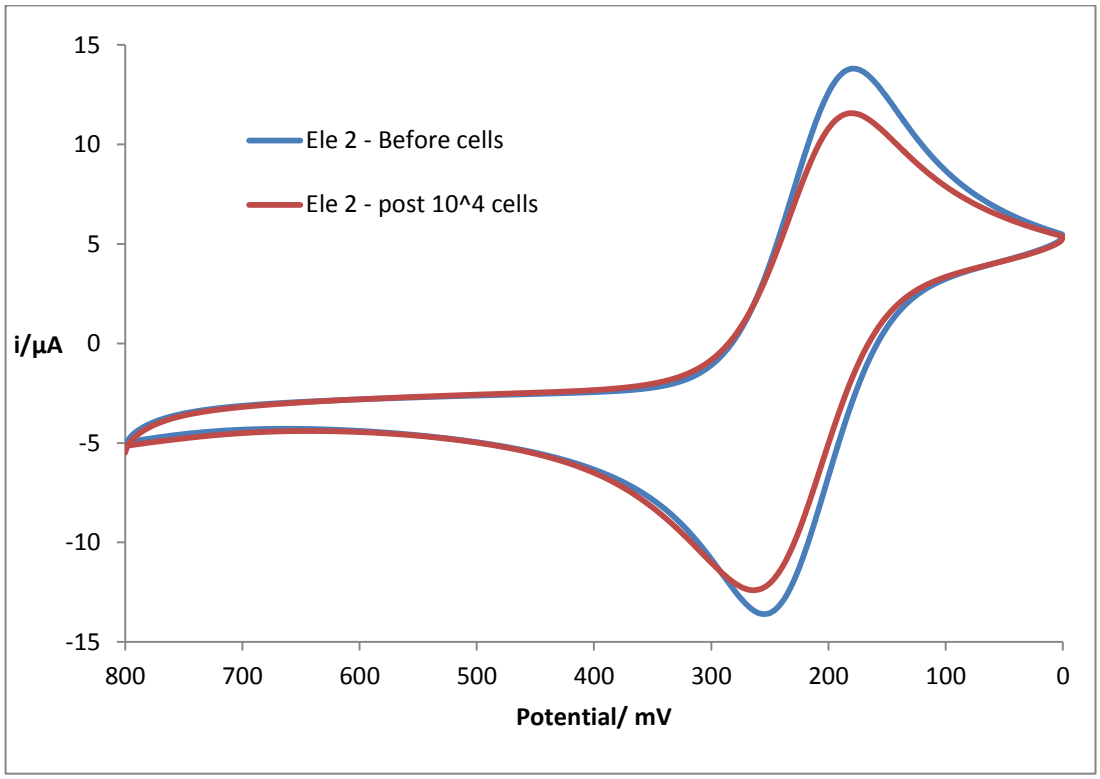

Figure. 2.6.A&B Cyclic voltammogram of two electrodes before (Blue) and after cell capture (Red) carried out in a 5mM FcMeOH solution of DPBS vs. Ag/AgCl at a scan rate of 100 mV/s

.

Figure 2.7. and *Figure 2.8.* show the impedance responses before and following capture of cells to the surface of the electrode. Prior to capture of cells, electrodes 1 to 5 have R values of 425 Ω, 441 Ω, 347 Ω, 385 Ω, and 381 Ω, with a mean value of 396.7 Ω and a standard deviation of 37.2 Ω. All R values for electrodes fall within one standard deviation of the mean with the exception of electrode 3, falling just outside this range, indicating a narrow band of R values for electrodes modified with an antibody monolayer. However, following the incubation and capture of cells to the surface of the electrode, the R values shift to a higher resistance corresponding with the number of cells applied to the electrode surface during incubation. However, once these increases in R are recordedand graphed (*Figure 2.9*) it can be observed that there is a poor correlation to the initial number of cells incubated with each electrode.

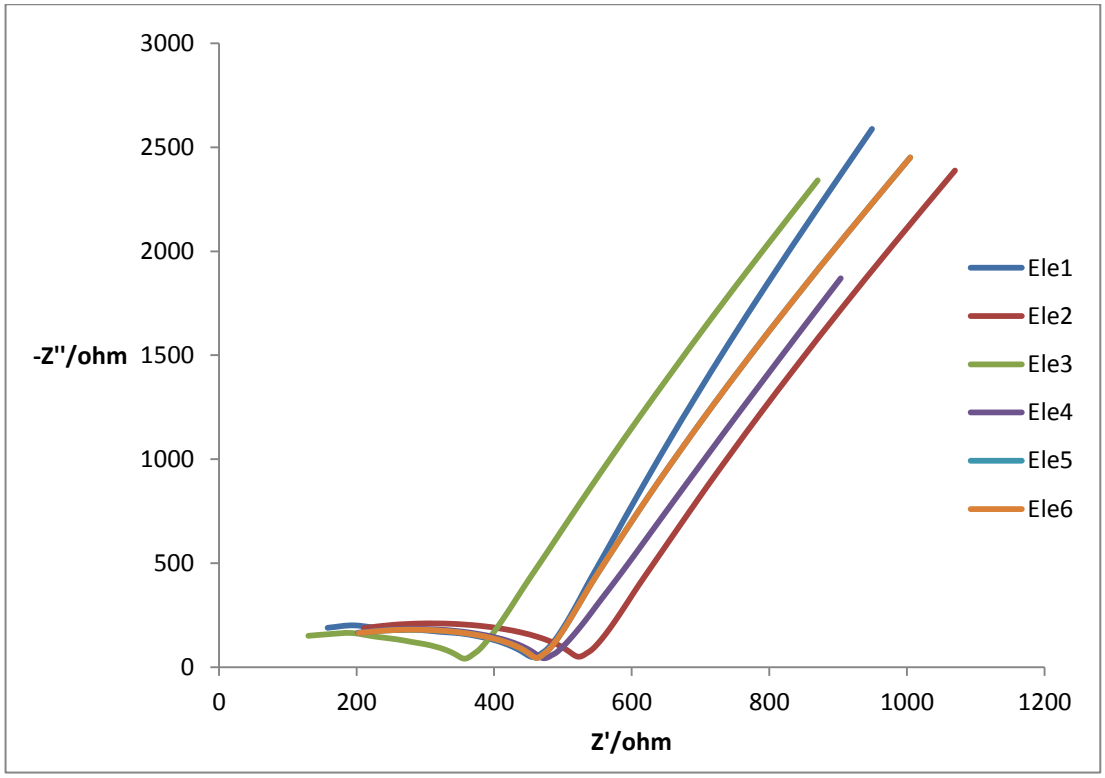

Figure 2.7. Nyquist plot of impedance of electrodes 1 – 5 with electrode 6 shown as control before cell capture carried out at open potential with an amplitude of 25mV vs Ag/AgCl in 1mM DPBS over a frequency range of 1 MHz to 0.1 Hz.

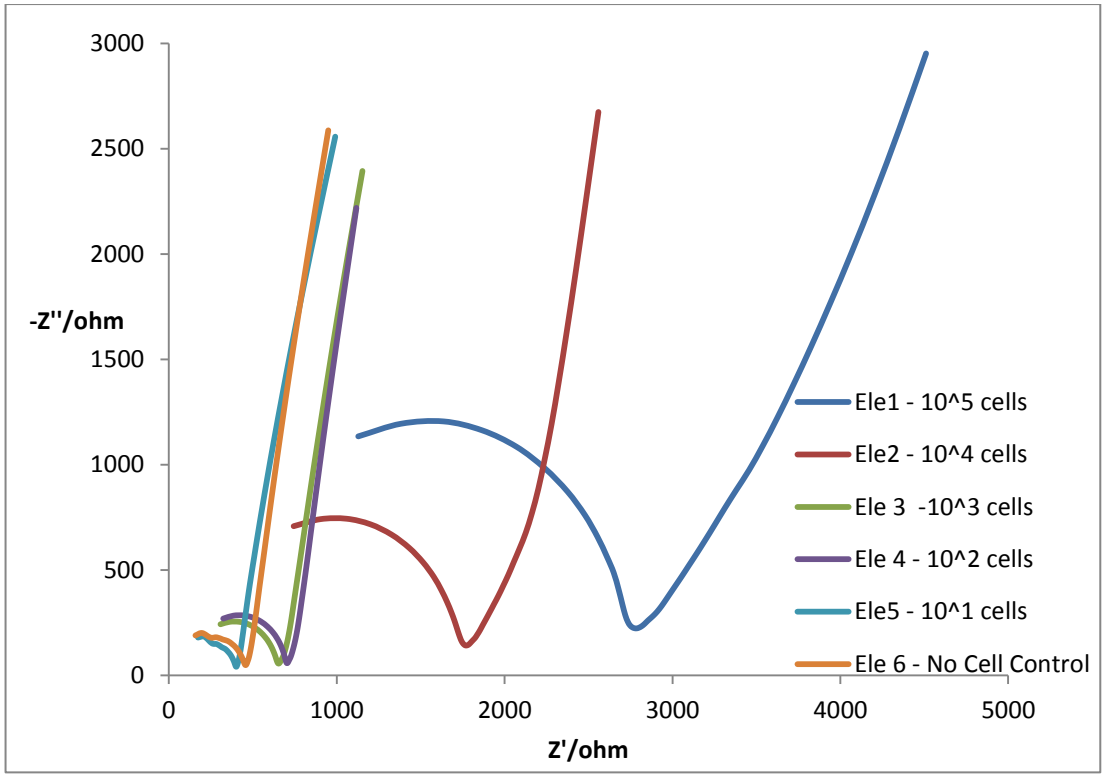

Figure 2.8. Nyquist plot of impedance of electrodes following incubation with cell numbers ranging from 10^5 to 10^1, with electrode 6 as control, carried out at open potential with an amplitude of 25mV vs Ag/AgCl in 1mM DPBS over a frequency range of 1 MHz to 0.1 Hz.

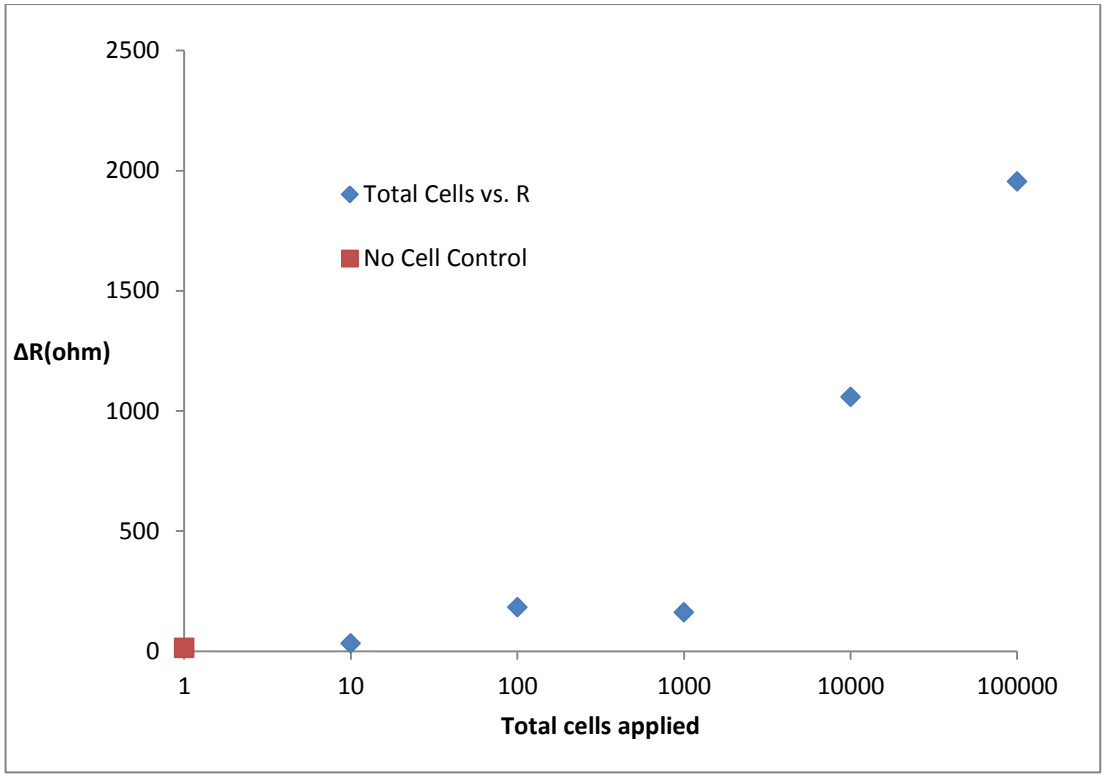

Figure 2.9. Graph showing the relationship between the change in impedance of each electrode before and after capture of varying numbers of cells.

Following impedance and voltammetry measurements, the electrodes were incubated in DiOC6 dye for 30 minutes and then imaged using an inverted fluorescent microscope in order to get a definitive cell count for each electrode and determine the total number of cells captured in each case. The images in *Figure 2.10.* show clearly that in all electrodes cell capture has been successful. Images were processed using ImageJ software and a cell count was taken for each electrode. Note that for the electrode incubated with 10^5 cells here, due to poor image quality and heavy grouping of cells a reliable count could not be achieved.

It is clear that *Figure 2.10. (A)* has the highest number of cells applied to the surface, corroborating the data from impedance measurements in *Figure 2.9.* However, the relationship between change in resistance and the number of cells on each electrode is not perfectly linear and deviations are seen at the lower end of the graph. In *Figure 2.10 (E)* only 2 cells were found to be captured on the surface, however the change in R following the capture of just two cells was shown to be 32.3Ω, giving a per cell value for contribution to resistance of 16.1Ω, which is far greater than that observed for any other sample.

(A): 10^5 cells

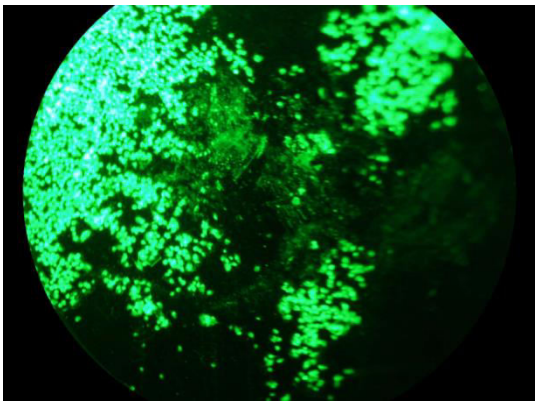

(B): 10^4 cells

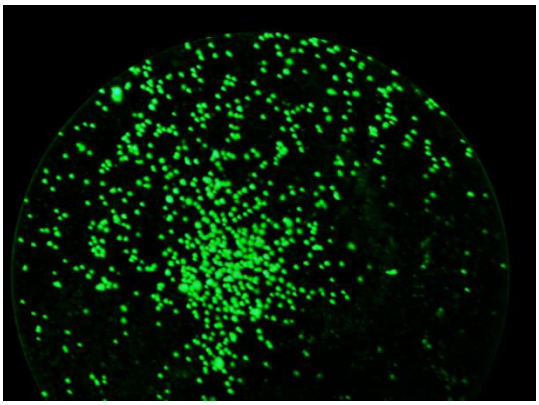

(C):10^3 cells

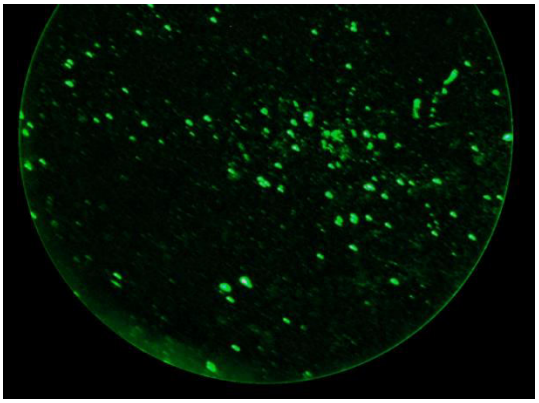

(D): 10^2 cells

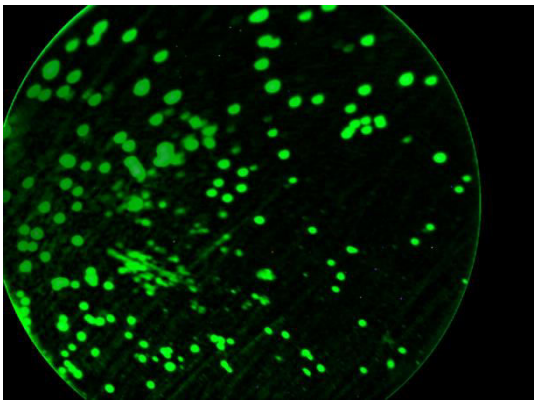

(E): 10^1 cells

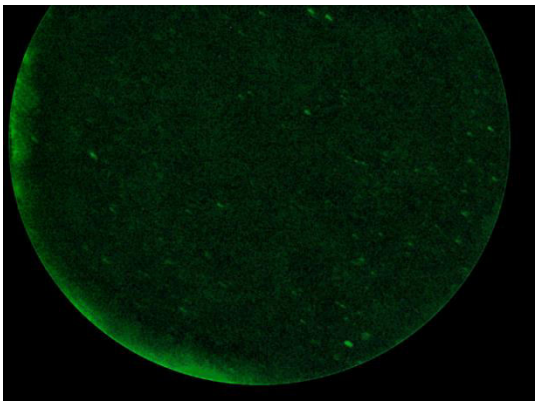

Figure 2.10. Fluorescent microscopy images of electrodes following incubation with varying concentrations of cells (10^5 - 10^1), staining with 25μM DiOC6 dye and fixing. Electrodes were imaged using an inverted fluorescent microscope with a 488 nm excitation wavelength.

To further probe the efficacy of this label free impedance based detection approach, the study was repeated in order to get a more complete picture of the relationship between measured impedance response and number of cells captured on the surface of an electrode and in *Figure 2.11(A) & (B)* the results of this are shown with no cell controls shown in red. It is clear here that there is a statistically relevant difference in the ΔR. Of the three control electrodes used in the study, following incubation in cell free media the mean change in impedance measured was 14.3Ω, where σ = 4.9Ω. A statistically significant difference in impedance measured after cells is considered to be 3σ + control, or 29Ω. Therefore, in this case, the change in impedance of 32Ω observed for 2 cells captured to the electrode surface is considered to be statistically relevant, albeit close to the limit of detection.

In *Figure 2.11 (B)* the measured change in impedance per cell captured is plotted against the number of cells captured to determine a linear range where the number of cells captured may be quantified. The large differences in the ohm per cell values between high and low cell counts may indicate the linear range for this assay may be in the range of > 100 cells, suggesting this approach may have issues with the reliable and quantitative detection of minimal residual disease biomarkers. This data suggests that there is a high margin for error associated with attempting to assign a per cell value at low (< 40) numbers of captured cells. This may be due to the fact that due to the variable shape of captured cells. As the change in impedance is related to the number of cells on the surface, each cell will not have an equal contribution to impedance as the surface area covered by each cell is different for each cell. This distribution of sizes of cells however, would be expected to average out at higher numbers and therefore the linear range for this assay may be seen to be only apparent when there is a high number of cells captured.

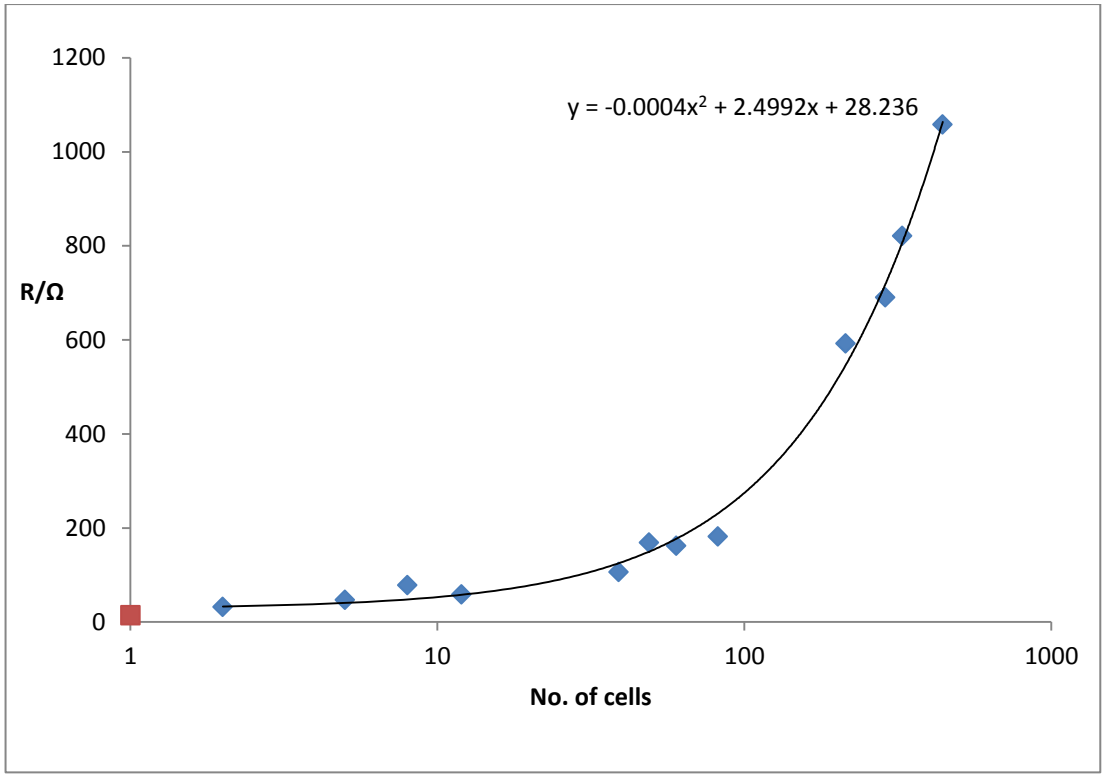

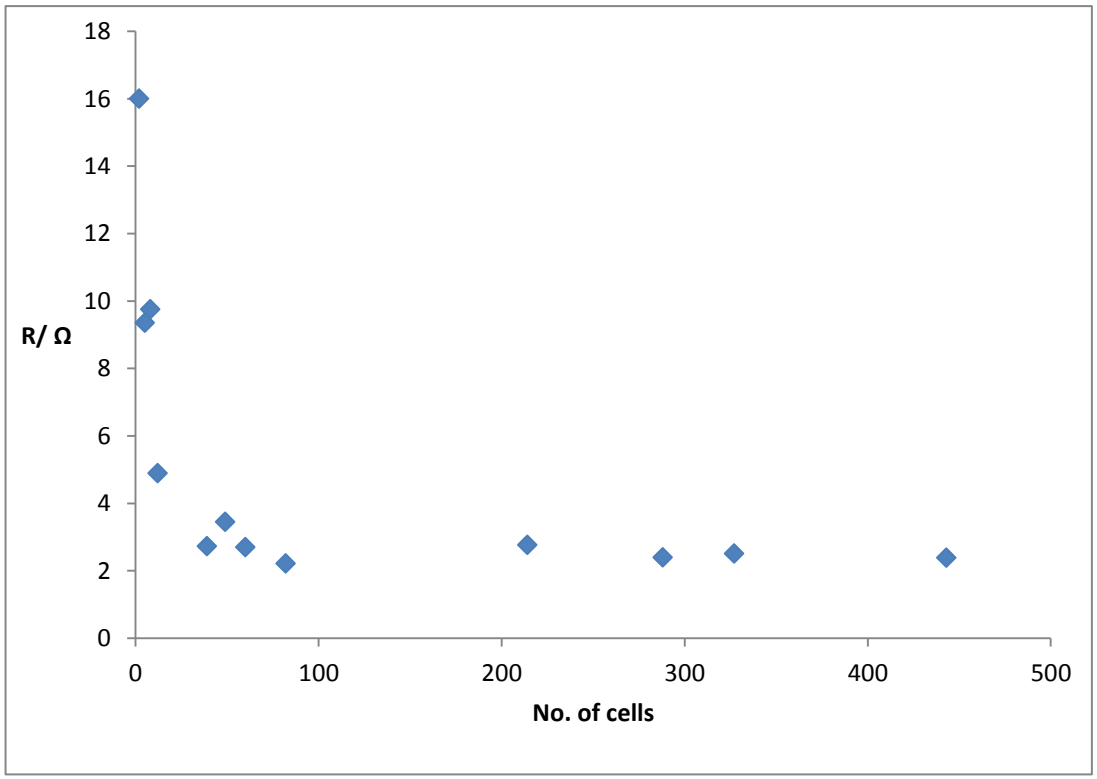

Figure. 2.11(A) & (B). Figure (A) plots the no. of cells captured to each electrode vs. the measured change in impedance with no cell control shown in red. Figure (B) shows the number of cells captured vs. the measured change in impedance per cell.

2.4.3. Platinum Nanoparticle Mediated Cell Detection.

While label free detection of cells has been demonstrated in the previous section, the sensitivity of this approach may not be adequate for applications that require the ability to reliably quantify the number of cells captured. The following section presents the results of labelling cells, post capture, with an electrocatalytic label capable of generating a measureable current proportional to that of the number of cells captured at the electrode surface. Here platinum nanoparticles capable of electrocatalytically reducing hydrogen peroxide were used. This was carried out as a comparison to the study of impedance detection of cells in a bid to improve the stringency of assay results and provide a greater degree of accuracy in the process of cell detection. Here, the electrocatalytic reduction of hydrogen peroxide at a fixed potential will result in a current that is proportional to the number of catalytic nanoparticles and thus the number of cells on the surface of the electrode. However, it should be noted that this effect will be only be reproducible if the number of electrocatalytic nanoparticles on each cell is the same.

The processes of fabricating an electrode surface for cell capture and carrying out capture of cells that have been discussed previously were carried out in the same manner for this study to the point of cell incubation. Once the incubation time was complete, the electrodes were washed with DPBS to remove any weakly bound cells and placed in supplemented-DPBS based suspension of antibody modified platinum nanoparticles for 30 minutes at 37°C. The nanoparticles were modified with anti-human GD2 mouse IgG antibodies in a similar fashion to that of the electrodes mentioned in previous sections. *Figure 2.12* shows the results of EDX analysis of antibody conjugated nanoparticles dried onto a planar gold on silicon substrate. The spectrum shows strong x-ray emissions for both gold and platinum. The map of platinum emission generated by the software however clearly shows the localisation of platinum to the large structure of dried. The lack of observed signals for possible dopants or surface tarnishing materials dissuades any argument that the surface of the PtNP may have been rendered electrocatalytically inert.

Project: PtNP Owner: Inca Operator	Sample: PtNP Dried to Gold Substrate Type: Default

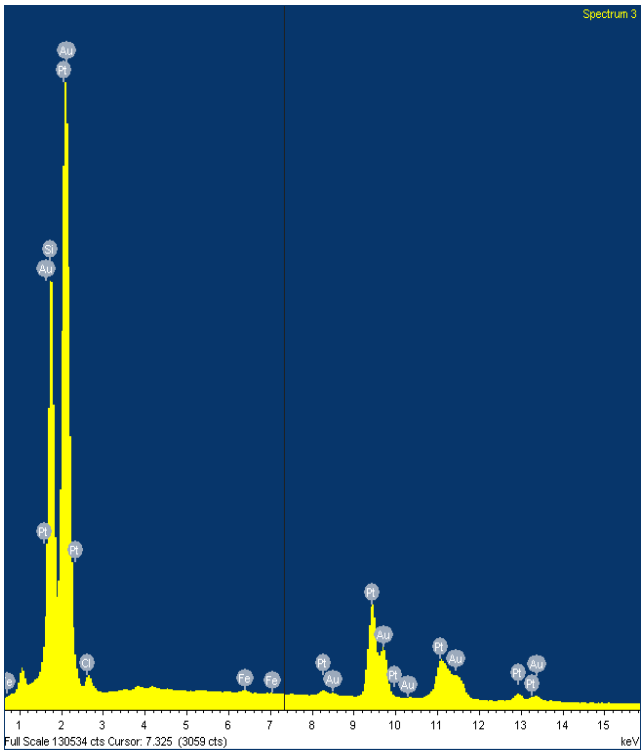

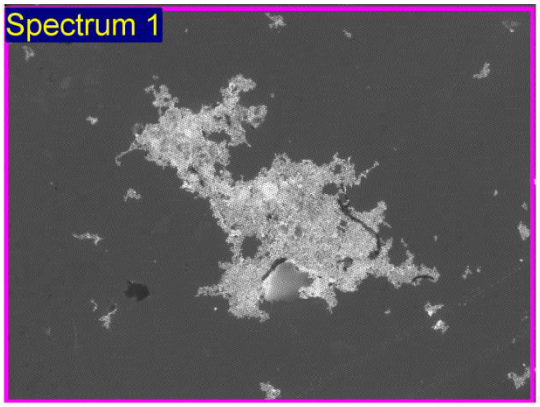

Electron Image 1

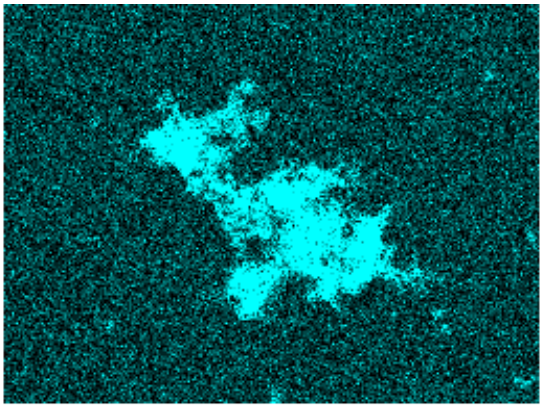

Pt La1

Comment: Antibody conjugated Platinum nanoparticles dried to the surface of a planar gold substrate for EDX analysis.

Figure 2.12. EDX analysis of PtNP-Ab dried onto gold substrate performed with an INCA Operator EDX system coupled to a Hitachi S5500 FeSEM at an accelerating potential of 20 kV

Following the incubation of electrodes with PtNP, the electrodes were placed in an electrochemical cell of 10 mM H_2SO_4 under an applied potential of -250mV vs. Ag/AgCl and following the injection of H_2O_2 the current due to the electrocatalytic reduction of H_2O_2 by the PtNPs was determined using the amperometric i/t curve function of a CHI760E potentiostat program. As the

Figure 2.13. shows the i-t curves generated for electrodes A to E during detection runs following an injection of hydrogen peroxide resulting in a total peroxide concentration of 2mM within the electrochemical cell. Table 2.1 Shows the current evolved for electrodes A - E during the detection program with the total number of cells applied, the number of cells counted on the electrode post detection and the current per cell evolved over the detection program. *Figure 2.14.* shows the plot of the current evolved due to peroxide reduction versus the number of cells on the electrode.

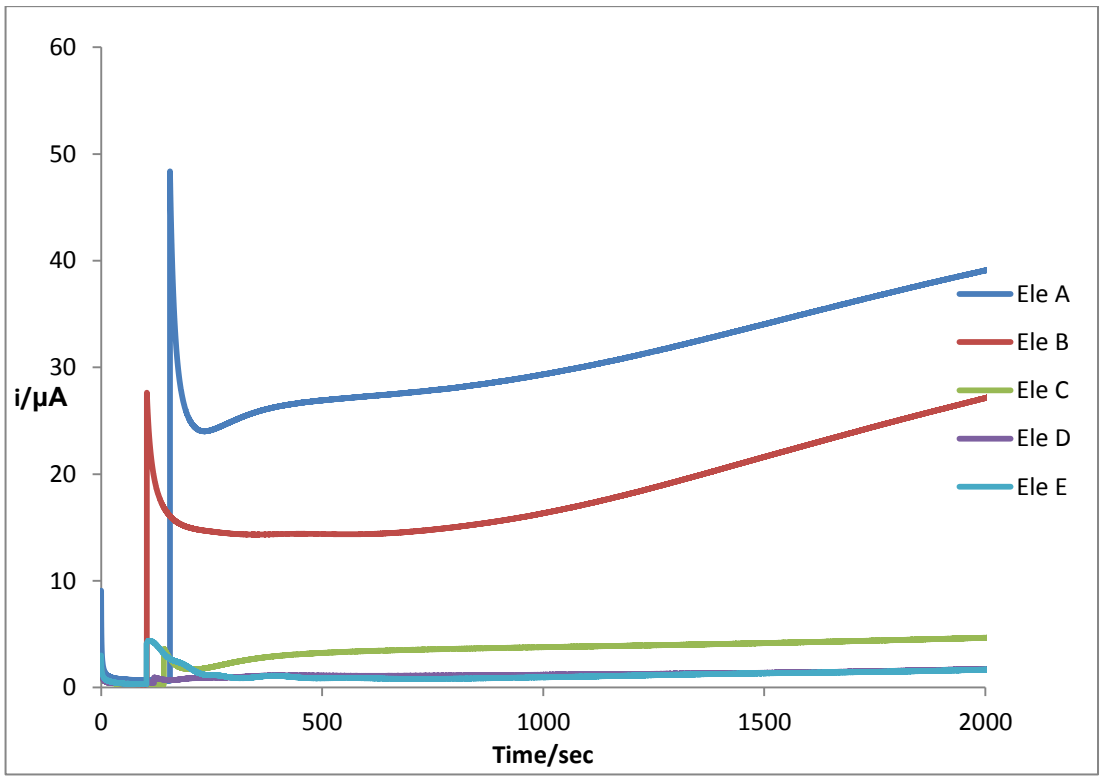

Figure 2.13. i-t curves generated for electrodes captured with cells that were labelled post capture with PtNP-Ab. Curves were generated under a constant potential of -250mV vs Ag/AgCl in 10 mM H_2SO_4. Following a minimum of 100 seconds program was paused and an injection of H_2O_2 to result in a concentration of 2 mM H_2O_2 within the electrochemical cell. 1900 seconds after the injection is made the program is halted and the final current is recorded.

Table 2.1. Results for the PtNP based detection of cells showing cells captured to the electrode as well as the current evolved during the detection program and current per cell value for each electrode.

Electrode	A	B	C	D	E	Control
Total Cells Applied	100000	10000	1000	100	10	0
Cells Captured	1637	1109	187	36	9	N/A
Δi (μA)	38.51	27.9	4.3	1.43	0.36	0.11
Δi/cell (μA)	0.0235	0.0243	0.0233	0.0367	0.0407	N/A

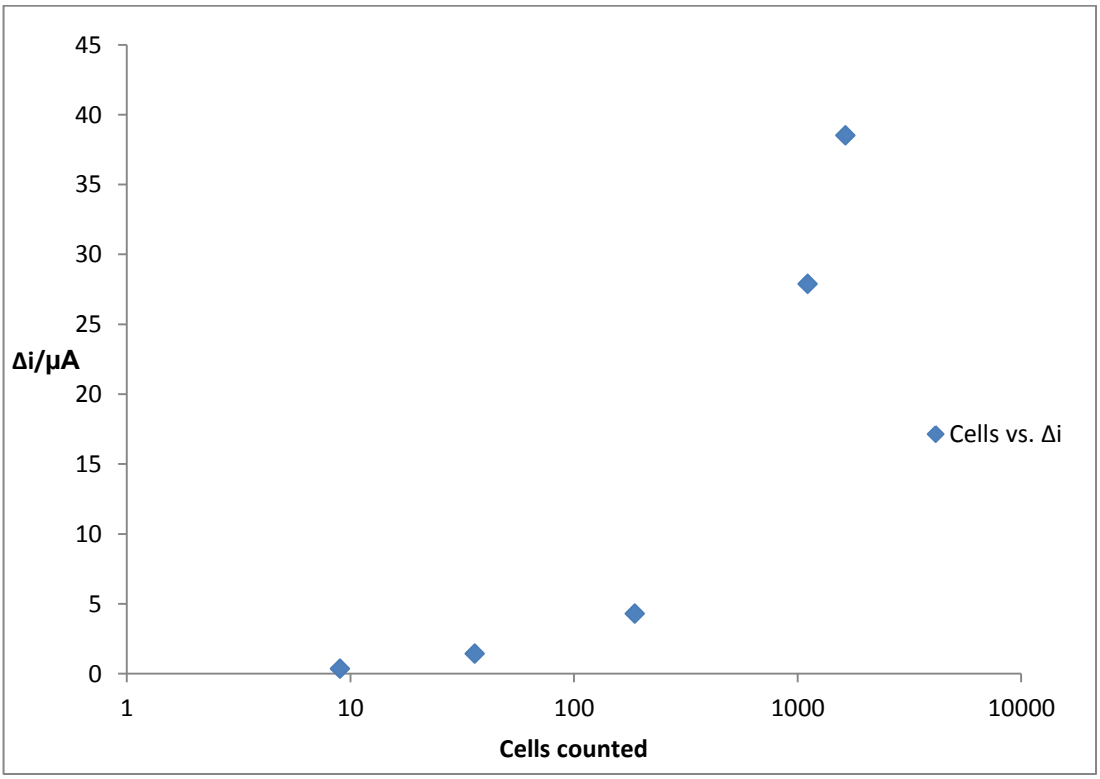

Figure 2.14. Graph showing the relationship between the Δi of an electrode and the number of cells captured to the electrode surface. At higher counts, linearity is observed, however at low counts current change per cell values have large deviations.

From these results it is clear that detection of captured cells through labelling with antibody conjugated platinum nanoparticles has been successfully carried out showing a linear correlation between, approximately 23.5nA per cell for samples captured with approximately 1600 to 180 cells. However, at lower cell counts per electrode (below 50 cells) the observed current per cell increases sharply. For example, electrode E, where 9 cells are captured generates a current of 0.36μA, which is approximately 50% higher than that expected on the basis of the higher coverage data, 0.21μA.

There are several processes that may contribute to the increased current per unit cell at low cell counts. First, the underlying gold surface of the polished planar electrode is weakly electrocatalytic to the reduction of hydrogen peroxide as well, resulting in a small current associated with each individual electrode that is negligible when a surface is covered in a high concentration of cells but will become the main contributor to the current response when no cells are present. Second, similarly to the results observed for the label free assay, the polymorphic nature and size of captured cells may play a role in the signal observed for each cell. The varied shape and size of each cell on the surface of an array may lead to discrepancies in the number of PtNP electrocatalysing the reduction of peroxide on the surface of the electrode. Often in a population of cancer cells, the size distribution of cells is broad and highly varied, often due to abhorrent cell cycle arrest resulting in binucleated cells [12]. It would be intuitive to assume that the larger cell would result in twice the amount of current as it would have twice as many nanoparticles bound to its surface. On a scale of many cells, these statistical size differences would be expected to be averaged out, but at lower cell counts, only a small proportion of binucleated cells would result in considerable errors in measured cell number. The physical shape of a cell on the surface of the electrode will also determine the distance of bound nanoparticles to the surface of the electrode and thus the electrical communication between the PtNP and the electrode. During capture of cells to the surface there may be small fragments of cell membrane in solution that contain GD2 and as a result are also captured to the electrode surface. Such fragments maybe too small to observe by fluorescent microscopy, but nevertheless have the capacity to become labelled with PtNP and will become electrocatalytically active. These smaller fragments may not contribute markedly to the current produced by the electrode at high cell counts as they may be

too scarce due to the lower degree of free space on the surface of an electrode with a high cell count, but for an electrode with a large surface area of free antibodies the additive effect on the electrode surface may produce a measurable current. Finally, the distance between adjacent cells and thus PtNPs must be considered. The surface of a PtNP the catalysis and subsequent diffusion of the catalytic substrate and products diffuse radially from the PtNP surface. This radial diffusion of materials to and from the PtNP surface controls the current produced by a single nanoparticle. However, as PtNP are brought into closer proximity of one another, the overlap of radial diffusion fields may lead to a decrease in the catalytic output and thus the current produced by each nanoparticle.

2.5. Conclusion.

The capture of cells to an electrode and their subsequent detection has been successfully carried out. The label free method based on measuring changes in the overall cell impedance due to the capture of cells increases linearly for cell counts between 40 and 443 cells. In this range the results show that an increase in resistance at the electrode of approximately 2.6 ohm per cell, with a standard deviation of 0.36 ohms. In Figure 2.11. (A) is it is clear that the calibration plot is biphasic and this is may be explained in terms of the changes in not simply the background resistance of the circuit being high, but instead changes in both capacitance and resistance when going from a low cell count to a high cell count. As explained previously in this chapter, the total impedance measured for the electrochemical cell will be dependent on both resistance and capacitance, and in cases where cell counts are low, accurate determination of the resistance associated with cells on the surface may be hampered by small changes in the capacitance of the large electrode surface. Then as higher cell counts are obtained on the electrode surface, the effect of shrinking the electrode surface area will result in changes in resistance being the dominant factor in the measured impedance for the electrochemical cell.

The labelled method, based on the measurement of current generated by captured electrocatalytic PtNP on the surface of captured cells, in comparison, offers assay results with a greater degree of accuracy at the high end of the scale, with a mean μA per cell value of 23.7 nA/cell, and a standard deviation of 0.5 nA, or 2.23%. However, this assay suffers from inaccuracies at the lower end of the scale with a deviation from the mean mentioned above of 17 nA/cell or 71.72%. This deviation at lower cell counts is far greater than the standard deviation observed for this data set and is likely this could be due to discrepancies in the extent to which each individual cell is labelled giving rise to greater current per cell values observed or increased spacing between electrocatalytic PtNP at low cell counts that will lower the effect of overlapping diffusion fields. There may also be a small baseline current that is negligible at high cell counts. It should also be noted that the overall current magnitude of 360 nA for electrode E is quite low, making it difficult to measure accurately with a macroscopic electrode.

When compared to the observed inaccuracy at the captured cell counts <10 for the label free impedance based detection method, 11.7 Ω/cell, the PtNP labelled assay still outperforms the label free assay, with regards to accuracy, by almost an order of magnitude. This data suggests that at very low captured cell counts the quantitative detection of captured cells is unreliable, possibly due to the contribution to measured impedance of cellular secretions becoming adhered to the surface or components of the complex growth media. As before, as high cell counts, these contributions appear negligible but limit the ability to quantitate low cell counts reliably.

In summation, the labelled assay performs best for reliable quantitation of captured cells on the surface of the electrode. However, neither method is suited to accurate quantitation of a total cell count at low (<10 cells) counts. Both methods have displayed the ability to perform reliable qualitative detection of captured cells at dynamic ranges of 100-1000 cells and show reasonable quantitation of cells counts within this range.

2.6. Bibliography

1. Yang, H.Y., Zhou, H.F., Hao, H.Y., Gong, Q.J., and Nie, K., *Detection of Escherichia coli with a label-free impedimetric biosensor based on lectin functionalized mixed self-assembled monolayer.* Sensors and Actuators B-Chemical, 2016. **229**: p. 297-304.
2. Yang, L.J., *Electrical impedance spectroscopy for detection of bacterial cells in suspensions using interdigitated microelectrodes.* Talanta, 2008. **74**(5): p. 1621-1629.
3. Hu, Y., Zuo, P., and Ye, B.-C., *Label-free electrochemical impedance spectroscopy biosensor for direct detection of cancer cells based on the interaction between carbohydrate and lectin.* Biosensors and Bioelectronics, 2013. **43**(Supplement C): p. 79-83.
4. Wang, R., Di, J., Ma, J., and Ma, Z., *Highly sensitive detection of cancer cells by electrochemical impedance spectroscopy.* Electrochimica Acta, 2012. **61**(Supplement C): p. 179-184.
5. Venkatanarayanan, A., Keyes, T.E., and Forster, R.J., *Label-Free Impedance Detection of Cancer Cells.* Analytical Chemistry, 2013. **85**(4): p. 2216-2222.
6. Gu, W.W. and Zhao, Y., *Cellular electrical impedance spectroscopy: an emerging technology of microscale biosensors.* Expert Review of Medical Devices, 2010. **7**(6): p. 767-779.
7. Zhao, Y., Hao, M.W., Wang, Y., Sha, Y.F., and Su, L.H., *Effect of electrolyte concentration on the capacitive properties of NiO electrode for supercapacitors.* Journal of Solid State Electrochemistry, 2016. **20**(1): p. 81-85.
8. Tadros, T., *Chapter 2 - Colloid and interface aspects of pharmaceutical science A2 - Ohshima, Hiroyuki*, in *Colloid and Interface Science in Pharmaceutical Research and Development*, K. Makino, Editor. 2014, Elsevier: Amsterdam. p. 29-54.
9. Modak, S., Gerald, W., and Cheung, N.K.V., *Disialoganglioside G(D2) and a novel tumor antigen: Potential targets for immunotherapy of desmoplastic small round cell tumor.* Medical and Pediatric Oncology, 2002. **39**(6): p. 547-551.
10. Wu, Z.L., Schwartz, E., Seeger, R., and Ladisch, S., *EXPRESSION OF GD2 GANGLIOSIDE BY UNTREATED PRIMARY HUMAN NEUROBLASTOMAS.* Cancer Research, 1986. **46**(1): p. 440-443.
11. Prabhakar, N., Arora, K., Arya, S.K., Solanki, P.R., Iwamoto, M., Singh, H., and Malhotra, B.D., *Nucleic acid sensor for M-tuberculosis detection based on surface plasmon resonance.* Analyst, 2008. **133**(11): p. 1587-1592.
12. Shi, Q. and King, R.W., *Chromosome nondisjunction yields tetraploid rather than aneuploid cells in human cell lines.* Nature, 2005. **437**(7061): p. 1038-42.

Chapter 3.

Detection of Neuroblastoma cells by miRNA expression profiling.

3. Detection of Neuroblastoma cells by miRNA expression profiling.

3.1. **Introduction**

Currently, there is a great deal of interest in biosensor fabrication and its application in the detection of minimal (residual) disease and theranostics [1-7].To this end, miRNA may be useful biomolecular targets. First, since they occur ubiquitously across all cell types and tissues[8], miRNA based detection systems have the potential to be applied to not only the detection of disease from any host cell regardless of phenotype, but they may also be applied to the detection of pathogenic disease in the instance of bacterial or fungal infection[9]. Second, as miRNA expression is one of the controlling factors of gene expression and thus phenotype, expression profiles of miRNA may be used to not only identify disease, but also give specific information about the disease state and therefore allow the tailoring of treatment plans to individual cases for efficient disease management[10, 11]. The third advantage of miRNA based biosensor systems is the chemical similarity of individual targets due to the relatively simple structure of nucleic acids when compared to other biomolecular targets such as proteins. However, while the general structure and scheme of detection may be conserved across all potential targets, the sequence of each individual target miRNA offers exceptional target specificity. This allows for the design of simple immobilisation strategies, purely by fabricating a capture oligonucleotide complementary to the target miRNA, avoiding the labour intensive antibody production and screening associated with other biomolecular biosensors. While the vast majority of miRNA based biosensors require amplification of the target miRNA[10, 12, 13], electrochemically based detection methods offer the ability to provide fast, ultrasensitive analysis, requiring only a fraction of the time that may be needed for either the isolation and preparation of histological samples in the case of cancer identification and classification.

The following section describes an amperometric biosensor applied to the childhood cancer, neuroblastoma. As with other amperometrically based miRNA detection schemes reported in the literature, this approach will rely on the hybridisation of a

miRNA target to a capture oligonucleotide on the surface of an electrode to bring about a current response that can be accurately measured. However, the specific advantage of this approach is the possibility to carry out cell capture, cell lysis and detection of miRNA at the electrode surface, thus creating regions on the electrode surface where intracellular miRNA is concentrated following lysis and reducing the dilution effects of lysing cells in bulk solution prior to hybridisation and detection. Another possible advantage to this approach would be the possibility of determining the expression profile of miRNA within each individual cell, by lysing the cell into a single microcavity. The total intracellular content of a specific miRNA target may be exposed to and subsequently hybridised to capture strands on the inner surface of a single microcavity allowing the miRNA concentration to be determined. An amperometric biosensor relies on the transduction and detection of a current resulting from an interaction of the sensor with its target biomolecule, in this case a miRNA, miR-132. miR-132 was chosen due to its upregulated expression levels observed in differentiating neuroblastoma cells. In a study by Chen et al, neuroblastoma cells treated with retinoic acid to promote differentiation exhibited a 2.67 fold increase in expression and were the most increasingly expressed miRNA observed during differentiation[14]. As a result, miR-132 can be used as a biomarker for this disease. In this scheme, a gold electrode is modified with a self-assembled monolayer of thiolated capture oligonucleotides complementary to an 11nt segment from the 5' terminus of the target miRNA. The remaining 11nt of the 3' terminus of the miRNA target is reserved for hybridisation with a second thiolated oligonucleotide strand complementary to this segment referred to as the probe. Following the hybridisation of the miRNA target to the capture oligonucleotide, a platinum nanoparticle uniformly decorated with probe oligonucleotide is bound to the array through hybridisation of the probe to the target miRNA (*see Figure 3.1.*). Once the platinum nanoparticles have been immobilised on the array, a potential is applied to the electrode and the current generated by the electrocatalytic reduction of hydrogen peroxide by the bound platinum nanoparticles measured which depends on the concentration of miRNA in the sample. This provides the basis the amperometric detection of miRNA.

Thus the aim of the following body of work detailed in this chapter is to create an electrode surface where the specific capture of neuroblastoma cells, their subsequent

lysis, and the detection of their intracellular miRNA target fraction may be detected and measured. By forming a three dimensional electrode surface that may be selectively chemically modified in different steps, ie cell capture and lysis on the exterior of the microcavity and miRNA detection on the interior of the microcavity, the intracellular miR-132 fraction of lysed cells may be concentrated to a dedicated detection surface in very close proximity following lysis.

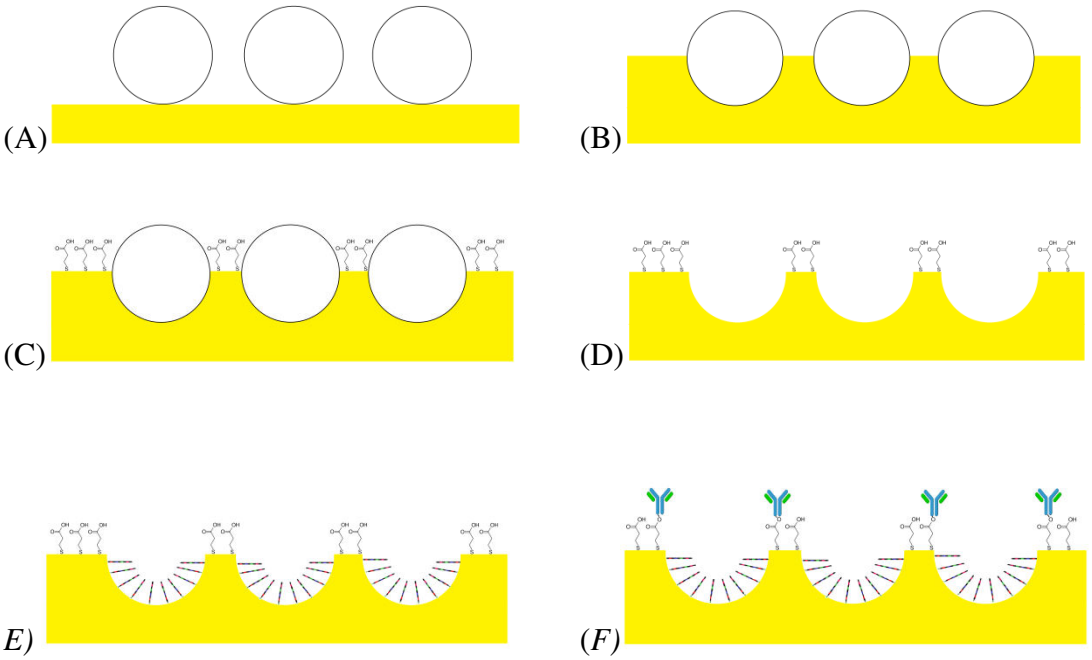

Figure 3.1. Fabrication of a fully modified microcavity array begins with the deposition of polystyrene template spheres to the surface of a gold-silicon wafer (A). Gold is then electrodeposited through the template spheres until microcavities are formed around the template spheres(B). The array is placed in an ethanolic solution of 3MPA until a monolayer is formed on the surface(C). The array is then placed in THF to remove the polystyrene template revealing the bare surface of the inner cavity(D). The array is placed in a 1μM solution of thiolated capture RNA until a monolayer is formed (E). The array is carboxy-termini of the 3MPA are then activated through EDC-NHS coupling and anti-GD2 antibodies are conjugated to the upper surface.

Figure 3.1. shows the electrodeposition of gold around a template of polystyrene spheres that gives rise to a three dimensional gold microcavity surface on an electrode. The primary advantages of this surface shape over traditional planar electrodes is that the surface may be modified in stages to produce two spatially

separated regions on the electrode capable of carrying out two separate functions; the exterior surface for capture of neuroblastoma cells and the interior of the microcavity for the hybridisation miRNA target and detection by electrocatalytic platinum nanoparticles. Initially polystyrene template spheres are deposited onto the surface of an electrode in suspension and allowed to dry, giving rise to layers of polystyrene template spheres packed onto the surface of the gold electrode. The electrode is then placed in a gold electrodeposition solution and a potential is applied to the electrode resulting in the deposition of gold around the layer of polystyrene template spheres on the electrode surface. Deposition is monitored by measuring the charge passed through the circuit. Once deposition is complete, the electrode is removed from the deposition solution and washed to remove excess polystyrene spheres, however, the polystyrene template spheres within the electrodeposited cavities remain in place. The electrode is then immersed in a solution of 3-mercaptopropionic acid (3MPA) and a self-assembled monolayer forms on the gold surface, however, this monolayer formation is restricted to the top surface of the cavity array as access to the interior surface of the microcavities is blocked by the polystyrene template spheres. Following this process, the electrode is washed and the polystyrene spheres are dissolved with tetrahydrofuran exposing a clean interior surface of the microcavity. This interior surface of the microcavity is then modified with a self-assembled monolayer of capture RNA oligonucleotide that is complementary to a portion of the miRNA target. Finally, antibodies specific to extracellular antigens expressed on tumour cells are conjugated to the carboxyl groups of the 3MPA monolayer through EDC-NHS coupling. This coupling method relies on a carboxylic acid that has been activated by the EDC-NHS to become coupled to an amine. As the nucleic acids within the microcavity are spatially separated from the carboxylic acids of the monolayer on the outer surface of the microcavity array, and the oligonucleotides possess no carboxylic acid units, no cross-coupling or antibody-oligonucleotide coupling would be expected. The coupling method is also carried out in a physiological temperature and pH and therefore is not expected to degrade oligonucleotides in the microcavity array.

The fully modified electrode is then incubated in a suspension of Neuroblastoma cells to allow capture of cells to occur. Osmotic lysis using ddH_2O is carried out on the captured cells and hybridisation of the target miRNA to the capture

oligonucleotide is allowed to occur. After a fixed time to ensure kinetic control over hybridisation, the electrode is washed to remove any remaining lysed cell fragments and unhybridised miRNA and placed in a solution of uniformly decorated probe platinum nanoparticles (PtNP) and the probes hybridise to the target miRNA. Following a wash to remove any unhybridised probe PtNP, the electrode is then placed in an electrochemical cell and the current produced under an applied fixed potential is measured to establish a baseline current produced by the microcavity array. Following this, an injection of hydrogen peroxide is made into the cell and the current is measured again. As platinum nanoparticles will readily catalyse the reduction of hydrogen peroxide at the applied potential, a current increase will be observed. The increase in current, attributed to the electrocatalytic reduction of hydrogen peroxide by PtNP, is directly related to the number of immobilised platinum nanoparticles on the array and therefore should be proportional to the intracellular concentration of miRNA target.

However, the ability of this detection scheme to carry out highly selective ultrasensitive detection of miRNA relies on several key factors. Initially the capture of neuroblastoma cells to the surface of the microcavity array must be followed by lysis in such a manner that the miRNA target is free to diffuse into modified microcavities within the array. Also the uniformly labelled electrocatalytic nanoparticles must diffuse into the microcavities in sufficient numbers to produce a signal for every capture-target hybridisation event. The production of a detectable signal from each of these single electrocatalytic nanoparticles on the surface of the array relies on good electrical conductance between the nanoparticle and the surface of the microcavity array. Finally, the signal from immobilised catalytic nanoparticles must be detectable against the background current produced by the underlying gold microcavity surface. For this to be possible the microcavity surface must ideally be completely electrochemically inert for the reduction of peroxide with the current response being dominated by immobilised nanoparticles.

3.2. Experimental

3.2.1. Materials

Gold-silicon wafer substrates were purchased from AMS bio. Techni Gold® 25 ES gold plating solution was purchased from Technic Europe. 5µm and 3µm polystyrene spheres were purchased from Bangs laboratories and 1µm polystyrene spheres were purchased from Polysciences. RGD custom thiolated capture peptide was purchased from Celtek. Anti-human GD2 monoclonal mouse antibody was purchased from Santa Cruz Biotechnology. All reagents, unless specified otherwise, were purchased from Sigma Aldrich. All solutions were prepared with double distilled water. Sk-N-AS Neuroblastoma cell line was provided by the research group of Prof. R. Stallings in the RSCI Dublin. Oligonucleotide sequences were purchased from Eurogentec and sequences were as follows:

Capture: 3' HS-AUU GUC AGA UG 5'

Target: 5' UAA CAG UCU ACA GCC AUG GUC G-3'

Probe: 3' U CGG UAC CAG C – SH 5'

3.2.2. Instrumentation

A three electrode electrochemical cell was used consisting of a platinum wire as a counter, a Ag/AgCl reference electrode and a gold working electrode fabricated from gold-silicon wafers with a 5x5mm working area. Electrodeposition, voltammetry and amperometry were carried out on a CHI 760D potentiostat. SEM images were obtained using a Hitachi S3400 scanning electron microscope and FeSEM images were obtained using a Hitachi S5500 Field Emission Electron Microscope. All mammalian cell culture was carried out in a biosafety level II laminar flow cabinet. AFM characterisation of substrates was carried out on a Vecco Bioscope II system using 0.01-0.025 Ohm-cm Antimony(n) doped Silicon tips sourced from Bruker.

3.3. Procedures

3.3.1. Microcavity Preparation

Working electrodes were prepared by scribing and breaking gold-silicon sheets into 15x5mm pieces. 50µl of a 1% w/v suspension of 5µm polystyrene spheres was drop cast onto a 5x5mm area of the electrode by masking the remaining electrode area. The suspension of polystyrene spheres pipetted onto the gold electrode surface was then allowed to dry. The electrode was then placed in 10ml of Techni Gold™ plating solution and a potential of -900mv was applied to the working electrode for various times. Microcavity growth was monitored by the accumulation of charge and confirmed by scanning electron microscopy. 3µm and 1µm cavity arrays were prepared in a similar fashion.

3.3.2. Microcavity Modification

Following the growth of microcavities, electrodes were placed in an ethanolic solution of 1mM 3-mercaptopropionic acid (3MPA) for a minimum of 8 hours to ensure full monolayer formation on the outer surface of the microcavity array. The electrode was then washed with ddH_2O and placed in tetrahydrofuran (THF) overnight to dissolve and remove polystyrene spheres. The electrodes were then washed with THF, ethanol and copious amounts of ddH_2O. A 5mM solution of N-Hydroxysulphosuccinamide sodium (NHS) + 1-ethyl-3-(3-dimethylaminopropyl)carbodiimide hydrochloride (EDC) was made up and electrodes were placed into this immediately and allowed to react for 15-30 minutes. Electrodes were then washed with ddH_2O and treated with 20µl of 200mg/µl solution of Anti-GD2 IgG for 2 hours. Following the conjugation of antibodies to the top surface of the cavities, the electrodes were placed in a solution of thiolated capture oligonucleotide for a minimum of 8 hours.

RGD modification: Due to the prohibitive cost of antibody modified electrodes, a synthetic peptide (referred to from here as RGD) containing the –R-G-D- peptide recognition sequence was used for the non-specific capture of cultured

Neuroblastoma cells As the broad superfamily of integrin proteins expressed on a cells surface that bind these RGD sequences are expressed ubiquitously through mammalian cell types, this form of cell capture is thought to be non specific. However, as the cells used in this work were derived from pure cultures of human neuroblastoma, there was no expectation of contamination expected from other cell types. Modification of cavities with RGD was carried out by placing electrodes in an ethanolic solution of 1mM:5mM RGD and thiolated polyethylene glycol (PEG) for a minimum of 8 hours and following this the polystyrene template spheres were removed with THF and the inner microcavity surface was modified with thiolated capture oligonucleotide.

3.3.3. Probe PtNP fabrication.

A 100mg/L solution of 70nm PtNP were made up ddH_2O. The maximum theoretical oligonucleotide loading of nanoparticles was $7.8x10^{12}$ oligos/cm^2, as calculated using the mean particle size and an estimate of the surface coverage of a close packed nucleic acid monolayer[15]. 1µM stock thiolated probe oligonucleotide was aliquoted into a suspension of PtNP and left on a rocking plate under moderate agitation for a minimum of 8 hours to produce nanoparticles uniformly functionalised with probe strand nucleic acids.

3.3.4. miRNA hybridisation and PtNP immobilisation and detection.

The modified microcavity arrays were placed in a solution of the miRNA target ranging from 1μM to 1pM for 5 hours and washed with copious amounts of DPBS before being placed in a suspension of PtNPs modified with probe strand nucleic acids overnight. (Note: no significant, ≥3bp, complementarity was observed between capture and probe strands. As both strands were immobilised to the electrode/nanoparticle at opposite ends, the possibility of forming duplexes is between these two strands was prohibited as they would both be oriented in the same direction, with respect to their 3' and 5' ends.) The arrays were then once again washed with copious amounts of DPBS and then placed in an electrochemical cell, with 0.01M H_2SO_4 as a supporting electrolyte. The amperometric i/t curve technique on the CHI 760D system was used to monitor the current produced from an applied potential of 100mV vs Ag/AgCl. For 600 seconds the current stabilised to an approximate range of 1-10x10^{-7} amps due to non-faradaic current and at 600 seconds the program was paused and H_2O_2 was injected into the cell to a final concentration of 200μM with moderate agitation to ensure a homogeneous solution, the program was resumed and a current increase was observed. At 2400 seconds the program was ceased and the final current was measured.

3.3.5. Neuroblastoma Cell Culture and Capture

Sk-N-AS cells were cultured using Eagle's Minimal Essential Media (EMEM). When being resuspended from an adherent state, cells were treated with Accutase to preserve extracellular adherent bodies. The cells were then counted using a haemocytometer and drop cast onto electrodes in EMEM for a minimum of 45minutes. Electrodes were then washed x4 with supplemented Dulbecco's Phosphate Buffered Saline (DPBS) to remove unbound cells and extracellular material. In cases where cells were to be imaged by SEM, cells were fixed in 3.7% v/v glutaraldehyde and dehydrated with an ascending concentration of acetone every 15 minutes until saturated at 100% acetone.

3.4. Results and Discussion

3.4.1 Microcavity Array Fabrication and Cell Capture.

In order to fabricate a substrate that could capture neuroblastoma cells and amperometrically detect hybridised miRNA-132, a three dimensional, conductive platform was first formed by electrodepositing an array of gold microcavities onto a gold coated silicon wafer through a template of polystyrene spheres using a fixed potential. The process, known as nanoscale lithography (NSL), allowed the liquid phase deposition of a single layer of cavities. The deposition of gold microcavities was monitored coulometrically. This charge was correlated with structural data from SEM and atomic force microscopy as well as cyclic voltammetry. Cyclic voltammograms of a 5x5mm substrate before and after microcavity deposition are shown in *Figure 3.3.* In the voltammograms, there are well defined gold oxidation peaks at approximately 800 mV vs Ag/AgCl. There is also a less well defined anodic peak between approximately 1075 mV and 1500 mV vs. Ag/AgCl resulting from reduction of the gold oxide surface[16]. The charge associated with reduction of gold oxide is approximately 390μC cm^{-2} and so by integrating the area under the gold oxide reduction peak in the cyclic voltammograms it is possible to measure the microscopic surface area of the gold electrode[17]. Therefore using the equation;

$$\frac{Ap}{390\ x\ 10^{-6}} = Surface\ area\ (cm^2)$$

Where Ap is the area of the peak at approximately 800 mV vs Ag/AgCl, the mean surface areas of the planar gold and the gold microcavity array were thus experimentally determined to be 025 (σ = 0.003) cm^2 and 0.85 cm^2 (σ = 0.06 cm^2) respectively (where n = 3), indicating the surface area of the gold electrode has increased significantly which is consistent with the formation of a three dimensional surface. However, this increase in surface area appears to be greater than expected as the surface area of the electrode, following the formation of hemispherical cavities on the entire surface would be expected to approach double the original surface area. This is due to the fact that the surface area of a hemisphere is given as $2\pi r^2$ whereas a

planar circular surface of the electrode, to which a microcavity would be deposited would be given as $2\pi r^2$. This suggests that following the electrodeposition of microcavity arrays, a much higher degree of surface roughness is observed, giving rise to a much greater measured surface area. *Figure 3.2.* shows SEM and AFM images of 3μm microcavity arrays. SEM was used confirm the electrodeposition of microcavity arrays and the degrees of ordering of the microcavity array. From these images it is clear that while parts of the microcavity array spontaneously pack in an efficient order, disordered, defective areas exist. AFM images show that the cavity depth measured for the microcavities is 1.5μm from the base of the microcavity to the exterior surface.

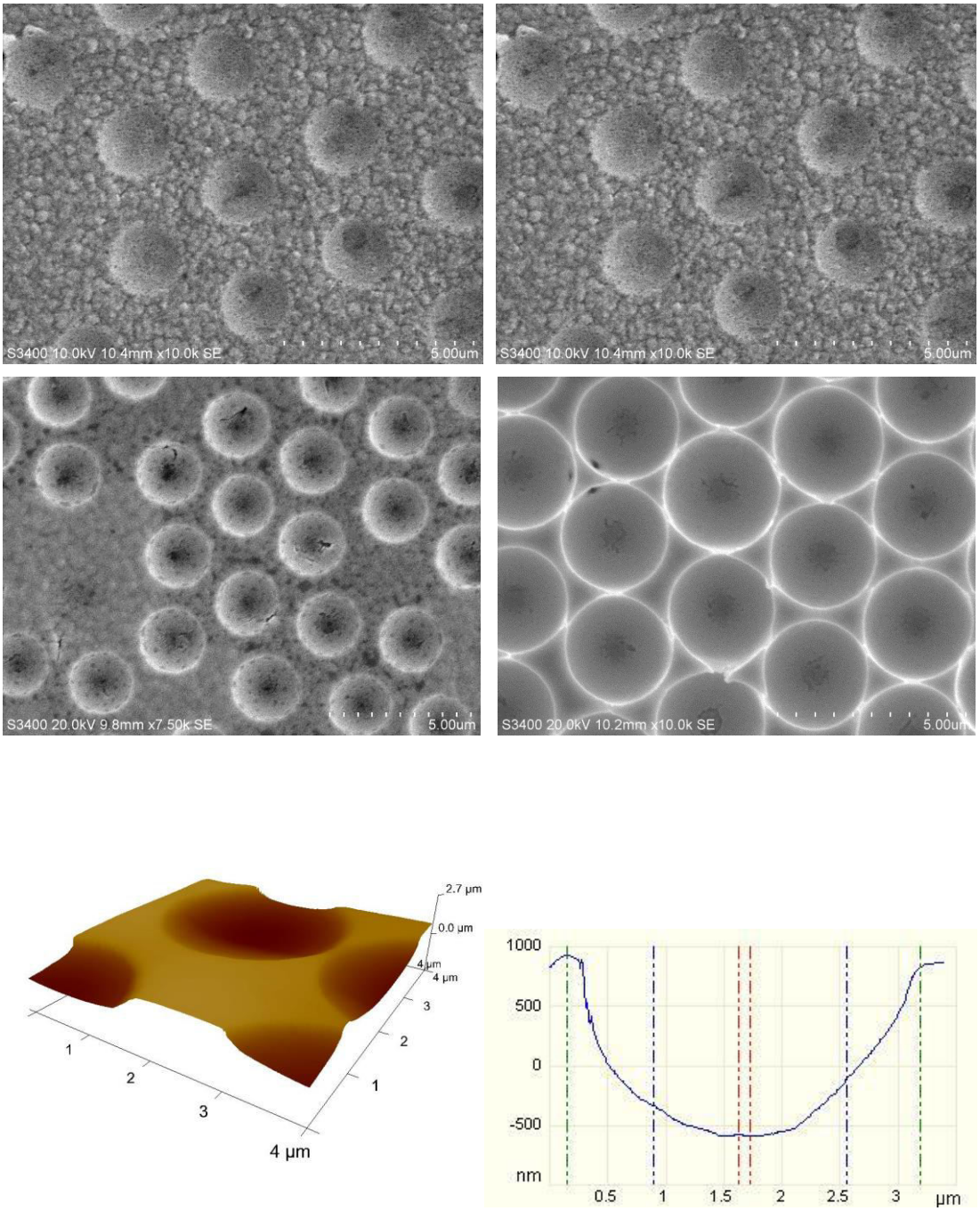

Figure 3.2. Scanning Electron Microscopy images obtained with a probe current of 35 µA and accelerating voltage of 20 kV showing the progression of microcavity electrodeposition. Atomic force microscopy data showing the formation of a three dimensional microcavity array comprised of microcavities with a depth of 1.5µm

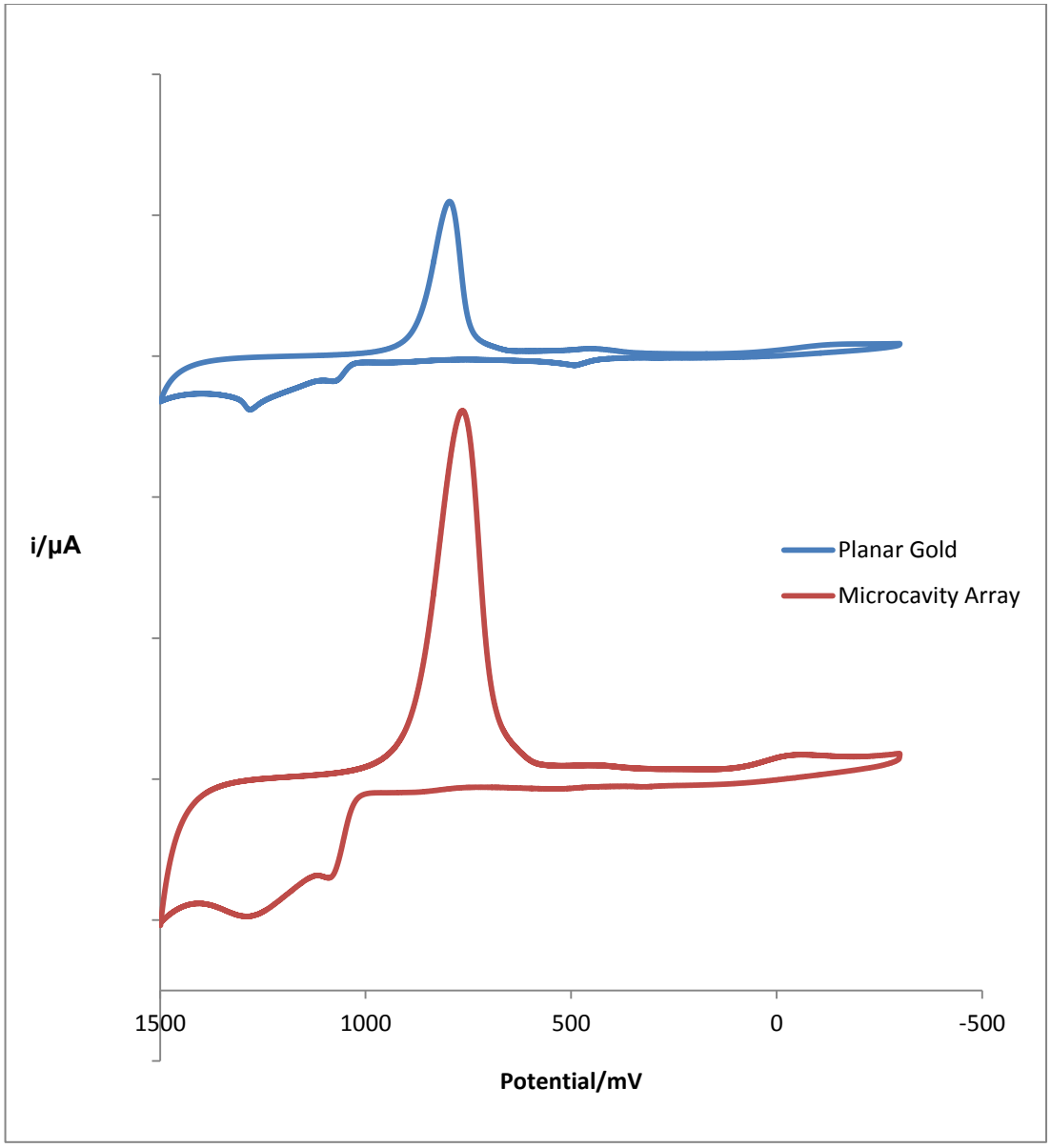

Figure 3.3. Cyclic voltammetry of a planar gold-silicon wafer carried out in 10mM H_2SO_4 vs Ag/AgCl at a scan rate of 100 mV/s before (blue) and after (red) the electrodeposition of a 5µM gold microcavity array to the surface. The increase in the oxide peak at approximately 800mV from planar gold to the microcavity array is indicative of an increase in the microscopic electrode surface area. Note: tick marks on the y-axis are given in 100 µA increments.

Following the electrodeposition of gold to form the microcavity array, excess polystyrene spheres are rinsed from the surface of the microcavity array. However, the spheres in direct contact with microcavities are retained. In order to functionalise the newly formed microcavity arrays for cell capture and miR-132 hybridisation the microcavity arrays were placed in an ethanolic solution of 1mM 3MPA for 8 hours to ensure the formation of a monolayer on the upper surface of the microcavity array while the retained polystyrene spheres in the microcavities protect the interior of the microcavities for selective modification in a later step. The short chain length of 3MPA has minimal hindrance on electron transfer from the surface of the electrode to the supporting electrolyte, which is a desirable trait here as electrocatalysis at platinum nanoparticles requires good conductivity between the surface of the electrode and the nanoparticles. However, due to this, quantitation of monolayer formation is difficult as the monolayer formed has only a minor blocking effect on the surface of the electrode. Therefore, for initial proof of monolayer formation at the exterior surface of the microcavity array, a microcavity array was modified with 16-mercaptohexadecanoic acid (MHDA) in a bid to demonstrate the spatially separate modifications to the microcavity array, i.e., antibodies for cell capture on the upper surface and capture nucleic acids on the cavity interiors. The 16 carbon chain effectively blocks the surface of the electrode giving a measurable decrease in the gold oxide reduction peak observed in a voltammogram and allowing accurate measurement of monolayer formation. The formation of a MHDA monolayer was confirmed with voltammetry. A decrease in the area of the gold oxide reduction peak in the cyclic voltammogram corresponded to the formation of a MHDA monolayer blocking the available surface of the gold microcavity array (*Figure 3.4*.). Using the peak for gold reduction in the voltammogram the microscopic surface area of the electrode was determined to be 0.044cm^2 and 0.0065cm^2 before and after monolayer formation respectively, ie. Approximately 83% the exterior surface of the array has been passivated, or 0.0435cm^2 of MHDA monolayer surface formed.

Following monolayer formation, the polystyrene template spheres were removed by dissolving the polystyrene with THF, exposing the clean gold surface within the microcavity. The removal of polystyrene template spheres was confirmed by cyclic voltammetry and SEM imaging. As the deposited gold microcavity array is in direct contact with the polystyrene spheres it was deposited around, the inner surface of the

microcavities was inaccessible to the MDHA solution during monolayer formation and therefore monolayer formation only occurs on the upper surface of the microcavity array. This is observed in the difference between the gold oxidation peaks of cyclic voltammograms following the deposition of the MHDA monolayer and following the removal of the polystyrene template spheres from the microcavity array. In cyclic voltammetry following the removal of polystyrene template spheres the gold oxidation peak increases area from $1.716x10^{-5}$ C to $1.626x10^{-4}$ C corresponding to an increase in the exposed gold surface area of the microcavity array from $0.065cm^2$ to $0.417cm^2$. This indicated that following the removal of polystyrene template spheres an unmodified gold surface was exposed, leading to the conclusion that monolayer formation had been restricted to the exterior surface of the microcavity array. A separate control was carried out to assess the possibility of MHDA being stripped by THF, that would skew the electrochemical surface area measurements carried out before and after polystyrene removal. This was carried out by taking a gold electrode with a surface fully modified with a self-assembled monolayer of MHDA and subjecting the electrode to the polystyrene removal procedure. Cyclic voltammograms were carried out before and following treatment of the electrode with THF and by comparison, the voltammetry concluded that no monolayer damage occurs from interactions between the MHDA alkanethiol monolayer and THF. Therefore, it was concluded that the increase in gold surface area observed following the removal of polystyrene template spheres was solely due to the exposure of interior surfaces of the microcavities, which remained unmodified due to occlusion of the microcavities by polystyrene template spheres.

By subtracting the surface array of the microcavity array before polystyrene removal from the surface area following polystyrene removal the newly exposed inner surfaces of the microcavity array was estimated to be $0.411cm^2$. Using this figure it was possible to estimate the number of cavities in the array that were available for modification. Assuming the formation of hemispherical microcavities, the inner surface of a single microcavity is $1.41x10^{-7}cm^2$, and then there would be an expected $2.9x10^6$ microcavities in the array for modification. For an ideal microcavity array of 5x5mm, the maximum number of hexagonally close packed 3μm diameter microcavities that could fit on this surface would be $3.2x10^6$.. This figure is based on the area of the 3μm circular opening of a microcavity being $7.07cm^2$, and the

maximum packing efficiency of a circles on a planar surface being 0.907. The discrepancy between the observed number of microcavities in the array ($2.9x10^6$) and the maximum number of microcavities possible ($3.2x10^6$) may be explained by several factors. Firstly, the estimated total number of microcavities is based on all microcavities in the array being identical with an ideal height of exactly 1.5µm. A minor deviation in the height to which all cavities were grown around the polystyrene template sphere of ±50nm or 3.33% of the cavity height would result in deviations from this value in the order of ± $1.00x10^5$ microcavities. Another source of discrepancies between the number of estimated and observed microcavities lies in the manner in which the polystyrene spheres are arranged on the surface of the electrode. As the polystyrene template spheres are drop cast onto the surface in a liquid suspension, packing of spheres on the surface of the electrode is entirely random and hexagonally closely packed microcavities are not seen throughout the entire surface due to the differences in rates at which spheres settle from suspension.

The number of microcavities detected through voltammetry is also solely based on the number of microcavities that have not been modified by the monolayer. Therefore, throughout washing and handling processes following initial microcavity electrodeposition, some polystyrene template spheres may become dislodged or loosened from the microcavity, prior to, or during, the monolayer modification, leading to such microcavities becoming electrochemically inert. However SEM imaging has shown that the vast majority of polystyrene spheres are retained during the electrodeposition of the gold and the overall number of polystyrene spheres lost would be expected to be very low. Lastly, electrodeposition of microcavities at the edges of the electrode (within approximately 50µm of the edge) will often result in the formation of microcavities with roughened inner surfaces. This may account for approximately 4% of the 5x5 microcavity array. Roughened inner surfaces may result in poor contact between the polystyrene template sphere and the inner microcavity surface, exposing portions of the inner surface of the microcavity to the monolayer solution.

Following the removal of polystyrene template spheres the microcavity inner surfaces were modified with 1µM thiolated capture RNA strand in order to form a monolayer capable of hybridising, and thus immobilising, miR-132 to the surface of the microcavity array for eventual detection. As before, the remaining unmodified

gold surface area was measured in order to determine the coverage of RNA capture monolayer. The area of the microcavity interiors before modification was 0.411cm^2 (from above) and following the treatment of the interior surfaces of the microcavities with thiolated capture RNA strand the remaining surface area of the microcavity array was determined by cyclic voltammetry to be 0.280 cm^2, therefore the total coverage of thiolated capture RNA was 0.131cm^2 of the electrode or 31.8% of the available surface within the microcavities. This is a significantly lower percentage coverage of oligonucleotide monolayer coverage than that observed for the alkanethiol monolayer formed on the outer surface of the microcavity array. This lower coverage may be attributed to the reduced capacity of larger molecules such as oligonucleotides to form regular and defect free monolayers as they are subject to steric interferences of adjacent constituents, particularly on a concave surface where steric interference from adjacent oligonucleotides would be amplified to some extent. However, as shown by Peterson et al, tightly packed monolayers of oligonucleotide can be detrimental to achieving maximal hybridisation of target due to steric effects of adjacent constituents within the monolayer. Assuming that the incomplete monolayer does not consist of regions of dense islands coupled with unmodified areas, the low coverage of thiolated RNA monolayer should provide adequate space for efficient hybridisation[18]. Following the formation of the RNA monolayer, the free carboxy termini of the 3MPA monolayer were then activated by EDC-NHS and anti-GD2 IgG was coupled to the surface. The disialoganglioside GD2 is a glycosphingolipid expressed on the membrane of neuroectodermal tumours[19] and was chosen as an antigen for antibody immobilisation on the basis of its prolific expression in neuroblastoma cell membranes.

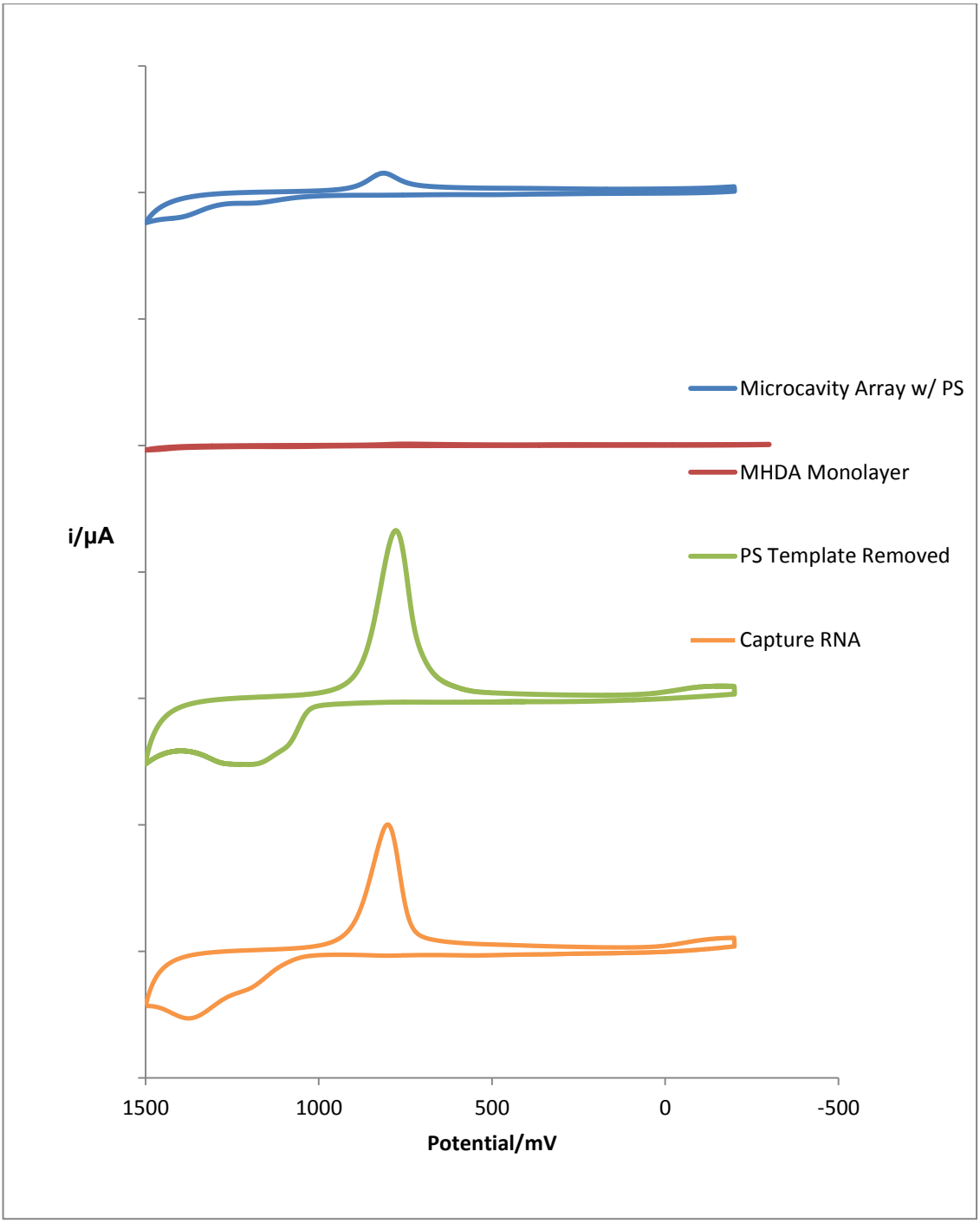

Figure 3.4. Cyclic voltammograms of a microcavity array at varying stages of modification in 10mM H_2SO_4 between 1500 and -200 mV at a scan rate of 100 mV s^{-1} vs. Ag/AgCl. Changes in the microscopic area of the microcavity array can be seen as changes in the charge related to the reduction of gold oxide. From the newly formed microcavity array (blue) to the formation of a MDHA monolayer (red) a decrease in the surface area can be observed. The removal of the polystyrene template (green) then leads to an increase in total surface area as the clean inner surface of the microcavities is exposed. Finally a decrease in the total surface area is observed as the capture RNA monolayer is formed (orange). Note: tick marks on the y-axis are given in 100 µA increments.

According to Wu et al[20] GD2 ganglioside comprises approximately 12% of the total cellular ganglioside content of human neuroblastoma. Considering that the total ganglioside content of neuroblastoma cells is approximately 400pmol/10^6 cells[21], then it can be assumed that each cell will express on its surface approximately 48amol of GD2 targets, or 2.9x10^8 GD2 molecules per cell. Confocal imaging has shown that the average true imprint of captured cells to be approximately 117 μm^2 per cell (See *Figure. 3.8.)* and if it is assumed that this accounts for half of the cells total area following capture (i.e. 50% of the cells extracellular surface area is in contact with the array), then it can be assumed that the region of the cell in contact with the electrode surface will contain 1.45x10^8 GD2 gangliosides, or half of the total cellular content of GD2 targets. Given that the average cellular imprint on the area is approximately 117 μm^2 this would lead us to expect a GD2 distribution of approximately 1.24x10^6 per μm^2, or 1.24 GD2 antigens per nm^2

A study by Celikkol-Aydin et al[22] has shown that effective antibody mediated cell capture to a substrate is observed only when the surface coverage of antibody on the substrate approaches a closely packed monolayer. Therefore, it is important to be able to determine if the amount of antibody applied to the upper microcavity surface is sufficient to form a closely packed surface of antibody molecules. During fabrication, the electrode surface is treated with 4µg of IgG, which corresponds to approximately 1.6x10^{13} units that are potentially bound to the electrode. As previously calculated, the total surface area of MDHA monolayer formed on the surface of the electrode is 0.0435cm^2. This gives rise to an expected IgG distribution on the upper surface of the electrode of 3.52x10^{14} units per cm^2 or 3.52units available in solution per nm^2 of MDHA monolayer. This would imply that a complete monolayer of antibody may be formed on the surface of the electrode as, considering that the diameter of an IgG molecule is widely reported in the literature to be between 20 and 40nm wide [23, 24], the amount of antibody units available is in great excess.

As calculated above, in the region of the electrode in contact with the cell there is expected to be approximately 1.24 GD2 antigens per nm^2 present. Considering the high affinity of the IgG for its antigen target and the abundance of antigen expressed per nanometre of cell surface, it can be concluded that cellular capture by IgG occurs rapidly once the cell has come in contact with the surface of the electrode and that

the controlling factor of cell capture is the proximity of the cell to the electrode surface. Therefore, it would be expected that over a time course maximum cellular adhesion will coincide with the time taken for cells to come in contact with the surface of the microcavity array, with the limiting factor for adhesion being steric hindrance of adjacent cells.

However, there are several key practical aspects of cell capture that may adversely affect the overall coverage and activity of the coupled IgG and therefore the efficacy of the cell capture. Initially, due to the sensitivity of polypeptide conformation to pH, the coupling of IgG to the 3MPA monolayer via EDC-NHS coupling must be carried out at a physiological pH and therefore there is a marked reduction in the reaction efficiency, as the optimum pH for the activation of carboxyl groups by EDC NHS is most efficient between pH 4 – 6, and is often performed in MES buffer. The conjugation of amines to activated carboxyl groups is then assisted by a slightly basic environment, at pH 8 [25]. This will lead to a reduction in the number of reactive 3MPA units available for the antibodies to bind to, possibly lowering the number of IgG units coupled to the array. Another key factor of this process is the orientation of the IgG following coupling and the activity of the IgG following the process. It is also important to consider the distribution of GD2 antigens on the surface of the cell. It has been shown that the vast majority of surface expressed gangliosides are confined within dense regions of the cell membrane known as lipid rafts. Lipid rafts are large regions of the cell membrane highly populated with signalling lipids, such as gangliosides, that also contain higher than average concentrations of cholesterol, causing the raft region to be quite rigid. As a result, GD2 gangliosides will be concentrated within a region on the cell membrane and will have a lower probability of interacting with IgG on the surface of the electrode. The rigidity of lipid rafts also leads to an inhibition in the lateral diffusion of gangliosides along the membrane such that antibody-antigen interactions will not be possible without near perfect alignment.

To assess the efficacy of antibody immobilisation, a static cell capture assay was carried out in which the microcavity arrays were incubated with neuroblastoma cells in parallel, an unmodified microcavity array was used as a control and a microcavity array modified with a non-specific capture oligopeptide, RGD. The assay is referred to as static as it does not have a flow component and all cell suspensions are placed

on the electrodes with no agitation/stirring. Following incubation with cells the arrays were washed with DPBS and fixed with 2.5% v/v glutaraldehyde. The microcavity arrays were then dehydrated and gold sputter coated for SEM imaging. *Figure 3.5.* shows the SEM images obtained from this experiment. From these images it is seen that the anti-GD2 antibody is capable of capturing cells. It is clear that 15 minutes of incubation is sufficient for initial cell capture, giving an estimated capture efficiency, i.e. 5.5% of the cells applied to the array were captured. Following 30 minutes this capture efficiency increases to approximately 8.7%, with similar values of 20% and 22% being obtained at 45 and 60 minutes, respectively. The similarity of these values indicates that following 45 minutes of incubation the number of cells becoming captured to the array reaches an apparent saturation point. This may be explained by reaching the maximum occupancy of the array. SEM images may prove to be misleading when observing the capture of cells on the surface of the array as cells treated for imaging appear retracted and are not truly indicative of the surface area taken up by the cell. Size comparisons with confocal imaging show that cells appear to be between ~12μm in diameter giving rise to the seemingly unoccupied regions of the array in SEM images.

T = 1 minute.

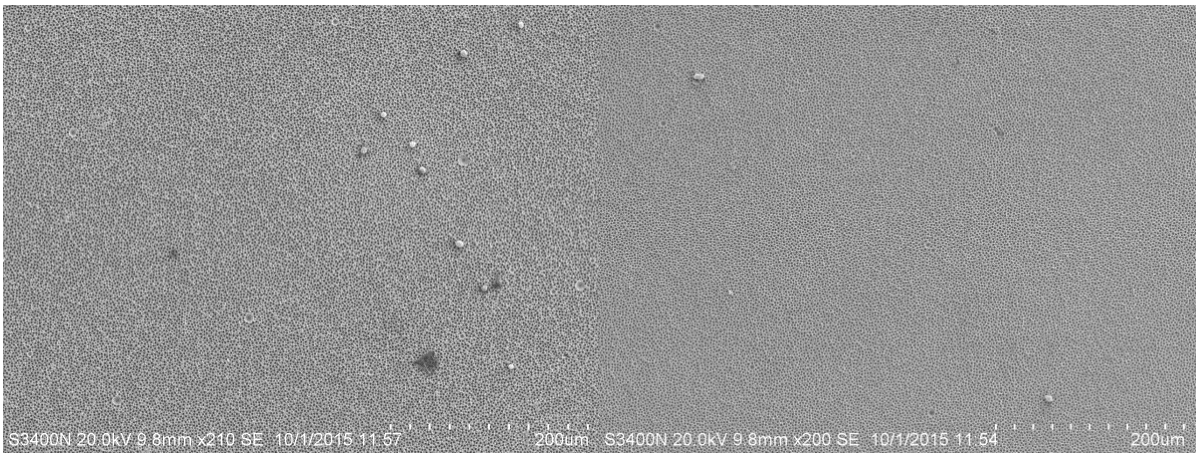

T=15 minutes

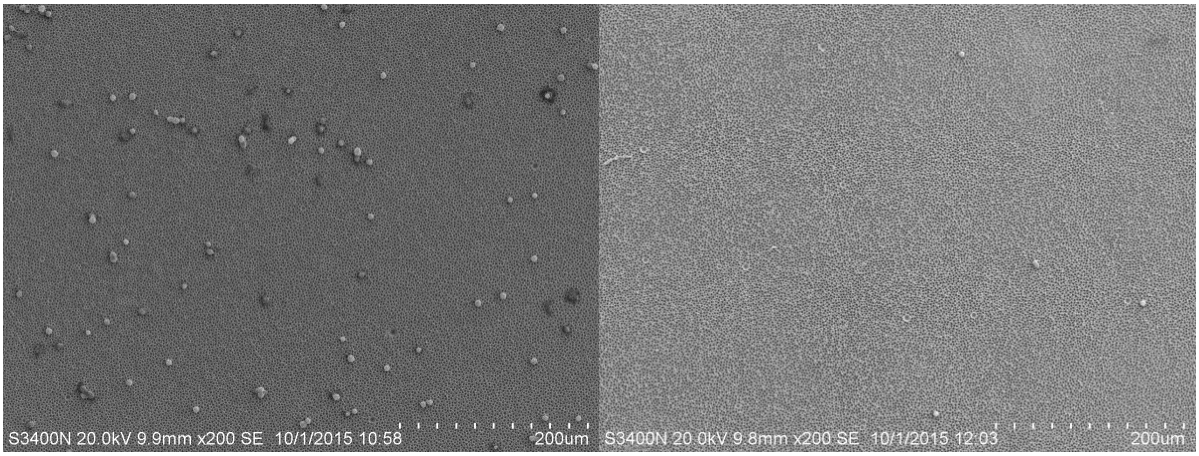

T = 30 minutes

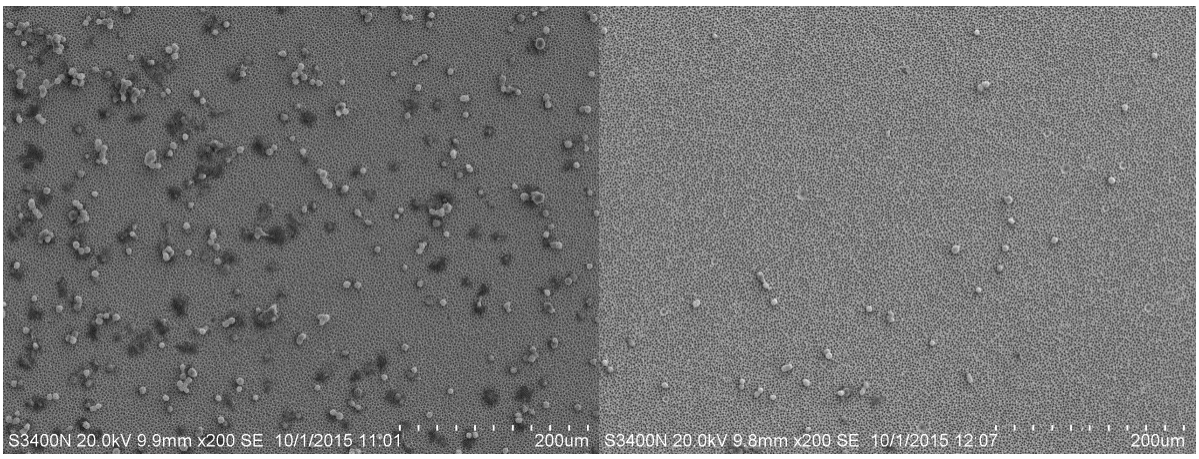

T = 45 minutes

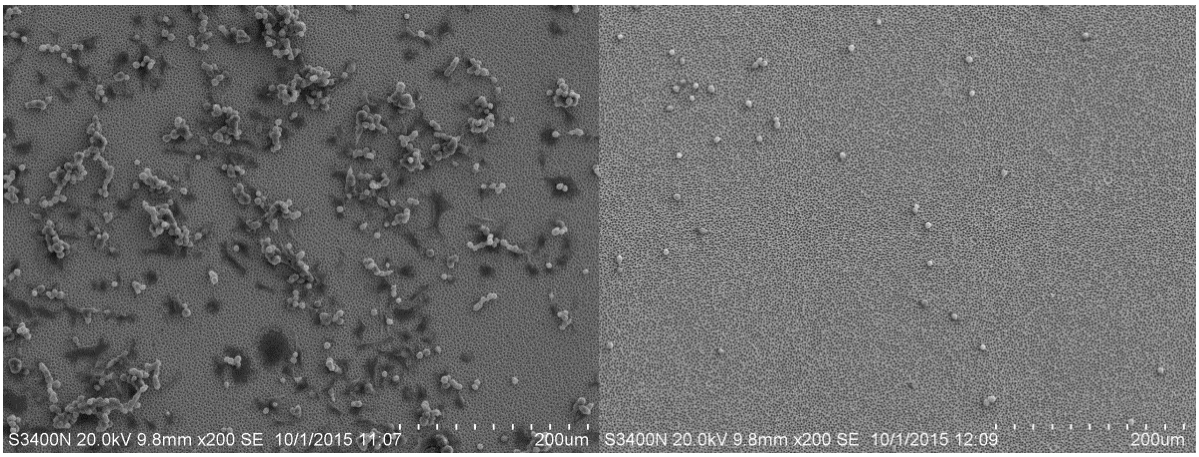

T = 60 minutes

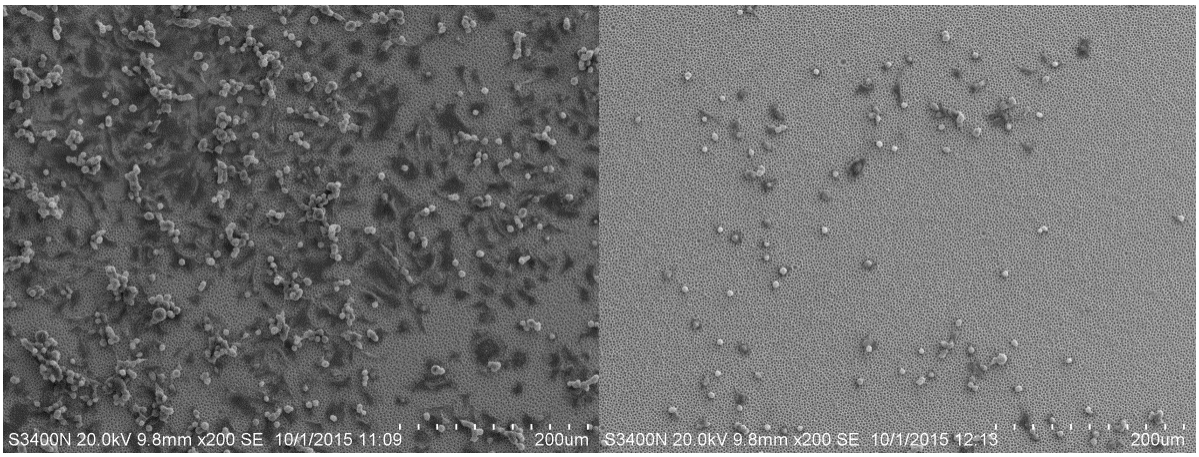

T=120 minutes

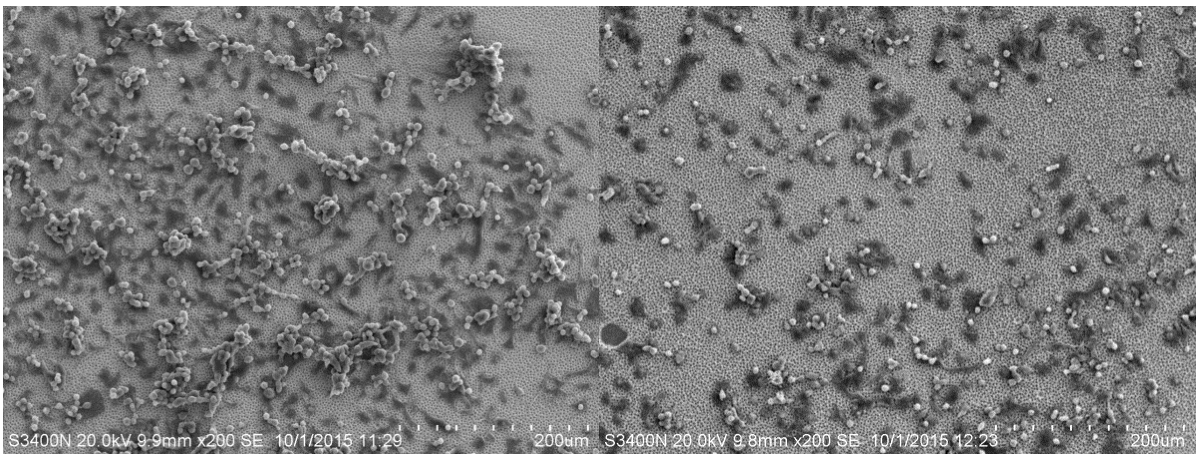

Figure. 3.5. SE SEM images of cells captured to microcavity arrays modified with anti-GD2 IgG (left) compared with microcavity arrays lacking a cell capture agent (right). A clear difference is seen in the capture efficiencies of microcavity arrays that have been modified with anti-GD2 IgG compared with those of unmodified microcavity arrays.

By comparison, in control samples, where no antibody modification was carried out, a dramatic difference is observed in the number of cells captured on the array. Very few cells are found in the control array due to non-specific physisorption. However, these physically absorbed cells contribute to a capture efficiency of only 0.6%, 2.3%, and 3.4% over 15, 30, and 45 minutes respectively. At longer incubation periods of one, two and three hours a significant number of cells can be seen adhered to the surface of the array due to physical adsorption, which would be expected for adherent cells such as the Sk-N-As cell line.

In a study parallel, the efficacy of an RGD oligopeptide monolayer for cell capture was assessed. From these images it can be seen that the RGD oligopeptide performs cell capture marginally more efficiently than the anti-GD2 antibody. This is assumed to be due to the broad range of extra cellular targets available to the RGD peptide. The arginine-glycine-aspartate (RGD) sequence within the oligopeptide is implicated in the recognition and binding of integrin proteins, a broad class of extracellular membrane proteins[26], and therefore is capable of interacting with many different targets to facilitate cell capture. However, due to the broad range of interactions the RGD oligopeptide is capable of it is not effective in carrying out the specific capture of tumour cells and is not suitable for use in a diagnostic device. However, as the cells used at this stage are prepared from pure cultures of human neuroblastoma, the decision was made that the use of the RGD oligopeptide for initial proof of concept was the most practical option due to its relatively low cost, ease of preparation and higher stability than that of the anti-GD2 antibody.

3.4.2. Viability of Captured Cells.

It is important to determine whether cells remained alive and viable following cell capture. In order to observe this, initially microcavity arrays were incubated with a fixed number of neuroblastoma cells for different amounts of time and then washed, fixed and prepared for SEM imaging in order to observe changes in cellular morphology as time progressed which would be indicative of living cells. *Figure 3.7.* shows SEM images of cells incubated on the surface of microcavity arrays for one, two and four hours. While cells in these images are fixed and dehydrated, which leads to changes in overall cellular morphology, a clear trend can still be seen of cells moving from a round to a dendritic morphology over a period of four hours, indicating that captured cells remain viable as they are capable of cellular processes such as cytoskeletal rearrangement required for changes in morphology.

Next it was decided to observe whether these cells would remain viable for long periods following cell capture to the microcavity arrays and this was done by initially capturing cells to the surface of a microcavity array for eight hours. Cells were then removed from the surface of the microcavity array by trypsinization and cultured in a multiwell plate overnight alongside a control sample of cells. As aerobic respiration and proliferation in cells occurs, resazurin, the blue dye component of Alamar Blue®, is irreversibly reduced to the red fluorescent resorufin. The progression of this reduction can be used to monitor the growth of cells and thus give indications about the viability of cells. Hence, the following day after cell capture Alamar Blue™ was introduced to the culture for eight hours and then the fluorescent intensity of each well was recorded using a plate reader.

Figure 3.6. shows the relative fluorescent intensities of samples of cells that had been captured to microcavity arrays for eight hours and then removed from the surface of the microcavity array by trypsinisation and cultured in a multiwell plate with resazurin. Fluorescent intensities for each sample indicate the amount of resorufin in each well due to aerobic respiration of cells. The number of cells in control wells equal those initially applied to the microcavity arrays as difficulties arise in determining the exact number of cells captured to arrays and subsequently recovered from arrays following immobilisation. This is due to the fact that imaging

and quantifying captured cells requires fixing and dehydration for imaging in SEM which would result in the death of cells. From this data it can be observed that while the fluorescent intensity of resorufin increases with the number of cells initially applied to the microcavity array, resorufin production is considerably lower than that of control samples, a sample of cells removed from a microcavity array initially treated with 75000 cells performs almost equally to that of a control sample or 25000 cells. A similar trend is observed in the sample produced from the microcavity array treated with 100000 cells as it appears to perform equally to that of a control sample of 65000 cells. This may be accounted for by the capture efficiency of cells previously to the surface of the array previously observed. As well as this, the subsequent trypsinizations can weaken or damage cells which may lead to a small percentage of cells dying from transfer between the microcavity array and the multiwell plate. Also in the process of trypsinization from the surface, viable cells may have been lost in transfer from the chip to the multiwell plate. Nevertheless, from these results it is clear that previously captured cells have maintained a degree of viability comparable to that of control cells. Therefore, it may be concluded that cells remain viable following immobilisation to the microcavity arrays, and the difference in the fluorescent intensity between samples of cells that had been captured to microcavity arrays and control cells is likely to be due to the number of cells captured initially and then retrieved following trypsinization.

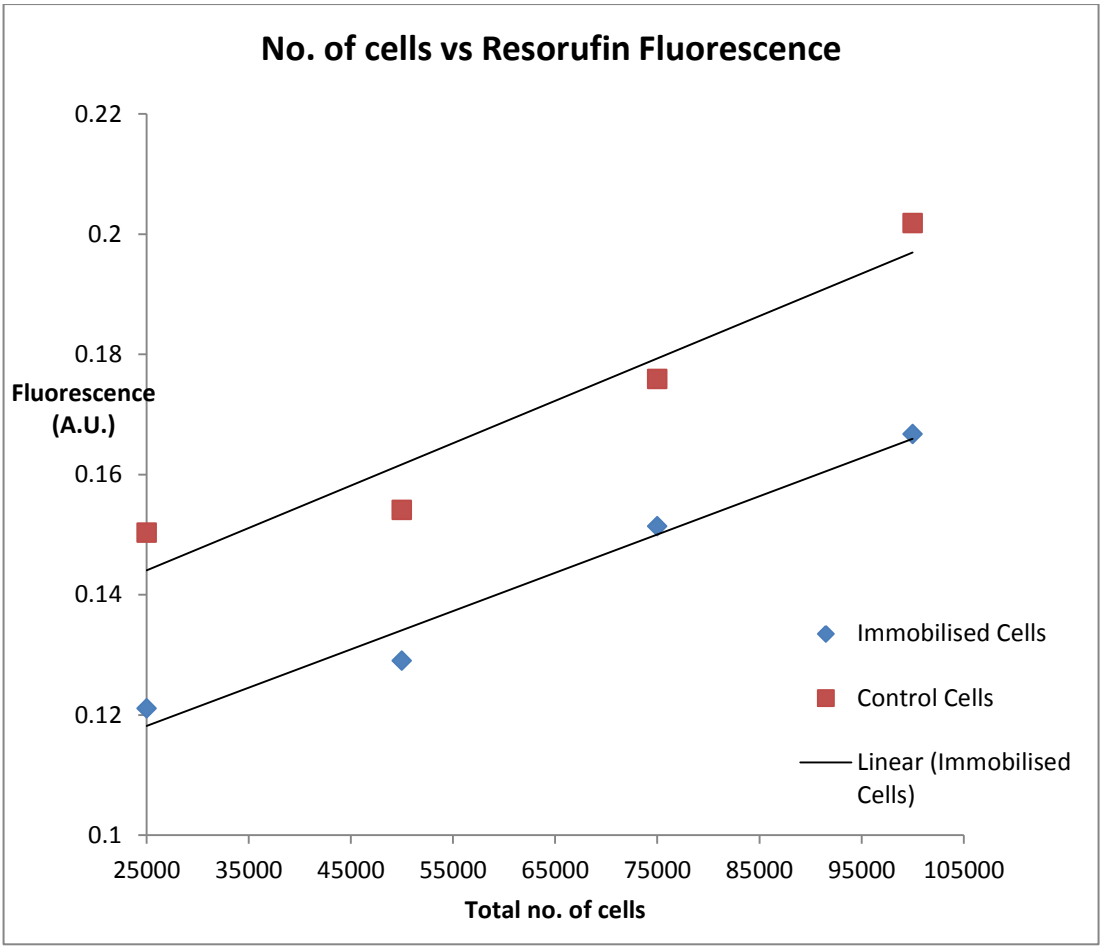

Figure 3.6. Spectrophotometric data from Alamar Blue™ assay of Sk-N-AS cells captured to microcavity arrays for eight hours and trypsinized from the surface, and control cells for comparison, showing the fluorescent intensity of resorufin as resazurin is reduced.

1 hour

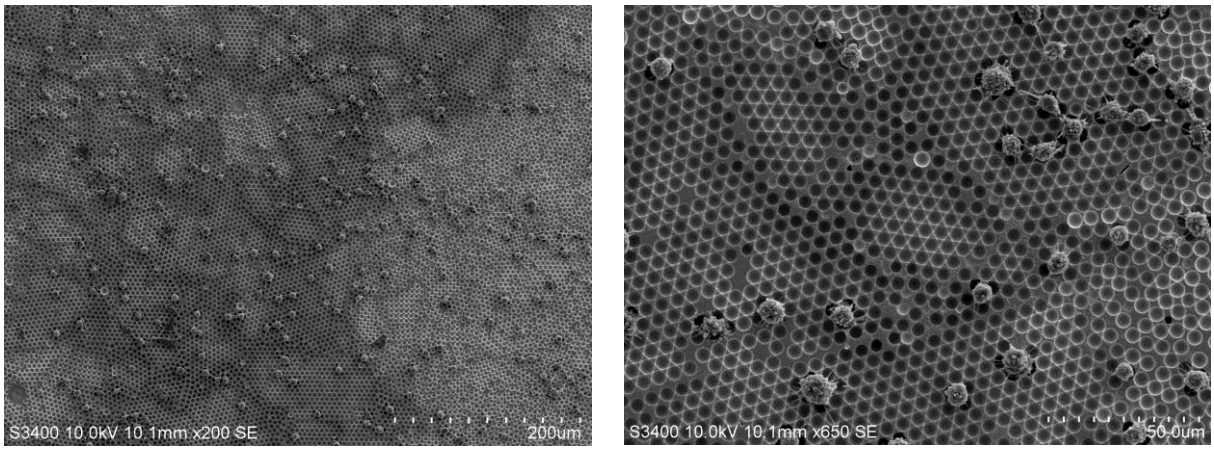

2 hours.

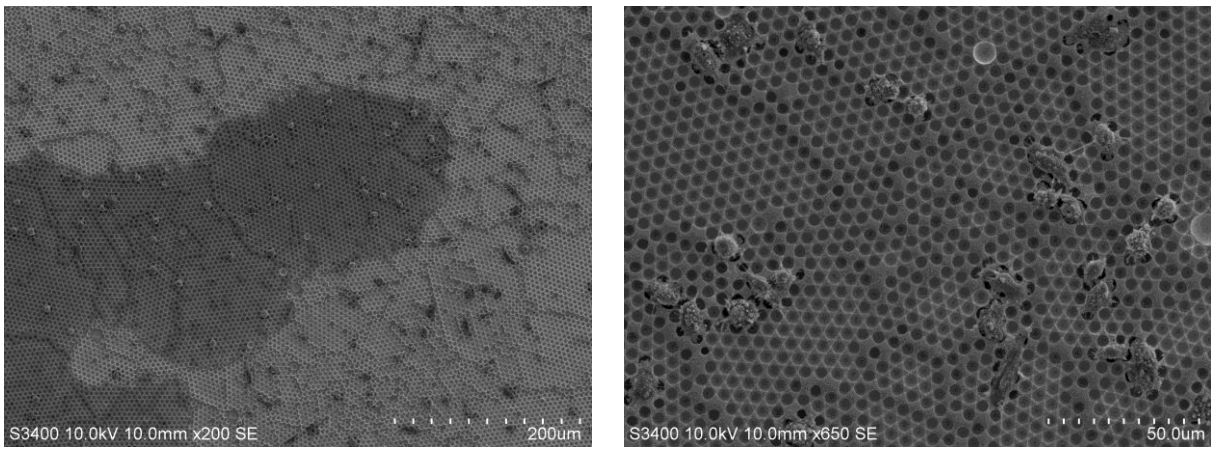

4 hours.

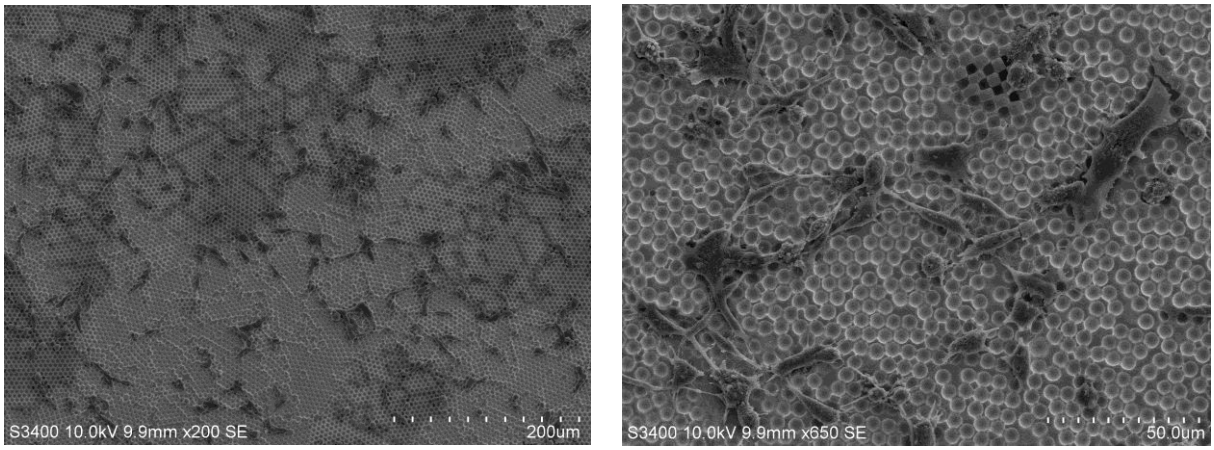

Figure 3.7. SEM images of antibody captured Sk-N-AS neuroblastoma cells on 5µm cavities following 1, 2 and 4 hours of incubation. Cells as time progresses cells are shown to be reverting from a spherical to a dendritic morphology typical of cultured neuroblasts giving preliminary indications that captured cells remain viable.

3.4.3. Cell Lysis and PtNP Detection.

In order for the intracellular concentration of miR-132 to be measured, *in-situ* cell lysis must be carried out to release the intracellular contents of the captured neuroblastoma cells, including their intracellular miRNA fraction, into the microcavity modified with capture RNA. Several lysis options were considered for the *in situ* lysis of captured cells. An ideal approach to lysis of cells in situ will cause 100% cell death, while avoiding the use of cytotoxic agents that may dysregulate the expression of miRNA within captured cells. The approach must also avoid the use of reagents that cause the degradation of RNA and also have some control of the activity of ribonuclease released from the cell following lysis. Another desired trait would be to cause the lysis of cells from within the underlying cavity, such that the intracellular miRNA fraction is exposed directly to the modified cavity below it, limiting the possibility of the miRNA target diffusing away from the array. Initially, electrochemical methods of effecting lysis from the underlying cavity array were considered. A mechanism proposed by Lee et al for the electrochemical disruption of cellular membranes by the generation of OH^- at the cathode would be capable of directly lysing a cell into a modified cavity. However, due to the sensitivity of RNA to basic conditions, this method is not compatible for use with RNA detection strategies as it would lead to both the degradation of intracellular miRNA as well as the degradation of the immobilised monolayer of capture RNA within the microcavity[27]. Enzymatic release of lipases from within the cavity was also considered, by using a mixed monolayer of immobilised capture RNA strands and lipases cross linked to the surface of the cavity by a oligopeptide linkage that may be cleaved by extracellularly expressed proteolytic enzymes from the captured cells. However, an approach such as this would require specifically engineered and chemically modified lipase to contain a recognition site for proteolytic release and a site for immobilisation to the surface of the microcavity which would lead to a greatly increased cost manufacture cost for each microcavity array. The mixed monolayer bulky enzymes and capture RNA may also impede the hybridisation of target miRNA to the capture RNA. Another consideration would be have to be made for the timing of lipase release from the surface of the microcavity. As the considered scheme would involve the use of extracellularly expressed protease to

affect the release of lipase from the surface of the microcavity, the extracellular expression of protease would have to be controlled to a time following the immobilisation of the cell to the surface of the microcavity, as early cleavage and release of lipase from the surface would result in diffusion of lipase out of the cavity and lysis of cells prior to immobilisation.

A far simpler approach was to carry out lysis by osmotic imbalance[28]. This was carried out by first washing the array with DPBS to remove any media and detritus from the array and the array was then wick dried and incubated in a hypotonic solution. The use of a hypotonic solution generates an osmotic imbalance between the intracellular and extracellular environments leading to an influx of water within the cell leading to the cells eventual lysis. As this method is virtually reagent free it is considered minimally damaging to the miRNA fraction of the neuroblastoma cell. As this method involves lysis by osmotic imbalance, sufficient osmotic pressure must be generated by a hypotonic solution in order to affect sufficient cell lysis. For this reason, care must be taken when transferring the microcavity array with the captured cells to the hypotonic solution so as to transfer as little media with the microcavity array as possible. This can be done with small washes with phosphate followed by wick drying with sterile filter paper. This allows the use of a minimal hypotonic solution in order to reduce dilution of intracellular miRNA following lysis. This method also however does not cause the direct lysis of cells into the underlying microcavity and as a result may be subject to the loss of miRNA target by diffusion away from the microcavity. Following lysis, the intracellular miRNA will also be exposed to many extracellularly expressed ribonucleases that will lead to the degradation of the target. To avoid this, the hypotonic lysis solution was made up with RNaseZAP™, a powerful ribonuclease inhibitor, and RNase free water and lysis was carried out in a sterile biosafety level II laminar flow cabinet. The efficacy of osmotic lysis was determined by SEM and confocal microscopy. *Figure 3.8.* shows confocal images of cells treated with DiOC6 and DRAQ-7 prior to and during the lysis process. DiOC6 is a fluorescent cytosolic stain used to image cells. DRAQ-7 is a commercially available cytotoxicity stain that is used to indicate the disruption of the cellular membrane. Prior to lysis, cells were treated with both stains and at t=-1 minute virtually no intracellular uptake of DRAQ-7 is observed. At t=0 cells were treated with deionised water and imaged at t=1 minute and every 2 minutes

following this to monitor lysis. From the images in *Figure 3.8*., at t=1 accumulation of DRAQ-7 within some nuclei is beginning, indicating the disruption of the membrane of these cells. At t=5 minutes a higher degree of DRAQ-7 uptake indicative of ~70% of cells is observed. At t=5 minutes, an increase in the fluorescent intensity of DRAQ-7 within nuclei is observed, indicating further permeation of the cell membrane and t times of t=15minutes and t=25 minutes an even greater degrees of fluorescent intensity is observed and virtually 100% of cellular nuclei now have accumulated DRAQ-7 indicating disruption of the cellular membrane and cell death.

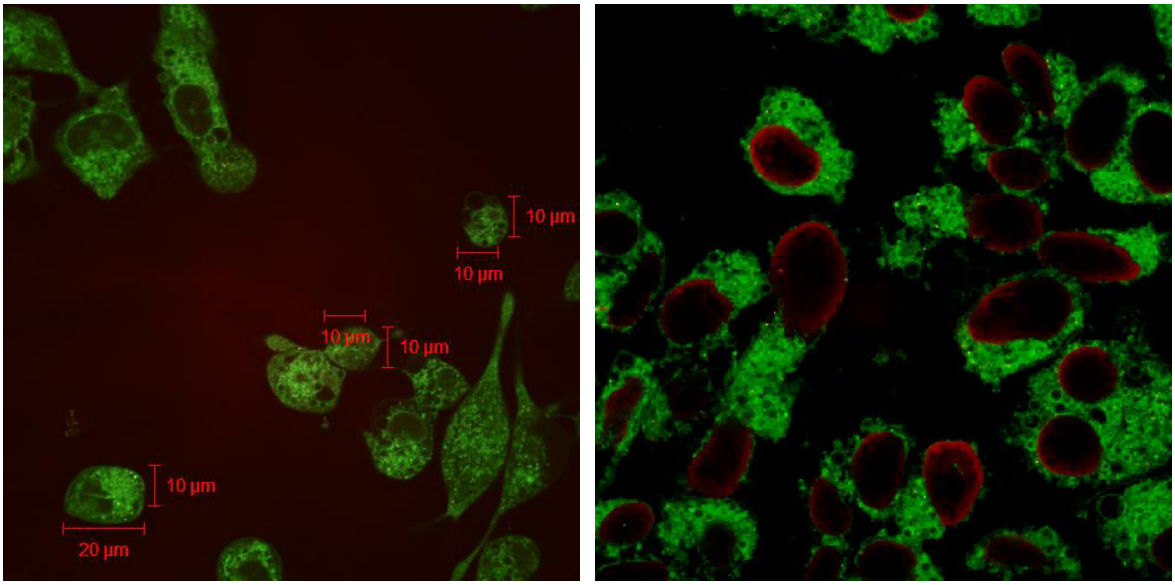

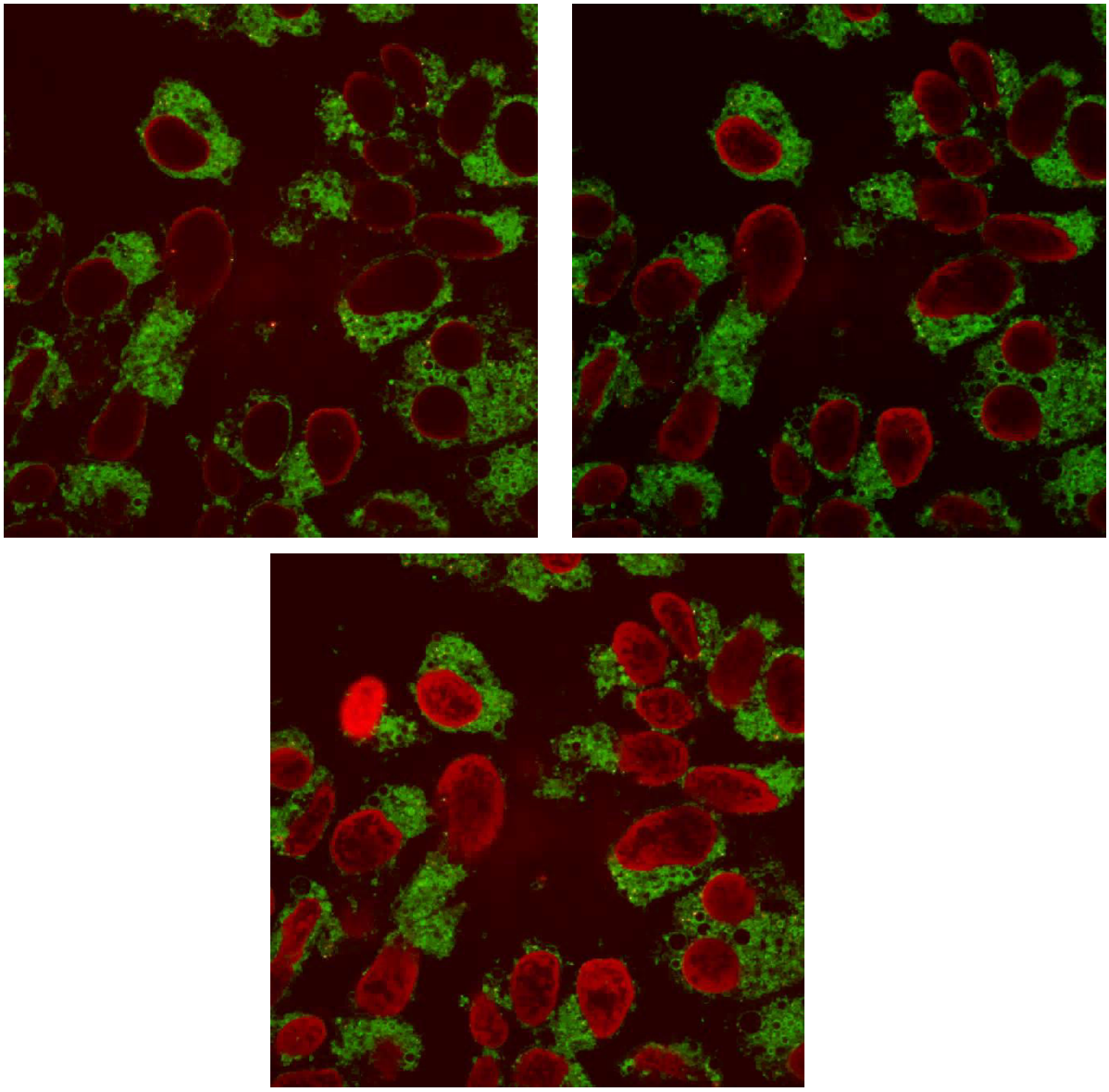

Figure 3.8. Confocal images of cells at x400 magnification treated with DiOC6 (green) and DRAQ-7 (red) dyes illuminated with a 488 nm Argon laser to show the progression of lysis by osmotic imbalance as an onset of DRAQ-7 localisation within nuclei.

Similarly SEM imaging has shown the method of osmotic lysis to be highly effective as virtually no intact cells could be observed following lysis and only small fragments of debris remained. Progressing from this, lysis and hybridisation were allowed to occur in a single step in a sterile environment for a minimum of six hours. After this time the microcavity arrays were placed in a suspension of uniformly decorated probe RNA platinum nanoparticles (proPtNP) at a concentration of 100mg/L (corresponding to approximately $7.13x10^{13}$ particles per litre or a concentration of $1.2x10^{-11}$ moles/litre or 12pM) for a minimum of eight hours to allow the hybridisation of the free 3' end of miR-132 to the probe strands on the proPtNP, immobilising the catalytic nanoparticle to the surface of the array. As the hybridisation of nanoparticle to the free end of the target miRNA strand was kinetically controlled by the availability of target hybridised to the surface, it was deemed that even in situations where the concentration of target was in excess of the concentration of PtNP, the hybridisation of nanoparticles to the surface would still follow a linear proportionality to the concentration of miRNA applied to the array.

Microcavity arrays, following the PtNP immobilisation step, were then imaged to determine whether PtNP hybridisation to the surface had been successfully carried out. *Figure.3.9.* shows a FeSEM image of nanoparticles immobilised within the surface of a microcavity indicating that hybridisation was successful and electrochemical detection should be then attempted. The nanoparticles immobilised to the surface through hybridisation with miR-132 could now be detected through the electrocatalytic reduction of H_2O_2 when a potential of -250mV was applied to the microcavity array. A potential of -250mV for the reduction of peroxide by platinum was chosen based on the onset of aqueous solvent reduction seen for platinum in cyclic voltammetry, in a bid to maximise the driving force for H_2O_2 reduction. Initially, seven microcavity arrays were incubated with from one to one hundred thousand neuroblastoma cells as well as a control that was incubated in sterile media. Following lysis and proPtNP hybridisation the microcavity arrays were placed in an electrochemical cell and an amperometric detection program was run on each individual microcavity array. The program consisted of the amperometric measurement of current versus time under a constant applied potential over a time of 2400 seconds. The initial current, prior to the injection of peroxide, is expected to be the current associated with the evolution of hydrogen from aqueous solvent at the

negative potential of -250mV, which may be observed as the onset of the limit of a potential window for aqueous solvent in a cyclic voltammogram of an electrode containing platinum. A sharp increase in current generated following the injection of peroxide is associated with the hydrolysis of hydrogen peroxide. For the initial 600 seconds the initial current was allowed to decrease to a stable minimum. At 600 seconds the program was paused and H_2O_2 was injected into the electrochemical cell to make up a concentration of 200mM H_2O_2 within the electrochemical cell, with minor agitation to ensure homogenous occupancy of the H_2O_2 within the electrochemical cell. The program was then immediately resumed and the current produced due to the electrocatalytic reduction of H_2O_2 was observed over the 1800 seconds. *Figure 3.10.* shows the i/t curves for the PtNP detection runs carried out on each microcavity chip, treated with a range of cells from $10^6 – 10^0$ cells and a control and *Figure 3.11.* shows a plot of the current produced by each microcavity array vs the number of cells applied. In this study, it could be seen that the highest concentration of cells applied to the microcavity array produced a current of approximately 2150µA, which was only about 50% of the target free control, which produced a current of approximately 4250µA. Taking the results of this assay as a whole it can be seen that a linear correlation between the number of cells applied to the microcavity array and the current produced from each array could not be established. There were several possible explanations of these results to be considered. First, due to the outward nature of cell lysis carried out in this experiment by osmotic imbalance, it is possible that miRNA target was not capable of diffusing into the cavity below the cell if the fragments of the cell or lysate debris blocked the inner surface of the microcavity. Secondly, due to the small volume of the microcavity the diffusion of materials into the microcavity will occur at a lower rate than that of bulk diffusion and this will hinder the hybridisation of miRNA target to capture RNA monolayer contained in microcavities, or adjacent microcavities in the case that outward lysed cells block microcavities below them, however, as microcavities are hemispherical in shape and therefore have a wide opening relative to the cavity size, the effect of this would be expected to be minimal. Another consideration was that the intracellular miR-132 fraction of a cell may not be freely circulating within the cytosol of a cell and subsequently released following lysis.

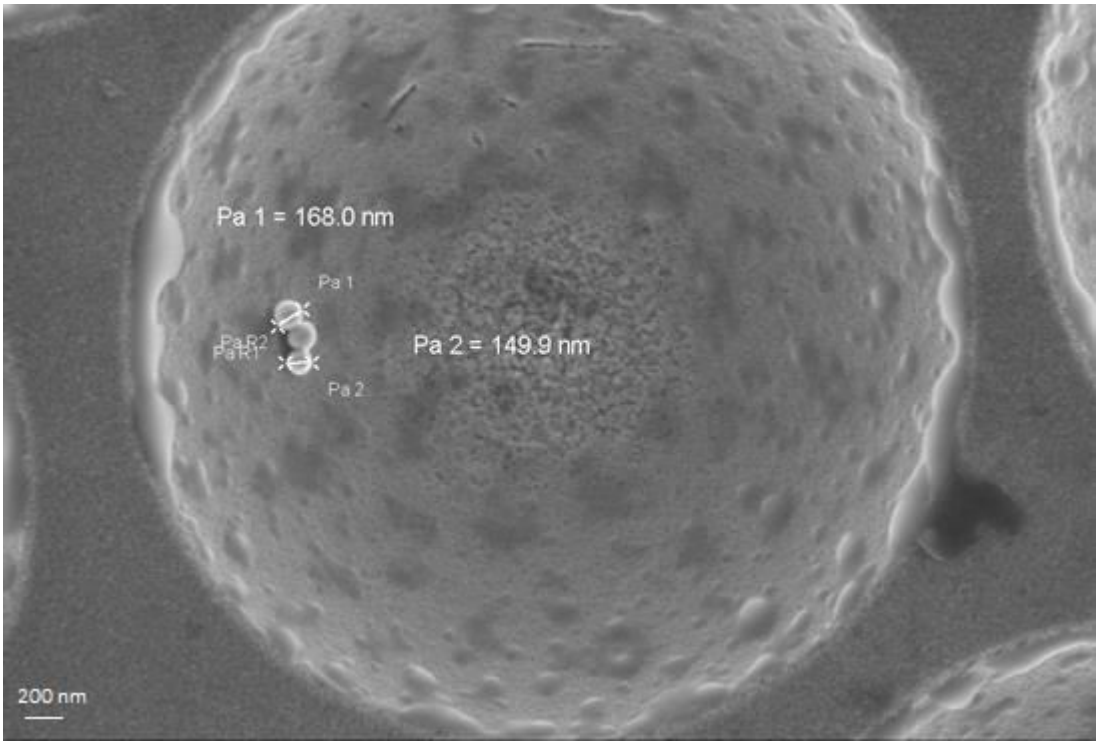

Figure 3.9. FeSEM image of microcavity surface at 20000x magnification using accelerating voltage of 20 kV and working distance of 3.4 mm, showing PtNP immobilised to the inner surface of a gold microcavity.

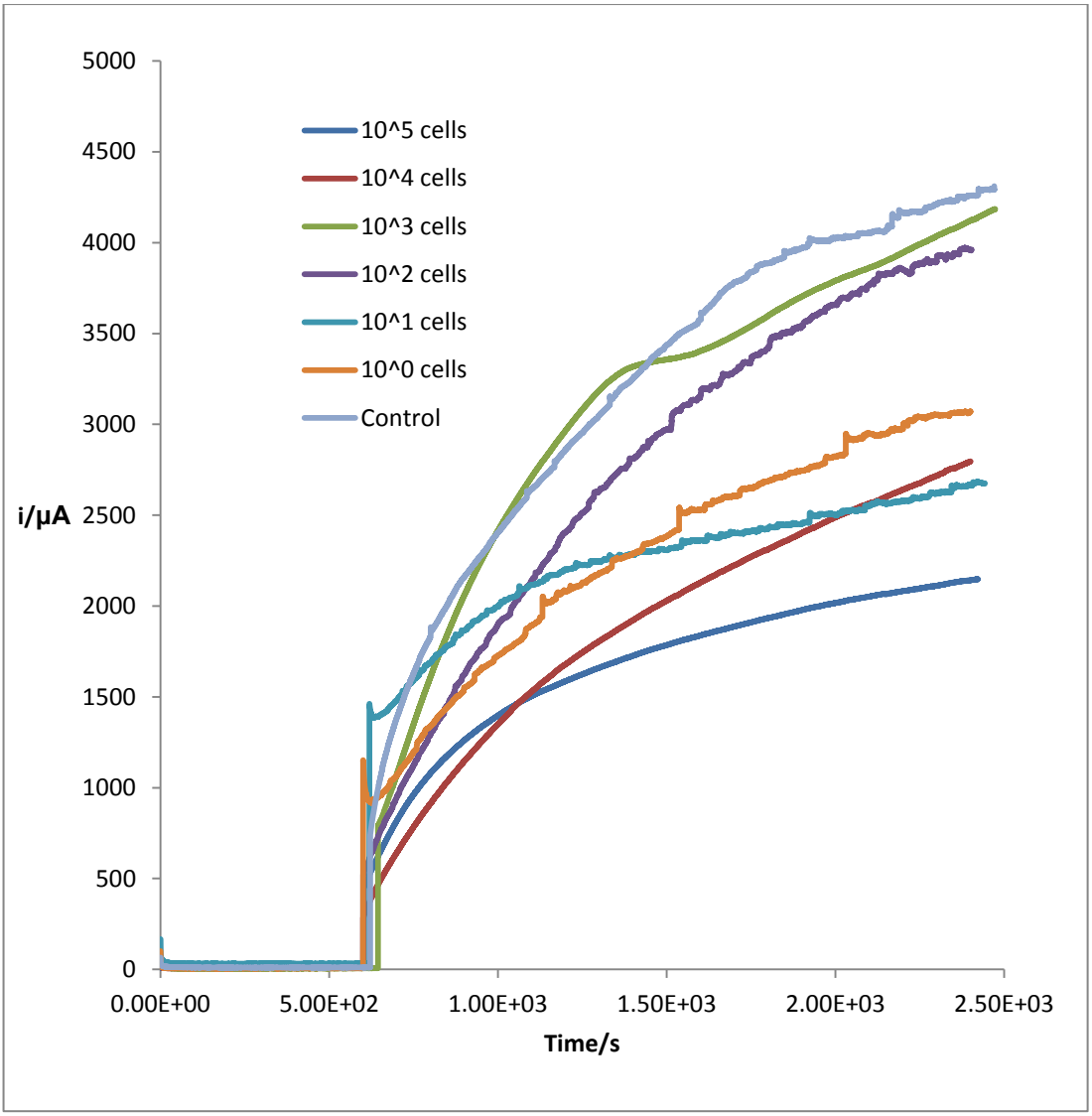

Figure 3.10. i/t curves for peroxide detection of immobilised PtNP in 10 mM H_2SO_4 at a potential of -250 mV vs Ag/AgCl for microcavity arrays ranging from 10^6 – 10^0 cells and no cell control. At 600 seconds the program is paused and an injection of H_2O_2 is made to 200mM, when the program is resumed a sharp current increase is observed. At 2400 seconds the program is stopped and the final current is recorded.

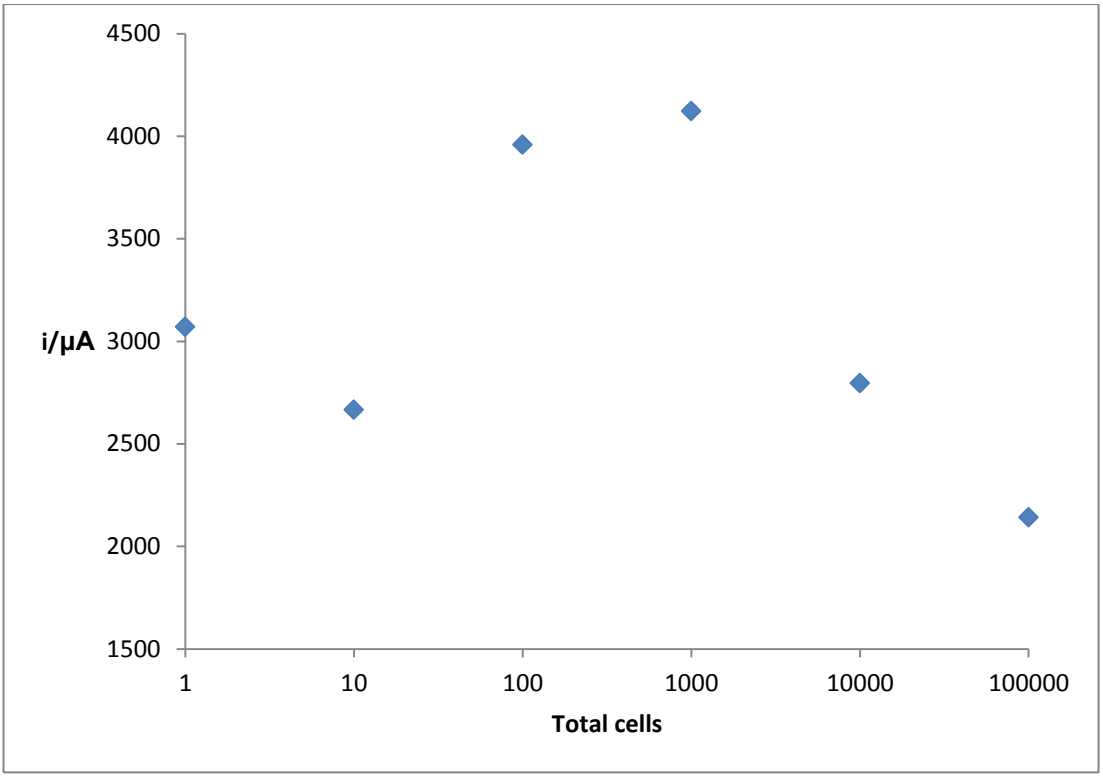

Figure 3.11. Final currents from PtNP detection runs vs total number of cells applied to microcavity arrays. Currents generation was carried out by the injection of H_2O_2, to a final concentration of 200 mM under an applied potential of -250 mV vs Ag/AgCl. 1800 seconds after the peroxide injection the final current is measured.

In order to reduce the complexity of the assay, experiments were performed using solutions of miR-132 as opposed to complex cellular samples. In this work, the arrays were exposed to miR-132 solutions with concentrations ranging from 1μM to 1aM derived from a synthetically produced stock and the detection assays were then run as before. Shown in *Figure 3.12*. below are the currents generated by hydrogen peroxide reduction over the detection program plotted against the known concentrations of miR-132 applied to the surface of the array, showing that the current generated by the microcavity array does not increase proportionally the concentration of miR-132 applied to the array. There were several possible reasons for this deviation from the expected. Initially, it was considered that these results may have been explained in terms of the denaturing of duplexes due to wash steps with dionized water, as this would result in the destabilisation of duplexes. For this reason the wash buffer was changed to DPBS and carried out again, however, this appeared to have no change in the observed results. It was hypothesised that the large discrepancies in the results were due to the background reduction of H_2O_2 by the underlying gold substrate, as gold is also electrocatalytically capable of reducing hydrogen peroxide, albeit at a much lower rate, however the total surface area of gold in the microcavity array may be large enough when compared to the PtNP, such that a considerable contribution to current evolution is made by gold.

It was also hypothesised that the potential applied to the array was causing excessive reduction of H_2O_2 at the microcavity, more so than that observed for a polished planar electrode and as the further negative a potential applied to a gold electrode is, the greater the increase in its ability to electrocatalytically reduce the aqueous solvent of the electrochemical cell. If a lower potential could be used to minimise the catalytic activity of the array surface yet still preserve the catalytic activity of PtNP, this may lead to a signal generated from PtNP alone and thus a current per unit nanoparticle and subsequently per target RNA strand on the surface of the microcavity could be established. To address these issues changes were made to the set-up of the program and the microcavity array fabrication process. Initially, the potential applied during the electrocatalytic detection was changed from-250mV to -100mV. While this change in potential yielded a lower current response for microcavity arrays compared to those performed at -250mV, it did not facilitate the establishment of a linear relationship between current produced during detection and

miR-132 concentration. Another possible explanation for the lack of a proportional response between current evolved during miRNA detection and concentration of miR-132 applied to the microcavity array was that, as the detection progressed, the background reduction of H_2O_2 at the microcavity surface led to the stripping of monolayer materials from the surface, leading to an increase in the available underlying surface area where H_2O_2 reduction could occur.

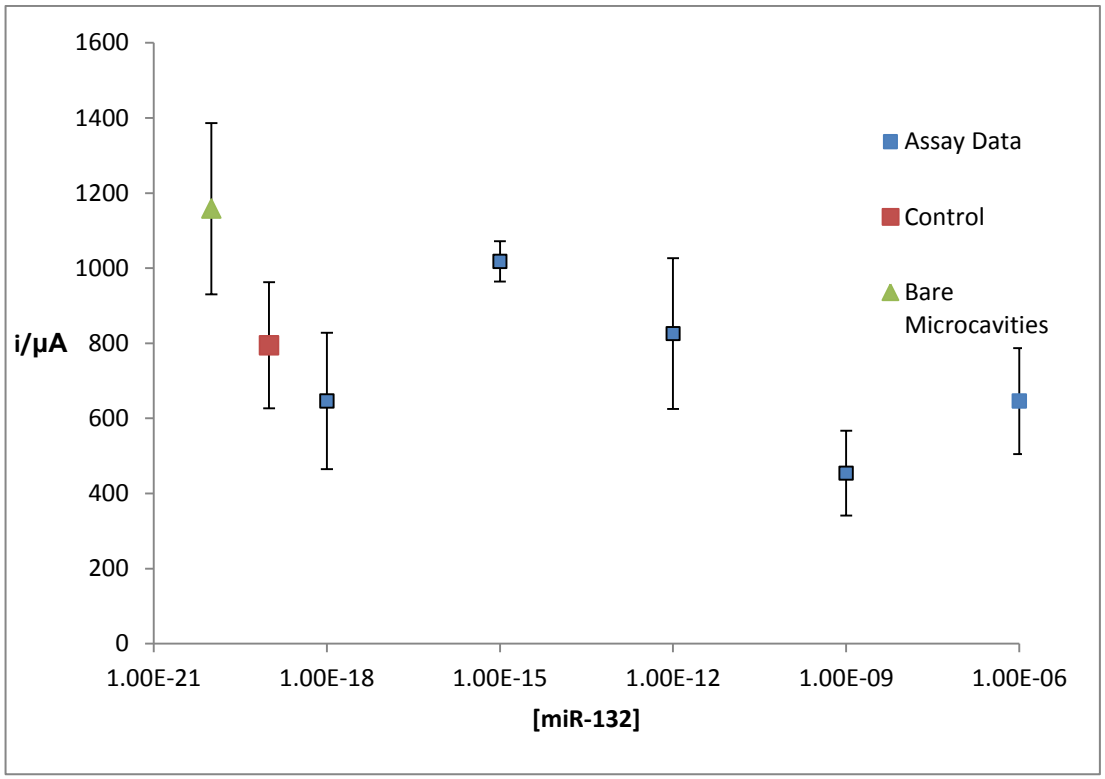

Figure 3.12. Currents evolved from amperometric i/t curves carried out on microcavity arrays in 10mM H_2SO_4 with 200mM H_2O_2 at an applied potential of -100mV vs. Ag/AgCl over a range of miR-132 concentrations from 1µM to 1aM showing no linear correlation to miRNA concentration. Error bars were generated from repeated independent electrodes where n = 3.

These assay results appear to demonstrate that there is a fundamental process occurring that is resulting in a current that is measured, independent of the concentration of miRNA target applied to the surface. The vast majority of detection runs performed under these conditions showed i-t curves that appeared to be increasing in magnitude throughout the experiment (see *Figure 3.13.* as example), rather than starting at a high current upon peroxide injection and eventually decaying

to a steady state current over time which was expected. Therefore, it was hypothesised that under the experimental conditions the reduction of peroxide at the surface of the microcavity array was effectively stripping the surface materials of the microcavity array as the detection program progressed. This stripping would increase the active surface area of microcavity, resulting in further background reduction of hydrogen peroxide and an increase in current. In order to assess the possibility that peroxide strips the miRNA monolayer during detection runs voltammetry was carried out on a monolayer blocked microcavity array prior to and following a detection run using ferrocene methanol as a solution phase redox probe to determine if the amount of exposed microcavity surface had increased. *Figure 3.14.* shows the voltammograms for a bare microcavity array, the array following modification by an alkanethiol monolayer, and following a detection run carried out on the array.

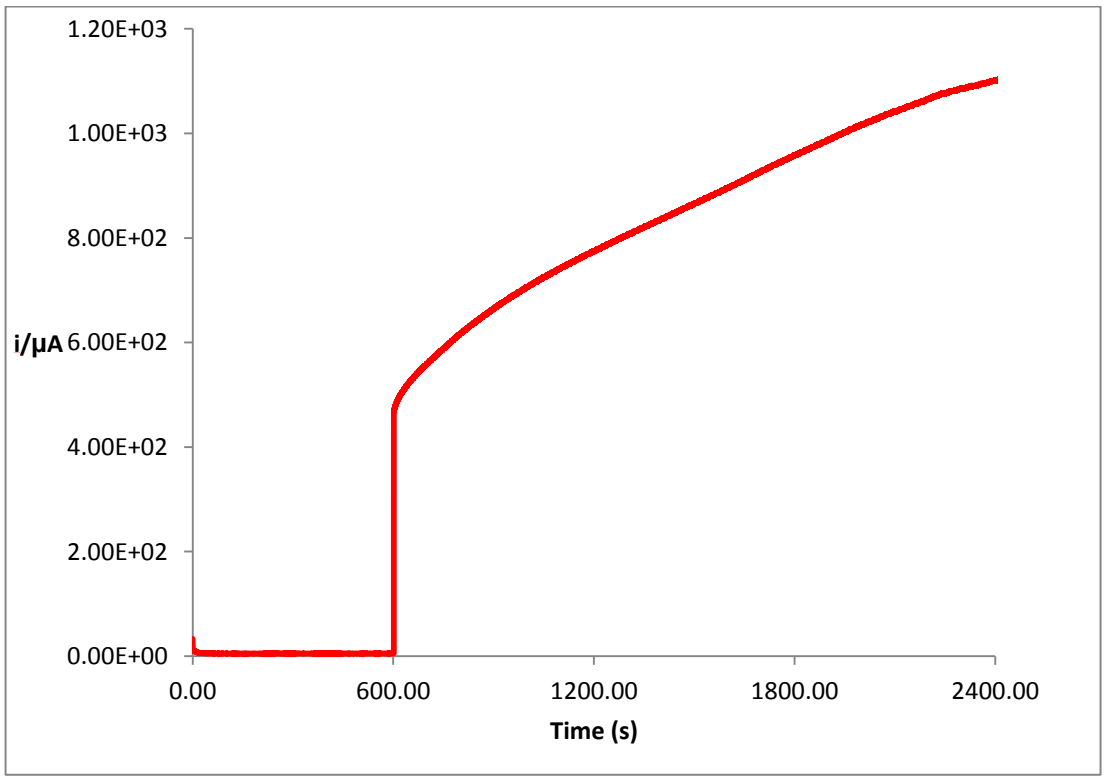

Figure 3.13. Example of i/t curve for peroxide detection of immobilised PtNP in 10 mM H_2SO_4 at a potential of -100mV vs Ag/AgCl. At 600 seconds the program is paused and an injection of H_2O_2 is made to 200mM, when the program is resumed a sharp current increase is observed. At 2400 seconds the program is stopped and the final current is recorded.

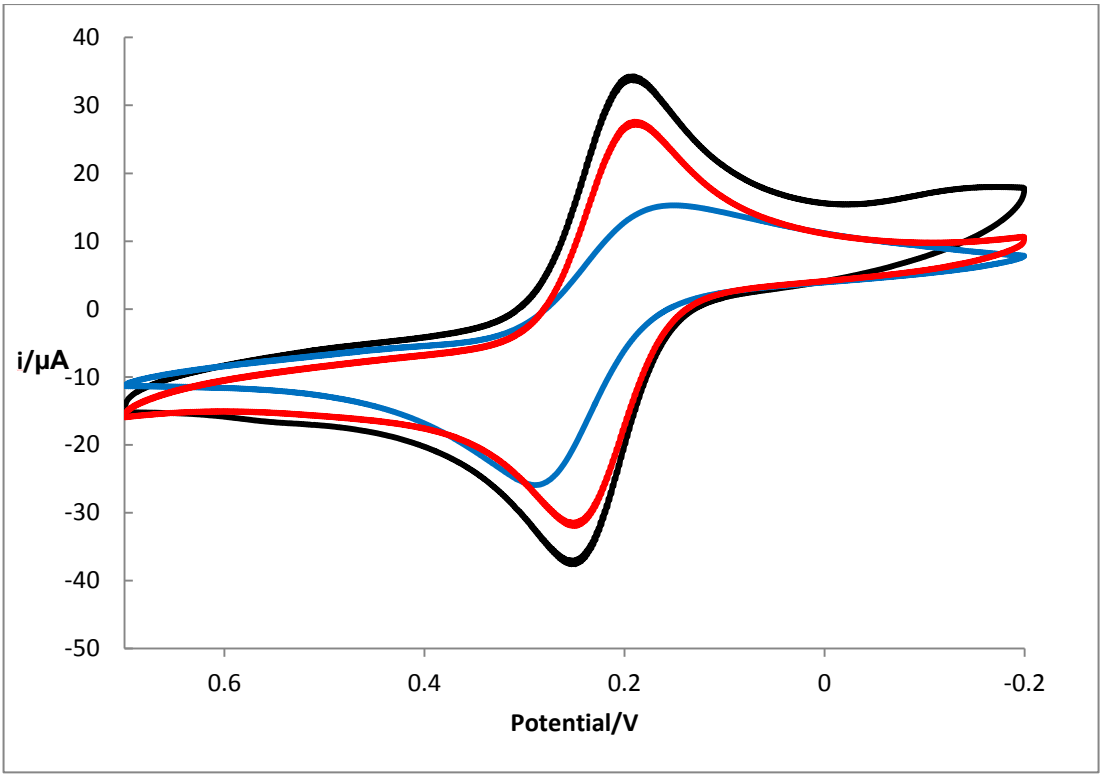

Figure 3.14. Cyclic voltammograms in 0.5mM FcMeOH vs. Ag/AgCl at a scan rate of 100 mV/s of a bare microcavity array (black), the microcavity array following modification with an alkanethiol monolayer (blue) and the microcavity array following amperometric i/t curve carried out in 10mM H_2SO_4 with 200mM peroxide under an applied potential of -100mV vs. Ag/AgCl (Red).

These results show that following a detection run in 200mM H_2O_2 the exposed surface area of the microcavity array increased, which was observed as an increase in the anodic/cathodic peak maxima in *Figure 3.14.* The voltammetry of the monolayer modified microcavity and that of the microcavity following an i-t curve in 200mM H_2O_2 at 100mV vs. Ag/AgCl, shows an increase in cathodic peak maxima of 14.6µA to 24.7µA, an increase of 69.1% from before detection to after detection. In fact the peak current following detection is 77.6% that of the unmodified microcavity. Therefore, it was determined that the reduction of peroxide at the electrode surface was causing the surface of the microcavity array to be stripped of its surface components exposing the underlying gold surface which in turn was leading to increased peroxide reduction. In a bid to minimise the extent of monolayer stripping by peroxide electrocatalysis, lower concentrations of peroxide were investigated. *Figure 3.15.* shows the resulting currents vs. peroxide concentration. These results

show that the current associated with reduction and oxidation of ferrocene is not significantly changed by the peroxide detection step when the concentration of peroxide is lower, i.e., between 2mM and 200μM. This result suggests that at lower concentration reduction of peroxide does not cause as extensive stripping of the film deposited on the interior microcavity surface. Also, the i-t curves do not show the systematic increase over time observed for higher peroxide concentrations. These data suggest that at the layers may be stable when low concentrations of peroxide are reduced. Significantly, *Figure 3.16.* shows that no appreciable increase can be seen in the oxidation and reduction peaks of the voltammograms of microcavity arrays following detection in 200μM peroxide and therefore it was deemed that at this concentration of peroxide a linear correlation between miR-132 concentration applied to the microcavity array and current produce by the probe PtNP could be established. An assay was run with microcavity arrays incubated with concentrations of miR-132 ranging from 1μM to 1pM of miR-132, and proPtNP. However, this assay proved unsuccessful and no linear relationship between current produced and miRNA concentration could be observed.

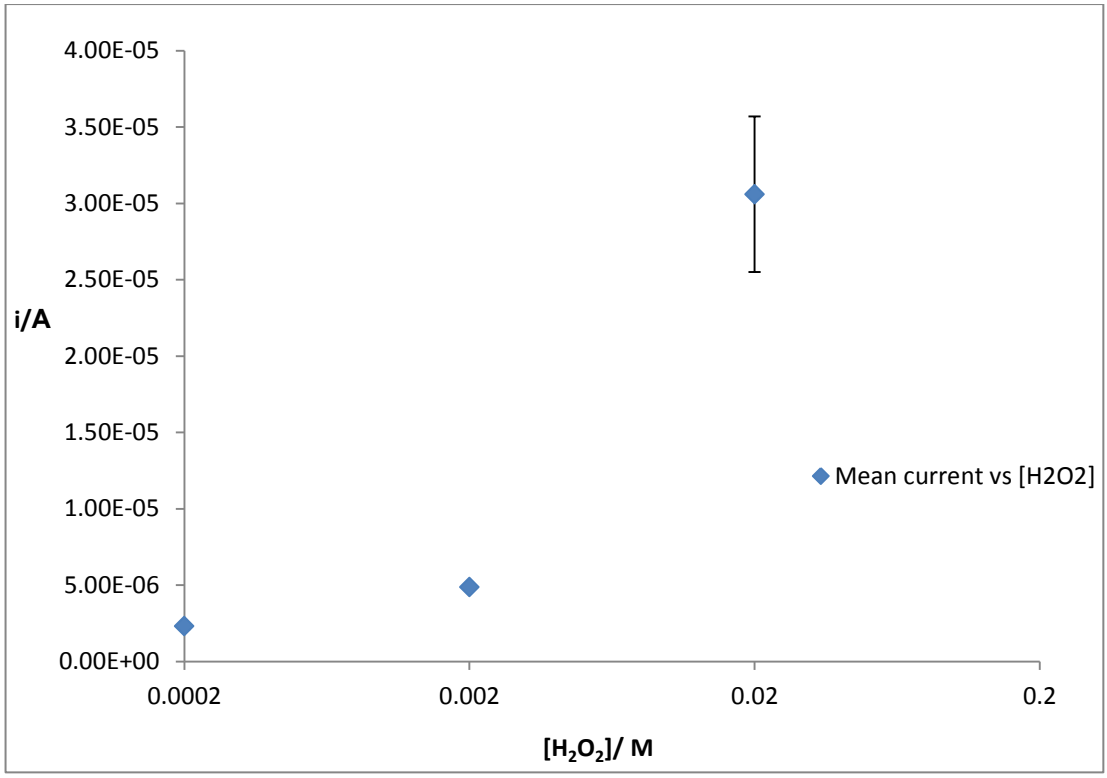

Figure 3.15. Currents evolved as a result of amperometric i/t curves carried out using gold microcavity arrays as working electrodes in 10mM H_2SO_4 with varying concentrations of H_2O_2 at -250 mV vs. Ag/AgCl.Error bars (not visible for 2 mM and 200μM) were generated from repeated independent elecrtrodes where n = 3.

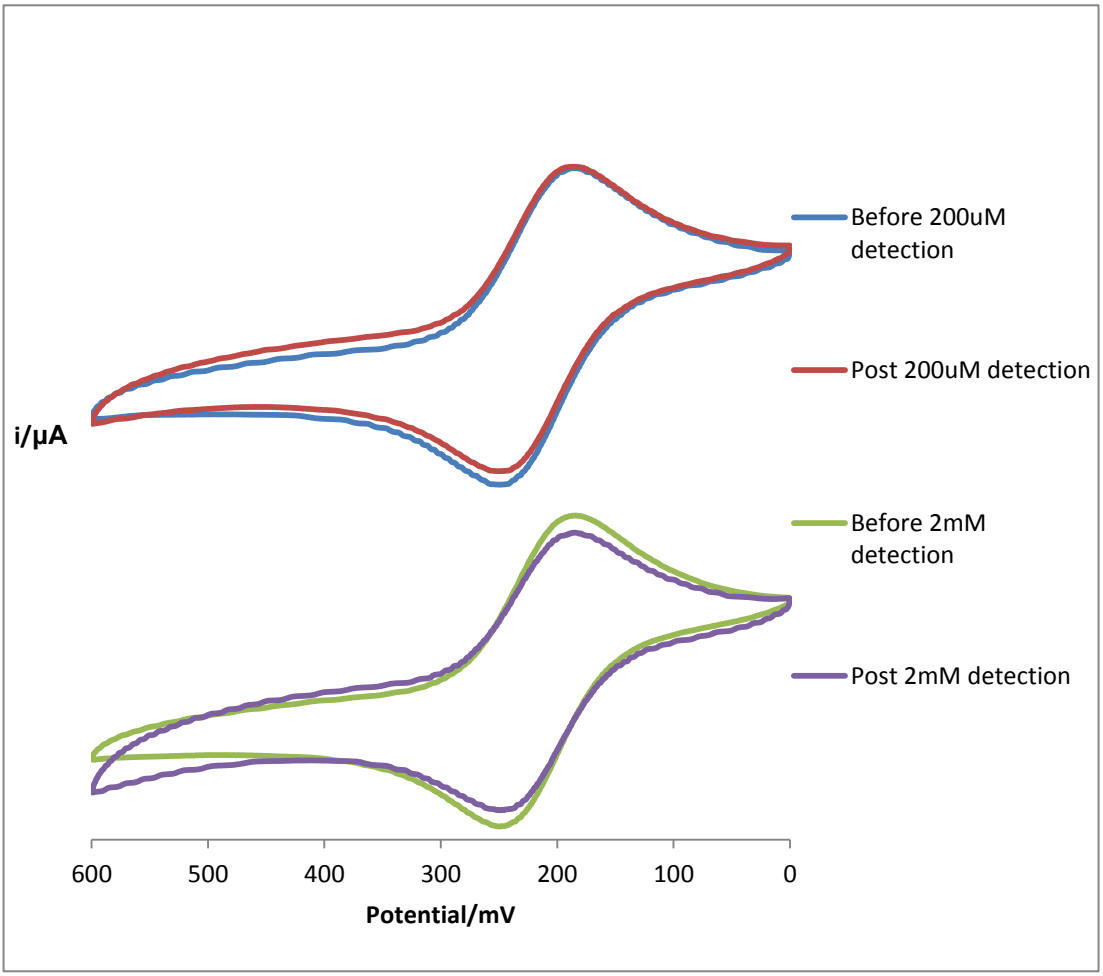

Figure 3.16. Voltammograms of microcavity arrays carried out in 2mM FeMeOH with 10 mM H_2SO_4 as supporting electrolyte from 0 to 600 mV vs. Ag/AgCl at a scan rate of 100 mV/s before and following amperometric i/t curves carried out in varying concentrations of H_2O_2 to investigate stripping of functional materials from the surface of the electrode.

At this point it seemed that the underlying gold substrate was the cause of discrepancies in current produced by the reduction of peroxide as all other attempts to change the assay parameters, such as reducing the applied potential during i-t curves from -250mV to -100mV and changing the concentration of peroxide used during i-t curves to 200µM, in order to produce more accurate results were unsuccessful.

The only remaining logical source of background signal, and thus error in measured peroxide reduction current catalysed by PtNP alone, was the underlying microcavity array itself. By comparing the results of miRNA detection assays carried out on both planar gold electrodes and microcavity arrays under the same conditions, (H_2O_2 concentration, applied potential, miRNA concentration, etc.), and normalising the results to the size of the electrodes electrochemical surface area, a value for current per cm^2, or J, could be determined. *Figure 3.17.* shows that values for J for microcavity arrays, compared to those for planar gold electrodes under the same assay conditions differ drastically. As the value for J in the microcavity samples both appears to be independent of concentration of miR-132 applied to the surface of the array, and is also greater than the current/ cm^2 produced for a planar gold electrode which was incubated with 1μM miR-132, it was suggested that current measured is independent of the number of PtNP applied to the surface of the microarray and that in the current set up, detection of current associated with the electrocatalytic reduction of H_2O_2 by PtNP is not possible. From this data and as well as data previously mentioned, it seems likely that electrodeposited gold is rougher than polished planar electrodes and therefore behaves differently. Specifically, increasing fractal properties of the surfaces of noble metals enhances electrocatalysis [29].

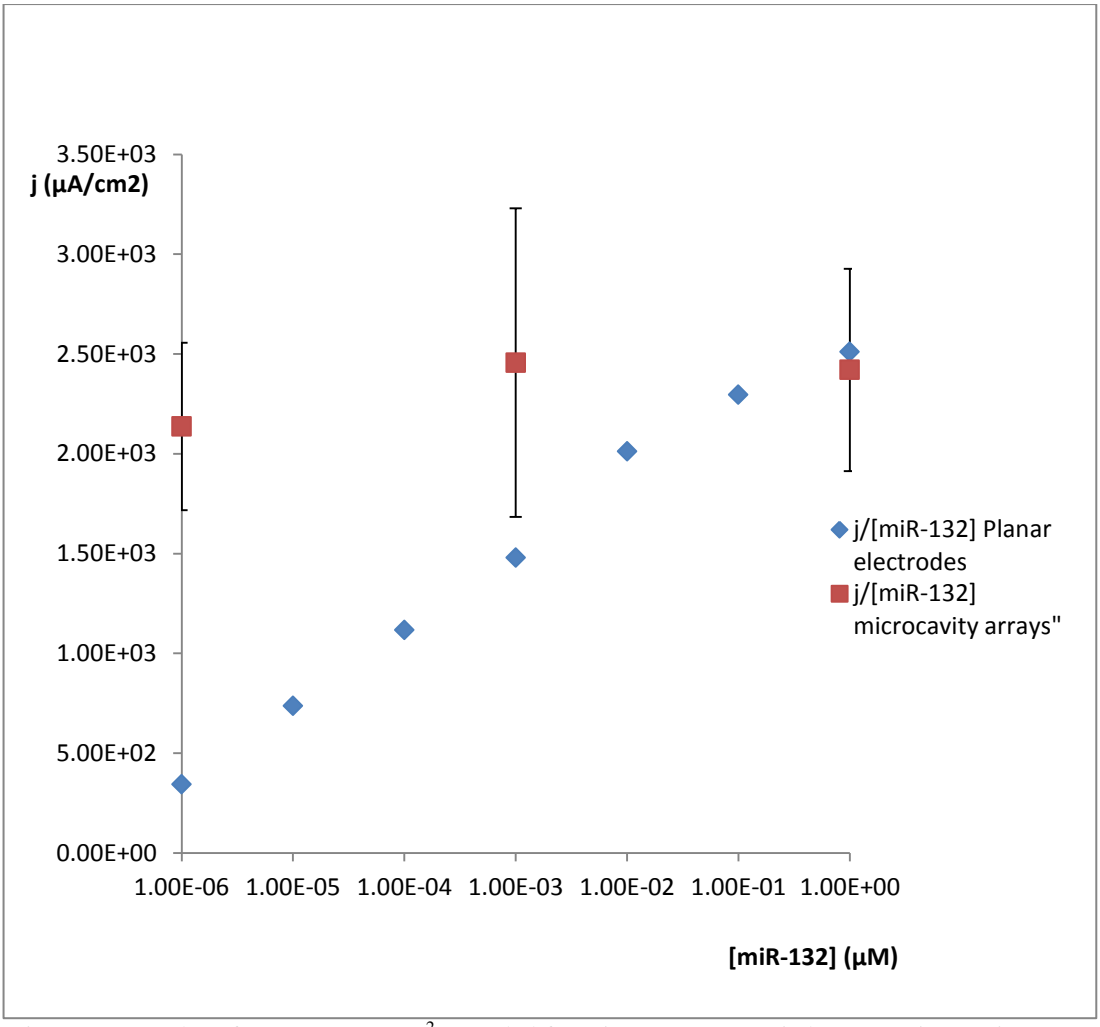

Figure 3.17. Values for current per cm^2 recorded for miRNA assay carried out on microcavity arrays (Blue) compared with those recorded for planar gold electrodes (Red). Error bars were generated from repeated independent electrodes where n = 3

Indeed, through high resolution imaging by Field emission Scanning Electron Microscopy (FeSEM) it was observed that the inner surfaces of the microcavities within the array exhibit significant roughness (*Figure 3.18*.). Even when their intrinsic electrocatalytic properties of these nanoscale imperfections may be inferior to the captured nanoparticles, their vastly larger area means that they will dominate the current associated with peroxide reduction making current very insensitive to the nanoparticle coverage/target concentration. It is interesting to note that while the presence of a roughened surface is detrimental to the measurement of a reliable amperometric signal due to enhanced electrocatalytic activity, increased roughening on a surface may be a favourable trait for spectroscopically based miRNA detection methods. For example, a roughened metal surface can result in surface enhanced raman spectroscopy (SERS) effects[30], which actually improve the sensitivity of detection. So while gold microcavity arrays may have been shown here to be incompatible with amperometric detection, they may be suited to the amplification of signal from a Raman or luminescent probe.

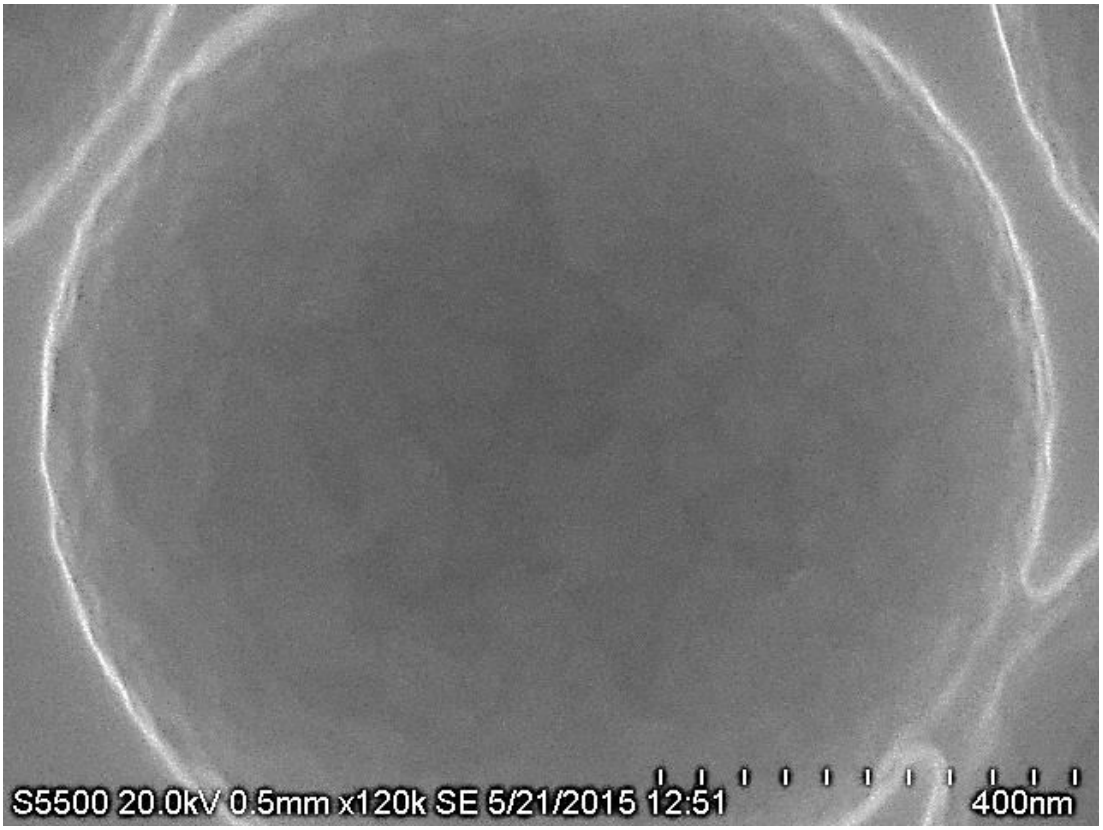

Figure. 3.18. Secondary emission FeSEM image of 1μm cavity at 120000x magnification under an accelerating voltage of 20 kV with visibly apparent nanoscale imperfections on the inner surface of the microcavity.

One possible solution to the excessive background reduction of peroxide at the roughened microcavity surface would be to anneal the surface by applying a sufficiently high temperature to reduce surface roughening without changing the microcavity structure. In an unpublished study by Jose in 2010[31], the effects of thermally annealing microcavity arrays were assessed for creating a smooth microcavity surface. In agreement with literature available on melting point depression, this study found that temperatures between 100°C and 500°C may be sufficient for the annealing of surface defects in the nanoscale. However, the study showed that at the higher end of the temperature scale, important structures of the microcavity array were lost due to excessive melting. In accordance with the results from these investigations, a maximum annealing temperature of 200°C was chosen and microcavity arrays were characterised by cyclic voltammetry before and after being placed in an oven for two hours at temperatures of 100°C, 150°C and 200°C.

Following this thermal annealing process, i-t curves were run as before in 200μM H_2O_2 to determine whether the annealing processes would have a profound effect on the minimization of excessive background reduction of H_2O_2 at the microcavity surface. This data was then compared with the data from the cyclic voltammograms from before, and following, thermal annealing to determine whether an significant change in microcavity surface current density was achieved.

Figure 3.19. shows cyclic voltammograms of microcavity arrays before and following temperate annealing resulting in a reduction of the microscopic surface area of the microcavity array by approximately 15%, 22% and 30% for temperatures of 100°C, 150°C and 200°C respectively. These results gave the indication that nanoscale imperfections in the surface of the microcavity array had been successfully annealed due to the phenomenon of melting point depression while still retaining the much larger microscale structures of the microcavities themselves. The voltammetry data also suggests that annealing had occurred on a chemical level due to the change in apparent shape of the gold reduction peak observed at approximately 1100 – 1500 mV. As observed most prominently in electrode 2, the shape of this reduction peak appears to shift towards a less positive value. This reduction peak of gold is in fact not a single broad peak, but a complex amalgamation of several peaks for the various crystal structures that gold may exist in on the surface. This shift towards a less positive potential for gold reduction is indicative of the formation of low index gold faces and is typical in the process of annealing[32].

This reduction in surface roughness was expected to have a profound effect on the background current produced by the reduction of H_2O_2 by the microcavity array. However, *Table 3.1.* shows that the decrease in the current due to the reduction of peroxide, Δi, was comparable to the loss in microscopic surface area, indicating that while temperature annealing was effectively reducing surface area, the current density of the microcavity array remained unchanged This indicated that the observed phenomenon of decreased microscopic surface area was not due to annealing of nanoscale defects and instead was due to the loss of microcavity surface area through melting of gold surface microstructures. Interestingly, the microcavity array termed “electrode 2” did show some improvement, as the change in as the ratio of Δi/ΔA is greater than a value of one (*see Table 3.1*), indicating that annealing may

have taken place. However, significantly more effective reduction of the background current would be needed in order for low concentrations of miRNA to be detected.

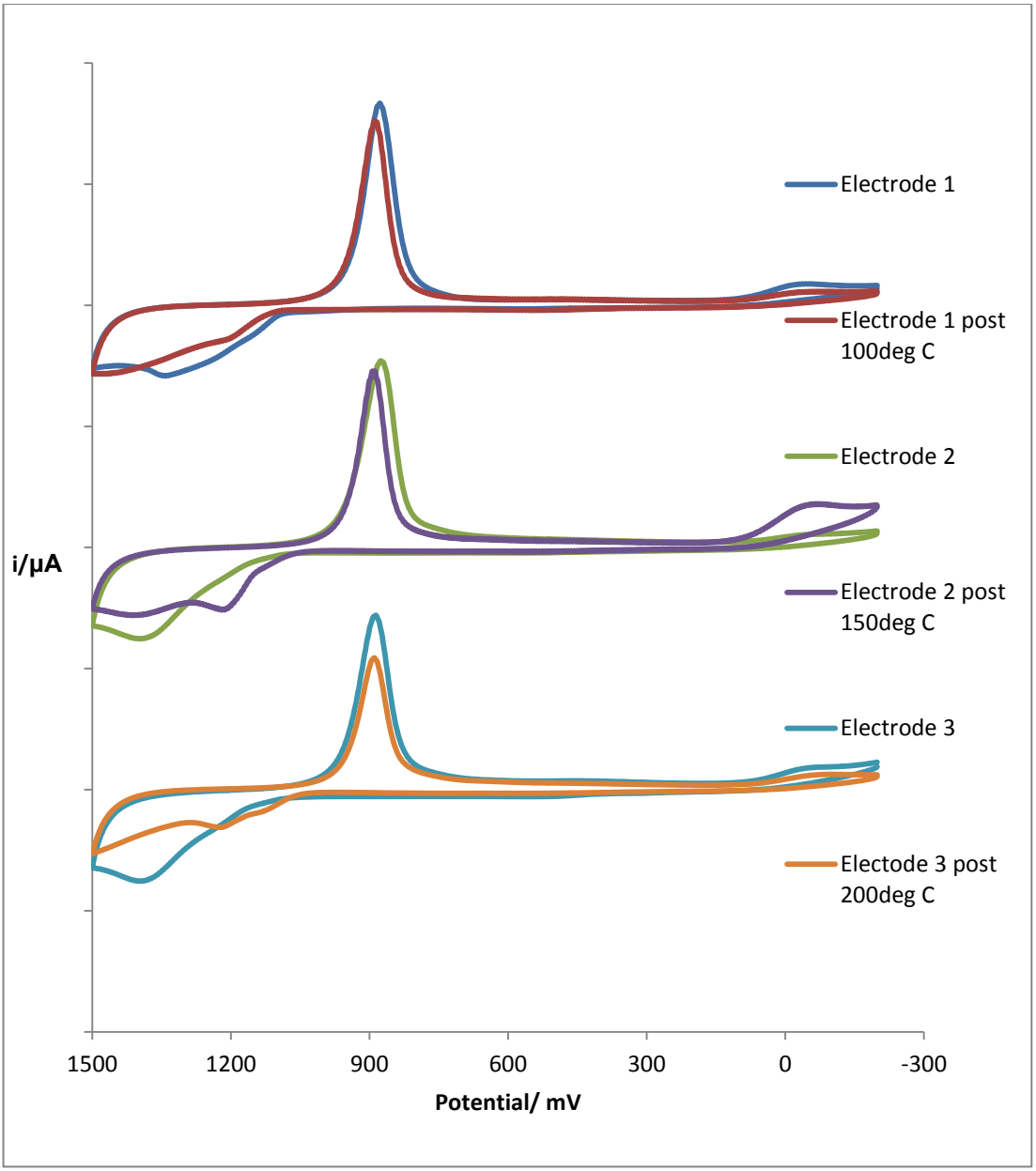

Figure 3.19. Cyclic voltammograms of 3µm microcavity arrays carried out in 10 mM H_2SO_2 vs Ag/AgCl at a scan rate of 100 mV/s before and following attempts to temperature anneal the nanoscale roughness of cavities. Through integration of the gold oxide reduction peak the microscopic surface area of the microcavity arrays were measured and shown to have decreased. This observation would suggest that nanoscopic imperfections in the surface of the microcavity array that are considered to be the cause of background peroxide reduction have been annealed together due to the phenomenon of melting point depression. Note: tick marks on the y-axis are given in 100 µA increments.

Table 4.1. Table of data from temperature annealing experiments showing the comparative changes in microscopic surface area of the microcavity array and the change in background current produced by the microcavity array due to the reduction of 200μM H2O2

Sample no.	Annealing Temp	Ap (A)	Ap After (A)	ΔA (%)	i Before (μA)	i After (μA)	Δi (%)	Δi/ ΔA
1	100	2.973E-4	2.517E-4	15.4	1.340	1.119	16.492	1.070
2	150	2.976E-4	2.318E-4	22.555	1.927	1.440	25.272	1.120
3	200	2.677E-4	1.858E-4	30.6	1.442	1.005	30.305	0.990

3.5. Conclusion.

Microcavity arrays for the selective immobilisation of neuroblastoma cells have been fabricated and are capable of performing as platforms for the immobilisation and *in situ* lysis of human neuroblastoma cells. Preliminary results of FeSEM imaging showed PtNP immobilised within the inner surface of the microcavity array following cell lysis, indicating the successful hybridisation of miRNA hybridisation. However, the current, expected for electrocatalytic reduction of hydrogen peroxide by the bound PtNPs, did not increase with increasing target concentration as expected. Significantly, decreasing the detection potential, or reducing the concentration of peroxide, did not improve the sensitivity. Further electrochemical and electron microscopy investigations suggest that nanoscale surface roughness in the electrodeposited microcavities results in the excessive electrocatalytic reduction of H_2O_2. Attempts to improve the surface morphology of the microcavities by thermally annealing the cavity arrays failed to decrease the background current to the point where the miRNA target could be detected with high sensitivity.

However, the microcavity surface can capture cells and allow them to be lysed. However, the miRNA concentration cannot be quantified using electrocatalytic detection of platinum nanoparticles. Nanotextured surfaces such as gold microcavity arrays are ideal substrates for fluorescent plasmonic enhancement of fluorophores[33] and as such, could be used as a platform for the enhanced detection of miRNA through optical means such as super resolution microscopy. The conductive gold microcavity arrays may also be an ideal platform for electrochemiluminescent detection of miRNA.

In recent years electrochemiluminescence (ECL) has gathered increasing interest in biosensing applications due to its simplified set up, high sensitivity, low background signal and speed of analysis[34]. Future work in this field could therefore be focused on the conjugation of a luminophore to a probe strand of RNA for use in the hybridisation to a free end of a miRNA strand immobilised to the inner surface of a microcavity array, in a similar way to the method described previously for probe strand modified PtNP immobilisation. In this scheme, cell immobilisation, cell lysis and target hybridisation would be carried out as described previously. The luminophore labelled probe would then be hybridised to the free end of the target

miRNA and under an applied potential and in the presence of a co-reactant species the luminophore could produce a luminescent signal. As the mechanism of ECL relies on the electrocatalytic oxidation of a co-reactant to generate a luminescent signal, the roughened surface of electrodeposited microcavities may prove to be advantageous to signal detection. This gives the potential for not only a means of detecting a miRNA target specific to the type of cell that is to be studied, for example neuroblastoma, but with microfabrication of fibre optic sensors and precision spatial confinement of signal collection (to a single microcavity), this method could theoretically be used to determine the miRNA profile of individual cells by carrying out detections within single microcavities. This approach would then have the potential to exploit the optical properties of metal surfaces may also be further exploited for the detection of immobilised ECL luminophore.

In summation the future direction of this research could be directed at combining the effects of surface enhanced fluorescence and ECL to enhance the luminescent signal of a luminophore bound probe oligonucleotide for ultrasensitive detection of miR-132 from captured and lysed human neuroblastoma cells. As previously shown, the specific objectives of neuroblastoma cell immobilisation and in situ lysis have been well characterised and with only minor augmentation of the miRNA detection scheme, an electrochemical/optical detection method for the detection of miR-132 has been chosen that better suits the cell immobilisation platform created and shows promise for ultrasensitive detection of miRNA targets.

3.6. Bibliography

1. Yin, H.S., Li, B.C., Zhou, Y.L., Wang, H.Y., Wang, M.H., and Ai, S.Y., *Signal-on fluorescence biosensor for microRNA-21 detection based on DNA strand displacement reaction and Mg2+-dependent DNAzyme cleavage.* Biosensors & Bioelectronics, 2017. **96**: p. 106-112.
2. Henihan, G., Schulze, H., Corrigan, D.K., Giraud, G., Terry, J.G., Hardie, A., Campbell, C.J., Walton, A.J., Crain, J., Pethig, R., Templeton, K.E., Mount, A.R., and Bachmann, T.T., *Label- and amplification-free electrochemical detection of bacterial ribosomal RNA.* Biosensors & bioelectronics, 2016. **81**: p. 487-94.
3. Campuzano, S., Pedrero, M., and Pingarron, J.M., *Electrochemical genosensors for the detection of cancer-related miRNAs.* Analytical and Bioanalytical Chemistry, 2014. **406**(1): p. 27-33.
4. Ge, Z.L., Lin, M.H., Wang, P., Pei, H., Yan, J., Sho, J.Y., Huang, Q., He, D.N., Fan, C.H., and Zuo, X.L., *Hybridization Chain Reaction Amplification of MicroRNA Detection with a Tetrahedral DNA Nanostructure-Based Electrochemical Biosensor.* Analytical Chemistry, 2014. **86**(4): p. 2124-2130.
5. Gao, Z.Q., Deng, H.M., Shen, W., and Ren, Y.Q., *A Label-Free Biosensor for Electrochemical Detection of Femtomolar MicroRNAs.* Analytical Chemistry, 2013. **85**(3): p. 1624-1630.
6. Shen, W., Deng, H.M., Ren, Y.Q., and Gao, Z.Q., *A label-free microRNA biosensor based on DNAzyme-catalyzed and microRNA-guided formation of a thin insulating polymer film.* Biosensors & Bioelectronics, 2013. **44**: p. 171-176.
7. Ramnani, P., Gao, Y.N., Ozsoz, M., and Mulchandani, A., *Electronic Detection of MicroRNA at Attomolar Level with High Specificity.* Analytical Chemistry, 2013. **85**(17): p. 8061-8064.
8. Bartel, D.P., *MicroRNAs: Genomics, biogenesis, mechanism, and function.* Cell, 2004. **116**(2): p. 281-297.
9. Furuse, Y., Finethy, R., Saka, H.A., Xet-Mull, A.M., Sisk, D.M., Smith, K.L.J., Lee, S., Coers, J., Valdivia, R.H., Tobin, D.M., and Cullen, B.R., *Search for MicroRNAs Expressed by Intracellular Bacterial Pathogens in Infected Mammalian Cells.* PLoS One, 2014. **9**(9).
10. Matin, F., Jeet, V., Clements, J.A., Yousef, G.M., and Batra, J., *MicroRNA Theranostics in Prostate Cancer Precision Medicine.* Clin Chem, 2016. **62**(10): p. 1318-33.
11. Bertoli, G., Cava, C., and Castiglioni, I., *MicroRNAs as Biomarkers for Diagnosis, Prognosis and Theranostics in Prostate Cancer.* Int J Mol Sci, 2016. **17**(3): p. 421.
12. Murray, M.J., Raby, K.L., Saini, H.K., Bailey, S., Wool, S.V., Tunnacliffe, J.M., Enright, A.J., Nicholson, J.C., and Coleman, N., *Solid Tumors of Childhood Display Specific Serum microRNA Profiles.* Cancer Epidemiology Biomarkers & Prevention, 2015. **24**(2): p. 350-360.
13. Gao, Z.Q., *A highly sensitive electrochemical assay for microRNA expression profiling.* Analyst, 2012. **137**(7): p. 1674-1679.

14. Chen, H.L., Shalom-Feuerstein, R., Riley, J., Zhang, S.D., Tucci, P., Agostini, M., Aberdam, D., Knight, R.A., Genchi, G., Nicotera, P., Melino, G., and Vasa-Nicotera, M., *miR-7 and miR-214 are specifically expressed during neuroblastoma differentiation, cortical development and embryonic stem cells differentiation, and control neurite outgrowth in vitro.* Biochemical and Biophysical Research Communications, 2010. **394**(4): p. 921-927.
15. Hill, H.D., Millstone, J.E., Banholzer, M.J., and Mirkin, C.A., *The Role Radius of Curvature Plays in Thiolated Oligonucleotide Loading on Gold Nanoparticles.* Acs Nano, 2009. **3**(2): p. 418-424.
16. A. J. Bard, L.R.F., *Electrochemical Methods: Fundamentals and Applications*. 2nd edition ed. 2001, New York: Wiley.
17. Trasatti, S. and Petrii, O.A., *REAL SURFACE-AREA MEASUREMENTS IN ELECTROCHEMISTRY.* Pure and Applied Chemistry, 1991. **63**(5): p. 711-734.
18. Peterson, A.W., Heaton, R.J., and Georgiadis, R.M., *The effect of surface probe density on DNA hybridization.* Nucleic Acids Research, 2001. **29**(24): p. 5163-5168.
19. Modak, S., Gerald, W., and Cheung, N.K.V., *Disialoganglioside G(D2) and a novel tumor antigen: Potential targets for immunotherapy of desmoplastic small round cell tumor.* Medical and Pediatric Oncology, 2002. **39**(6): p. 547-551.
20. Wu, Z.L., Schwartz, E., Seeger, R., and Ladisch, S., *EXPRESSION OF GD2 GANGLIOSIDE BY UNTREATED PRIMARY HUMAN NEUROBLASTOMAS.* Cancer Research, 1986. **46**(1): p. 440-443.
21. Ladisch, S., *Biological Significance of Tumor Gangliosides: Shedding, Transfer, and Immunosuppression*, in *Frontiers in Bioactive Lipids*, J.Y. Vanderhoek, Editor. 1996, Springer US. p. 215 - 221.
22. Celikkol-Aydin, S., Suo, Z.Y., Yang, X.H., Ince, B., and Avci, R., *Sharp Transition in the Immunoimmobilization of E. coli O157:H7.* Langmuir, 2014. **30**(26): p. 7755-7761.
23. Chen, Y., Cai, J.Y., Xu, Q.C., and Chen, Z.W., *Atomic force bio-analytics of polymerization and aggregation of phycoerythrin-conjugated immunoglobulin G molecules.* Molecular Immunology, 2004. **41**(12): p. 1247-1252.
24. Saber, R., Sarkar, S., Gill, P., Nazari, B., and Faridani, F., *High resolution imaging of IgG and IgM molecules by scanning tunneling microscopy in air condition.* Scientia Iranica, 2011. **18**(6): p. 1643-1646.
25. Xia, N., Xing, Y., Wang, G.F., Feng, Q.Q., Chen, Q.Q., Feng, H.M., Sun, X.L., and Liu, L., *Probing of EDC/NHSS-Mediated Covalent Coupling Reaction by the Immobilization of Electrochemically Active Biomolecules.* International Journal of Electrochemical Science, 2013. **8**(2): p. 2459-2467.
26. Bellis, S.L., *Advantages of RGD peptides for directing cell association with biomaterials.* Biomaterials, 2011. **32**(18): p. 4205-10.
27. Lee, H.J., Kim, J.H., Lim, H.K., Cho, E.C., Huh, N., Ko, C., Park, J.C., Choi, J.W., and Lee, S.S., *Electrochemical cell lysis device for DNA extraction.* Lab on a Chip, 2010. **10**(5): p. 626-633.
28. Graham, J.M., *Homogenization of mammalian cultured cells.* ScientificWorldJournal, 2002. **2**: p. 1630-3.

29. Arvia, A.J., Salvarezza, R.C., and Triaca, W.E., *Noble metal surfaces and electrocatalysis. Review and perspectives.* Journal of New Materials for Electrochemical Systems, 2004. **7**(2): p. 133-143.
30. Chen, L., Liu, F.X., Zhan, P., Pan, J., and Wang, Z.L., *Ordered Gold Nanobowl Arrays as Substrates for Surface-Enhanced Raman Spectroscopy.* Chinese Physics Letters, 2011. **28**(5): p. 4.
31. Jose, B., *Biomimetic photonic nanocavity arrays* in *School of Chemical Sciences*. 2010, Dublin City University: Dublin, Ireland. p. 168 - 199.
32. Hamelin, A., *Cyclic voltammetry at gold single-crystal surfaces .1. Behaviour at low-index faces.* Journal of Electroanalytical Chemistry, 1996. **407**(1-2): p. 1-11.
33. Oo, S.Z., Silva, G., Carpignano, F., Noual, A., Pechstedt, K., Mateos, L., Grant-Jacob, J.A., Brocklesby, B., Horak, P., Charlton, M., Boden, S.A., and Melvin, T., *A nanoporous gold membrane for sensing applications.* Sensing and Bio-Sensing Research, 2016. **7**: p. 133-140.
34. Chen, X.M., Su, B.Y., Song, X.H., Chen, Q.A., Chen, X., and Wang, X.R., *Recent advances in electrochemiluminescent enzyme biosensors.* Trac-Trends in Analytical Chemistry, 2011. **30**(5): p. 665-676.

Chapter 4.

Detection of miR-132 by Electrochemiluminescence.

4. Detection of miR-132 by Electrochemiluminescence.

4.1. Introduction.

In recent times there has been a great deal of reports in the field of biosensor research that utilise the technique of electrochemiluminescence for signal transduction and by association biomarker detection[1-7]. The vast majority of reports utilising ECL as a biosensing method are based on immunoassays for protein and peptide based biomarkers.[1-5] However, there are also reports of nucleic acid based biosensors [8-11]. Nucleic acid based biosensors have advantages over their antibody based immunoassay counterparts, not least of which is the ability to synthesise capture and probe sequences. The regular structure of nucleic acid chains, when compared to that of macro polypeptides such as antibodies, makes nucleic acid immobilisation systems attractive approaches to biosensor design. Strands of nucleic acids complementary to the nucleic acid target, e.g.. a miRNA, are simple to design and produce, and their target binding characteristics are relatively straightforward to predict. In contrast, due to the complex nature of the 3D structure of polypeptide chains, as well as the fact that the hypervariable regions of antibodies may contain hundreds of peptide subunits, antibodies have a highly complex binding site leading to difficulties in predicting the how a target may be captured on the surface of a sensor.

Another advantage nucleic acid based biosensors often have over their antibody based immunosensing counter parts is their intrinsic ability to keep the probe analyte in very close proximity to the surface of biosensor. The typical length of a miRNA molecule is approximately 22bp, which will have a physical length of between 5 and 7 nm[12]. Therefore, in the case of an ECL based miRNA sandwich assay, the distance between the probe molecule, an ECL luminophore, and the surface of the electrode will be < 10 nm. In contrast, antibodies are typically in the range of 10 – 40 nm in size[13], and therefore in a sandwich assay scheme similar to that of the scheme described in this work, employing a capture and probe antibody to

immobilise and label the target respectively will result in the ECL luminophore being several tens of nanometres from the surface of the electrode. This is a very important consideration with regards to ECL, as the overall efficiency of the reaction is heavily dependent on the rate of electron transfer between the luminophore and electrode and the diffusive rate of the co-reactant from the electrode upon oxidation of the luminophore[14].

This push in the direction of ECL based biosensing is at least partially due to the inherent advantages of ECL, especially the low background signal. As ECL is a method for the conversion of electrical energy to radiative energy, there is no potential for signal contamination from the excitation method, such as light scattering or auto fluorescence observed in other spectroscopic techniques[15]. The technique may also be multiplexed for the detection of many different biomolecules and signal acquisition is fast, leading to the high throughput analysis of complex samples.

To this end, the aim of the work carried out in the following chapter was to create an electrochemiluminescent system for the ultrasensitive and highly selective detection of miRNA targets through a hybridisation sandwich assay on a nanotextured electrode surface, that may facilitate the enhancement of electrochemiluminescent signal. As previously mentioned, the expression of miR-132 is upregulated in neuroblastoma cells and thus a system was devised that could potentially increase the sensitivity of ECL based miRNA detection by exploiting surface effects of the electrode surface itself. Recently reports have emerged of surface enhanced electrochemiluminescence (SEECL) being employed to increase the light output of an ECL luminophore[7, 16]. It is well understood that strongly enhanced electromagnetic fields may be excited when noble metal nanostructures are irradiated electromagnetically, for example, monochromatic light focused onto metal nanoparticles on a surface[17, 18]. This electromagnetic field is the result of a delocalised coherent oscillation of electrons at the interface between the surface of the nanoparticle and the surrounding dielectric medium, eg. air, solvent, etc., and is referred to as a surface plasmon[19]. This enhanced electromagnetic field will enhance the spectroscopy of molecules placed within it [19], giving rise to a signal enhancement that may be exploited for the purpose of detecting ultralow concentrations of materials for example. This approach for signal enhancement is

known broadly as surface enhanced spectroscopy and is the underlying mechanism for a number of analytical techniques such as surface enhanced raman spectroscopy (SERS)[18], metal enhanced fluorescence (MEF) and surface enhanced infrared absorption spectroscopy (SEIRAS)[20]. It is precisely this mechanism that is exploited by SEECL. Lakowicz et al. first reported the enhancement of ECL by a surface plasmon, postulating that in this case it is the emission of the luminophore that excited the surface plasmon, as opposed to a beam of incident light in the case of MEF for example[21]. This radiative plasmon model relies on the resonant energy transfer between the luminophore and the plasmon itself and is therefore heavily dependent on the distance between the two. Wang et al. [16] demonstrated this distance dependency, showing that an approximately 8 fold increase in ECL signal could be achieved by separating nanoparticles and luminophores by approximately 7 nm. Thus it is the aim of the following body of work detailed here, to exploit this distance dependent effect to improve miRNA detection, by exploiting the chain length of the miRNA itself.

Figure. 4.1. shows the fabrication of the proposed miRNA detection platform. A self-assembled monolayer of 16-phosophonohexadecanoic acid is formed on the surface of an Indium Tin Oxide (ITO), is used as a template through which metal nanoparticles may be electrodeposited.

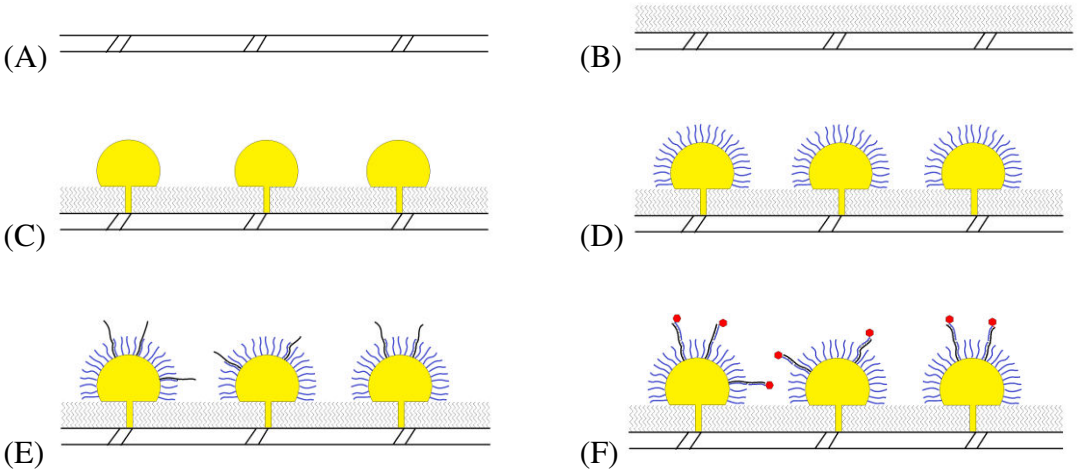

Figure.4.1. Schematic representation of electrode fabrication and miR-132 detection strategy. A planar ITO electrode (A) is functionalised with a self-assembled monolayer of 16-phosphonohexadecanoic (B). Metal nanoparticles are then electrodeposited through the monolayer (C) and then a self-assembled monolayer of thiolated capture oligonucleotide is formed on the surface of the metal nanoparticles (D). The electrodes are then incubated in a solution of miRNA target and a portion of the target, miR-132, hybridises to the capture strand on the nanoparticles (E). An oligonucleotide-luminophore probe is then allowed to hybridise to the free end of the miRNA target (F) and this probe is then detected through electrochemiluminescence.

By applying a brief over potential, up to -1600 mV for 20 ms to the ITO electrode in a suitable deposition solution, for example 1mM $HAuCl_4$ in the case of gold nanoparticles, nucleation sites are formed in defect sites in the monolayer surface that will facilitate nanoparticle growth. Immediately after this nucleation potential is applied, a moderate negative potential, between -100mV and -200mV depending on particle size required, is applied to the electrode surface for a fixed time and nanoparticles are formed at nucleation sites. This approach to nanoparticle formation ensures good control over the size and distribution of nanoparticles formed, as nanoparticles will preferentially grow at the pre-nucleated sites, and are unlikely to nucleate and grow through the 16 carbon monolayer at the relatively moderate potential applied during the nanoparticle growth phase[22]. Thus each nanoparticle is formed under the same conditions for the same duration leading to a desirable size distribution.

Following on from this the nanoparticles are functionalised in a single step for the capture and subsequent detection of miRNA targets by the application of a 3'-

thiolated strand of nucleic acid 11bp long and complementary to the 5’ end of the miRNA target, referred to herein as the capture strand. As the metal nanoparticles here are of coinage metals (Au, Ag, Pt) the 3’-thiolated ends of the capture strands will readily bond to the surface of the nanoparticles resulting in the formation of a monolayer of capture strands that will facilitate the immobilisation of miRNA targets from solution. Upon incubation of the electrode with the desired miRNA target, miR-132, 5’ end of this target will hybridise to a capture strand on the surface of the nanoparticle resulting in an immobilised miR-132 with a free single stranded 3’ end. This 3’ end is then free to hybridise to another nucleic acid strand, this time functionalised at its 5’ end with the ECL luminophore, a ruthenium polypyridyl complex, referred to here as the probe strand. As the probe strand will have a sequence complementary to that of the 3’ end of miR-132, any unbound probe strand will be washed from the array, thus the number of ECL luminophores on the surface of the electrode will be proportional to the number of miR-132 strands immobilised on the electrode and thus subsequently proportional to the concentration of miR-132 in solution. The electrode is then placed in a custom ECL cell and undergoes anodic cycling, to produce an ECL signal.

4.2. Experimental.

4.2.1. Materials.

Planar gold electrodes and ITO/Glass sheets were purchased from IJ Cambria, Wales, UK. Ruthenium (II) (bis-2,2-bipyridyl)-2(4aminophenyl) imidazo[4,5-f][1,10]phenanthroline was prepared by Dr. Ciarán Dolan of Dublin City University. All other solvents and reagents were purchased from Sigma Aldrich. All aqueous solutions were prepared using deionised water. Oligonucleotide sequences were purchased from Eurogentec and identical to those mentioned in Chapter 3.

4.2.2. Instrumentation.

A three electrode electrochemical cell was used throughout this work consisting of a platinum wire as a counter, an Ag/AgCl reference electrode and a working electrode. All electrochemical measurements were carried out using a CHI 760E potentiostat within a faraday cage. Confocal microscopy was carried out using a Leica TSP8 Confocal/STED microscope system. FeSEM images were obtained with the use of a Hitachi S5500 Field Emission Scanning Electron Microscope. ECL measurements were carried out with the use of a CHI660c potentiostat coupled to an Oriel 70680 photo multiplier tube equipped with a high voltage power supply with an applied bias of -850 mV and an Oriel 70701 amplifier / recorder unit.

4.3. Procedures.

4.3.1. Nanotextured Electrode Surface Preparation

Working electrodes, composed of Indium Tin Oxide (ITO) on a glass substrate, were cut to a size of 17x7mm and cleaned by ultrasonication in methanol for 15 minutes. Electrodes were then immersed in a solution of 2mM 16-phosphonohexadecanoic acid in methanol for a minimum of 16 hours to form a self-assembled monolayer on the surface of the electrode. The electrodes were then washed and wrapped with hydrophobic Teflon to produce a working area on the electrode of 7x7mm. The working area of the electrode was then immersed in a nanoparticle deposition solution and a nucleation and growth potential were applied to the electrode in separate steps of -1600mV and -100mV respectively. Deposition of gold nanoparticles was carried out in 1mM $HAuCl_4$ in 100mM NaCl, deposition of platinum nanoparticles was carried out in 1mM $KPtCl_6$ in 100mM H_2SO_4, and silver nanoparticle deposition was carried out in 1mM $AgNO_3$ in 100mM HNO_3 with 15mM citric acid.

4.3.2. Surface Modification of Nanoparticles with C16-Ru

Nanoparticle modified electrodes were placed in an ethanolic solution of 16-mercaptohexadecanoic acid for a minimum of 8 hours to form a self-assembled monolayer on the surface of the nanoparticles. The amino functionalised, luminescent dye was then coupled to the carboxyl termini of this monolayer using 3mM DDC/1mM NHS in dimethyl formamide.

4.3.3. Preparation of oligo-Dye probe conjugate.

A 1:1 10mM solution of sodium 4-((4-(cyanoethynyl)benzoyl)oxy)-2,3,5,6-tetrafluorobenzenesulphonate (CBTF) and dye was prepared in dimethylsulphoxide (DMSO) and stirred at room temperature for 1 hour. Following this, an aliquot of the reaction mixture was removed and diluted to a concentration of 100 μM in phosphate buffered saline (PBS). A 100 μl aliquot of this was then combined with 100 μl of 100 μM thiolated probe oligonucleotide and diluted to a final concentration of 1 μM oligonucleotide and stirred at room temperature overnight.

4.3.4. Capture oligonucleotide monolayer formation and miRNA target hybridisation and detection.

Nanoparticle modified electrodes were placed in a 1μM solution of thiolated oligonucleotide (capture) for a minimum of 12 hours to form a self-assembled monolayer on the surface of the metal nanoparticles for target miRNA hybridisation. The electrodes were then incubated in a solution of miRNA target in PBS for 8 hours and then washed with PBS to remove non-specifically bound target. The electrodes were finally placed in a 1μM solution of probe oligo-dye conjugate overnight. Following this, the electrodes were washed with PBS to remove non-specifically bound probe and mounted into custom electrochemical cells for ECL. ECL was measured in 100mM phosphate buffer with 50mM tripropylamine (TPA) as co-reactant.

4.4. Results and Discussion.

4.4.1. Determination of ECL Dye Efficiency.

Initially, work was carried out to identify a metallo-organic dye for use with ECL, that may also be functionalised for use in miRNA detection assay. Important aspects of the dye such as solubility in aqueous media, potential for conjugation to a probe RNA strand, and most importantly ECL efficiency were determined. The ECL efficiency of the dye would be a key aspect in controlling the dynamic range of the assay with a target limit of detection in the sub-picomolar range. The dye, [ruthenium (II) (bis-2,2-bipyridyl)-2(4aminophenyl) imidazo[4,5-f][1,10]phenanthroline] $(ClO_4^-)_2$, (referred to as $RuPICNH_2$ from here on) was selected on the basis that it was soluble in aqueous solutions and contained an amine group on the pic ligand that could be used as a site for conjugating the dye to a nuclei acid.

In order to determine the ECL efficiency of the dye, the redox activity and ECL output of the dye must be correlated to that of a similar compound that may be used as a standard. For ruthenium polypyridyl compounds the standard most widely implemented in the literature is Ruthenium (II) Tris-2,2-bypyridine ($RuBpy_3$)[15]. It is widely accepted that the ECL efficiency of this is 0.05 and is typically used as the standard for ECL efficiency calculations of similar ruthenium polypyridyl complexes due to its relatively high efficiency[15].

Solution phase ECL was carried out using conventional planar glassy carbon electrode of 3 mm in diameter. A standard 3 electrode system was employed, with an Ag/AgCl reference electrode and a Pt wire for an auxiliary electrode. In order to measure the working area of the glassy carbon working electrode a cyclic voltammogram was carried out in 2mM ferrocene methanol solution with 100mM phosphate buffer as supporting electrolyte, and cycled between 800 mV and -200 mV. In *Figure 4.2.* an example of these CV obtained is shown. This was carried out between each ECL measurement in order to compensate for any changes in the electrode surface.

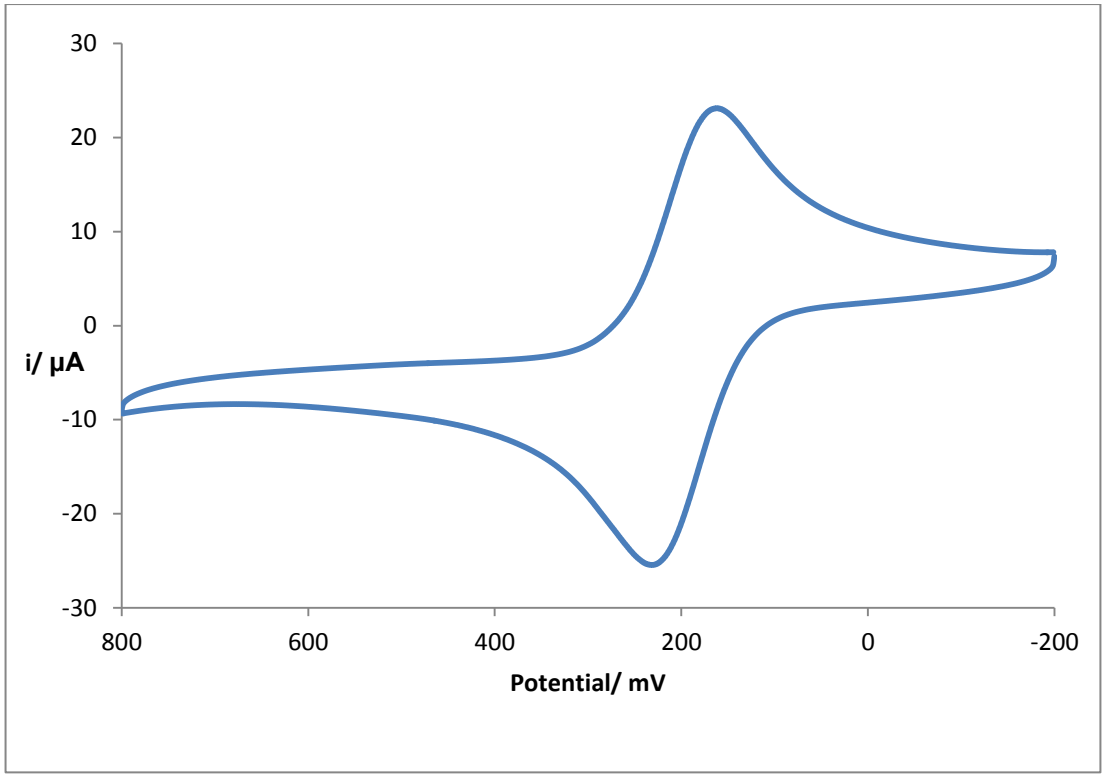

Figure. 4.2. Cyclic voltammogram of a 3 mm diameter glassy carbon electrode between 800 and -200 mV Vs. Ag/AgCl carried out in 2mM FcMeOH and 100mM phosphate buffer as supporting electrolyte at a scan rate of 100 mV/s.

In this voltammogram a redox process is observed centred at approximately 200 mV and was used to assess the condition of the electrode throughout the process of determining the ECL efficiency of the dye. This process was used to monitor changes in the electrochemical surface area of the electrode as the surface area of the electrode is proportional to the charge associated with each process. Therefore the any deviations in size of the electrode surface through modification, polishing, fouling, etc. could be accounted for. Furthermore this provided a method for normalising results obtained from individual electrodes. By integrating the area under oxidation and reduction peaks (A_{pc} and A_{pa}), the charge associated with each process was measured at $3.41e^{-5}$ C and $3.32e^{-5}$ C, respectively. This indicated that the process was almost perfectly reversible, as A_{pc}/A_{pa} resulted in a value of 0.97, where a value of 1 would be expected for a perfectly reversible process. Furthermore separation between anodic peak current (I_{pa}), 230 mV, and cathodic peak current (I_{pc}), 162 mV, was 68 mV at a scan rate of 100 mVs^{-1}, indicating a good rate of electron transfer as this correlates well with the ideal value of 56.5/*n*, where *n* is the

number of electrons involved in the process[23]. These parameters were used to monitor the condition of the electrode throughout the ECL efficiency determination.

In *Figure 4.3*. the solution phase voltammetry data for $RuPICNH_2$ is shown. In order to determine the ECL efficiency correctly, a concentration of $RuPICNH_2$ was required that could be used for both ECL, to determine the ECL output of the dye when reacted with a co-reactant, and redox voltammetry, in order to determine the charge associated with the oxidation of the dye under these conditions. However, due to the relatively poor redox voltammetry observed for $RuPICNH_2$ in aqueous conditions, as well as the high background current and capacitance observed in aqueous solution, it was difficult to determine the charge associated with the oxidation of $RuPICNH_2$ during the ECL reaction. In a bid to increase the signal to noise ratio of $RuPICNH_2$, the charge associated with the oxidation of the compound during ECL was estimated through fast scan rate voltammetry at a low dye concentration of 20 μM. In *Figure 4.3*. the voltammetry of $RuPICNH_2$ performed in 100 mM phosphate buffer vs. Ag/AgCl at scan rates between 20 Vs^{-1} and 7.5 Vs^{-1} can be seen with the Ru^{2+} to Ru^{3+} process observed to take place at approximately 1100 mV.

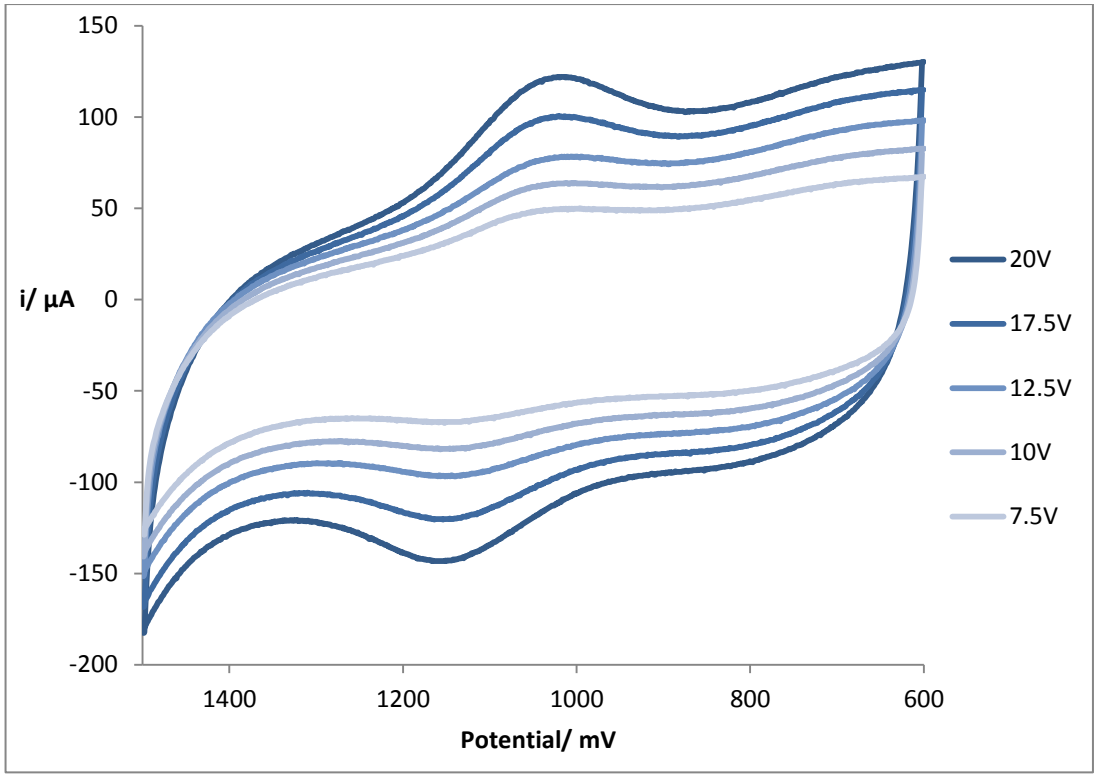

Figure 4.3. Solution redox voltammetry shown for 20µM $RuPICNH_2$ in 100mM phosphate buffer. Voltammetry was carried out using a 3 mm diameter glassy carbon electrode and a potential window of 600 – 1500 mV vs. Ag/AgCl at scan rates between 20 and 7.5 V s^{-1}. The single electron oxidation/ reduction process of $RuPICNH_2$ is observed at approximately 1100 mV vs. Ag/AgCl.

The A_{pc} measured for the oxidation at variable scan rates was then used to construct a curve relating the charge passed to the scan rate. Thus the charge passed due to the oxidation of $RuPICNH_2$ at a scan rate of 100mV s^{-1} was estimated to be approximately 4.83e-8 C.

However, due to the high scan rate used to generate a measurable current associated with $RuPICNH_2$ oxidation, it may be the case that the current generated is primarily due to surface adsorbed species In the case of a diffusive, or solution based, voltammetry regime, the I_{pc} would be proportional the square root of the scan rate ($\upsilon^{1/2}$), whereas in a surface confined regime the I_{pc} would be proportional to the scan rate (υ)[24]. To probe this, a plot of log υ vs. log I_{pc} was generated and is shown in *Figure. 4.4.* This would be the basis for determining if the charge measured was as a result of oxidation of surface confined $RuPICNH_2$ or solution based (diffusive) species. As seen here the slope for this proportionality is greater than the value of 0.5 expected for a redox process under semi-infinite linear diffusion control. Therefore,

the charge measured contains a contribution from surface confined $RuPICNH_2$, and this data cannot be used to determine the efficiency of $RuPICNH_2$ as an ECL luminophore.

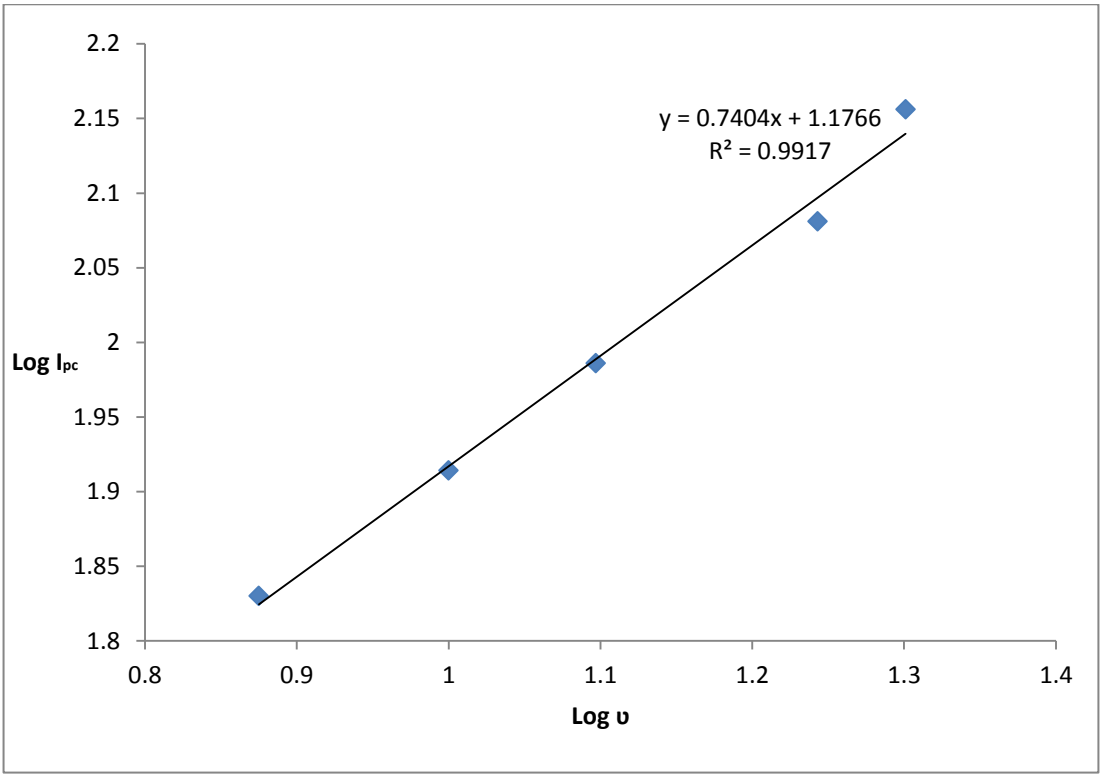

Figure.. 4.4. Plot of log υ vs. Log I_{pc} for $RuPICNH_2$ aqueous voltammetry data. Voltammetry was carried out using a 3 mm diameter glassy carbon electrode and a potential window of 600 – 1500 mV vs. Ag/AgCl at scan rates between 20 and 7.5 V s^{-1} vs. Ag/AgCl.

In order to overcome the issue with low $RuPICNH_2$ concentration and poor signal to noise ratio of the individual oxidative process, a different voltammetric technique was employed, differential pulse voltammetry (DPV). In DPV, a series of regular voltage pulses are measured along a linear potential sweep. Prior to each pulse, the current is measured and the resulting change in current is plotted as a function of potential. This then allows the measurement of current arising from redox processes from exceptionally low concentrations of analyte as the measurement of charging current is minimised and current measured is only due to faradaic processes[25].

This technique was therefore applied to 25µM solutions of $RuPICNH_2$ and $RuBpy_3$ in 10mM PBS vs. Ag/AgCl using a 3mm diameter glassy carbon working electrode and

a platinum wire as counter electrode. A potential increment of 5 mV was employed and voltage amplitude of 50 mV and pulse period of 50 ms. In *Figure. 4.5.* the resulting voltammograms are observed for both $RuPICNH_2$ and $RuBpy_3$.

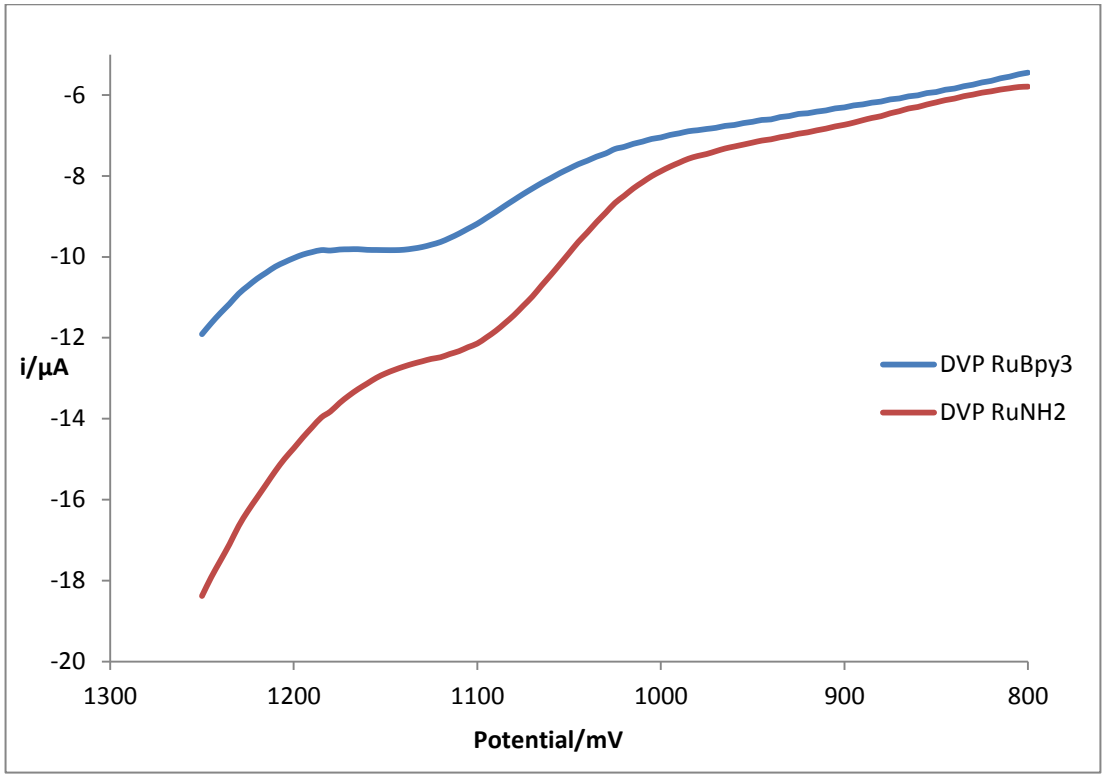

Figure. 4.5. Differential pulse voltammetry data for 25µM $RuPICNH_2$ and 25µM $RuBpy_3$ in 10mM PBS with a 3 mm diameter glassy carbon working electrode and platinum counter electrode, carried out vs. Ag/AgCl. Oxidation of both compounds is observed at approximately 1100 mV.

As seen in *Figure. 4.5.*, with the exclusion of non-faradaic current, the charge associated with the oxidation of both ruthenium compounds at a concentration of 25µM could be measured and was shown to be 9.95e-2 µC and 8.11e-2 µC for $RuPICNH_2$ and $Rubpy_3$ respectively.

Now that the charge associated with the oxidation of both compounds could be accurately measured, the same working electrode was then placed in a solution of 25 µM $RuPICNH_2$ and 10mM PBS with 100µM tripropylamine (TPA) as co-reactant and under a single potential cycle from 200 to 1800 to 200 the resulting ECL output

was measured. In *Figure. 4.6*. the ECL output for both compounds in is shown. Here the onset of ECL is observed at approximately 800 mV coinciding with the oxidation of co-reactant and the oxidation of both compounds is observed at approximately 1100 mV as a sharp increase in ECL intensity. For both compounds the max ECL intensity occurs at approximately 1400 mV. The mean maximum ECL intensity for both $RuPICNH_2$ and $RuBpy_3$ was 2.329A.U. and 7.255A.U., respectively. With these values the ECL efficiency of $RuPICNH_2$ could then be determined, using $RuBpy_3$ as a standard, with the following equation;

$$\phi ECL = \phi ECL0 \left(\frac{i}{Q}.\frac{Q0}{I0}\right)$$

where ϕECL_0 is the efficiency of $RuBpy_3$, I and I_0 are the ECL intensity of $RuPICNH_2$ and $RuBpy_3$ respectively and Q and Q_0 are the charge passed due to the oxidation of $RuPICNH_2$ and $RuBpy_3$ respectively. As a result, the ECL efficiency of $RuPICNH_2$ was determined to be 0.013. This efficiency is therefore approximately 26% of the standardised ECL efficiency of $RuBpy_3$, given as 0.05.

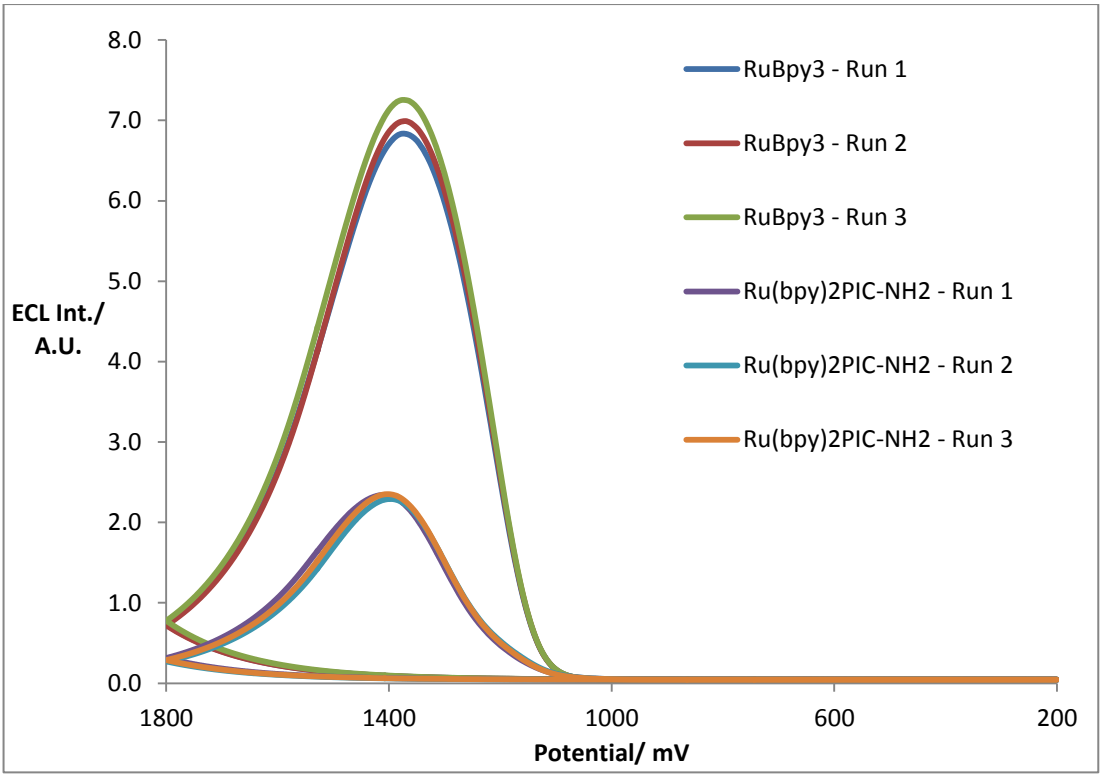

Figure 4.6. ECL output of solution of 2µM $Ru(bpy)_2PIC\text{-}NH_2$ in 10mM PBS with 10mM TPA as co-reactant Vs. Ag/AgCl at a scan rate of 100 mV/s. The onset potential of ECL signal is observed to be between 700 and 800 mV and the oxidation of Ruthenium compounds is observed at approximately 1100 mV.

4.4.2. miRNA Assay on Conventional Gold electrodes.

To develop the miRNA assay, the probe strand of nucleic acid had to be conjugated to the luminophore so that the ECL intensity could be measured in a nucleic acid sandwich assay. The probe strand, a 11bp DNA strand, has a nucleic acid sequence complementary to the 3' end of the miRNA target, miR-132, and also possesses a free thiol group at its 5' end. This free thiol group could be used as a site for the conjugation of the $RuPICNH_2$ luminophore.

For this conjugation reaction to take place a reactive cross linker is required. The most commonly applied method of thiol conjugation is the use of maleimide derivatives. [26] However, traditional bifunctional crosslinkers for amine to thiol conjugation, such as succinimidyl-4-(N-maleimidomethyl)cyclohexane-1-carboxylate (SMCC) were deemed to be unsuitable. This was largely due to the instability of the compound itself and its tendency to hydrolyse in aqueous media[27]. It has also been reported to have a remarkable instability in plasma[28]. Due to the low concentration of DNA probe that would be used in the reaction, as well as the inherent difficultly in purifying and drying a DNA conjugate to the point where it would be a stable solid that could be stored for extended times, a crosslinker was required that would give a high yield and remain stable in solution for at least the duration of the assay incubation time.

The crosslinker sodium-4-((4-(cyanoethynyl)benzoyl)oxy)-2,3,5,6-tetrafluorobenzenesulfonate (CBTF) shown in *Figure. 4.7*, was recently reported by Kolodych et al[29]. This hetero bifunctional crosslinker has two reactive groups, an ester and a reactive cyanoethynyl group, that will bond to amines and thiols respectively. At the ester end of the compound, a tetrafluorobenzenesulfonate group acts as a leaving group to facilitate the formation of an amide between ester and amine. Then the compound is capable of reacting with a thiol to result in a remarkably stable conjugate. The reaction is carried out in two steps, first $RuPICNH_2$ is dissolved in DMSO with a molar equivalent of CBTF and stirred for approximately 10 minutes at room temperature. An aliquot of this reaction mixture, equal to molar equivalent of DNA-thiol to be conjugated, is then added to the thiolated DNA in PBS (pH 7.4) and stirred for a minimum of 60 minutes. The ability to carry out this reaction in such mild conditions cannot be understated, especially

when taking into consideration the instability of DNA under adverse pH or high temperature conditions. The remarkably short reaction time of approximately 70 minutes is also highly advantageous for working with unstable biological conjugates.

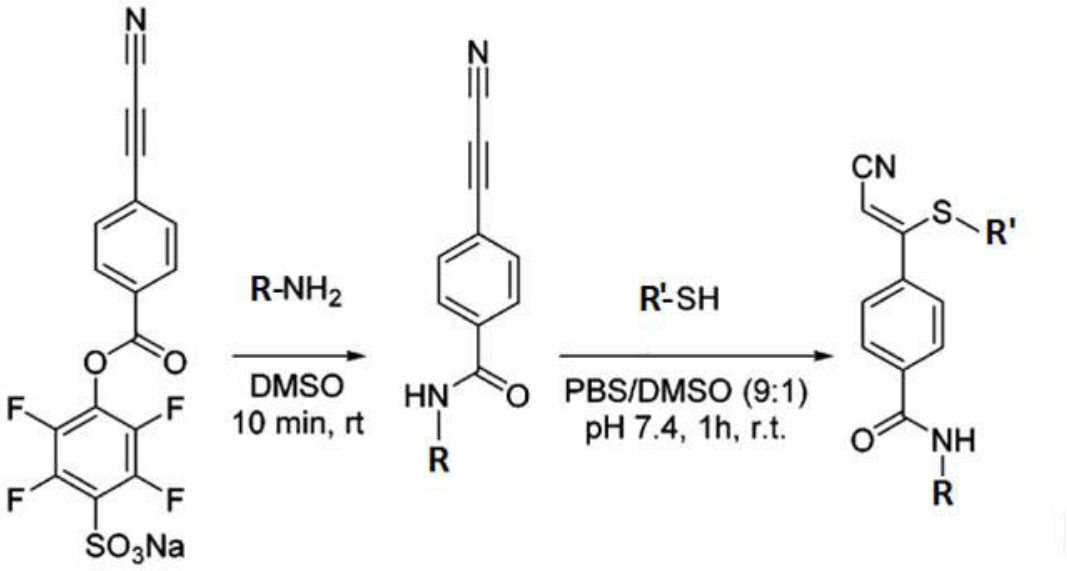

Figure 4.7. Reaction Scheme for the Conjugation of thiolated probe oligonucleotide strand to $RuPICNH_2$ luminophore via CBTF crosslinker. First step of the reaction is carried out in DMSO at room temp. for a minimum of 10 minutes followed by addition to an biomimetic aqueous solution of oligonucleotide and reacted for a minimum of 60 minutes. Reproduced from Kolodych, S., Koniev, O., Baatarkhuu, Z., Bonnefoy, J.Y., Debaene, F., Cianferani, S., Van Dorsselaer, A., and Wagner, A., *CBTF: New Amine-to-Thiol Coupling Reagent for Preparation of Antibody Conjugates with Increased Plasma Stability.* Bioconjugate Chemistry, 2015. **26**(2): p. 197-200

As the thiolated DNA probe strand was expensive (€200 / 100 nmol aliquot) and considering the difficulty that would have been associated with the purification of the $RuPICNH_2$-DNA conjugate, and also the remarkably low expected yield, purification was not attempted. Due to the nature of the assay that the reaction mixture would be used in, the possible contaminants were not seen as a problem as unconjugated $RuPICNH_2$ luminophore would be washed from the electrode surface along with the tetrafluorobenzenesulfonate. There remained the possibility that unconjugated DNA may be present in the reaction mixture, but the high efficiency of bond formation between thiol and cyanoethynyl, it was deemed that this fraction of the DNA would be negligible.

Once the $RuPICNH_2$ luminophore was conjugated to the probe strand established, the efficacy of the proposed miRNA based ECL assay was determined. A polished conventional gold electrode was incubated in a solution of thiolated capture strand DNA to form a monolayer of capture strand as previously established in Chapter 3. Once the monolayer was formed, the electrode was then incubated in a solution of miR-132 for 3 hours and then washed and incubated in a 1μM solution of $RuPICNH_2$-DNA conjugate for 5 hours *(see Figure 4.1.)*.

Following this, the electrode was washed with copious amounts of PBS and placed in an ECL cell containing 50mM TPA as co-reactant and the resulting ECL output of the electrode is shown in *Figure. 4.8*. below. Here, the onset of TPA oxidation is visible at approximately 700 mV and the maximum ECL intensity is observed at a potential of approximately 1200 mV.

The study was then broadened to the use of multiple independently prepared electrodes in order to determine the effect of changing miR-132 concentration would have and whether or not the technique could be applied to the quantitative analysis of miRNA. A range of miR-132 concentrations was chosen between 1 μM and 10 pM, and incubated with the electrode as before. A control for the assay was also prepared in a similar fashion, but the electrode was incubated in clean buffer with no miRNA target. The ECL output of each electrode was then measured in 10mM PBS and 50mM TPA.

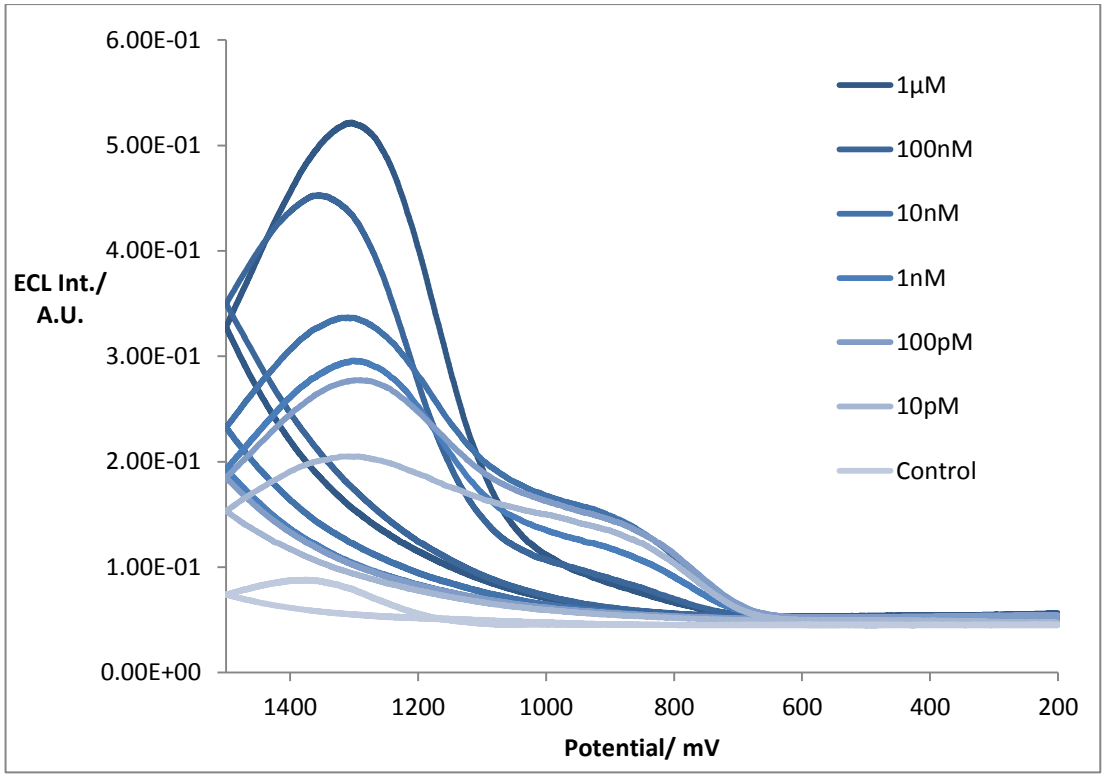

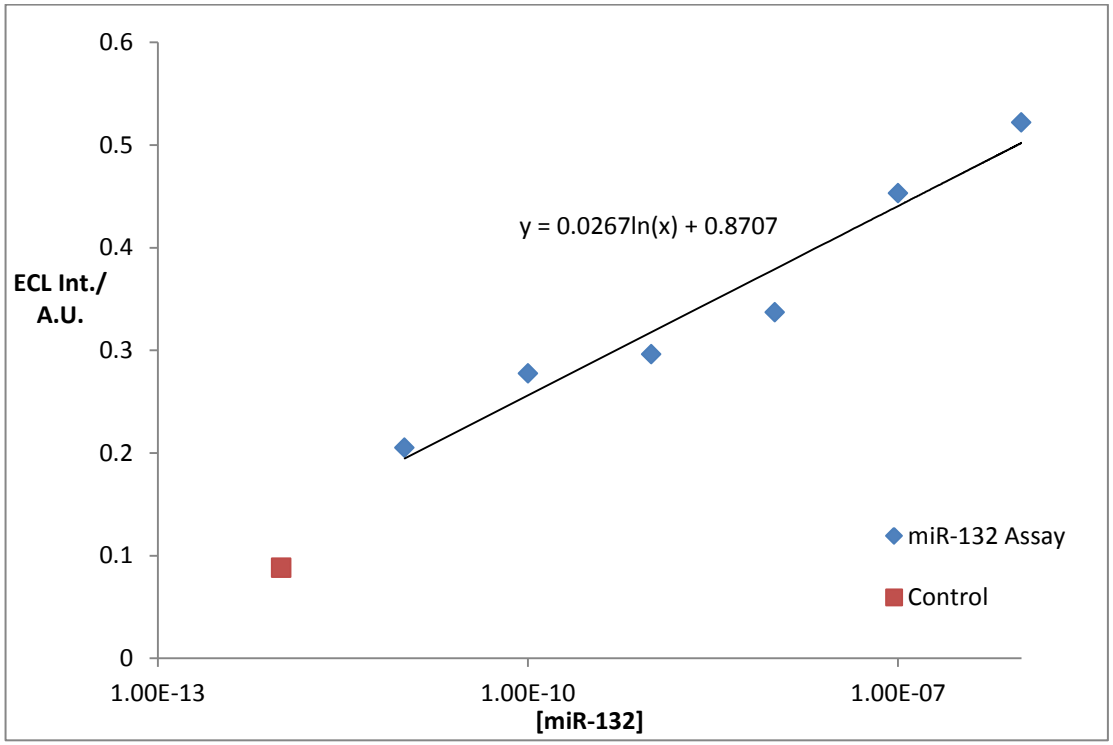

Figure 4.8. ECL data for miR-132 detection assay carried out on planar gold electrodes in 10mM DPBS and 50mM TPA as co reactant. ECL signal was generated by cyclic voltammetry between 200 and 1800 mV vs. Ag/AgCl at a scan rate of 100 mV/s.

From the data above it can be observed that a linear correlation can be observed between the log concentration of miR-132 applied to the surface of the electrode and ECL intensity of each electrode. Shown in red is the ECL intensity for a control electrode, which was incubated in PBS and in the absence of miRNA target. This was used to determine the degree of ECL intensity arising from non-specifically bound luminophore. If all data points are normalised to this value, the log function of this graph is then given as;

$y = 0.0267\ln(x) + 0.7824$

By extrapolating this line to the x-axis (y=0) this was then used to estimate a theoretical limit of detection of the assay,which was determined to be 2.543e-13 M of miR-132, or 254.3 fM.

The overall ECL intensity might be expected to be directly proportional to the concentration of miRNA applied to the electrode. However, this is not the case, as the result do not show that a ten-fold increase in the concentration of miR-132 target incubated with the electrode, does not yield a ten-fold output in ECL intensity observed, as the ECL output is proportional to the number of miR-132 targets immobilised to the surface, which is itself a function of the association constant between the capture and target nucleic acid strands (5.598×10^9 M). Also, the hybridisation of miR-132 to the capture oligonucleotide strand is hindered further due to the steric effects of hybridisation in a densely packed monolayer on the electrode surface. As the capture oligonucleotide monolayer becomes more densely hybridised, the hybridisation of additional miR-132 will become thermodynamically unfavourable due to steric hindrance in the monolayer environment. According to Peterson et al.[30] a densely packed monolayer of oligonucleotides may be subjected to a hybridisation limit of approximated 15%.

4.4.3. Metal Nanoparticle Electrodeposition and Characterisation.

While the assay for the quantification of miR-132 was successful, there is an interest in seeing if plasmonic enhancement could further reduce the limit of detection. Therefore, a nanotextured surface was produced on the electrode which could increase the ECL intensity and perhaps improve the signal-to-noise ratio. Firstly, the increased electrode surface area may provide a larger surface for both TPA oxidation and miR-132 immobilisation and probe hybridisation. Secondly, 3-dimensional nanotextured surfaces exhibit improved mass transport kinetics, which could result in faster rates of TPA oxidation and therefore improved rates of luminophore excitation. But by far the most promising method for luminescent signal enhancement would be from the surface plasmon enhancement of the luminophore by the nanotextured surface. It has been widely reported in the literature that nanotextured surfaces, such metal nanoparticles immobilised to an electrode, have the potential to improve the luminescence of dye molecules located in close proximity so that they are directly influenced by the surface plasmon of the nanoparticle. In fact this forms the basis for the majority of surface enhanced spectroscopy, and in more recent times reports of this surface enhancement being applied to ECL have appeared. Therefore, a new electrode design consisting of a transparent and conductive indium tin oxide (ITO) surface onto which nanoparticles would be electrodeposited was formed.

In order to from nanoparticles on the surface of electrodes, ITO working electrodes were first cut to 17x7mm dimensions and ultrasonicated in methanol for 15 minutes. The electrodes were then placed in a 1mM solution of 16-phosphonohexadecanoic acid for a minimum of 16 hours to form a self-assembled monolayer on the surface of the ITO through which nanoparticles could be electrodeposited. The successful formation of a monolayer on the electrodes surface was then confirmed by voltammetry in 2mM FcMeOH in 100mM KCl. *Figure. 4.9.* shows the redox voltammetry of FcMeOH for an ITO electrode before and after monolayer formation. The depression of redox activity of the FcMeOH following the formation of a C_{16} monolayer can be directly attributed to electrode passivation and an effective decrease in the electrochemical surface area of the electrode by the alkane-phosphono monolayer. Some of the redox activity of the electrode is preserved following the formation of this monolayer, indicating that defect sites are present in the monolayer. However, this is favourable as these sites will act as nucleation sites for nanoparticle growth[22].

Following monolayer formation, electrodes were wrapped with hydrophobic Teflon tape to give a working area on the electrode of 7x7mm. The working area of the electrode was then placed in an appropriate electrodeposition solution and a double potential step was applied to the working electrode to form nanoparticles on the surface. A large negative overpotential for a short time is used to form nucleation sites through the monolayer on the electrode surface and then a growth potential is applied immediately after this for an appropriate time in order to form nanoparticles of a desired size. Following the electrodeposition of metal nanoparticles on the electrode, an increase in the electrochemical surface area of the electrode is observed as expected. Due to the three dimensional nature of the nanoparticles formed on the surface of the electrode the effective surface area of the electrode then increases to approximately the same size as a bare electrode coincidentally.

It was expected that this approach would result in nanoparticles with a narrow size dispersion as nucleation only occurs during the overpotential step and thus all nanoparticles formed are electrodeposited for the same amount of growth time under the same growth potential. In this case for all types of nanoparticle the nucleation

potential was -1600mV and was applied for 20 milliseconds and the growth potential used was -100mV. The growth time was varied in order to obtain the desired size of nanoparticles.

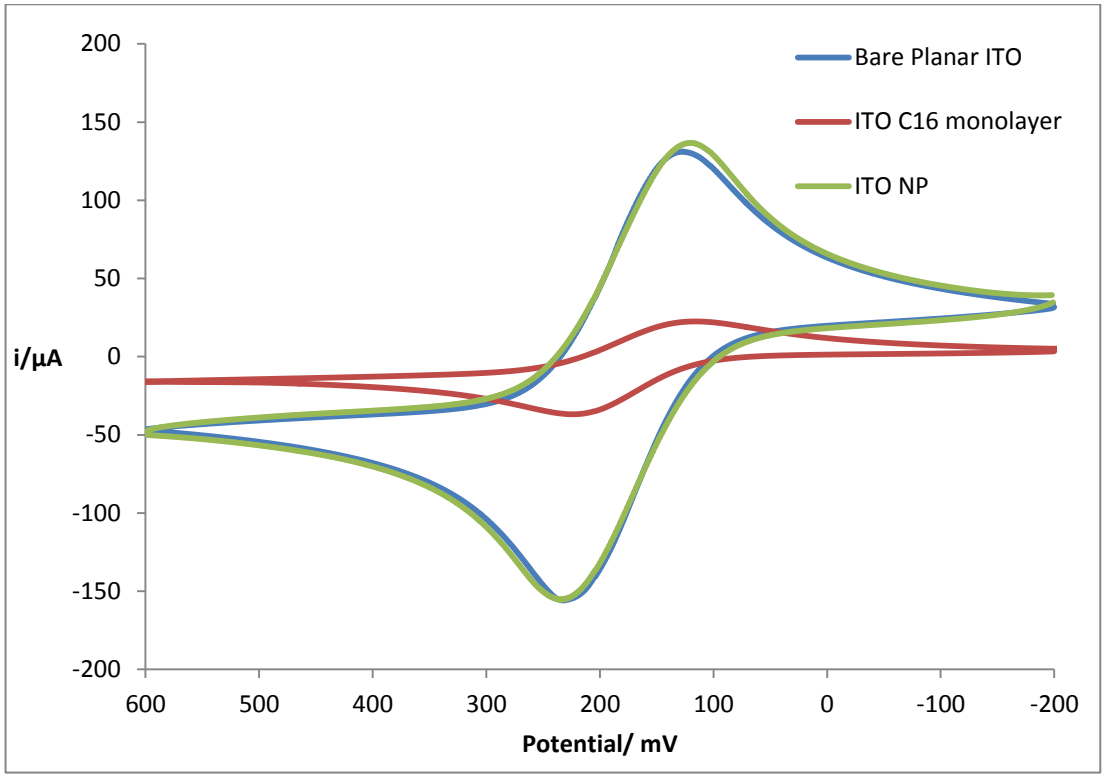

Figure 4.9 Cyclic voltammograms of ITO electrode throughout the fabrication of metal nanoparticles on the electrode surface. 2 mM FcMeOH in 100 mM PB was used to determine the electrochemical surface area of a bare ITO electrode (Blue), electrode following the formation of a C_{16} monolayer on the surface (Red) and following the electrodeposition of nanoparticles to the surface (green). Voltammetry was carried out vs. Ag/AgCl at a scan rate of 100 mV/s.

With this approach, nanoparticle deposition protocols were optimised to produce nanoparticles with a narrow size dispersion, regular shape and high abundance. The concentration of $HAuCl_4$ and growth time were varied and the size, distribution and degree of homogeneity of nanoparticles for each growth time was determined by voltammetry and electron microscopy. *Figure 4.10.* shows voltammograms of ITO electrodes in 10mM H_2SO_4 vs Ag/AgCl following gold nanoparticle deposition for varying growth times. By integration of the oxide monolayer formation peak at approx. 800mV the total surface area of gold electrodeposited to the electrode can be determined. Following this, the electrodes were then imaged using FeSEM to determine the average diameter of nanoparticles on the surface of the electrode. These two area values were then used to determine the number of nanoparticles on the surface of the electrode. In *Figure 4.10.(A)* nanoparticles formed from a 3mM $HAuCl_4$ deposition solution appear to have a poor size distribution, forming particles between approximately 50 and 300 nm with varying degrees of irregularity. By decreasing the growth time from 60 seconds to 10 seconds a greater degree of regularity could be achieved, however, size dispersion was poor and nanoparticles appeared to be formed closely packed and conjoined in parts. *Figure 4.10.(C)* shows that the use of 1 mM $HAuCl_4$ results in well separated nanoparticles with a good size distribution.

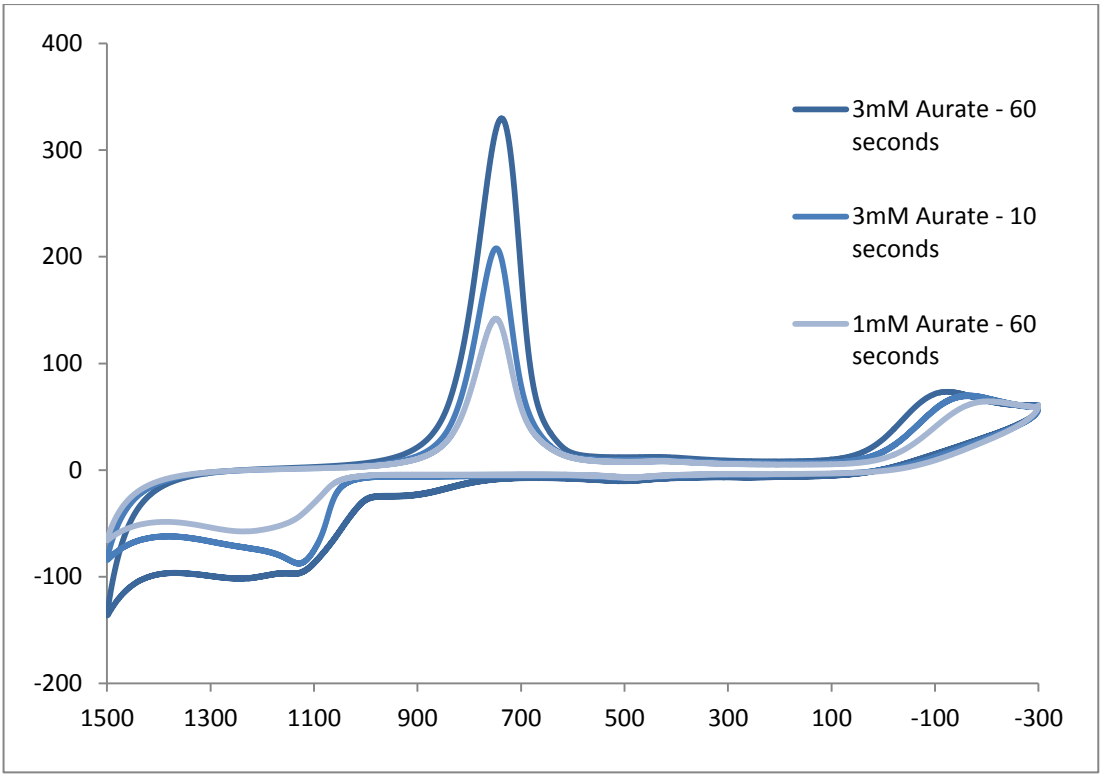

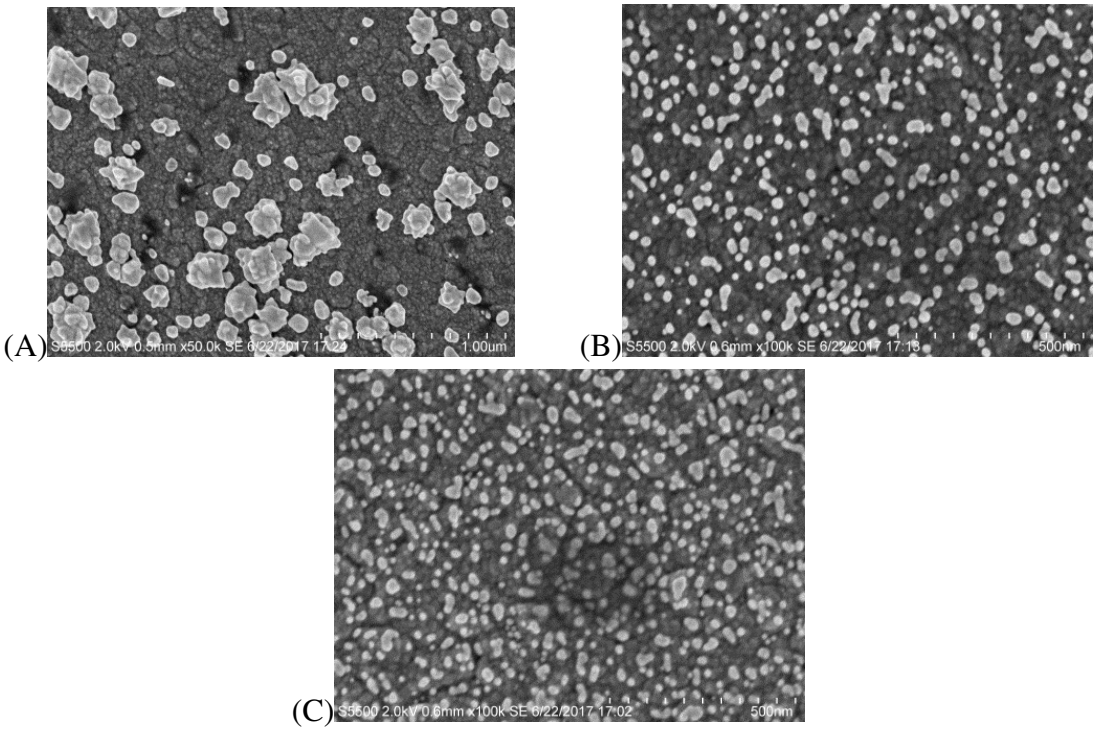

Figure 4.10. Cyclic voltammetry and FeSEM images of nanoparticles formed at varying concentrations of $HAuCl_4$ with varying deposition times. Cyclic voltammetry of ITO AuNP substrates was carried out in 10 mM H_2SO_4 Vs. Ag/AgCl at a scan rate of 100 mV/s, and integration of the gold oxide formation peak at approximately 800 mV was used to determine the overall surface area of gold electrodeposited to the electrode surface. FeSEM SE imaging was carried out under an accelerating potential of 2.0 kV.

Therefore the formation of gold nanoparticles (AuNP), a 1mM aqueous solution of $HAuCl_4$ with 100mM KCl as a supporting electrolyte was used. A three electrode electrochemical cell was set up, with a platinum wire as auxiliary electrode and a Ag/AgCl reference electrode. The working end of the ITO electrode was submerged in the deposition solution and the deposition program was carried out using the multi-potential steps function on the potentiostat.

Electrodeposition of platinum nanoparticles (PtNP) and silver nanoparticles (AgNP) was carried out in a similar fashion, but from a solution of 1mM $KPtCl_6$ in 10mM H_2SO_4 and 1mM $AgNO_3$ in 10mM KNO_3 with 15mM citric acid, respectively. The deposition curves for AuNP, AgNP and PtNP are shown in *Figure 4.11.*

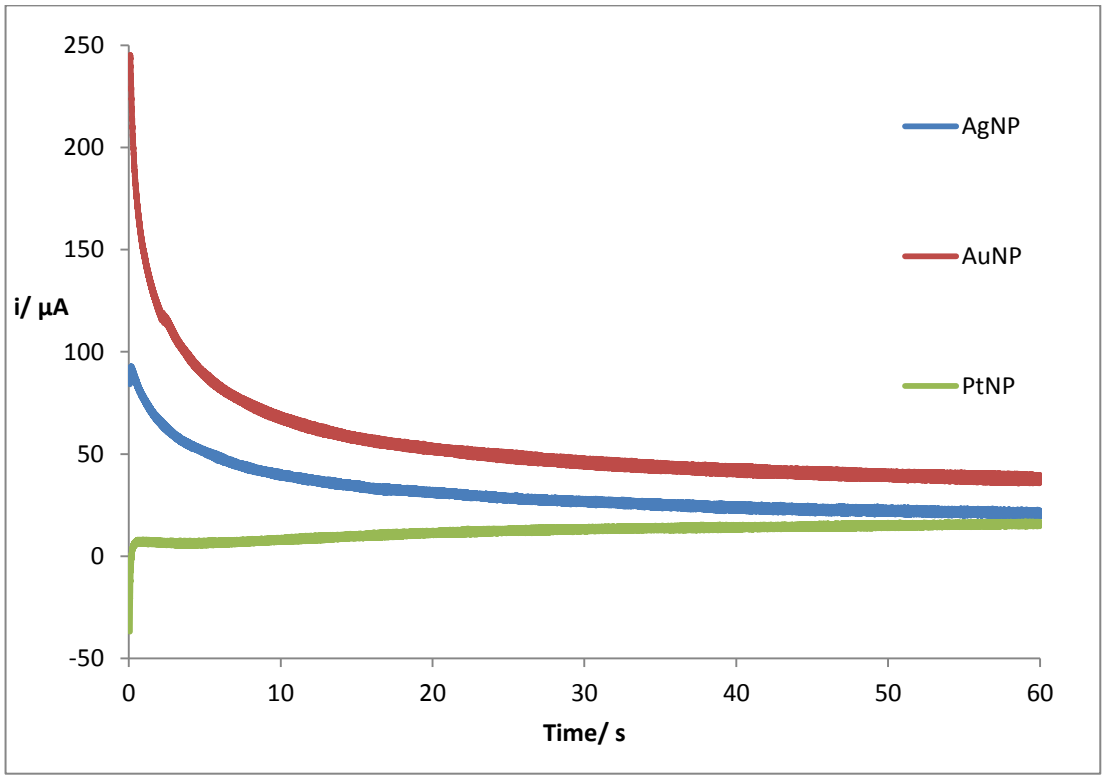

Figure 4.11. Amperometric i/t curves generated during electrodeposition of nanoparticles to the surface of ITO electrodes. Note, the initial 20 ms nucleation overpotential had been omitted in order to show detail. Values for charge passed during deposition of AgNP, AuNP and PtNP were 188, 331 and 72.3 mC respectively.

A similar practice for the determination of size distribution and total particle number deposited was adopted for the formation of PtNP also and in *Figure. 4.12*. the voltammetry of PtNP formed on the surface of electrodes is shown. The typical Pt oxide formation peak may be observed at approximately 230 mV and and may be used to determine the overall surface area of Pt electrodeposited to the surface area of the electrode by integration of the peak area and using a value for the charge associated with oxide monolayer formation of 210μC [31]. Smaller peaks for Pt may also be observed at -110 mV and -220 mV and at approximately -300 mV the onset of hydrogen gas evolution due to water electrolysis may be observed.

However, for silver nanoparticles (AgNP), the surface area of AgNP on the electrodes could not be reliably obtained due to the instability of silver at oxidising potentials. *Figure 4.13.* shows that successive cycles of voltammetry of AgNP on the surface of an ITO. At approximately 700 mV the oxidation of silver to AgO may be observed and at approximately 200 mV the reduction of AgO is observed[32]. It can be observed that successive cycles of voltammetry result in a loss of the oxidative and reductive processes associated with silver nanoparticles and thus a loss in total nanoparticle surface area on the electrode surface.

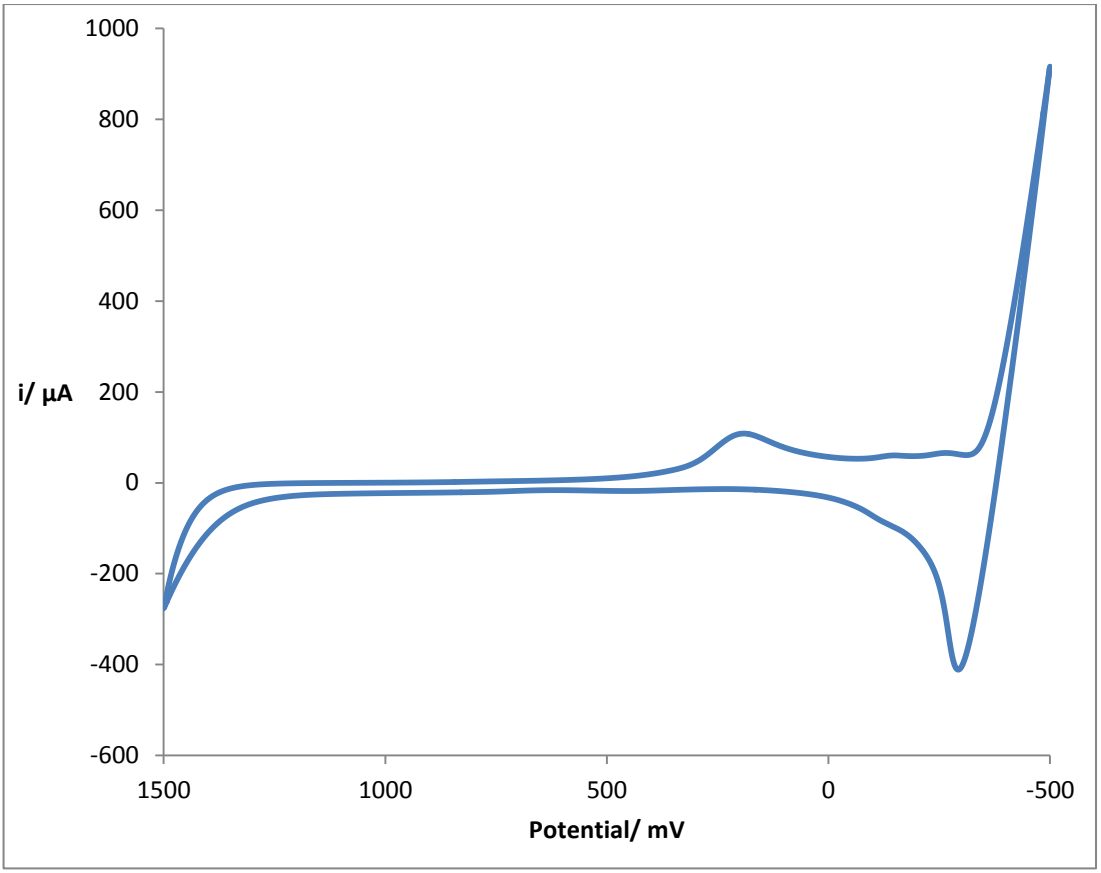

Figure. 4. 12. Cyclic voltammogram of PtNP electrodeposited to ITO electrode between 1500 and -300 mV Vs. Ag/AgCl at a scan rate of 100 mV/s.. carried out in 10mM H_2SO_4 as supporting electrolyte. At approximately 200 mV the peak associated with Pt reduction is observed indicating the formation of PtNP on the surface of the electrode. Further evidence of PtNP formation is observed as the onset of current at approximately -350 mV due to the evolution of hydrogen gas by water hydrolysis at the Pt surface. Through integration of the platinum reduction peak at approximately 200mV the surface area of Pt deposited to the surface of the electrode may be determined.

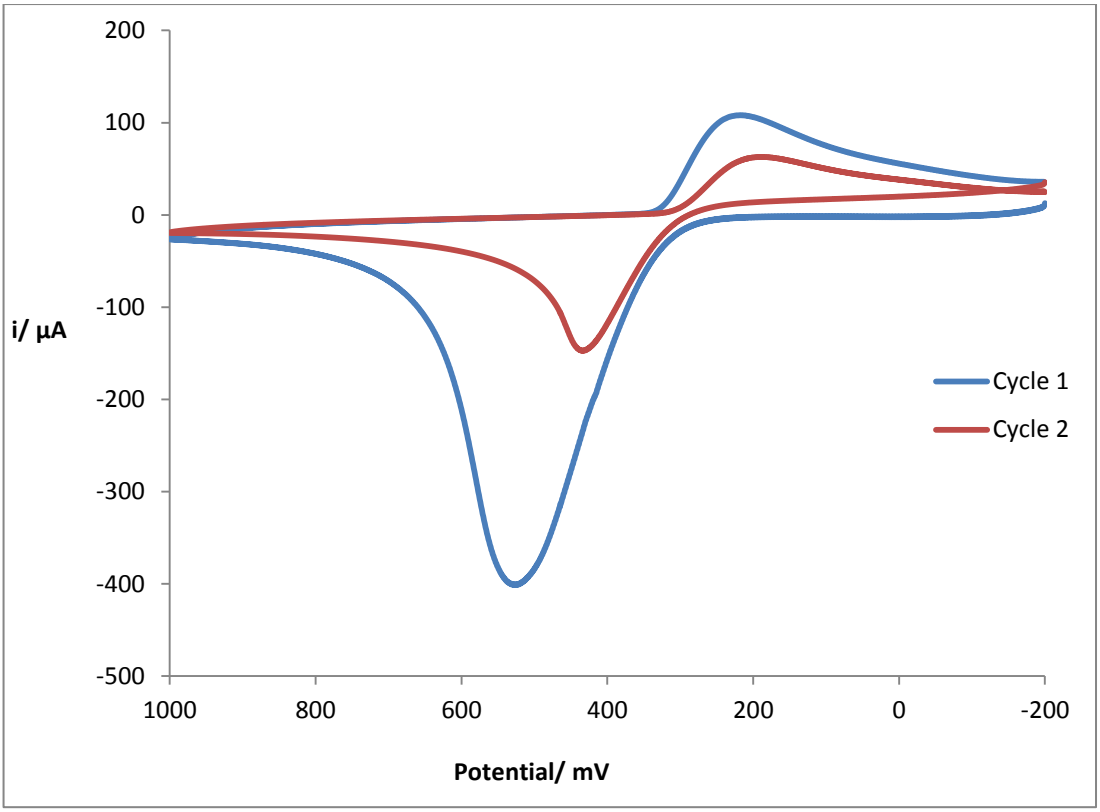

Figure 4.13. Cyclic voltammogram of AgNP electrodeposited to ITO electrode between 1000 and -200 mV Vs. Ag/AgCl at a scan rate of 100 mV/s.. carried out in 10mM H_2SO_4 as supporting electrolyte. Oxidative and reductive peak maxima associated with AgNP occur at approx. 550 and 200 mV vs. Ag/AgCl respectively.

In *Figure. 4.14.* FeSEM images of each nanotextured electrode surface are shown. These images were used to determine the size and size distribution of nanoparticles deposited to the surface of the electrode and in *Figure 4.15.* these distributions are shown. Table 4.1. shows the results obtained from these distribution data sets as well as the total estimated nanoparticle abundance

	Diameter of nanoparticles (nm)								
	Min	Max	Mean	Median	SA of NP/ nm2	SA of NP in cm2	Apc (µC)	S.A./ cm2	Total NP
AuNP	5.540	96.43987	45.16106	43.97497	6361.73	6.36173E-11	183.8	0.471282	7.408E+09
AgNP	11.12	193.3841	71.78391	71.254	15926	1.5926E-10	N/A	N/A	1.428E+09
PtNP	11.1	226.6947	92.18024	88.32579	24494	2.4494E-10	140.2	0.118814	4.851E+08

Table 4. 1. Values for nanoparticle size and distribution electrodeposited to the surface of ITO electrodes. Nanoparticle abundance for AuNP and PtNP was determined from the mean particle size and the total surface area of each respective metal through voltammetry. In the case of AgNP, the total number of nanoparticles was determined for a fixed area using FeSEM imaging and then extrapolated to the entire electrode surface.

From this data as well as the data sets below it is clear that this method for the electrodeposition of noble metal nanoparticles yields an array of particles, directly adsorbed to the surface of an ITO electrode, with a relatively narrow size distribution in the case of AuNP and AgNP, yielding what may result in a nanotextured electrode surface capable of enhancing the luminescent properties of immobilised ECL luminophores. However, in the case of PtNP there is poor control over the distribution of size showing an almost even distribution of size from 20 to 140 nm.

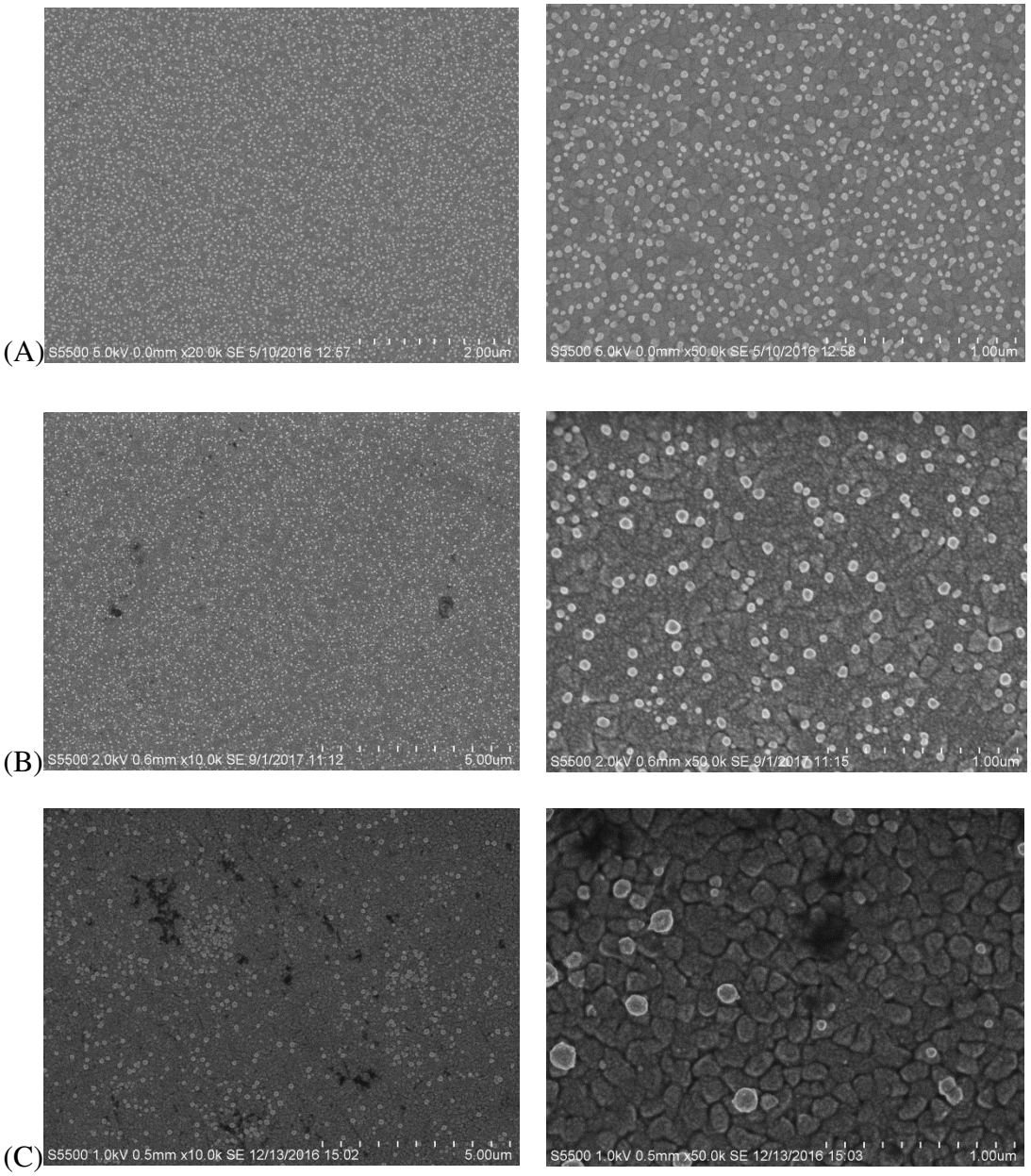

Figure. 4.14. FeSEM images of (A)AuNP, (B)AgNP and (C)PtNP electrodeposited to ITO electrodes. Imaging shows that AuNP and AgNP samples exhibit good size and spatial distribution on the electrode surface, while PtNP electrodeposited to the surface show markedly poorer spatial distribution on the electrode surface and a broader distribution of nanoparticle diameter.

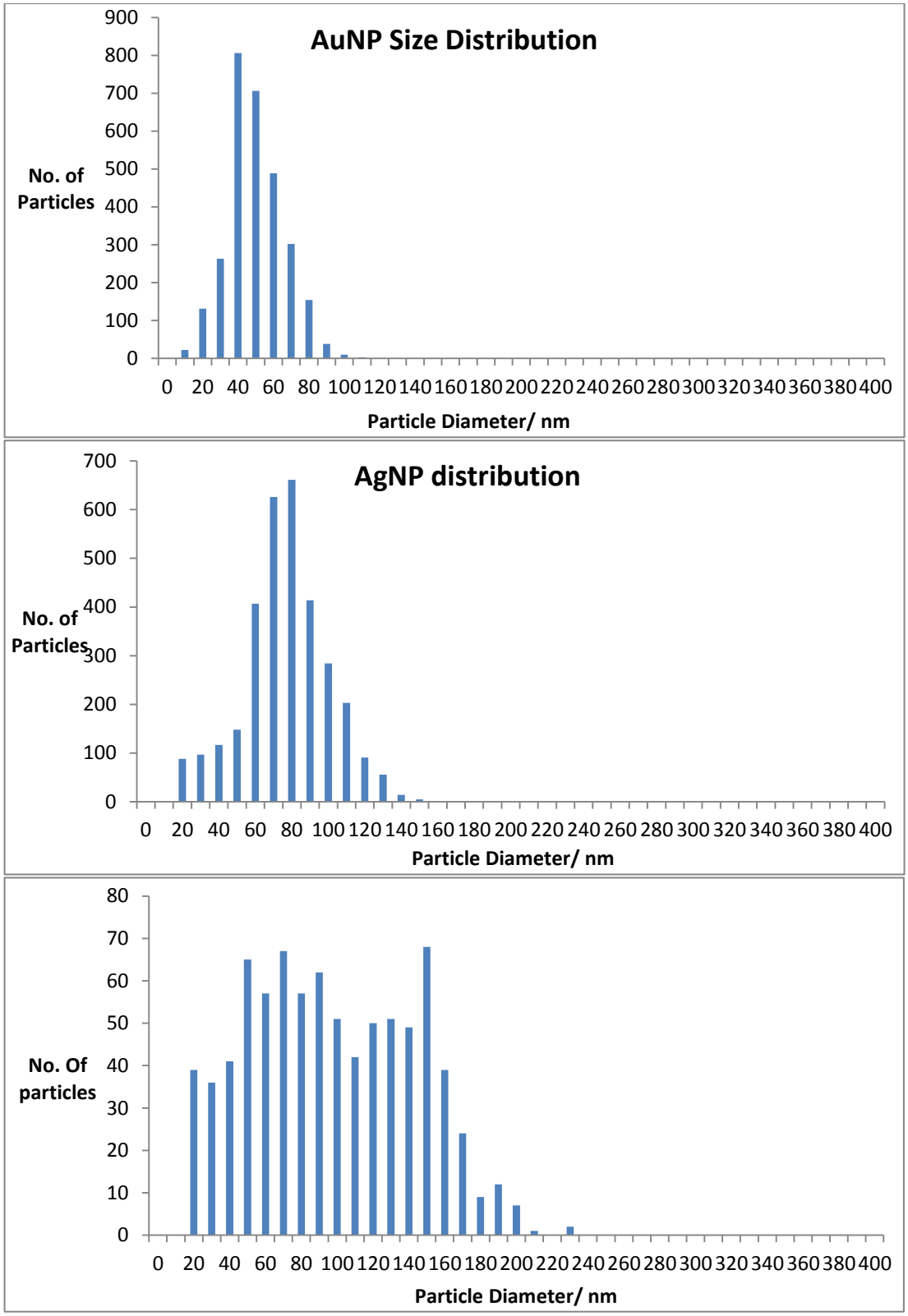

Figure. 4.15. Size distribution data for AuNP, AgNP and PtNP respectively. AuNP and AgNP deposition yields particles with an average size of 45nm and 71nm respectively, however the electrodeposition of PtNP shows poor control over size.

The localised surface plasmon resonance of each nanotextured electrode surface was also measured in order to determine the suitability of the metal nanoparticles for providing a plasmonic enhancement to the emission of luminophores at the surface of the electrode. In *Figure 4.16.* the absorption spectrum of a ITO electrode with AuNP is overlaid with that of the absorption spectra of commercial nanoparticles in solution ranging in size from 20 to 80 nm. For the commercial AuNP the λ_{max} of the 20, 40 and 80nm nanoparticles were 522 nm, 526 nm and 547 nm respectively.

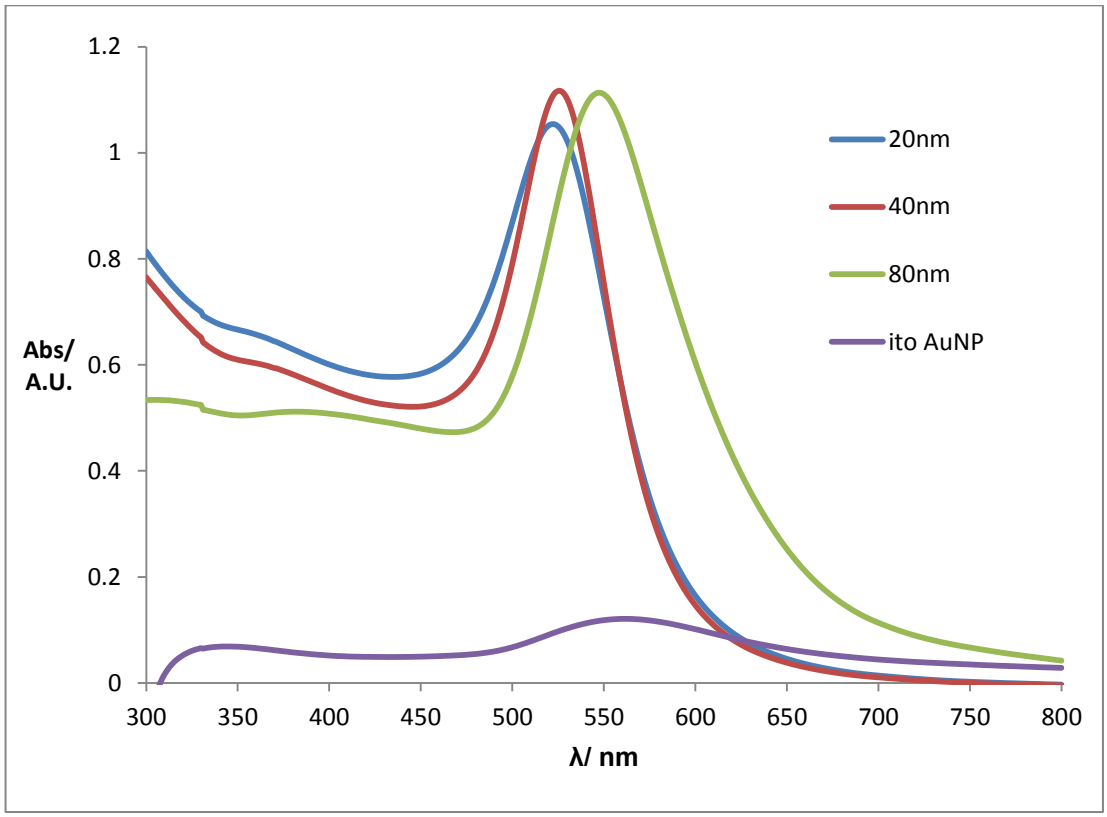

Figure. 4.16. Overlaid absorption spectra of AuNP electrodeposited to an ITO electrode with that of commercial nanoparticles in solution of varying sizes. Absorbencies of both solution and surface bound nanoparticles were determined in deionised water using a 5x7 mm windowed cuvette and a pathlength of 1 cm.

Interestingly for the sample of AuNP electrodeposited to the ITO electrode surface, which had a mean particle diameter of 42 nm (determined by FeSEM imaging) the λ_{max} is significantly redshifted to 562 nm, compared with that of the 40 nm commercial nanoparticles in solution. This tendency for the LSPR of electrodeposited AuNP to be shifted towards longer wavelengths may be an advantage in terms of plasmonic enhancement of luminescence. As the λ_{max} of the ECL luminophore is approximately 610 nm, if gold nanoparticles of a particular size may be deposited that have a significantly overlapping absorption spectrum with that of the luminophores emission spectrum, this would potentially facilitate the radiative plasmon model of metal enhanced fluorescence discussed by Lakowicz et al.. In this scheme, a resonance energy transfer occurs from the excited state luminophore to that of the nanotextured surface, in this case the underlying metal nanoparticle, and this excited state created in the nanoparticle itself then decays radiatively[21, 33]. The nature of the enhancement occurs due to the much shorted lifetime of the excited state in the nanoparticle itself, typically in the order of femtoseconds. Thus luminophores coupled to the nanoparticle plasmon in this scheme may then undergo a greater number of excitation and emission cycles.

In *Figure. 4. 17.* the absorption spectra for both 40 nm commercial AuNP and AuNP electrodeposited to an ITO electrode with an average size of 42 nm are normalised to the number of nanoparticles in solution/ surface bound from which the absorption spectra were measured. The surface bound nanoparticles appear to exhibit a much stronger absorption that that of their solution based commercial counterparts. This may be explained as a result of the distribution of size of particles produced. The size distribution observed is broader than that of commercially produced nanoparticles and it is seen size distribution data that a significant number of particles exist above the mean value of 42 nm. As larger nanoparticles generally exhibit larger extinction coefficients it is suggested that this greater absorbance may be due in part to the contribution of larger nanoparticles in the array. This explanation is also supported by the broadened plasmon absorption peak observed.

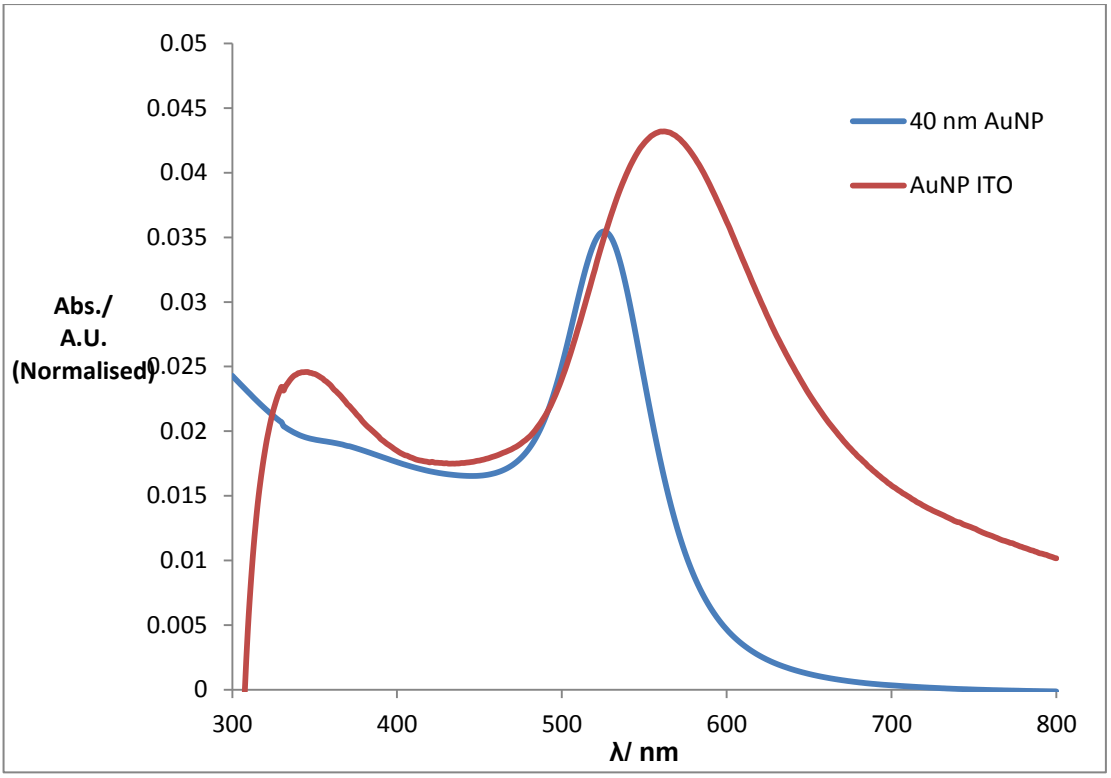

Figure. 4.17. Absorption plots of both commercial 40nm AuNP in solution and AuNP electrodeposited to the surface of an ITO electrode normalised to the number of nanoparticles in each sample.

In *Figure.4.18.* the plasmon absorption bands of PtNP and AgNP are also shown alongside AuNP. It should be noted that for PtNP the absorption peak is very broad and poorly defined, as expected as the LSPR of Pt is quite weak and the overall surface coverage of PtNP formed on the electrode was low, as well as a broad size distribution, when compared to that of AuNP and AgNP depositions. In sharp contrast, the surface plasmon of AgNP is shown to be well defined and occurs at approximately 428 nm, which is in good agreement with literature reports of silver colloids, occurring close to the near UV region[18]. This may indicate that AgNP may be suitable for enhancing the emission of luminophores bound to their surface due to their considerable spectral overlap between the absorption of the nanoparticles and the absorption of the luminophore. However, as the method for luminophore excitation is electrochemically based, and therefore lacking in an incident source of light, in comparison to optical excitation, this scheme for enhancement of luminescence would not be valid in a ECL based assay. Coupled with the poor stability of AgNP under oxidative potentials required to generate ECL, the possibility of AgNP enhancing ECL was not considered further.

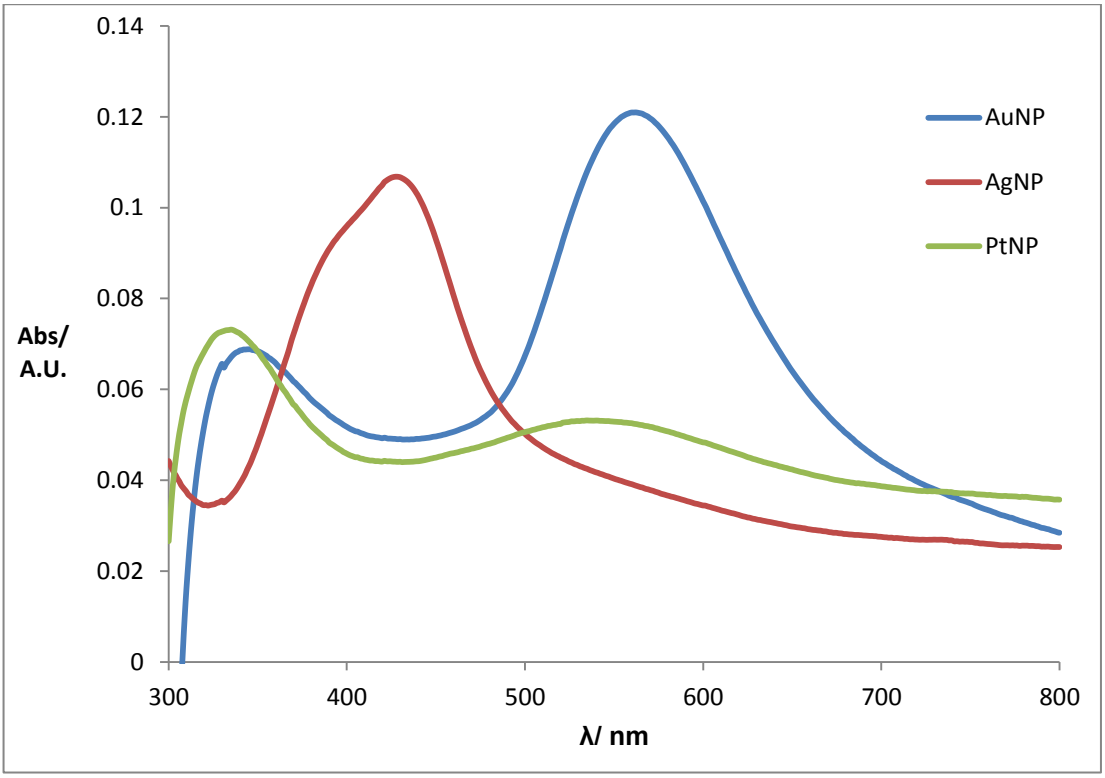

Figure 4. 18. Overlaid surface plasmon absorption spectra of AuNP AgNP and PtNP deposited to the surface of ITO electrodes. The λ_{max} for AuNP, AgNP and PtNP were 562 nm, 428 nm and 520 nm respectively.

4.4.4. Surface Enhanced Raman Spectroscopy of Nanotextured Electrodes.

Once the formation of nanoparticles on the surface was optimised and characterised, it was then determined whether or not these nanotextured surfaces had the potential to bring about any surface enhancement of the ECL luminophore. As the overall surface coverage of dye would be at a maximum of 10^{-10} mol cm^{-1} on a 2 dimensional surface (monolayer surface coverage)[34], experimentally it was deemed that fluorescent spectroscopy was not sensitive enough to detect luminescence at such small scales. However, Raman spectroscopy is well suited to the detection of molecules at surface concentrations of 10^{-11} and lower. The effect of silver nanoparticles resulting in a strong enhancement of Raman signal is well documented in the literature[18, 35]. Reports of Gold being utilised in SERS are also abundant, albeit with a poorer performance being reported in most cases than that of silver[17].

In order to measure the effect of surface enhancement by different nanotextured surfaces, nanoparticles were electrodeposited to ITO electrodes as previously described using 16-phosphonohexadecanoic acid as a template for nanoparticle formation. The resulting gold and platinum nanoparticles were then characterised spectroscopically and electrochemically. The electrodes were then placed in a 2mM ethanolic solution of 16-mercaptohexadecanoic acid for a minimum of 16 hours to form a monolayer of carboxylic acid termini on the surface of the nanoparticles, as well as a monolayer of carboxylic acid termini on the surface of the ITO as a result of the formation of a 16-phosphonohexadecanoic acid monolayer during nanoparticle formation. The ECL luminophore $RuPICNH_2$ was then conjugated to the carboxylic acid termini surface through carbodiimide crosslinking chemistry. This was carried out in dimethylformamide (DMF) using dicyclohexylcarbodiimide (DCC) and N-hydroxysuccinimide (NHS) as this nanoparticle/ monolayer/ dye system had no sensitivity to organic solvents and the yield for organic carbodiimide chemistry based on DCC being markedly higher than that of its aqueous based ethyl-dimethylaminpropylcarbodiimide (EDC) counterpart. Following the conjugation reaction electrodes were washed with copious amounts of DMF to remove any unbound luminophore. The Raman spectra of the electrodes were then measured,

with a nanoparticle free ITO electrode used as a control. The resultant Raman spectra are shown in *Figure. 4.19.* where it can be seen that the PtNP electrode is almost identical to the control. The gold and silver nanoparticle samples show a broad peak at approximately 1600 cm^{-1} that may be the result of poor resolution of two peaks expected at approximately 1560 and 1605 cm^{-1} as a result of a C=C stretch mode. However, it is clear any signal enhancement is modest.

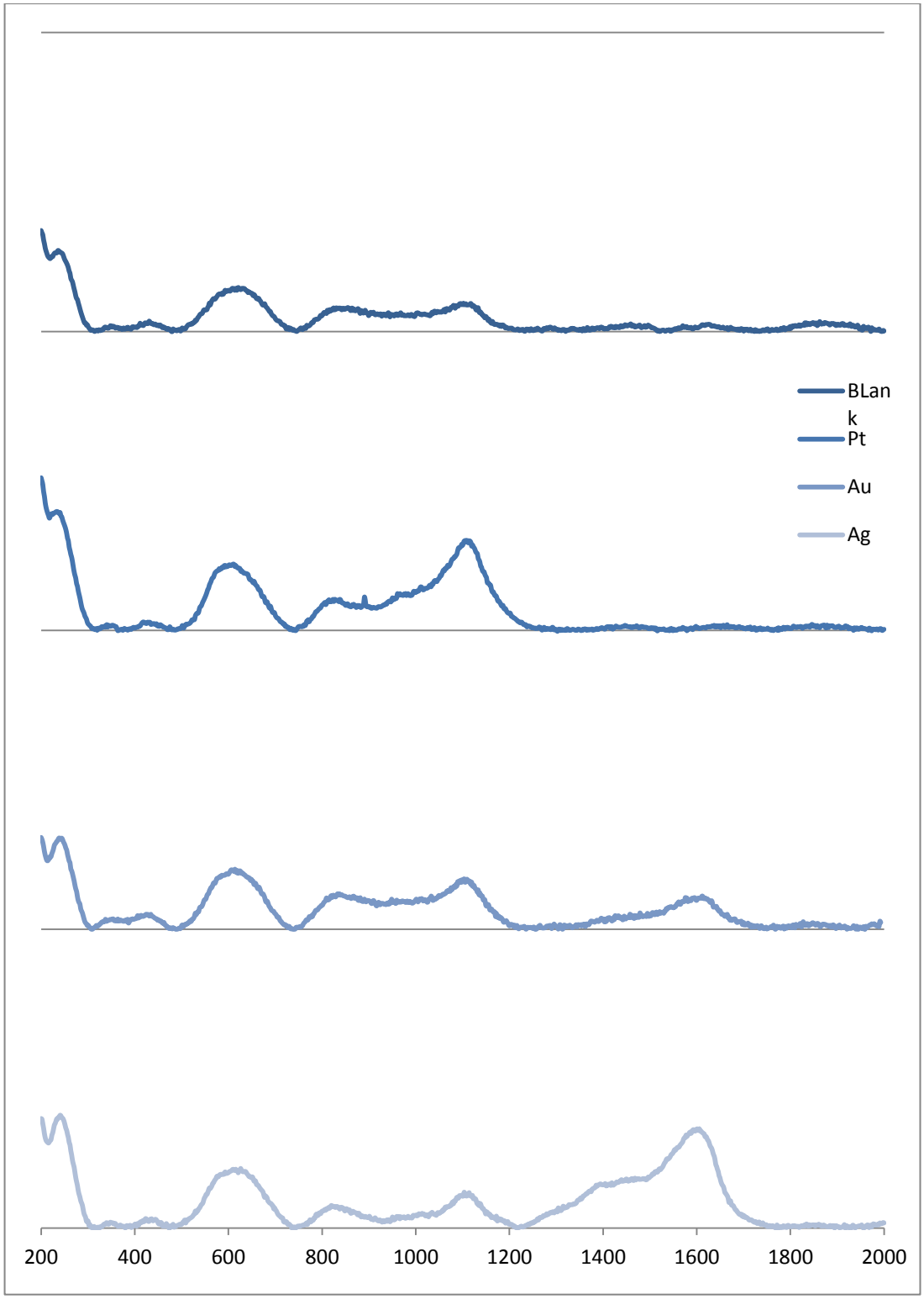

Figure. 4.19. Raman spectra of nanoparticle-ITO electrodes with C_{16} monolayers on the surface conjugated to $RuPICNH_2$. Samples were excited with a 514 nm laser at 100% intensity using a 50x objective with a 300 μm for 10 accumulations and an acquisition time of 10. For both AuNP and AgNP, a peak can be seen at ~1600 cm^{-1}, believed to be a combination of peaks associated with C=C stretch modes of the bipyridyl groups, however this cannot be resolved.

There are many reports of nanoparticles improving the spectroscopic characteristics of luminophores within close proximity, however it is well understood that there is a strong and somewhat counter intuitive relationship between distance and enhancement. There exists a maximum range at which the plasmon may extend to and ultimately where dye and plasmon may be in range for resonance energy transfer to occur and bring about enhancement[21]. This distance depends on a number of key factors including the quantum yield of the dye, spectral overlap of the plasmon absorption band and the luminophores emission wavelength, and the size and shape of the nanoparticles, but is usually limited approximately 10 nm. However, there also exists a minimum distance that molecules must be before an appreciable enhancement is achieved and quenching by acceptor states in the nanoparticle avoided. Therefore, it was decided to compare the Raman results of the monolayer-$RuPICNH_2$ conjugation (16 carbons chain, approx. 2 nm) with that of $RuPICNH_2$-DNA hybridised to the surface (22bp, approx. 5.5-7.5 nm). In these experiments, nanoparticles were electrodeposited on an electrode and a thiolated DNA capture strand monolayer was formed on the surface. The electrode was then incubated in 10 µM miR-132 and then in the $RuPICNH_2$-probe conjugate. Thus, the surface was decorated with $RuPICNH_2$. A lower surface coverage was expected due to a number of factors, chiefly that there would only be hybridisation at the surface of the nanoparticles and not in the spaces between. Also due to steric hindrance of the monolayer itself. In fact it has been reported that a closely packed, surface confined monolayer of nucleic acids can hybridise to target in solution at an efficiency of approximately 10%.

However, as seen in *Figure. 4.20.*, both gold and silver nanoparticle decorated surfaces had an enhancement effect of the Raman signal for $RuPICNH_2$ immobilised to the surface via nucleic acids. In contrast, the blank and platinum nanoparticle samples remained featureless, which was expected due to both the poor morphology of PtNP on the surface and its weak ability to facilitate SERS. In both gold and silver samples there were strong bipyridyl vibrational modes visible at ~1570 and ~1610 cm^{-1} associated with C=C stretching and at ~1330 and ~1495 cm^{-1} associated with C=N stretching. The AgNP sample also exhibited well defined peaks for C-C, CCH, and Ring breathing modes at ~1280, ~1190, and ~1030 cm^{-1} respectively. These

modes, while present in the AuNP sample, were only marginally observable over the background.

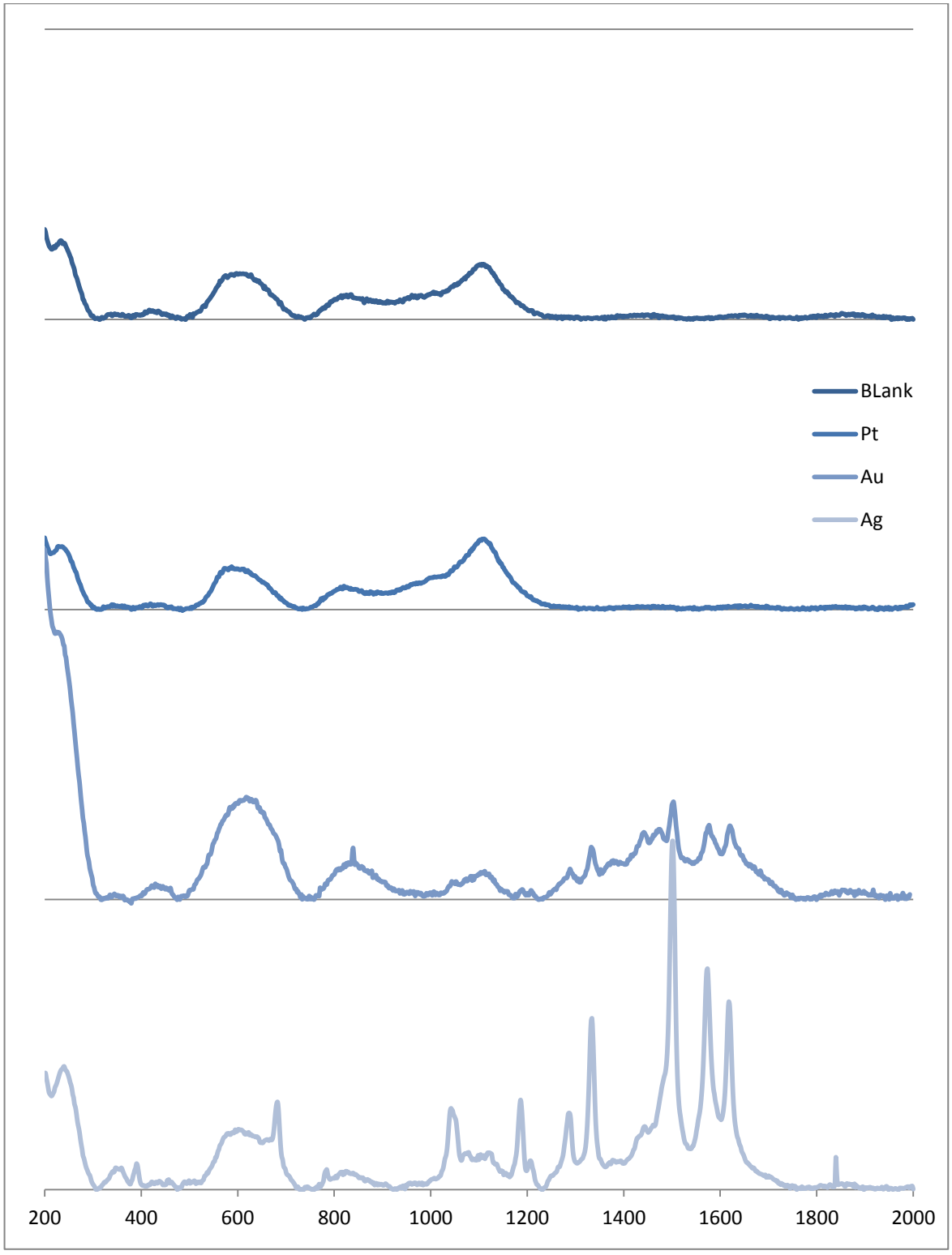

Figure. 4.20. Raman spectra of nanoparticle-ITO electrodes with $RuPICNH_2$ immobilised to the surface through hybridised miRNA. Samples were excited with a 514 nm laser at 100% intensity using a 50x objective with a 300 µm for 10 accumulations and an acquisition time of 10. Both AuNP and AgNP electrodes exhibit strong raman signals associated with the bipyridyl groups of $RuPICNH_2$.

Finally, in order to get conclusive proof that both monolayer $RuPICNH_2$ and DNA-$RuPICNH_2$ samples did indeed have $RuPICNH_2$ bound to the surface, and thus suggesting that the observed increase in raman signal was due to SERS, rather than a lack of bound luminophore, all samples were imaged using confocal microscopy. In *Figure 4.21.* images of all samples used in the previously mentioned raman studies are shown. It should be noted that the resolving power of light microscopy is limited by wavelength and numerical aperture[36] and therefore in these images samples appear to have nanoparticles much larger than those seen in FeSEM images. All examples where $RuPICNH_2$ was conjugated to a monolayer on the surface of the electrode rather than through a nucleic acid chain have much higher apparent background luminescence (between nanoparticles), whereas samples in which the $RuPICNH_2$ was immobilised to the surface through a nucleic acid strand hybridisation appear to have better differentiation between nanoparticles and the space between them. Regardless, it was observed that each sample showed the presence of $RuPICNH_2$ bound to the surface in some form, and thus it was concluded that the differences in Raman spectra observed were due to the enhancement of signal from the underlying nanoparticles and their distance from the nanoparticle itself.

(A)

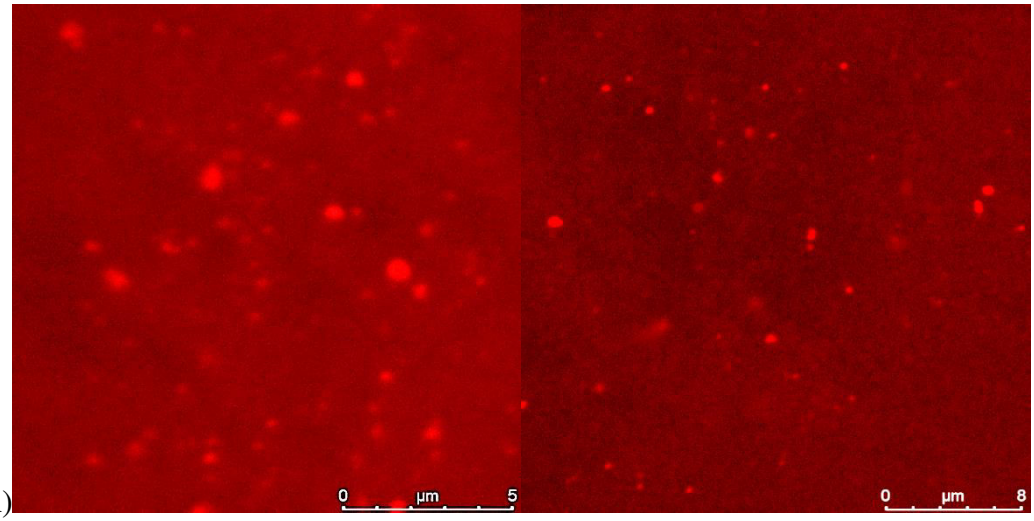

(B)

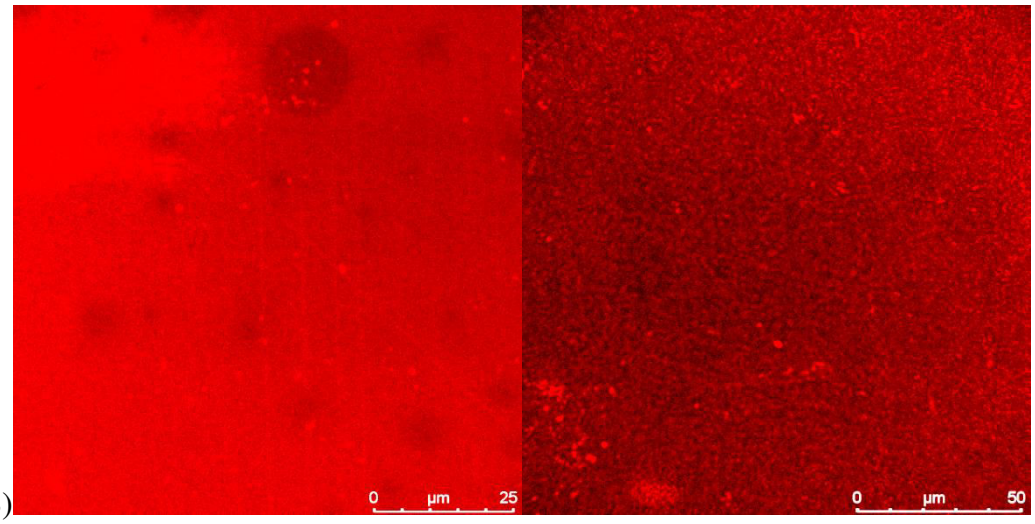

(C)

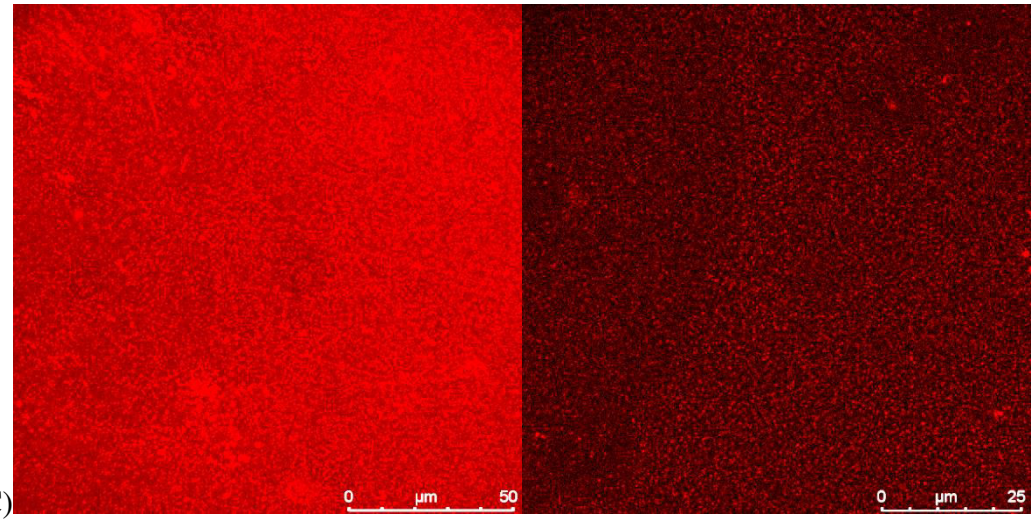

Figure. 4.21. Confocal microscopy images of ITO-NP electrodes used in raman study. Images on the left are PT, Au and Ag monolayer-luminophore conjugated surfaces respectively, exhibiting a high degree of background luminescence due to conjugation of luminophore to the entire electrode surface. Images on the right are of miRNA bound luminophore exhibiting better nanoparticle definition.

4.4.5. ECL detection of miR-132 on gold nanoparticle ITO electrodes.

Following on from this, the nanotextured electrode surface's ability to improve the sensitivity of miRNA detection was investigated. As AuNP-ITO electrodes were seen to have both favourable electrochemical stability, compared to that of AgNP, as well as favourable optical properties, compared to that of PtNP, they were chosen as the nanotextured surface that would best suit the enhancement of the electrochemical detection of miR-132 through ECL.

To begin with, AuNP ITO electrodes were compared alongside planar ITO electrodes in ECL using a 500 nM solution of $RuPICNH_2$ and 50mM TPA in 100mM phosphate buffer. The resulting ECL intensities are shown in *Figure. 4.22*. Here it can be seen that the maximum ECL intensity of the AuNP ITO electrode, approximately 2.21 A.U., is over 3 times greater than that of the bare planar ITO electrode, which was 0.69. As the surface area of the nanoparticles is determined to be $0.47cm^2$ from voltammetry, and if the area between nanoparticles is assumed to be rendered electrochemically inert by the phosphonohexadecanoic acid monolayer formation prior to nanoparticle deposition, then the surface area of both bare ITO (7 x 7mm, or $0.49cm^2$) and the surface area of the ITO-AuNP electrodes can be considered to be similar. Thus it is suggested that the difference in ECL intensity observed between these electrodes is not due to changes in surface area. This indicated that the surface was a good candidate for the enhancement of ECL intensity compared to that of planar conventional gold electrodes previously observed in this chapter.

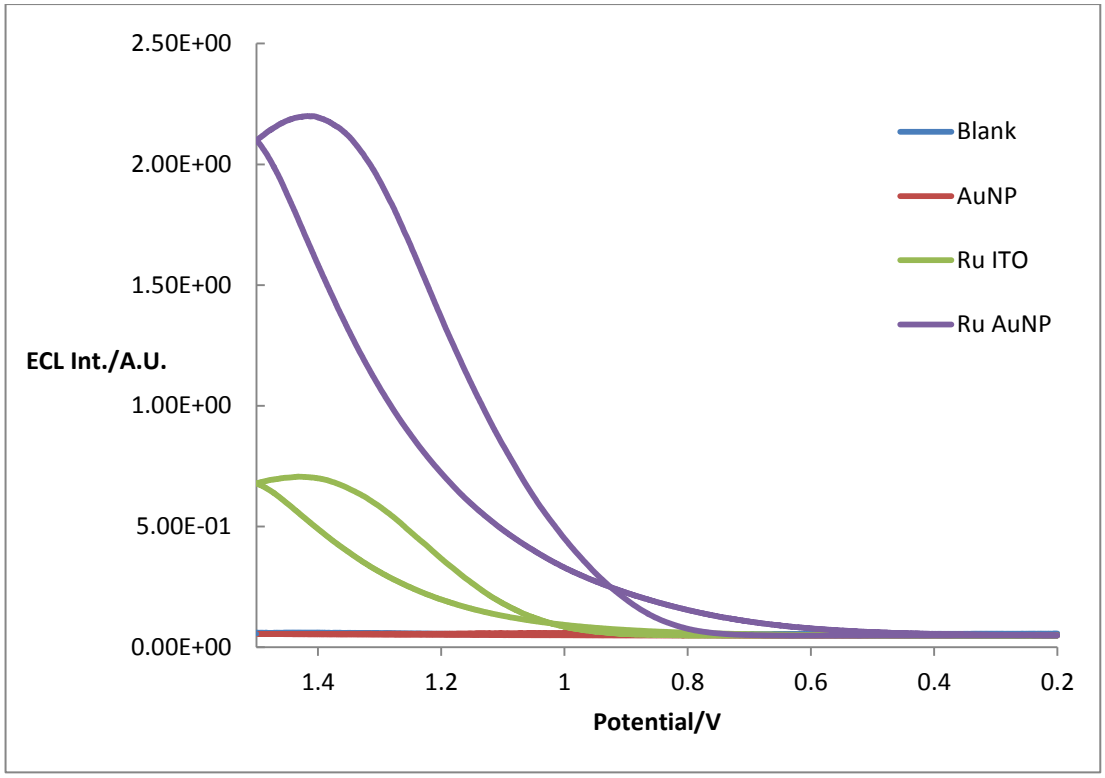

Figure. 4.22. Overlaid ECL outputs of planar ITO (Blue) and AuNP ITO (Red) in the absence of $RuPICNH_2$, and planar ITO (Green) and AuNP-ITO (Purple) in the presence of 500 nM $RuPICNH_2$. All ECL was carried out in 100mM phosphate buffer with 50mM TPA as co-reactant vs. Ag/AgCl at a scan rate of 100 mV/s.

With these results in mind an assay was carried for the detection of miR-132 was carried out using AuNP ITO electrodes. The formation of a nanotextured surface was carried out as previously mentioned in this chapter and surface plasmon absorption of each ITO-NP electrode was determined in order to ensure homogeneity between samples. The surface area of AuNP formed on each electrode was also determined so that assay results could be normalised with respect to the electrochemically active area. The electrodeposited AuNP were then placed in a solution of 1µM thiolated capture oligonucleotide for a minimum of 16 hours to form a monolayer of capture oligo nucleotide on the surface of the nanoparticles. The individual, independent, electrodes were then incubated with varying concentrations of miR-132 for a fixed time, after which they were washed and incubated in a solution of probe oligonucleotide/luminophore conjugate. Following the final incubation, electrodes were then washed with copious amounts of DPBS and then placed in a custom ECL cell from which the ECL output of each electrode could be measured.

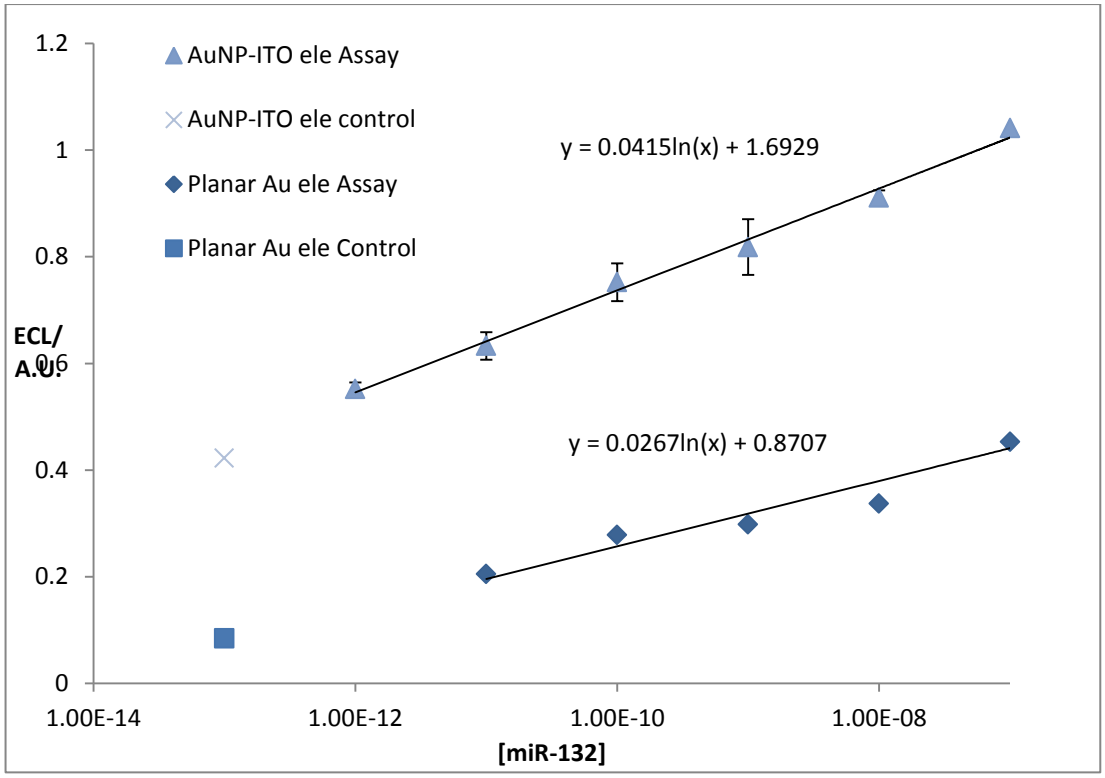

Figure. 4.23. ECL intensities of Planar and AuNP ITO electrodes plotted as a function of [miR-132] incubated with the electrode surface. All ECL measurements were carried out in 100mM phosphate buffer vs. Ag/AgCl with 50mM TPA as co-reactant.

In *Figure 4.23* the data resulting from this assay is presented alongside the data obtained for the assay using planar gold electrodes in *Figure 4.8*, Controls where electrodes were incubated in clean buffer ie. no miRNA target, are also shown for each respective assay. It is important to note that for the purpose of comparison, the data from the AuNP-ITO assay has been normalised to the surface area of the smaller planar gold electrodes that it is being compared to here. This was carried out in a bid to relate the ECL output of the relatively large AuNP-ITO electrodes to that of the smaller planar gold electrodes.

If the value for ECL intensity of controls is subtracted from each assay respectively this data suggests that an enhancement of the ECL output is observed, as the signal output for each data point in the assay carried out on AuNP-ITO electrodes is approximately 2.5 times greater than that of the results of the assay carried out on planar gold electrodes. However the overall magnitude of the ECL intensity seen from control samples is still quite appreciable, most likely to non-specific binding of luminophore to the surface of the electrode. The ratio between the output of ECL in

the control versus assay samples is similar for both planar and nanoparticle modified electrode substrates and therefore it can be concluded that the amount of non-specific binding remained almost constant for both planar gold electrodes and AuNP-ITO electrodes. Therefore, using the data above and subtracting the value for controls from the overall ECL output for each electrode the equation of this calibration curve is then given as;

$$y = 0.0415 \ln(x) + 1.2509$$

Which can then be used to calculate the theoretical limit of detection of this assay, which is given as 8.29 e-14 moles or 83fM. When compared to the theoretical limit of detection of the assay carried out on planar gold electrodes, of 252 fM, this does not appear to be statistically appreciable and thus the limit of detection of both assays is considered to be statistically the same.

The overall increase in ECL for this assay is encouraging, and does suggest that some enhancement to the ECL is occurring, however, the nature of this enhancement is not immediately clear. There are three distinct possible factors that may be contributing to the enhancement observed, increased surface area of the electrode, plasmonic enhancement of the dye by the underlying nanoparticle and improved mass transport diffusion of coreactant. Initially the surface area argument may be easily dissuaded, as the results observed in *Figure. 4.23.* have been normalised in order to relate them the surface area of the planar conventional gold electrodes used to generate the data for *Figure 4.8.* It may be argued that the area between nanoparticles, ie. the ITO surface, may also contribute to the electrode surface area, however, this area has been observed to be passivated by a monolayer during nanoparticle electrodeposition and would not be expected to facilitate charge transfer in an appreciable way compared with that of the gold nanoparticle surface. Also, controls for both of the above mentioned assays are close to equal in proportion to the assay results, suggesting that a larger electrode does not result in a larger signal.

The observed signal enhancement must then be attributed to either plasmonic enhancement or improved mass transport diffusion. The case for plasmonic enhancement however lacks additional evidence such as shortening of luminescent lifetime and also the magnitude of ECL enhancement is much smaller than that reported previously in the literature[16].

This approximate 2.5 fold increase in ECL intensity observed for the AuNP ITO based assay, compared to that of the planar gold electrode assay is far more likely to be due to the 3 dimensional nature of the AuNP ITO electrodes, and their ability to facilitate the fast mass transport diffusion of co-reactant to and from their surface, due to radial diffusion around the surface of the individual nanoparticles, as opposed to the linear diffusion that would be observed for a planar gold electrode surface.

4.5. Conclusion

An assay for the detection and quantitative analysis of miR-132 by electrochemiluminescent detection of $RuPICNH_2$ has been described. A method for the conjugation of the luminescence reporter luminophore, $RuPICNH_2$ was optimised and shown to be effective both through confocal microscopy and ECL. Initial assays carried out on planar gold electrodes have shown that a theoretical limit of detection of sub picomolar miR-132 concentrations was achievable on a planar electrode substrate. Attempts were made to address this issue by the formation of a nanoparticle decorated substrate that would facilitate the plasmonic enhancement of $RuPICNH_2$ luminescence. The optimisation and characterisation of such nanoparticle electrode surfaces is also reported , showing good control over size and distribution for metal nanoparticles electrodeposited to the electrode surface. Furthermore, the particles deposited to the surface display distinct plasmonic properties that are resonant with either the metal complex absorbance (AgNP) or emission (AuNP) making them attractive for both ECL and optical emission based assays.

Attempts were then made to exploit the plasmonic properties of these nanotextured surfaces. Initially, surface enhanced raman spectroscopy gave good evidence that enhancement of luminescence could be possibly facilitated by gold nanoparticles on the surface of the electrode. However, this did not appear to be the case when examined by ECL analysis, and any improvement in signal was likely due to enhanced diffusional mass transport of co-reactant to the surface of the electrode. i.e., a contribution from radial diffusion when nanoparticles are present.

Future work would likely be focused in two directions. Firstly on carrying out lifetime studies on the ECL emission of $RuPICNH_2$ to determine whether the observed luminescent enhancement observed on nanoparticles may be attributed to a decreased lifetime. If this is the case it would make a strong case for the observed enhancement to be plasmonic in nature as it is well understood that in the scheme of radiative plasmon enhancement the emission from resonant energy transfer from luminophore to nanoparticle results in markedly reduced luminescent lifetimes. The other direction of future work would be focused on identifying novel luminophores

that may be exploited in the same way $RuPICNH_2$ was in this ECL detection approach. However, with a spectral overlap between the emission of the luminophore and the plasmon absorption of the nanoparticle surface, such as Iridium (III) luminophores, that have been shown to be compatible with ECL and also display strong emission at approximately 540 nm, markedly closer to the spectral region for the plasmon absorption band of the AuNP electrodeposited to the electrode surface in this chapter. In this scenario, the resonance energy transfer would occur from the excited state luminophore, to the nanoparticle, which may then radiate a photon under certain conditions. This radiative plasmon model of luminescence enhancement, first described by Lakowicz et al. is thought to be the most likely mechanism for the examples of SEECL reported in the literature[21, 33] and therefore would be of great interest for further studies.

4.6. Bibliography

1. Guo, Z.Y., Wu, L., Hu, Y.F., Wang, S., and Li, X., *Potential-resolved "in-electrode" type electrochemiluminescence immunoassay based on functionalized g-C3N4 nanosheet and Ru-NH2 for simultaneous determination of dual targets.* Biosensors & Bioelectronics, 2017. **95**: p. 27-33.
2. Shang, F., Liu, Y., Wang, S., Hu, Y.F., and Guo, Z.Y., *Electrochemiluminescence Immunosensor Based on Functionalized Graphene/Fe3O4-Au Magnetic Capture Probes for Ultrasensitive Detection of Tetrodotoxin.* Electroanalysis, 2017. **29**(9): p. 2098-2105.
3. Pur, M.R.K., Hosseini, M., Faridbod, F., and Ganjali, M.R., *Highly sensitive label-free electrochemiluminescence aptasensor for early detection of myoglobin, a biomarker for myocardial infarction.* Microchimica Acta, 2017. **184**(9): p. 3529-3537.
4. Sardesai, N., Pan, S.M., and Rusling, J., *Electrochemiluminescent immunosensor for detection of protein cancer biomarkers using carbon nanotube forests and Ru-(bpy)(3) (2+)-doped silica nanoparticles.* Chemical Communications, 2009(33): p. 4968-4970.
5. Egashira, N., Morita, S., Hifumi, E., Mitoma, Y., and Uda, T., *Attomole detection of hemagglutinin molecule of influenza virus by combining an electrochemiluminescence sensor with an immunoliposome that encapsulates a Ru complex.* Analytical Chemistry, 2008. **80**(11): p. 4020-4025.
6. Yin, H.S., Li, B.C., Zhou, Y.L., Wang, H.Y., Wang, M.H., and Ai, S.Y., *Signal-on fluorescence biosensor for microRNA-21 detection based on DNA strand displacement reaction and Mg2+-dependent DNAzyme cleavage.* Biosensors & Bioelectronics, 2017. **96**: p. 106-112.
7. Wang, D.F., Li, Y.Y., Lin, Z.Y., Qiu, B., and Guo, L.H., *Surface-Enhanced Electrochemiluminescence of Ru@SiO2 for Ultrasensitive Detection of Carcinoembryonic Antigen.* Analytical Chemistry, 2015. **87**(12): p. 5966-5972.
8. Li, Z.J., Sun, L.J., Zhao, Y., Yang, L.B., Qi, H.L., Gao, Q., and Zhang, C.X., *Electrogenerated chemiluminescence aptasensor for ultrasensitive detection of thrombin incorporating an auxiliary probe.* Talanta, 2014. **130**: p. 370-376.
9. Ge, Z.L., Lin, M.H., Wang, P., Pei, H., Yan, J., Sho, J.Y., Huang, Q., He, D.N., Fan, C.H., and Zuo, X.L., *Hybridization Chain Reaction Amplification of MicroRNA Detection with a Tetrahedral DNA Nanostructure-Based Electrochemical Biosensor.* Analytical Chemistry, 2014. **86**(4): p. 2124-2130.
10. Xu, Z.Q., Liao, L.L., Chai, Y.Q., Wang, H.J., and Yuan, R., *Ultrasensitive Electrochemiluminescence Biosensor for MicroRNA Detection by 3D DNA Walking Machine Based Target Conversion and Distance-Controllable Signal Quenching and Enhancing.* Analytical Chemistry, 2017. **89**(16): p. 8282-8287.
11. Feng, Q.M., Shen, Y.Z., Li, M.X., Zhang, Z.L., Zhao, W., Xu, J.J., and Chen, H.Y., *Dual-Wavelength Electrochemiluminescence Ratiometry Based on Resonance Energy Transfer between Au Nanoparticles Functionalized g-C3N4 Nanosheet and*

Ru(bpy)(3)(2+) for microRNA Detection. Analytical Chemistry, 2016. **88**(1): p. 937-944.

12. Bienertova-Vasku, J., Mazanek, P., Hezova, R., Curdova, A., Nekvindova, J., Kren, L., Sterba, J., and Slaby, O., *Extension of microRNA expression pattern associated with high-risk neuroblastoma.* Tumor Biology, 2013. **34**(4): p. 2315-2319.
13. Saber, R., Sarkar, S., Gill, P., Nazari, B., and Faridani, F., *High resolution imaging of IgG and IgM molecules by scanning tunneling microscopy in air condition.* Scientia Iranica, 2011. **18**(6): p. 1643-1646.
14. Pittman, T.L. and Miao, W.J., *Examination of Electron Transfer Through DNA Using Electrogene rated Chemiluminescence.* Journal of Physical Chemistry C, 2008. **112**(43): p. 16999-17004.
15. Richter, M.M., *Electrochemiluminescence (ECL).* Chemical Reviews, 2004. **104**(6): p. 3003-3036.
16. Wang, D.F., Guo, L.H., Huang, R., Qiu, B., Lin, Z.Y., and Chen, G.N., *Surface Enhanced Electrochemiluminescence of Ru(bpy)(3)(2+).* Scientific Reports, 2015. **5**: p. 7.
17. Saha, K., Agasti, S.S., Kim, C., Li, X.N., and Rotello, V.M., *Gold Nanoparticles in Chemical and Biological Sensing.* Chemical Reviews, 2012. **112**(5): p. 2739-2779.
18. Garrell, R.L. and Schultz, R.H., *SURFACE-ENHANCED RAMAN-SPECTROSCOPY USING NONAQUEOUS COLLOIDAL SILVER.* Journal of Colloid and Interface Science, 1985. **105**(2): p. 483-491.
19. Moskovits, M., *SURFACE-ENHANCED SPECTROSCOPY.* Reviews of Modern Physics, 1985. **57**(3): p. 783-826.
20. Ataka, K., Stripp, S.T., and Heberle, J., *Surface-enhanced infrared absorption spectroscopy (SEIRAS) to probe monolayers of membrane proteins.* Biochimica Et Biophysica Acta-Biomembranes, 2013. **1828**(10): p. 2283-2293.
21. Lakowicz, J.R., *Radiative decay engineering 5: metal-enhanced fluorescence and plasmon emission.* Analytical Biochemistry, 2005. **337**(2): p. 171-194.
22. Liu, H., Favier, F., Ng, K., Zach, M.P., and Penner, R.M., *Size-selective electrodeposition of meso-scale metal particles: a general method.* Electrochimica Acta, 2001. **47**(5): p. 671-677.
23. Climent, V. and Feliu, J.M., *Cyclic Voltammetry*, in *Reference Module in Chemistry, Molecular Sciences and Chemical Engineering*. 2015, Elsevier.
24. Nicholson, R.S., *THEORY AND APPLICATION OF CYCLIC VOLTAMMETRY FOR MEASUREMENT OF ELECTRODE REACTION KINETICS.* Analytical Chemistry, 1965. **37**(11): p. 1351-+.
25. Howard, E., Cassidy, J.F., and O'Gorman, J., *Electroanalysis using differential pulse methods at a microelectrode.* Electroanalysis, 1998. **10**(17): p. 1208-1210.
26. Hermanson, G.T., *Bioconjugate Techniques*. 2 ed. 2008: Academic Press.
27. Koniev, O., Leriche, G., Nothisen, M., Remy, J.S., Strub, J.M., Schaeffer-Reiss, C., Van Dorsselaer, A., Baati, R., and Wagner, A., *Selective Irreversible Chemical Tagging of Cysteine with 3-Arylpropiolonitriles.* Bioconjugate Chemistry, 2014. **25**(2): p. 202-206.
28. Shen, B.Q., Xu, K.Y., Liu, L.N., Raab, H., Bhakta, S., Kenrick, M., Parsons-Reponte, K.L., Tien, J., Yu, S.F., Mai, E., Li, D.W., Tibbitts, J., Baudys, J., Saadi, O.M., Scales, S.J., McDonald, P.J., Hass, P.E., Eigenbrot, C., Nguyen, T., Solis, W.A., Fuji, R.N.,

Flagella, K.M., Patel, D., Spencer, S.D., Khawlil, L.A., Ebens, A., Wong, W.L., Vandlen, R., Kaur, S., Sliwkowski, M.X., Scheller, R.H., Polakis, P., and Junutula, J.R., *Conjugation site modulates the in vivo stability and therapeutic activity of antibody-drug conjugates.* Nature Biotechnology, 2012. **30**(2): p. 184-189.

29. Kolodych, S., Koniev, O., Baatarkhuu, Z., Bonnefoy, J.Y., Debaene, F., Cianferani, S., Van Dorsselaer, A., and Wagner, A., *CBTF: New Amine-to-Thiol Coupling Reagent for Preparation of Antibody Conjugates with Increased Plasma Stability.* Bioconjugate Chemistry, 2015. **26**(2): p. 197-200.
30. Peterson, A.W., Heaton, R.J., and Georgiadis, R.M., *The effect of surface probe density on DNA hybridization.* Nucleic Acids Research, 2001. **29**(24): p. 5163-5168.
31. Daubinger, P., Kieninger, J., Unmussig, T., and Urban, G.A., *Electrochemical characteristics of nanostructured platinum electrodes - a cyclic voltammetry study.* Physical Chemistry Chemical Physics, 2014. **16**(18): p. 8392-8399.
32. Petersen, S.L. and Tallman, D.E., *SILVER COMPOSITE ELECTRODE FOR VOLTAMMETRY.* Analytical Chemistry, 1988. **60**(1): p. 82-86.
33. Zhang, J., Gryczynski, Z., and Lakowicz, J.R., *First observation of surface plasmon-coupled electrochemiluminescence.* Chemical Physics Letters, 2004. **393**(4-6): p. 483-487.
34. Eckermann, A.L., Feld, D.J., Shaw, J.A., and Meade, T.J., *Electrochemistry of redox-active self-assembled monolayers.* Coordination Chemistry Reviews, 2010. **254**(15-16): p. 1769-1802.
35. Driskell, J.D., Seto, A.G., Jones, L.P., Jokela, S., Dluhy, R.A., Zhao, Y.P., and Tripp, R.A., *Rapid microRNA (miRNA) detection and classification via surface-enhanced Raman spectroscopy (SERS).* Biosensors & Bioelectronics, 2008. **24**(4): p. 917-922.
36. Muller, T., Schumann, C., and Kraegeloh, A., *STED Microscopy and its Applications: New Insights into Cellular Processes on the Nanoscale.* Chemphyschem, 2012. **13**(8): p. 1986-2000.

Chapter 5.

Conclusion and Future Work.

5. Conclusion and Future Work.

This thesis reports on electrochemical approaches for the detection of cellular and genetic biomarkers of Neuroblastoma. Here the focus was on developing assays for the sensitive and selective detection of minimal disease biomarkers.

The initial chapter was focused on reviewing the current literature surrounding neuroblastoma and miRNA, as well as the current and emerging approaches in detection of cellular and genetic biomarkers and their underlying mechanics. Following on from this, Chapter 2 was focused on the immobilisation of neuroblastoma cells to an electrode surface and their subsequent detection by electrochemical impedance spectroscopy and amperometry. The outcome of this was that while both approaches were capable of carrying out qualitative detection of cells immobilised to the surface of an electrode at low counts (<10 cells), signal output was not linear and quantitative data could not be reliably extracted from this assay for cell counts lower than approximately 100 cells.

Chapter 3 was focused on the development of microcavity arrays for the immobilisation and lysis of neuroblastoma cells and the subsequent detection of miRNA targets within. This chapter was primarily concerned with the formation of a bifunctional microcavity array where the outer and inner surfaces of the microcavity array could be independently modified. The outer surface of the microcavity arrays was developed as a cell capture platform, while the inner surfaces of the microcavities were modified with an self-assembled monolayer of oligonucleotides complementary to miR-132, a miRNA whose expression is upregulated in neuroblastoma. Following cell lysis and immobilisation of miR-132 to the inner surface of the microcavity, an electrocatalytic PtNP modified with probe oligonucleotide could then be hybridised to the immobilised miRNA target. This PtNP, under an applied potential, could then carry out the electrocatalytic reduction of H_2O_2 producing a current proportional to the number of PtNP immobilised to the microcavity and thus, proportional to the number miRNA targets immobilised to the microcavity surface. The outcome of this work was that while cell immobilisation and lysis was carried out successfully, the subsequent detection of miRNA by amperometry proved to be inadequate, due to the excessive background reduction of

H_2O_2 by the microcavity surface itself. It was determined that this excessive current generation by the microcavity surface was a result of the formation of the microcavities themselves. Measures were taken to attempt to reduce the influence of the microcavity array on current generation, however these proved unsuccessful.

Chapter 4 was then focused on carrying out the detection of miR-132 by electrochemiluminescence. Here the miRNA target would once again be detected through immobilisation to a surface by an oligonucleotide and then hybridisation of a probe, however in this case the probe was now a luminophore that could be excited electrochemically to produce a measurable light output. Initial assay results carried out on planar gold electrodes showed that ECL output could be correlated with the concentration of miR-132 applied to the electrode surface, however the assay had poor sensitivity. Therefore the latter half of this chapter was reported the attempts made to enhance signal output through development of electrodes with nanotextured surfaces. Throughout this work, the formation and characterisation of electrodeposited nanoparticles was reported. Gold and Silver nanoparticle surfaces were shown to give surface enhanced raman spectroscopy of luminophores when they were bound to the surface by miRNA hybridisation, or at a distance of approximately 7 nm. This signal enhancement was then shown to be distance dependant as surfaces with luminophores bound closely to the surface of nanoparticles by a self-assembled monolayer, approximately 2 nm in length. This approach of nanoparticle mediated surfaced enhanced electrochemiluminescence was applied to the detection of miRNA as previously described. While signal enhancement was observed, the sensitivity of the assay did not increase and it was unclear whether or not the perceived signal enhancement was due to plasmonic enhancement of luminophore emission, or due to the enhanced kinetics of the nanotextured surface.

To elucidate the exact mechanism of enhancement observed here, future work would initially be concerned with the study of the change in luminescent lifetime of luminophores during ECL signal generation. If a change in the lifetime of luminophores bound to the surface of nanoparticles was observed to be shortened, this would suggest that the enhancement of luminescent emission observed at nanotextured surfaces was due to plasmonic enhancement rather than improved mass transport diffusion of coreactant.